TU Delft

Delft University of Technology

Document Version
Final published version

Citation (APA)
Lee, Y. C. (2026). *Applying the Nonlinear Fourier Transform to Non-Integrable Real-World Ocean Waves: Analysis of Rogue Waves and Soliton Gases*. [Dissertation (TU Delft), Team Raf Van de Plas].
https://doi.org/10.4233/uuid:8c757f7b-5f6c-43f0-8f6c-9a7ef6d2c30e

Important note
To cite this publication, please use the final published version (if applicable).
Please check the document version above.

Copyright
In case the licence states “Dutch Copyright Act (Article 25fa)”, this publication was made available Green Open Access via the TU Delft Institutional Repository pursuant to Dutch Copyright Act (Article 25fa, the Taverne amendment). This provision does not affect copyright ownership.
Unless copyright is transferred by contract or statute, it remains with the copyright holder.

Sharing and reuse
Other than for strictly personal use, it is not permitted to download, forward or distribute the text or part of it, without the consent of the author(s) and/or copyright holder(s), unless the work is under an open content license such as Creative Commons.

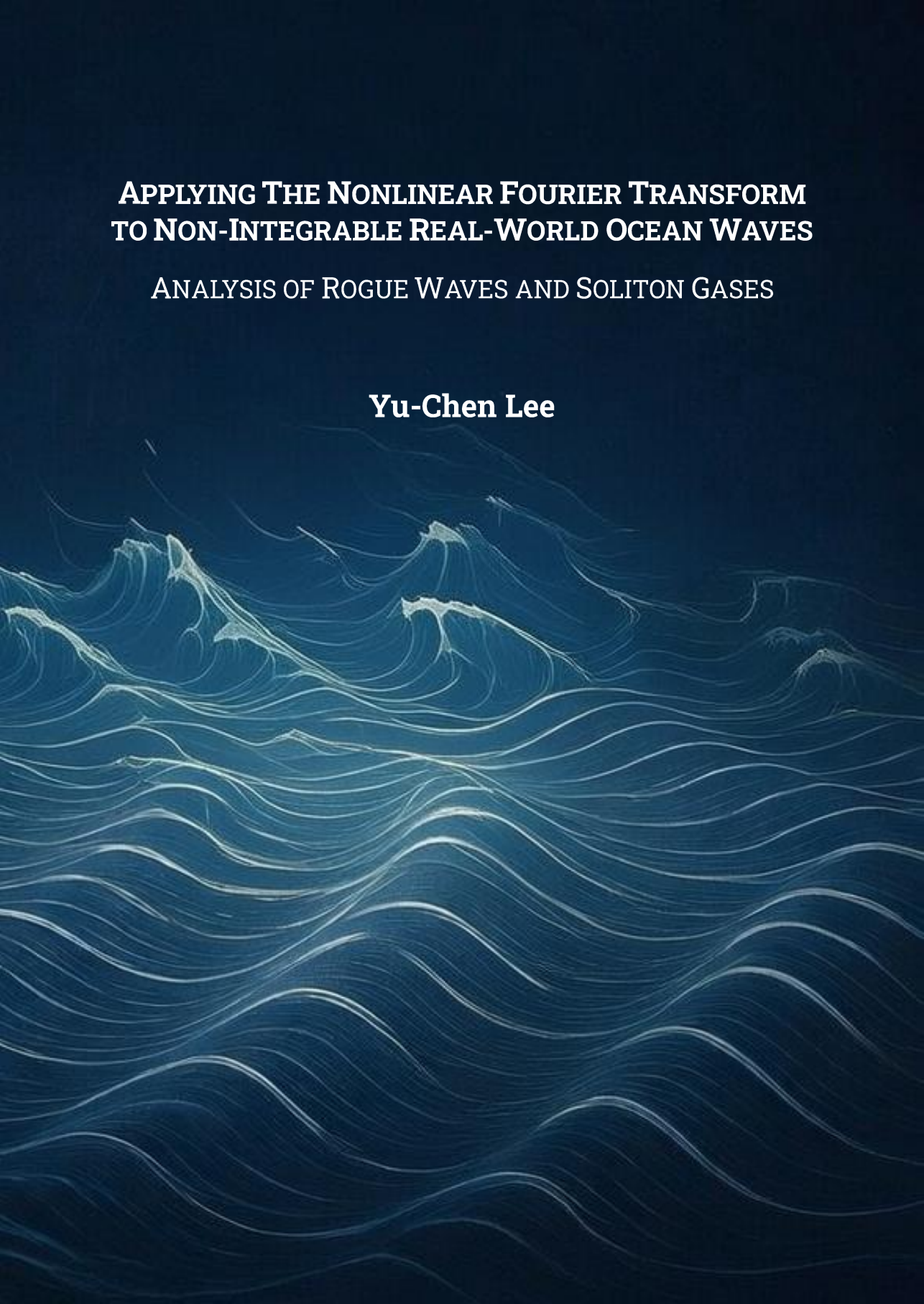
Takedown policy
Please contact us and provide details if you believe this document breaches copyrights.
We will remove access to the work immediately and investigate your claim.

This work is downloaded from Delft University of Technology.

Applying The Nonlinear Fourier Transform to Non-Integrable Real-World Ocean Waves

Analysis of Rogue Waves and Soliton Gases

Yu-Chen Lee



Applying the Nonlinear Fourier Transform to Non-Integrable Real-World Ocean Waves

Analysis of Rogue Waves and Soliton Gases

Applying the Nonlinear Fourier Transform to Non-Integrable Real-World Ocean Waves

Analysis of Rogue Waves and Soliton Gases

Dissertation

for the purpose of obtaining the degree of doctor
at Delft University of Technology
by the authority of the Rector Magnificus,
Prof. dr. ir. H. Bijl,
chair of the Board for Doctorates
to be defended publicly on
Thursday, 01 October 2026, 10:00

by

Yu-Chen LEE

This dissertation has been approved by the promotors.

Composition of the doctoral committee:

Rector Magnificus,	chairperson
Prof. Dr.-Ing. S. Wahls,	Karlsruhe Institute of Technology, Germany / Delft University of Technology *promotor*
Prof. Dr. ing. R. Van de Plas,	Delft University of Technology, *promotor*
Independent members:	
Prof. dr. H.M. Schuttelaars	Delft University of Technology
Prof. dr. ir. T. van den Bremer	Delft University of Technology
Prof. Dr. H. Kalisch	University of Bergen
Prof. Dr. N. Hoffmann	Hamburg University of Technology
Reserve members:	
Prof. dr. B.H.K. De Schutter,	Delft University of Technology

Y.-C. Lee has received funding from a 2019 Key Fields Scholarship, the Ministry of Education, Taiwan.



Keywords: Nonlinear Fourier transforms, Nonlinear Schrödinger equation, Korteweg–de Vries equation, Water waves, Rogue waves, Soliton gases

Printed by:

Cover by: Yu-Chen Lee, image generated with ChatGPT

Copyright © 2026 by Y. Lee
ISBN 978-94-6518-455-5
An electronic copy of this dissertation is available at
https://repository.tudelft.nl/.

TO MY PARENTS, MY BROTHERS, MY FRIENDS

with love, gratitude, and admiration

Mathematics compares the most diverse phenomena and discovers the secret analogies that unite them.

Joseph Fourier

CONTENTS

Summary xiii

Samenvatting xvii

1 Introduction 1
- 1.1 Background of nonlinear Fourier transforms (NFTs) on water waves 2
  - 1.1.1 From linear to nonlinear Fourier transform 2
  - 1.1.2 From Linear Gaussian Statistics to Soliton Nonlinearity 3
  - 1.1.3 Integrable Systems and Exact Nonlinear Analysis 4
- 1.2 Motivation and research gap 5
- 1.3 Partial Differential Equations for Describing the Propagation of Water Waves 6
  - 1.3.1 Partial Differential Equations: Historical Development and Applications 6
  - 1.3.2 KdV solitons and characteristics 6
  - 1.3.3 The Korteweg–De Vries equation for shallow water waves 8
  - 1.3.4 The nonlinear Schrödinger equation for deep water waves 9
  - 1.3.5 NLS solitons and characteristics 11
  - 1.3.6 Rogue Wave Prototypes 12
  - 1.3.7 Soliton Gas Theory 14
- 1.4 Theory of nonlinear Fourier transforms 15
  - 1.4.1 Concepts of the nonlinear Fourier transform 15
  - 1.4.2 The nonlinear Schrödinger equation with vanishing boundary conditions 16
  - 1.4.3 The nonlinear Schrödinger equation with periodic boundary conditions 17
  - 1.4.4 The Korteweg–De Vries equation with periodic boundary conditions 19
  - 1.4.5 Comparison of FFT and Periodic KdV-NFT for Shallow Water Wave Evolution 20
- 1.5 Research Questions 22
- 1.6 Outline of the dissertation 22
  - 1.6.1 Chapter 2: Nonlinear Fourier Classification of 663 Rogue Waves Measured in the Philippine Sea 22
  - 1.6.2 Chapter 3: Evaluation of Nonlinear Fourier-based Maximum Wave Height Predictors under the Nonlinear Schrödinger Equation 23
  - 1.6.3 Chapter 4: Impact of Directional Spreading on Nonlinear KdV-Soliton Spectra in Intermediate Water 23

1.6.4 Chapter 5: When Do JONSWAP Spectra Lead To Soliton Gases In Deep Water Conditions? . . . 24
1.6.5 Chapter 6: Interpretation of Soliton Energy Ratios Measured in Directional Wave Fields . . . 24
1.6.6 Chapter 7: Observation of Suppressed Soliton Gases in the Open Ocean . . . 25
1.7 Data availability statement . . . 25

2 Nonlinear Fourier Classification of 663 Rogue Waves Measured in the Philippine Sea 27
2.1 Introduction . . . 29
2.2 Rogue wave Definition . . . 31
2.3 Rogue wave data acquisition and pre-processing . . . 33
2.3.1 Description of rogue wave data . . . 33
2.3.2 Reconstruction of Surface Wave Elevation . . . 34
2.4 Interpretation of the nonlinear Fourier spectrum by the NLSE-NFT . . . 35
2.5 Four types of nonlinear spectra of rogue wave samples in the ocean . . . 40
2.6 Data analysis of wave samples with four types of nonlinear spectra: stable, small and large breather, soliton . . . 45
2.7 Relationship of unstable modes in nonlinear spectra to rogue waves . . . 53
2.8 Summary and discussion . . . 55

3 Evaluation of Nonlinear Fourier-based Maximum Wave Height Predictors under the Nonlinear Schrödinger Equation 59
3.1 Introduction . . . 60
3.2 Example of NLS-NFT spectrum . . . 61
3.3 Simulation setup . . . 63
3.4 Comparison with Linear Propagation . . . 63
3.5 Advantages and Limitations of the NLS Equation . . . 65
3.6 Review of NFT-based Criteria for Rogue Wave Prediction . . . 67
3.7 Evaluation of NFT-based Criteria for Predicting Maximum Wave Height . . . 68
3.8 Conclusions . . . 70

4 Impact of Directional Spreading on Nonlinear KdV-Soliton Spectra in Intermediate Water 73
4.1 Introduction . . . 75
4.2 Methods . . . 76
4.2.1 The High-Order Spectral method . . . 76
4.2.2 Example of periodic KdV-NFT spectrum . . . 77
4.3 Simulation setup . . . 78
4.4 Results . . . 82
4.4.1 Statistical characteristics during nonlinear evolution . . . 82
4.4.2 Comparison with spectral characteristics obtained from KdV-dynamics 84
4.4.3 Change of the nonlinear KdV-soliton spectrum under HOS dynamics 86
4.4.4 Quantification of the impact of directional spreading on nonlinear KdV-soliton spectra in intermediate water conditions . . . 89

4.4.5 Comparison with linear Fourier modes . . . 92
4.5 Discussion and Conclusions . . . 92

5 When Do JONSWAP Spectra Lead To Soliton Gases In Deep Water Conditions? 97
5.1 Introduction . . . 98
5.2 Simulation setup . . . 99
5.3 Soliton Energy Ratio . . . 100
5.4 An example of nonlinear Fourier analysis . . . 101
5.5 Soliton energy ratios of JONSWAP models . . . 103
5.6 JONSWAP spectral characteristics of the soliton gas-like sea states . . . 105
5.7 Conclusions . . . 109

6 Interpretation of Soliton Energy Ratios Measured in Directional Wave Fields 111
6.1 Introduction . . . 112
6.2 Methods . . . 113
6.2.1 Nonlinear Schrödinger Equation for Deep Water Waves . . . 113
6.2.2 Nonlinear Fourier Transform for Vanishing Boundary Conditions . . . 114
6.2.3 Calculation of soliton energy ratio . . . 115
6.3 Simulation setup for directional wave fields . . . 116
6.4 Characteristics of the soliton energy ratio . . . 119
6.5 Influence of retention angle after directional truncation . . . 122
6.6 Discussion and Conclusions . . . 126
6.7 Appendix: The peak period does not influence the soliton energy ratio for JONSWAP spectra (if the time and frequency grids are rescaled) . . . 131

7 Field observation of soliton gases in the deep open ocean 133
7.1 Introduction . . . 134
7.2 Data acquisition . . . 136
7.3 Method . . . 137
7.3.1 Nonlinear Schrödinger equation . . . 137
7.3.2 Nonlinear Fourier Transform . . . 137
7.3.3 Soliton Amplitudes and Velocities . . . 139
7.3.4 Soliton Energy Ratio Calculation . . . 139
7.4 Statistical Wave Parameters for Sea State Characterization . . . 140
7.5 Results . . . 141
7.5.1 Identifying Soliton Gas Sea States . . . 141
7.5.2 Statistical Properties of Soliton Gas Sea States . . . 143
7.5.3 Discussion on Directional Interference in Soliton Gas Seas . . . 143
7.6 Conclusion and Outlook . . . 148

8 Conclusions and Recommendations 149
8.1 Conclusions . . . 150
8.2 Recommendations for Future Work . . . 152

Acknowledgements 177

Curriculum Vitæ 181

List of Publications **183**

SUMMARY

RESEARCH QUESTIONS

The mechanisms behind the generation of extreme waves, such as rogue waves, remain a topic of active debate among scientists. Traditionally, the analysis of these waves has been conducted using the linear Fourier transform (LFT). Despite the effectiveness, the LFT is limited in its ability to capture nonlinear phenomena. Understanding these nonlinear phenomena requires specialized nonlinear tools. Nonlinear Fourier transforms (NFTs) offer unique insights into the composition of water waves by decomposing them into physically meaningful nonlinear components such as solitons. This thesis investigates the application of NFTs to real-world water waves, with a focus on rogue waves and so-called soliton gases, which are sea states dominated by nonlinearly interacting solitons. The following research questions will be discussed:

1. What are the characteristics of rogue waves in the nonlinear Fourier domain?
2. What are the effects of directional spreading on sea states with solitons?
3. Do soliton gases actually occur in the open ocean?

DESIGN METHODS

This thesis employs NFTs to analyze nonlinear waves in hydrodynamics. NFTs can be used to solve so-called integrable nonlinear partial differential equations by transforming the complex evolution of temporal or spatial series into nonlinear Fourier components in the nonlinear Fourier domain. Two specific partial differential equations are considered in this thesis, namely the nonlinear Schrödinger (NLS) equation for deep-water waves and the Korteweg–de Vries (KdV) equation for shallow water waves. Our wave analysis framework is built upon the Fast Nonlinear Fourier Transform (FNFT) software library, with additional pre-processing and analysis procedures developed in MATLAB. The FNFT library is open-access and available for download from GitHub: https://github.com/FastNFT/FNFT.

RESULTS

With ocean wave data from both numerical simulations and field measurements, we demonstrate how the NFT can be applied to such data. Analyzing deep water rogue waves in the open ocean using the periodic NFT based on the NLS equation, we classify the nonlinear spectrum into four types (stable, small breather, large breather and soliton) with the goal of identifying nonlinear spectral patterns typical for rogue waves.

We found that the type with stable modes is the most typical, while the rogue waves with large wave height are mostly of the large breather or soliton type, characterized by large Benjamin–Feir Index (BFI) and steepness (Chapter 2). We also demonstrate that the amplitude of the maximum spectral components can be used as an indicator to predict maximum wave height during evolution (Chapter 3). Recent studies have found that solitons can retain their characteristics under small or moderate directional interference in deep water, which is an important finding when interpreting nonlinear spectra of real-world measurements. However, no study has examined this problem for shallow water. We therefore simulate how directional spreading affects soliton amplitudes in shallow-water wave fields. The results show that the KdV-soliton spectra obtained from the NFT remain quite stable for cases with small directional spreading. However, for large directional spreading, their applicability is limited to short propagation times and distances (Chapter 4).

The theory of highly nonlinear sea states dominated by solitons, so-called soliton gases, has made much progress in recent years. However, it is not yet clear how practically relevant soliton gases are. To characterize conditions under which soliton gases could occur, we generate time series based on various JONSWAP spectra. These time series are then analyzed using the NFT to obtain the nonlinear spectrum. Our results show that, for JONSWAP seas, larger values of α, β, and shorter waves lead to soliton gas-like conditions in deep water (Chapter 5). In the open ocean, directional effects are an important aspect of wave dynamics. Real ocean waves exhibit significant directional spreading, which can disrupt nonlinear focusing mechanisms by redistributing energy across different propagation directions. We therefore further examine how soliton energy ratios, which quantify how close a time series is to a being a pure soliton gas, change under directional filtering. The results show that, after truncating the sidebands in the directional spectrum, highly nonlinear soliton-dominated seas retain most soliton energy in the main propagation direction under small directional spreading. However, with increasing directional spreading, the soliton energy ratio decreases but still dominates the overall energy. (Chapter 6). Finally, we identify soliton gas-like seas in measured data from Taiwanese waters. This is the first time that soliton gas-like seas have been observed in the open ocean, exhibiting extremely rare and distinct statistical characteristics. Our findings show that the identified soliton gas-like seas are characterized by short-period waves with relatively small wave heights, accompanied by extreme steepness and elevated BFI values. These states are exceptionally rare, representing only 0.054% of our dataset (Chapter 7).

CONCLUSIONS

This dissertation establishes the nonlinear Fourier transforms (NFTs) as a powerful and robust tool for analyzing nonlinear ocean waves, particularly their applicability to non-integrable real-world oceans. By applying the NFTs to diverse data including numerical simulation and field measurement, we have identified the distinctive characteristics of rogue waves in the nonlinear Fourier domain. Furthermore, investigating the influence of directional spreading reveals that NFTs can approximate wave evolution under directional spreading more effectively than the linear Fourier transform. Finally, the analysis

provides evidence that sea states corresponding to soliton gases can occur under certain conditions in the open ocean. Overall, these findings provide critical theoretical insights and practical guidance for understanding nonlinear wave dynamics and contribute to a deeper physical interpretation of extreme wave formation in natural marine environments.

SAMENVATTING

ONDERZOEKSVRAGEN

De mechanismen achter het ontstaan van extreme golven, zoals monstergolven (rogue waves), blijven een onderwerp van actief wetenschappelijk debat. Traditioneel wordt de analyse van deze golven uitgevoerd met behulp van de lineaire Fouriertransformatie (LFT). Ondanks de effectiviteit ervan is de LFT beperkt in haar vermogen om niet-lineaire fenomenen te beschrijven. Het begrijpen van deze niet-lineaire fenomenen vereist gespecialiseerde niet-lineaire hulpmiddelen.

Niet-lineaire Fouriertransformaties (NFT's) bieden unieke inzichten in de samenstelling van watergolven door deze te ontleden in fysisch betekenisvolle niet-lineaire componenten, zoals solitonen. Dit proefschrift onderzoekt de toepassing van NFT's op reële watergolven, met een focus op monstergolven en zogenoemde solitongassen, dat wil zeggen zeetoestanden die worden gedomineerd door niet-lineair interagerende solitonen.

De volgende onderzoeksvragen worden besproken:

1. Wat zijn de kenmerken van monstergolven in het niet-lineaire Fourier-domein?
2. Wat zijn de effecten van directionele spreiding op zeetoestanden met solitonen?
3. Komen solitongassen daadwerkelijk voor in de open oceaan?

ONTWERPMETHODEN

Ons onderzoek toont aan hoe dit belangrijke wiskundige instrument wordt toegepast om niet-lineaire golven in de hydrodynamica te analyseren. De NFT's kunnen worden gebruikt om bepaalde niet-lineaire partiële differentiaalvergelijkingen op te lossen door de complexe evolutie van temporele of ruimtelijke reeksen om te zetten in niet-lineaire Fourier-componenten in het niet-lineaire Fourier-domein. In dit onderzoek worden twee specifieke partiële differentiaalvergelijkingen onderzocht, namelijk de niet-lineaire Schrödingervergelijking (NLS) voor diepwatergolven en de Korteweg–de Vriesvergelijking (KdV) voor ondiepwatergolven. Ons raamwerk voor golfanalyse is gebaseerd op de Fast Nonlinear Fourier Transform (FNFT) softwarebibliotheek, met aanvullende voorverwerkings- en analyseprocedures ontwikkeld in MATLAB. De FNFT-bibliotheek is open access en beschikbaar voor download via GitHub `https://github.com/FastNFT/FNFT`.

RESULTATEN

Met oceaangolfgegevens uit zowel numerieke simulaties als veldmetingen laten wij zien hoe de NFT op dergelijke data kan worden toegepast. Door diep water monstergol-

ven in de open oceaan te analyseren met behulp van de periodieke NFT gebaseerd op de NLS-vergelijking, classificeren wij het niet-lineaire spectrum in vier typen (stabiel, kleine breather, grote breather en soliton), met als doel niet-lineaire spectrale patronen te identificeren die typisch zijn voor monstergolven. Wij constateren dat het type met stabiele modi het meest voorkomt, terwijl monstergolven met grote golfhoogten voornamelijk behoren tot het type grote breather of soliton, gekenmerkt door een hoge Benjamin–Feir-index (BFI) en steilheid (Hoofdstuk 2). Daarnaast laten wij zien dat de amplitude van de maximale spectrale componenten kan worden gebruikt als indicator om de maximale golfhoogte tijdens de evolutie te voorspellen (Hoofdstuk 3). Recente studies hebben aangetoond dat solitonen in diep water hun eigenschappen kunnen behouden onder kleine of matige directionele verstoring, wat een belangrijke bevinding is bij de interpretatie van niet-lineaire spectra van metingen in de praktijk. Tot op heden is dit probleem echter niet onderzocht voor ondiep water. Daarom simuleren wij hoe directionele spreiding de solitonamplitudes beïnvloedt in ondiep-water-golfvelden. De resultaten tonen aan dat de KdV-solitonspectra verkregen met de NFT vrij stabiel blijven bij kleine directionele spreiding. Bij grote directionele spreiding is de toepasbaarheid echter beperkt tot korte voortplantingstijden en -afstanden (Hoofdstuk 4).

De theorie van sterk niet-lineaire zeetoestanden die worden gedomineerd door solitonen, zogenoemde solitongassen, heeft de afgelopen jaren grote vooruitgang geboekt. Het is echter nog onduidelijk hoe praktisch relevant solitongassen zijn. Om de omstandigheden te karakteriseren waaronder solitongassen kunnen optreden, genereren wij tijdreeksen op basis van verschillende JONSWAP-spectra. Deze tijdreeksen worden vervolgens geanalyseerd met behulp van de NFT om het niet-lineaire spectrum te verkrijgen. Onze resultaten laten zien dat voor JONSWAP-zeetoestanden grotere waarden van α en β, evenals kortere golven, leiden tot solitongas-achtige omstandigheden in diep water (Hoofdstuk 5). In de open oceaan spelen directionele effecten een belangrijke rol in de golfdynamica. Reële oceaangolven vertonen een aanzienlijke directionele spreiding, die niet-lineaire focusmechanismen kan verstoren door energie over verschillende voortplantingsrichtingen te herverdelen. Daarom onderzoeken wij verder hoe soliton-energieratio's, die kwantificeren hoe dicht een tijdreeks bij een zuiver solitongas ligt, veranderen onder directionele filtering. De resultaten tonen aan dat, na het afsnijden van de zijbanden in het directionele spectrum, sterk niet-lineaire, door solitonen gedomineerde zeetoestanden bij kleine directionele spreiding het grootste deel van de solitonenergie behouden in de hoofdvoortplantingsrichting. Bij toenemende directionele spreiding neemt de soliton-energieratio echter af, maar blijft deze dominant ten opzichte van de totale energie (Hoofdstuk 6).

Tot slot identificeren wij solitongas-achtige zeetoestanden in gemeten gegevens uit Taiwanese wateren. Dit is de eerste keer dat solitongas-achtige zeetoestanden in de open oceaan zijn waargenomen, waarbij zij uiterst zeldzame en onderscheidende statistische kenmerken vertonen. Onze bevindingen tonen aan dat de geïdentificeerde solitongas-achtige zeetoestanden worden gekenmerkt door golven met korte perioden en relatief kleine golfhoogten, in combinatie met extreme steilheid en verhoogde waarden van de BFI. Deze toestanden zijn uitzonderlijk zeldzaam en vertegenwoordigen slechts 0,054% van onze dataset (Hoofdstuk 7).

CONCLUSIES

Dit proefschrift positioneert de niet-lineaire Fouriertransformaties (NFT's) als een krachtig en robuust instrument voor de analyse van niet-lineaire oceaangolven, in het bijzonder wat betreft hun toepasbaarheid op niet-integreerbare, realistische oceaansystemen. Door NFT's toe te passen op uiteenlopende datasets, waaronder numerieke simulaties en veldmetingen, hebben wij de onderscheidende kenmerken van monstergolven in het niet-lineaire Fourier-domein geïdentificeerd. Daarnaast toont het onderzoek naar de invloed van directionele spreiding aan dat NFT's de golfontwikkeling onder directionele spreiding beter kunnen benaderen dan de lineaire Fouriertransformatie. Tot slot levert de analyse bewijs dat zeetoestanden die overeenkomen met solitongassen onder bepaalde omstandigheden in de open oceaan kunnen voorkomen. Samen bieden deze bevindingen essentiële theoretische inzichten en praktische handvatten voor het begrijpen van niet-lineaire golfdynamica en dragen zij bij aan een diepere fysische interpretatie van het ontstaan van extreme golven in natuurlijke mariene omgevingen.

1

INTRODUCTION

True Laws of Nature cannot be linear.

Albert Einstein

CHAPTER ABSTRACT

This chapter provides an introduction, including the motivation, research gap, research questions, and methodology. Based on a brief background introduction, we first illustrate the motivation for this research and identify the existing research gap. We then introduce two well-known partial differential equations (PDEs) used to describe water wave dynamics. In particular, the dynamics of ocean waves are commonly modeled by the nonlinear Schrödinger (NLS) equation and the Korteweg–De Vries (KdV) equation, which describe the behavior of deep water waves and shallow water waves, respectively. These PDEs can be solved analytically using nonlinear Fourier transforms (NFTs). We also provide an introduction to the theory of NFTs. After this overview, we present the research questions addressed in this thesis. Finally, we outline the structure of the dissertation.

Parts of this chapter have been published in Lee et al., ASME, 2022 [1]; Lee et al., ASME, 2023 [2]; Lee et al., PLoS one, 2024 [3]; Lee et al., Wave Motion, 2025 [4]

1

1.1. Background of nonlinear Fourier transforms (NFTs) on water waves

1.1.1. From linear to nonlinear Fourier transform

For decades, our understanding of water waves has been grounded in linear theory, which assumes that complex sea states can be described as a linear superposition of many independent, non-interacting sinusoidal waves [5]. However, real ocean waves can exhibit strong nonlinearity, particularly in shallow water or when waves become large and steep. These steeper waves interact nonlinearly, fundamentally altering their shape and propagation speed in ways linear theory cannot describe [6, 7]. For example, when applied to shallow water solitary waves (coherent, localized structures), the fast Fourier transform (FFT) decomposes these waves into a broad spectrum of many linear sinusoidal components. This description is not physically robust, as it fails to capture their particle-like stability and evolution.

We first provide a brief introduction to the linear Fourier Transform, which is a widely used signal processing method across numerous scientific and engineering disciplines. The linear Fourier Transform allows converting a time-based signal to the frequency domain, resulting in its Fourier spectrum. This Fourier spectrum is generally complex-valued, containing both amplitude and phase information for each linear sinusoidal mode representing the free-surface elevation and its dynamics. Because the physical signal is real-valued, the spectrum exhibits conjugate symmetry, and in ocean engineering it is therefore common to consider only the one-sided spectrum. When these two conjugate modes are combined, their imaginary parts cancel and the result is a real-valued oscillation. This combined contribution can be written as a single cosine wave whose amplitude is determined by the magnitude of the complex coefficient and whose phase is given. For discrete data, the discrete Fourier transform (DFT) has proven indispensable for data analysis across many fields, with the subsequent development of the fast Fourier transform (FFT) providing remarkable computational efficiency. Linear spectral methods are routinely applied in coastal and ocean engineering to analyze sea states and to design marine structures and vessels capable of withstanding wave loading [8]. However, with growing interest by scientists in complex nonlinear systems, they discovered that the linear Fourier transform was somewhat limited when depicting nonlinear phenomena. This led to the development of the nonlinear Fourier transforms (NFTs), which are better suited for analyzing nonlinear systems.

Nonlinear Fourier transforms, also known as forward scattering transforms, are powerful mathematical tools that extend the concept of the classical Fourier transform to nonlinear systems [6, 9]. Similar to the linear FFT, which decomposes a wave train into cosine waves with specific wavenumbers and frequencies, NFTs can decompose nonlinear coherent wave trains into nonlinear components based on their governing partial differential equations (PDEs). Here, *coherent* refers to structured, phase-related wave forms that maintain their shape and dynamical identity over time. A well known nonlinear component, the *soliton*, is a solution of these PDEs that NFTs can detect and that maintains its shape and speed during propagation. A classical example is the soliton described by the Korteweg-de

Vries (KdV) equation discovered by Zabusky and Kruskal (1965) [10]. Building on this foundational work, pioneering developments in the late 1960s by Gardner et al. [11] established that an NFT can solve the Korteweg-de Vries (KdV) equation for shallow water waves. They demonstrated that the NFT linearizes the KdV equation with obtained solutions that correspond to solitons. Different integrable systems are associated with distinct spectral problems, leading to different NFTs for the corresponding PDEs. The NFT that solves the NLS equation with vanishing boundary conditions was developed by Zakharov and Shabat [12]. Several years later, this method was extended to other nonlinear partial differential equations [9, 13]. These different partial differential equations can describe a range of nonlinear systems, making the NFT applicable across various fields, including plasma physics, hydrodynamics, and optical fibers.

1.1.2. From Linear Gaussian Statistics to Soliton Nonlinearity

Linear wave theory, which forms the foundation of conventional ocean wave analysis, assumes that ocean waves can be represented by the wave spectrum as superpositions of sinusoidal components with fixed amplitudes and random phases uniformly distributed over $[0, 2\pi)$. Under the central limit theorem, the surface wave elevation follows Gaussian statistics [5]. However, real ocean waves exhibit systematic deviations from Gaussian statistics, particularly under extreme conditions of strong nonlinearity.

Stokes wave theory extends the linear framework by accounting for higher-order nonlinear corrections through perturbative expansion in the wave steepness parameter [14]. The perturbative approach yields successive corrections to the wave profile, resulting in a nonlinear shape compared to linear sine waves:

$$\eta(x,t) = a\cos(\theta) + \epsilon a^2 k \cos(2\theta) + \epsilon^2 a^3 k^2 \cos(3\theta) + O(\epsilon^3), \tag{1.1}$$

where a is the wave amplitude, $k = 2\pi/\lambda$ is the wave number with wavelength λ , $\theta = kx - \omega t$ is the wave phase, and ϵ is a small dimensionless nonlinearity parameter proportional to the wave steepness. Each term represents a harmonic component at integer multiples of the fundamental frequency. These harmonic corrections modify the Gaussian probability distribution, demonstrating skewness (asymmetry between crests and troughs) and excess kurtosis (heavy tails indicating enhanced extreme event probability) [15, 16].

However, the perturbative approach treats nonlinearity as a correction to linear dynamics rather than recognizing coherent nonlinear structures such as solitons and breathers, as fundamental structures underlying nonlinear systems. Harmonic decomposition through conventional Fourier analysis cannot distinguish between linear superpositions of harmonics and solitonic structures because both produce similar frequency spectra, yet their dynamical evolution and statistical properties differ significantly [6, 17]. Soliton nonlinearity describes waves as exact nonlinear solutions that maintain coherence during propagation, undergo elastic interactions with other solitons, and concentrate energy through focusing mechanisms capable of producing extreme amplitudes that exceed the predictions of Stokes wave theory

[18]. To address this fundamental distinction, this study uses the NFT to quantify solitonic content in wave fields, thereby providing a more physically appropriate characterization of nonlinear systems than conventional linear methods.

1.1.3. Integrable Systems and Exact Nonlinear Analysis

The NFT serves as an analytical tool for analyzing nonlinear partial differential equations (PDEs) that exhibit integrable system properties. In this context, integrability is often established with the existence of a Lax pair, expressing the nonlinear equation through two compatible linear operators [19]. This reformulation enables the application of the NFT, wherein analytical solutions are obtained. With this approach, the nonlinear spectrum is determined, which consists of a discrete part with eigenvalues and a continuous part with scattering data. The full nonlinear spectrum captures the essential characteristics of the wave field to describe the nonlinear evolution of the system [6]. A fundamental consequence of integrability is that if the system is perfectly integrable and fully governed by an integrable partial differential equation, the nonlinear spectrum remains invariant during temporal evolution, similar to the conservation of linear Fourier modes in dispersive linear systems [13]. Furthermore, one feature of NFTs is that, when sea states are linear, the nonlinear spectrum closely resembles that of the linear FFT [6].

While the nonlinear Fourier transform was originally developed for exactly integrable systems, real-world ocean waves are inherently non-integrable. They exhibit directional spreading, finite depth variations, wind energy input, and wave breaking, all of which break integrability and violate the assumption of the one-dimensional NLS equation and the KdV equation of unidirectional propagation, constant depth, and non-wave breaking conditions. Nevertheless, recent developments in photonics have demonstrated the utility of NFTs as signal processing tools for analyzing systems with non-integrable parts, such as dissipation models [20–23]. Turitsyn et al. (2021) emphasized that the NFT is analogous to the traditional Fourier transform to enable characterization of localized coherent structures in dissipative systems in the anomalous dispersion regime [23]. This suggests potential applicability of NFTs for analyzing real ocean waves of a non-integrable nature.

Here, we briefly review some literature on NFT applications to water wave analysis. NFTs have been successfully applied to predict rogue waves in simulated random oceanic sea states generated from JONSWAP spectral models [24, 25]. Laboratory experimental data have been analyzed using the NFT under idealized conditions to demonstrate that the nonlinear dynamics of water waves can be governed by integrable partial differential equations [6, 17, 26, 27]. In real ocean environments where the governing dynamics deviate from perfect integrability due to directional spreading, dissipation, and wind forcing, the nonlinear spectrum exhibits temporal variation rather than remaining constant. Despite this limitation, the NFT is still employed as a signal processing tool for analyzing field-measured data, and coherent nonlinear structures such as breathers and solitons have been identified in measured nonlinear spectra [28, 29]. Here, a breather refers to a localized wave structure whose amplitude oscillates periodically in time or space, effectively ‘breathing’ up

and down while remaining spatially coherent. A noteworthy example is the discovery of NLS soliton turbulence in the land-locked lagoons of Currituck Sound, North Carolina, using the NFT [28]. When the dynamics of a system are described by an ensemble of solitons, the system is referred to as a soliton gas [30–33]. A recent study applying the NFT based on the KdV equation to North Sea data found that outstanding solitons in the nonlinear spectrum could serve as indicators of the occurrence of rogue waves [34]. Although there have been several applications of the NFT to ocean waves, understanding the reliability of NFT analysis in the presence of non-integrable effects represents an important study for extending nonlinear spectral methods to hydrodynamics.

1.2. Motivation and research gap

Despite the recent development of the NFT and its successful applications in laboratory experiments and several field studies [27–29, 34, 35], its potential for analysis of real-world ocean wave data remains unclear. Most previous studies applying the NFT to water waves have been restricted to numerical simulations, controlled laboratory experiments, and field experiments in coastal land-locked lagoons, where conditions closely approximate the idealized assumptions underlying the governing partial differential equations [6, 13, 17, 26, 36]. These studies have demonstrated that the NFT can reveal coherent nonlinear structures such as solitons and breathers within measured wave trains, offering a fundamentally different interpretation of wave dynamics compared to traditional linear spectral methods [6, 7]. However, a critical research gap persists: *the reliability and interpretation of NFT analysis when applied to large datasets of real-world ocean measurements have not been thoroughly investigated, particularly in the presence of non-integrable effects that fundamentally violate the integrable system assumptions underlying NFT theory.*

Real ocean waves deviate substantially from the idealized, perfectly integrable systems described by nonlinear partial differential equations such as the KdV and NLS equations. In natural environments, directional spreading, energy dissipation through wave breaking, wind forcing, and finite-depth variations introduce non-integrable effects that violate the assumptions underlying these equations. As a result, the nonlinear spectrum obtained from the NFT may only remain representative over short propagation distances, and potentially altering solitonic structures. Understanding the quantitative impact of such mechanisms on NFT spectra is therefore essential for advancing NFT from a theoretical framework towards a practical analytical tool for real ocean data analysis.

To address these problems, this work aims to explore the impact of non-integrability on NFTs for ocean waves using simulations and field measurement data. Rogue waves and soliton gases are particularly interesting nonlinear phenomena for which NFTs are especially suited for analysis and classification. Examining how deviations from integrability influence NFTs is therefore essential for assessing their reliability and applicability to realistic wave fields in ocean engineering and coastal engineering.

1

1.3. Partial Differential Equations for Describing the Propagation of Water Waves

1.3.1. Partial Differential Equations: Historical Development and Applications

Partial differential equations (PDEs) are mathematical relations involving functions of multiple independent variables and their partial derivatives with respect to those variables [37]. A PDE governs the evolution of a field, a quantity that often varies in space and time. This makes PDEs indispensable for modeling spatially distributed phenomena such as fluid motion [38], electromagnetic waves [39], and quantum systems [40]. PDEs are commonly classified as hyperbolic, parabolic, or elliptic, depending on the structure of their highest-order derivatives, with each class exhibiting distinct physical and mathematical characteristics [37].

The study of PDEs started in the 18th century, when mathematicians and physicists began formulating mathematical descriptions of natural phenomena. The first PDE, the one-dimensional wave equation, was derived by Jean le Rond d'Alembert in 1752 and later extented to two and three dimensions [41, 42]. Shortly after, Leonhard Euler formulated the Euler equations for incompressible fluid flow in 1755, laying the foundation for modern fluid mechanics [38]. In 1760, Joseph-Louis Lagrange introduced the minimal surface equation [43]. These breakthroughs were followed by systematic developments throughout the 19th and early 20th centuries, including the Laplace equation (1813) [44], the heat diffusion equation [45], the Navier–Stokes equations (1845) [46, 47] and the Schrödinger equation (1926) [40].

The emergence of nonlinear partial differential equations in the late 19th and 20th centuries marked a turning point in understanding wave phenomena beyond the linear regime. In 1895, Diederik Korteweg and Gustav de Vries derived the Korteweg–de Vries (KdV) equation to describe weakly nonlinear, weakly dispersive shallow-water waves, revealing that solitary waves can propagate without changing shape [48]. Nearly a century later, the nonlinear Schrödinger (NLS) equation emerged as a universal model governing the slow modulation of weakly nonlinear, quasi-monochromatic wave trains in dispersive media [13, 49]. In the following sections, we focus on the KdV and NLS equations and their roles in modeling water wave dynamics.

1.3.2. KdV solitons and characteristics

Solitons represent one of the most remarkable phenomena in nonlinear wave dynamics, first observed in water waves by John Scott Russell in 1834 along the Union Canal near Edinburgh. Russell documented a "singular and beautiful" wave of translation that maintained its form and speed over considerable distances, describing what would later be recognized as the first scientific observation of a solitary wave [50]. A photograph of the solitary wave that was recreated in an experiment in a canal is shown in Fig. 1.1. For decades, Russell's discovery was met with skepticism, as it contradicted the theories of Airy and Stokes. It remained a curiosity until the mathematical description by Joseph Boussinesq in 1877 provided

an equation that served as a precursor to the KdV equation [51]. Korteweg and de Vries in 1895 derived the equation that now bears their names, and demonstrated that such waves emerge naturally from the balance between nonlinear steepening and linear dispersion [48]. The term "soliton" was coined much later, in the 1960s, following the discovery that these waves possess particle-like properties. They maintain their identity through collisions with other solitons, emerging from interactions with only a phase shift but otherwise unchanged in amplitude or velocity. The speed of a solitary wave U can be determined by its amplitude a above the free surface of finite depth h:

$$U = \sqrt{g(h+a)}, \tag{1.2}$$

where g is the gravitational acceleration. The soliton was controversial at the time due to the argument that periodic wave trains in Stokes' theory fail to describe such waves [14]. Soon, the existence of solitons was confirmed by Boussinesq, who derived an equation that described the evolution of shallow water waves [52, 53]. This equation admits solitons as solutions in the sech^2 form:

$$\eta(x,t) = a\text{sech}^2[(3a/h^3)^{(1/2)}(x \pm Ut)], \tag{1.3}$$

where $\eta(x,t)$ represents the free surface elevation, x is the spatial coordinate, t is time, and the $\pm$ sign indicates waves propagating in either direction. The coefficient $(3a/h^3)^{1/2}$ determines both the spatial scale and the steepness of the soliton, illustrating the fundamental nonlinear relationship where larger amplitude solitons are narrower and travel faster.



Figure 1.1: Soliton on the Scott Russell Aqueduct on the Union Canal near Heriot-Watt University, 12 July 1995. Photo from [50].

1

1.3.3. The Korteweg–De Vries equation for shallow water waves

The Korteweg–De Vries (KdV) equation describes the evolution of weakly nonlinear and dispersive progressive unidirectional free-surface waves in shallow water with constant depth [48]. The spatial KdV equation can be expressed as

$$u_t + c_0 u_x + \alpha u u_x + \beta u_{xxx} = 0, \tag{1.4}$$

where $u = u(x,t)$ is the elevation of the free surface elevation at location x and time t, the subscripts denote partial derivatives, $c_0 = \sqrt{g h_0}$ is the linear phase speed in shallow water, g is the gravitational acceleration, h_0 the water depth, $\alpha = 3c_0/2h_0$ is the coefficient of the nonlinearity, and $\beta = c_0 h_0^2/6$ is the coefficient of the dispersive term. The temporal change term u_t represents the local rate of change of surface elevation at a fixed spatial location. This term quantifies how the wave profile evolves in time. The linear advection term $c_0 u_x$ describes wave propagation at the shallow water phase speed. The nonlinear term $\alpha u u_x$ arises from the convective acceleration in the momentum equation and causes wave crests to propagate faster than troughs, leading to progressive steepening of the wave profile. The dispersive term βu_{xxx} represents the leading-order dispersive correction to linear shallow water theory. The third spatial derivative accounts for the wavelength-dependence of phase velocity, whereby different wavelength components propagate at slightly different speeds, leading to spatial spreading of wave packets.

The KdV equation has several assumptions: shallow water, unidirectionality, weak nonlinearity, and a flat bottom. In particular the first two assumptions are often violated by real-world measurements. While shallow water is commonly defined by $kh < \pi/10$, this is not a sharp cut-off. The KdV equation can be used with larger kh, at the price of decreased accuracy. In the literature, various cut-off criteria for the applicability of the KdV equation have been used: $kh \leq 1$ [26], $kh \leq 1.36$ [54], and $kh \leq 1.14$ [55]. These criteria exceed the usual range of shallow water ($kh < \pi/10$) and extend into the intermediate water range ($\pi/10 < kh < \pi$). Figure 1b in [54] illustrates that $kh = 1.14$ corresponds to a 6% mismatch between the shallow water dispersion relation and the dispersion relation of the KdV equation, while $kh = 1.36$ corresponds to a mismatch of 14%. When the threshold kh exceeds 1.363, the modulational instability arises [56, 57], causing the underlying wave dynamics to be better described by the nonlinear Schrödinger equation.

When a system is fully governed by the KdV equation, soliton dynamics will often occur during evolution. This has been demonstrated in physical experiments e.g. by Bruehl et al. (2016) [17], as shown in Fig. 1.2. The wave generator initially produces linear cosine waves. When these waves propagate through shallow water, the profile first develops a characteristic asymmetry with a steepening front and flattening rear slopes, evolving toward bore-like shapes. With continued propagation, the bore-like structure does not break but instead resolves into a train of discrete solitons. These solitons exhibit characteristic sharp crests. The leading soliton, which has the largest amplitude, travels fastest and separates progressively from the smaller trailing solitons. This experiment of wave evolution from linear cosine waves through bore-like shapes to distinct solitonic structures, demonstrates

the fundamental mechanism underlying KdV dynamics. This process cannot be described by conventional linear Fourier methods and thus requires further nonlinear Fourier analysis.

Recent field measurements conducted along the lagoon borders on the Pacific coast of central Chile have revealed the presence of solitonic wave trains consistent with the Korteweg–de Vries (KdV) framework [58]. These observations represent natural evidence for KdV-type solitons occurring in a coastal environment outside laboratory or simulated settings. The observed KdV solitonic wave trains are shown in Fig. 1.3, demonstrating soliton occurrence not only in the laboratory but also their existence in the real field.

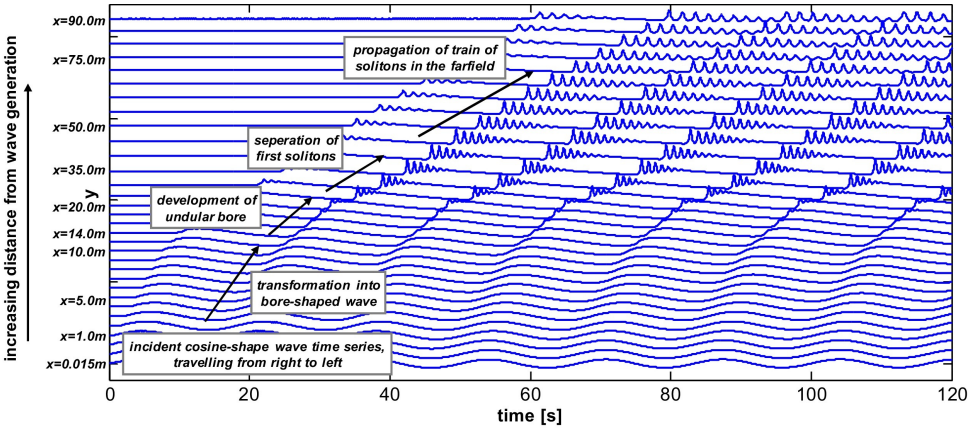


Figure 1.2: Physical experiments on nonlinear dynamics of shallow-water wave evolution in a wave flume [17], Applied Ocean Research, https://doi.org/10.1016/j.apor.2016.09.009. License obtained through permission from Elsevier. No changes were made.

1.3.4. The Nonlinear Schrödinger Equation for Deep Water Waves

The nonlinear Schrödinger (NLS) equation is commonly used to describe the evolution of slowly varying envelopes of unidirectional progressive free-surface waves in deep water ($k_0 h \geq 1.363$), where k_0 is the wave number and h is the water depth. It captures the interplay between the nonlinear self-focusing effect and dispersion.

The unnormalized NLS equation describes the evolution of the envelope,

$$\mathrm{i}\left[C_g^{-1} A_t + A_x\right] + \mu C_g^{-3} A_{tt} + \nu C_g^{-1} |A|^2 A = 0, \tag{1.5}$$

where C_g is the group velocity of a wave packet. Here, A is the slowly varying complex envelope, which can be constructed from the measured surface elevation using the Hilbert transform: $A(t) = [\eta(t) + \mathrm{i}\mathscr{H}\{\eta(t)\}]e^{-\mathrm{i}\omega_c t}$ [6, 59, 60], where $\mathrm{i} = \sqrt{-1}$, ω_c is the carrier angular frequency, and $\mathscr{H}\{\eta(t)\}$ denotes the Hilbert transform,

1

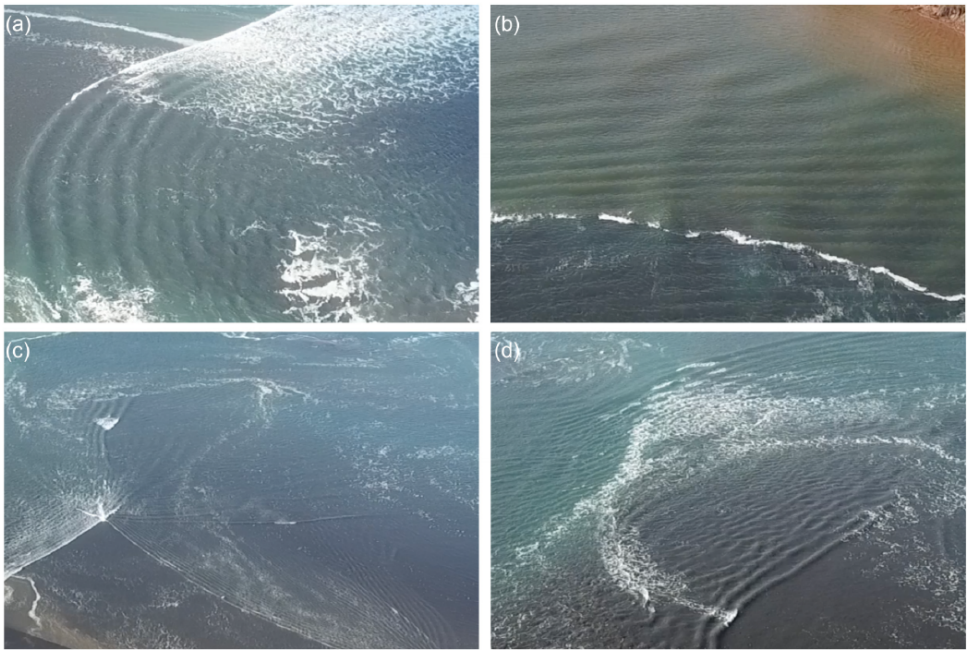


Figure 1.3: Field observation of different phenomenon of KdV solitonic wave trains propagating at the lagoon borders on the Pacific coast of central Chile [58], Physical Review Research, https://doi.org/10.1103/9zhq-j1sj. This figure is under the terms of the Creative Commons Attribution 4.0 International license from the American Physical Society. No changes were made.

defined as $\mathscr{H}\{\eta(t)\} = \frac{1}{\pi}\int_{-\infty}^{\infty}\frac{\eta(\tau)}{t-\tau}\,\mathrm{d}\tau$. In practice, the Hilbert transform is computed using the FFT [61]. The values of the coefficients for gravity waves in finite water depth h are given from the dispersion relation $\omega_0^2 = g k_0 \sigma$, $\sigma = \tanh k_0 h$ [62]:

$$C_g = \frac{c}{2}\left[1 + \frac{\left(1-\sigma^2\right)k_0 h}{\sigma}\right], \text{ where } \mathrm{c} = \frac{\omega_0}{k_0}, \tag{1.6}$$

$$\mu = \frac{-g}{8k_0\sigma\omega_0}\left\{\left[\sigma - k_0 h\left(1-\sigma^2\right)\right]^2 + 4k_0^2h^2\sigma^2\left(1-\sigma^2\right)\right\}, \tag{1.7}$$

$$\nu = \frac{-k_0^4}{2\omega_0}\left(\frac{c}{2\omega_0}\right)\left\{\frac{\left(9-10\sigma^2+9\sigma^4\right)}{2\sigma^2} + \frac{4c^2 + 4\left(1-\sigma^2\right)cC_g + gh\left(1-\sigma^2\right)^2}{C_g^2 - gh}\right\}. \tag{1.8}$$

The product of the depth-dependent coefficients should be greater than 0, $\mu\nu > 0$ (or $k_0 h \geq 1.363$), in order to arrive at the normalized focusing NLS equation

$$\mathrm{i}u_X + u_{TT} + 2|u|^2 u = 0 \tag{1.9}$$

where $u(X,T)$ represents the complex envelope of the wave field, X and T are the normalized forms for space and time, and l is the period of the time series. To proceed from (1.5) to (1.9), we apply the following change of coordinates:

$$X = \frac{\mu}{C_g^3}x, \quad T = t - \frac{x}{C_g}, \quad u(X,T) = \rho A(X,T), \quad \rho = \sqrt{\frac{C_g^2 \nu}{2\mu}}. \tag{1.10}$$

The parameter ρ is called the nonlinear parameter by Osborne [6]. By substituting $A = \rho^{-1}u$ in the temporal NLS equation, one obtains (1.9). See, e.g., Ref. [63]. Please note that the parameter ρ is not dimensionless. The NLS equation (1.9) is normalized in the sense that its coefficients are independent of physical parameters such as the water depth.

When applying to field-measured or laboratory data, the surface wave elevation has to be transferred to the envelope. The Hilbert transform is used to calculate the complex wave envelope from the wave-surface elevation after removal of the carrier wave [60]. The Hilbert transform method is accurate to the same order as the NLS equation for narrowband wave-trains [64], and thus commonly used for the NFT analyses [6, 29, 65].

1.3.5. NLS Solitons and Characteristics

The NLS soliton describes the evolution of complex wave envelopes or groups of carrier waves in deep water. Depending on the boundary conditions, solitons governed by the NLS equation can exist either on a zero background (ZBG) or on a finite background (FBG).

The fundamental soliton solution to the focusing NLS equation is the bright soliton, which appeared as a localized elevation on a zero background. A bright soliton on zero background refers to a localized wave packet that decays to zero amplitude as $x \to \pm\infty$, as shown in Fig. 1.4 (a) [66]. This localized wave packet propagates without distortion and interacts elastically with other solitons. Following collisions, each soliton re-emerges preserving its original amplitude and velocity, with only a phase shift, which is a characteristic feature of integrable systems.

The single bright soliton solution with amplitude parameter η is given by

$$\psi(x,t) = 2\eta \exp\left(2i\eta^2 t\right) \operatorname{sech}\left(2\eta(x - 4\eta^2 t - x_0)\right), \tag{1.11}$$

where x_0 is an arbitrary constant determining initial position [9]. This solution exhibits remarkable properties, such as the amplitude 2η remaining constant during propagation, and the velocity $4\eta^2$ showing that higher-amplitude solitons propagate faster [13]. In contrast to the bright soliton, the dark soliton solution takes the form of a tanh function, representing a localised intensity dip on a non-zero background.

More generally, the bright soliton solution can be parametrized by a complex spectral parameter $\lambda = \rho + i\sigma$:

$$\psi(x,t) = 2\sigma \exp\left(2\mathrm{i}(\rho^2 - \sigma^2)t + \mathrm{i}\phi_0\right) \operatorname{sech}\left(2\sigma(x - 4\rho\sigma t - x_0)\right) e^{2\mathrm{i}\rho x}, \tag{1.12}$$

where ϕ_0 is an arbitrary phase constant [13]. The amplitude is $A = 2\sigma$, the velocity is $4\rho\sigma$, and the frequency shift is $\omega_0 = 2(\rho^2 - \sigma^2)$. These parameters collectively

determine the soliton propagation characteristics and can be extracted from the nonlinear spectrum via eigenvalue analysis [6].

In contrast, a soliton on a finite background exists on top of a nonzero continuous wave, as shown in Fig. 1.4 (b) [66]. In this case, the soliton is a localized modulation or disturbance riding on a finite amplitude carrier wave. Examples include Akhmediev breathers, Kuznetsov–Ma breathers, and the Peregrine soliton, which are often associated with modulational instability and regarded as rogue wave prototypes, as described in the next section.

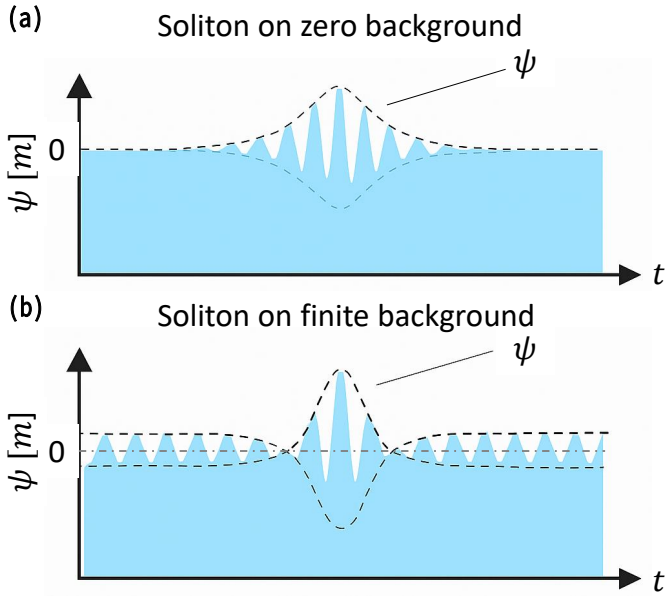


Figure 1.4: Wave envelope profiles of NLS solitons in deep water, showing (a) soliton on zero background (b) soliton on finite background. Reproduced from Dudley et al. (2014) [66], Nature Photonics, https://doi.org/10.1038/nphoton.2014.220. License obtained through permission from Springer Nature. No changes were made.

1.3.6. Rogue Wave Prototypes

Rogue waves in oceans are extreme, rare events defined as waves whose maximum height exceeds twice the significant wave height. To mathematically model these phenomena, the focusing NLS equation possesses exact analytical solutions, notably the Peregrine soliton and the Kuznetsov-Ma and Akhmediev breathers, which are widely regarded as prototypes for rogue waves [67–69]. Each solution exhibits distinct spatiotemporal localization properties and represents different physical scenarios of extreme wave formation through modulational instability mechanisms, as shown in Fig 1.5.

The Peregrine soliton, discovered by Howell Peregrine in 1983, represents a spatially localized structure with only one oscillation in time [70]. It captures the feature of rogue waves that their propensity to appear from nowhere and disappear without trace [71]. The maximum amplitude of the Peregrine soliton is exactly three times the amplitude of the unperturbed uniform wave train. The Peregrine solution to the dimensionless focusing NLSE is given by

$$\psi(x,t) = \left[1 - \frac{4(1+2\mathrm{i}t)}{1+4x^2+4t^2}\right] e^{\mathrm{i}t}, \tag{1.13}$$

where $\psi(x,t)$ is the complex wave envelope, x is the spatial coordinate in a frame moving with the group velocity, and t is time. This solution reaches its maximum normalized amplitude at the origin of the coordinate at $t=0$ and $x=0$, yielding an amplification factor of three compared to the background plane wave state.

The Kuznetsov-Ma (KM) breather, independently derived by Kuznetsov (1977) and Ma (1979) [72, 73], represents a periodic-in-time but localized-in-space solution to the NLSE. Unlike the Peregrine soliton, the KM breather describes a wave structure that appears, reaches maximum amplitude, disappears, and then reappears periodically at the same spatial location. The KM breather solution is expressed as

$$\psi(x,t) = \left[1 + \frac{2(1-2a)\cosh(\beta t) - \mathrm{i}\beta\sinh(\beta t)}{\sqrt{2a}\cosh(bx) - \cosh(\beta t)}\right] e^{\mathrm{i}t}, \tag{1.14}$$

where $a = (1+\sqrt{\beta^2+1})/4$, $b = 2\sqrt{2a-1}$.

The Akhmediev breather (AB), discovered by Akhmediev, Eleonskii, and Kulagin in 1985 [74], exhibits complementary properties to the KM breather: it is periodic in space but localized in time. The AB represents the growth and decay of unstable modes during modulational instability, describing how a spatially periodic perturbation on a uniform background evolves to maximum amplitude and then returns to the background. The Akhmediev breather solution is

$$\psi(x,t) = \left[\frac{(1-4a)\cosh(\beta x) + \sqrt{2a}\cos pt + \mathrm{i}\beta\sinh(\beta x)}{[\sqrt{2a}\cos(pt) - \cosh(\beta x)]}\right] e^{\mathrm{i}t}, \tag{1.15}$$

where a is a modulation parameter, $\beta = \sqrt{8a(1-2a)}$ and $p = 2\sqrt{1-2a}$. Meanwhile, the general solution for solitons on a finite background of the NLSE can be written as a unified expression that merges three classes into a single general formula [75].

These localized solutions enhance our understanding of nonlinear dynamics that fundamentally differ from linear systems. They emerge naturally through modulational instability (MI), a mechanism by which weak perturbations on a plane-wave background grow exponentially within specific unstable frequency bands [49, 76]. Once MI is triggered, the amplification of these perturbations leads to the subsequent formation of NLS breathers and solitons [77–79]. In hydrodynamics, researchers have successfully generated these NLS solutions in physical experiments, providing experimental validation of the theoretical predictions [80–83]. These results demonstrate that rogue waves can develop even from calm and apparently safe sea states. Despite these advances, quantitative comparisons between theoretical rogue

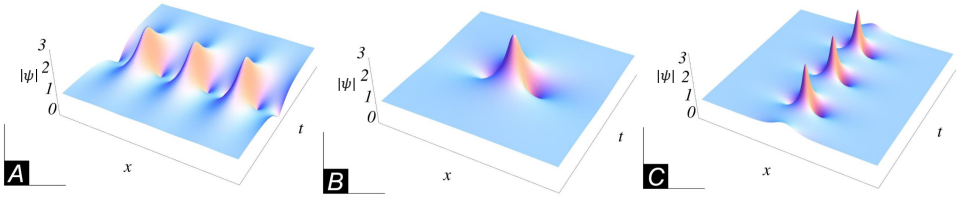


Figure 1.5: Three classes of soliton on finite background solutions of the NLSE. (A) Akhmediev breather (B) Peregrine soliton (C) Kuznetsov-Ma breather. Reproduced from Onorato et al. (2013) [69], PLOS ONE, https://doi.org/10.1371/journal.pone.0054629, licensed under CC BY 3.0. Changes: symbol updated for consistency with our NLS notation.

wave prototypes and observed rogue waves in the real ocean remain scarce. Notably, Onorato et al. (2021) found that windowed NFT analysis reveals the existence of nonlinear modes in the nonlinear spectrum [29]. This finding motivates further investigation on measured rogue waves as discussed in the present study.

1.3.7. Soliton Gas Theory

The concept of a soliton gas was introduced by V.E. Zakharov in 1971 as a theoretical framework for large collections of weakly interacting solitons in integrable systems [30]. Zakharov derived an approximate kinetic equation for the KdV equation that governs the statistical evolution of soliton velocities in a rarefied soliton gas. A rarefied soliton gas refers to a state composed of solitons with random amplitudes and phases, distributed sparsely enough that they interact only occasionally. A significant development in the 2000s by El and Kamchatnov was the extension to dense soliton gases, where solitons heavily overlap and interact continuously [31, 84]. With a spectral distribution function $f(x,t;\lambda)$, the evolution of a soliton gas distribution is governed by a conservation equation,

$$\frac{\partial f}{\partial t} + \frac{\partial (sf)}{\partial x} = 0, \tag{1.16}$$

where the eigenvalues λ are transferred along the spatial domain with mean velocity $s(x,t;\lambda)$. There is no exchange of eigenvalues between different intervals.

In the case of a dense soliton gas of the KdV equation, the effective velocity accounting for mutual interactions is determined by the kinetic integral equation:

$$s(\lambda) = 4\lambda^2 + \frac{1}{\lambda}\int_0^\infty \ln\left|\frac{\lambda+\mu}{\lambda-\mu}\right| f(\mu)[s(\lambda)-s(\mu)]\,d\mu, \tag{1.17}$$

The first term $4\lambda^2$ is the velocity of an isolated soliton.

This framework of kinetic theory can also be applied to the focusing NLS equation [31, 85]. In contrast to the KdV case where solitons are characterized by real-valued spectral parameters, NLS solitons possess complex eigenvalues with their interactions

governed by the Zakharov–Shabat spectral problem. The integral equation of the NLS soliton gas velocities is given by

$$s(\lambda) = -4\,\mathrm{Re}(\lambda) + \frac{1}{\mathrm{Im}(\lambda)} \iint_{\Lambda_+} \ln \left| \frac{\mu - \lambda^*}{\mu - \lambda} \right| [s(\lambda) - s(\mu)] f(\mu)\, d\xi\, d\zeta, \tag{1.18}$$

where $\mu = \xi + i\zeta$ is the complex eigenvalue, and Λ_+ is the upper half-plane. The $-4\,\mathrm{Re}(\lambda)$ term represents the free soliton velocity. More details can be found in a recent paper by Suret et al. (2024)[33], which presents a summary of soliton gas theory, numerical investigations, and experimental observations.

Soliton gases have been reproduced in controlled laboratory experiments in wave tanks to demonstrate the evolution and predictive capability of soliton gas theory [65, 86–88]. However, whether soliton gas conditions occur in realistic open ocean environments remains an open research question. Characterizing the occurrence and properties of soliton gas conditions in measured ocean data constitutes an important step for further investigation in this dissertation.

1.4. Theory of nonlinear Fourier transforms

1.4.1. Concepts of the nonlinear Fourier transform

The NFT is a powerful mathematical tool that can be used to analyze the evolution of certain partial differential equations (PDEs). One of the key advantages of the NFT is its ability to transform nonlinear problems into linear ones. This simplifies the complex computation of the direct evolution of nonlinear PDEs. To illustrate this, we consider the nonlinear Schrödinger (NLS) equation as an example, as depicted in Fig. 1.6. As we mentioned, directly solving the NLS equation in the time domain is often challenging. However, applying the NFT converts this hydrodynamical signal of time series $u(x_1, t)$ at initial location x_1 into scattering data $S(x_1, \lambda)$. Thus, the problem can be transformed from the time domain into a nonlinear spectral domain. It is more simple to evolve the scattering data from x_1 to certain distance x_2. After the evolution in the nonlinear spectral domain, the inverse NFT is employed to transform the evolved scattering data $S(x_2, \lambda)$ back into the time domain. This reconstructs the final solution of the time series $u(x_2, t)$, achieving the results of the original nonlinear problem.

The above process shows the advantages of NFTs in which surface waves are decomposed into scattering data in the nonlinear domain. This decomposition ensures that the nonlinear spectrum remains invariant during propagation, enabling exact evolution without the accumulation of numerical errors. Moreover, nonlinear spectral components can sometimes be identified directly from measured time series during evolution, revealing soliton amplitudes that are otherwise hidden within the background wave field [17]. Such nonlinear phenomenon cannot be described using conventional linear Fourier analysis.

1

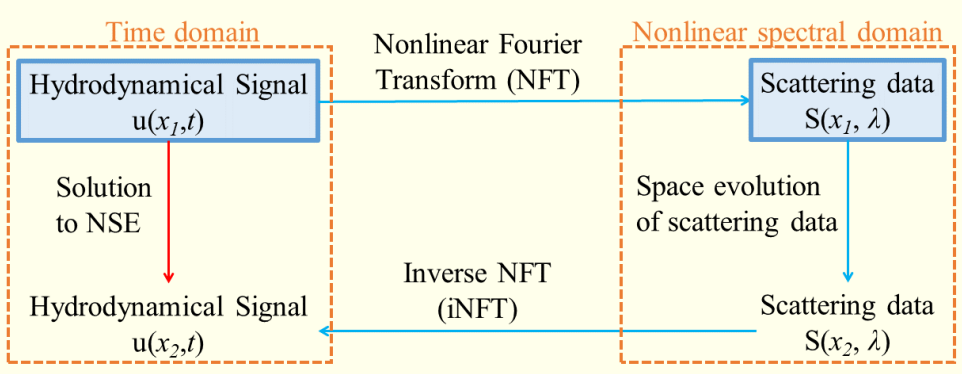


Figure 1.6: Flowchart Illustrating the Concept of the Nonlinear Fourier Transform

1.4.2. The nonlinear Schrödinger equation with vanishing boundary conditions

The nonlinear Fourier transform (NFT) is used to solve the NLS equation based on the integrability of the Zakharov-Shabat system [9, 12, 13]. The solutions of the NFT for the NLS equation depend on the boundary conditions. The vanishing boundary condition is one of the most commonly used for NFTs. The direct space-evolution of the complex envelope governed by the NLS equation can be complicated. The advantage of the NFT is that the evolution of nonlinear Fourier components is very simple. One can apply the inverse nonlinear Fourier transform (iNFT) to the propagated spectrum to obtain the solution at other points in space.

We now discuss how the nonlinear spectrum is computed. The scattering problem for the NLS equation is

$$\Psi_T = Q(\zeta)\Psi, \quad Q = \begin{pmatrix} -i\zeta & u(X_0,T) \\ -\kappa u(X_0,T)^* & i\zeta \end{pmatrix}, \tag{1.19}$$

where ζ is the complex spectral parameter, and * represents complex conjugation. Two pairs of linearly independent Jost functions $\Psi = [\phi(\zeta) \quad \overline{\phi}(\zeta)]$ and $\Psi = [\psi(\zeta) \quad \overline{\psi}(\zeta)]$ are found by solving Eq.(7.4). The Jost functions are defined by the boundary conditions

$$\begin{aligned} \phi(\zeta) &= \begin{bmatrix} 0 \\ e^{-i\zeta T} \end{bmatrix} + o(1) \quad \text{as} \quad T \to -\infty, \\ \overline{\phi}(\zeta) &= \begin{bmatrix} e^{i\zeta^* T} \\ 0 \end{bmatrix} + o(1) \quad \text{as} \quad T \to -\infty, \\ \psi(\zeta) &= \begin{bmatrix} e^{i\zeta T} \\ 0 \end{bmatrix} + o(1) \quad \text{as} \quad T \to \infty, \quad \text{and} \\ \overline{\psi}(\zeta) &= \begin{bmatrix} 0 \\ e^{-i\zeta^* T} \end{bmatrix} + o(1) \quad \text{as} \quad T \to \infty. \end{aligned} \tag{1.20}$$

The above pairs of functions are related through the scattering coefficients $a(\zeta)$,

$b(\zeta)$, $\overline{a}(\zeta)$, and $\overline{b}(\zeta)$:

$$\begin{aligned}\Phi(\zeta) &= a(\zeta)\psi(\zeta) + b(\zeta)\overline{\psi}(\zeta),\\ \overline{\Phi}(\zeta) &= \overline{b}(\zeta)\psi(\zeta) + \overline{a}(\zeta)\overline{\psi}(\zeta).\end{aligned} \tag{1.21}$$

The scattering coefficients $a(\zeta)$ and $b(\zeta)$ are the basis for forming the nonlinear spectrum. The nonlinear spectrum consists of two components: the continuous spectrum and discrete spectrum. The continuous spectrum is described by the *reflection coefficient*

$$r(\zeta) = b(\zeta)/a(\zeta). \tag{1.22}$$

It represents the radiation components in the time series. The discrete spectrum contains the discrete eigenvalues $\{\zeta_k = \xi_k + \mathrm{i}\eta_k\}$, $k = 1, ..., N$, where N is the total number of solitons in the signal. They are the zeros of the scattering coefficient $a(\zeta)$ with a positive imaginary part. The eigenvalues are complemented by the residues

$$r_k = b(\zeta_k)/a'(\zeta_k), \quad \text{where} \quad a'(\zeta_k) = \partial a/\partial\zeta_k. \tag{1.23}$$

The discrete spectrum corresponds to the soliton components.

The inverse nonlinear Fourier transform (iNFT) recovers the time domain signal from the nonlinear spectrum. This is classically achieved by using the Gelfand-Levitan-Marchenko equation (GLME) [9, 13, 89]:

$$\begin{aligned}K_2^*(T,S) + \int_T^\infty K_1(T,s)F(s+S)\,ds = 0,\\ K_1(T,S) - \int_T^\infty K_2^*(T,s)F^*(s+S)\,ds = F^*(T+S),\end{aligned} \tag{1.24}$$

where the integral kernel $F(T)$ is given as

$$F(T) = \frac{1}{2\pi}\int_{-\infty}^{\infty} r(\zeta,T)e^{\mathrm{i}\zeta T}\,d\zeta - i\sum_{k=1}^{N} r_k(T)e^{\mathrm{i}\zeta T}. \tag{1.25}$$

Finding $K(T,S)$ by solving the GLME, enables us to recover a complex envelope in the time-space domain:

$$u(X_0,T) = -2K_1(T,T). \tag{1.26}$$

More information about the inverse nonlinear Fourier transform (iNFT) can be found in [9, 12, 13].

1.4.3. The nonlinear Schrödinger equation with periodic boundary conditions

The periodic NFT is more complicated than its vanishing counterpart [90]. Recent studies have extensively applied periodic NFTs to optical systems [91], shallow water waves [7, 17], deep water waves, [6, 63] and simulated NLS equation systems [92].

The NLS equation has exact solutions known as finite gap solutions [93]. These solutions can be constructed from the so-called main spectrum E_k and the auxiliary spectrum $\mu_k(0,0)$ as follows. The finite gap solutions are given by

$$[\log u(X,T)]_T = 2\mathrm{i}\sum_{k=1}^{g}\mu_k(X,T) + 2\mathrm{i}K, \quad K = -\frac{1}{2}\sum_{k=1}^{2g+2}E_k. \tag{1.27}$$

1

Here, the μ_k are auxiliary functions known as hyperelliptic modes and E_k are certain complex constants that are independent of time and space. The number g of hyperelliptic modes here, which is also known as the number of "gaps" or the "genus" in the literature, is assumed to be finite for mathematical reasons. The dynamics of the complex envelope $u(X,T)$ are originally governed by the auxiliary functions μ_k, which evolve on the Riemann surface. A Riemann surface is a connected one-dimensional complex analytic manifold, which is vital to the studies on the behavior of complex-valued functions [94]. The auxiliary functions satisfy the following equations on the hyperelliptic Riemann surface of the function $\sqrt{P(z)}$:

$$[\mu_k]_T = -2\mathrm{i}\frac{\vartheta_k\sqrt{P(\mu_k)}}{\prod_{j\neq k}(\mu_k-\mu_j)}, \quad P(z) := \prod_{j=1}^{2g+2}(z-E_j) \tag{1.28}$$

$$[\mu_k]_X = 4\mathrm{i}\left(\sum_{j=1}^{g}\mu_j + K - \mu_k\right)\frac{\vartheta_k\sqrt{P(\mu_k)}}{\prod_{j\neq k}(\mu_k-\mu_j)} \tag{1.29}$$

This Riemann surface is a double covering of the complex plane with the pairs of branch points E_k. In order to distinguish two different points, the Riemann sheet indices $\vartheta_k = \vartheta_k(X,T) \in \{\pm 1\}$ are used to change the signs corresponding to $P(\mu_k)$, crossing the chosen branch cut of the square root function. Given the constants E_k, initial values for auxiliary functions $\mu_k(X_0,T_0)$, the Riemann sheet indices $\vartheta_k = \vartheta_k(X_0,T_0)$ and $u(X_0,T_0)$, we can recover $u(X,T)$ for any desired value of X by solving these specific equations. These values can be obtained from a single time signal $u(X_0,T)$ through spectral analysis of the Zakharov-Shabat operator. See, e.g., [93].

Alternately, it is possible to solve Eqs. (1.28) and (1.29) analytically using Riemann theta functions in order to implement the inverse periodic NFT. The inverse periodic NFT is a mapping from the main spectrum E_k and initial conditions for the auxiliary spectrum $\mu_k(X_0,T_0)$ and sheet indices $\vartheta(X_0,T_0)$ to a solution of the complex envelope $u(X,T)$. The exact solutions are of the form

$$u(X,T) = u_0\frac{\theta\left(\mathbf{k}X - \boldsymbol{\omega}T + \boldsymbol{\phi}^- \mid \boldsymbol{\tau}\right)}{\theta\left(\mathbf{k}X - \boldsymbol{\omega}T + \boldsymbol{\phi}^+ \mid \boldsymbol{\tau}\right)}e^{\mathrm{i}(k'X-\omega'T)} \tag{1.30}$$

where u_0 is a scalar constant, $\boldsymbol{\tau}$ is a so-called Riemann matrix, $\boldsymbol{k}$ is a vector of wave numbers, $\boldsymbol{\omega}$ is a vector of frequencies, $\boldsymbol{\phi}^-$ and $\boldsymbol{\phi}^+$ are two different phase vectors, and k' and ω' are the physical Stokes wave corrections to the dispersion relation. The Riemann theta function is defined by

$$\theta(\boldsymbol{z} \mid \boldsymbol{\tau}) = \sum_{\mathbf{n}\in\mathbb{Z}^g}\theta_{\mathbf{n}}e^{\mathbf{i}\mathbf{n}\cdot\mathbf{z}} \tag{1.31}$$

where $\theta_{\mathbf{n}} = \exp[i\pi\mathbf{n}\cdot\boldsymbol{\tau}\mathbf{n}]$ and $\mathbf{n}$ is an integer vector of length N. More details on Riemann theta functions and the solution of periodic NLS equation can be found in [6].

The main spectrum consists of the E_k, which are connected by curves known as spines. Just like the main spectrum, the spines remain constant during propagation

with respect to the NLS equation. In principle, spines are redundant because the signal is already uniquely specified by the main and auxiliary spectrum together with the sheet indices. However, they play an important role when the Riemann theta form of the solution in (1.31) is computed. Spines provide valuable information about the general characteristics of the solution $u(X,T)$, as they impose topological constraints on the trajectories of the auxiliary spectra $\mu_k(X,T)$ [95, p. 49]. Like the main and auxiliary spectrum, the spines can be found by spectral analysis of the Zakharov-Shabat operator.

1.4.4. The Korteweg–De Vries equation with periodic boundary conditions

We now consider the nonlinear Fourier transform with periodic boundary conditions. The periodic KdV-NFT is defined for so-called finite gap solutions of the KdV equation. Finite gap solutions are linear superpositions of finitely many hyperelliptic functions $\mu_i(x,t)$, representing nonlinearly interacting nonlinear waves [6, 26, 96]:

$$\lambda u(x,t) = -E_1 + \sum_{i=1}^{N} \left[2\mu_i(x,t) - E_{2i} - E_{2i+1}\right], \tag{1.32}$$

where $\lambda = \alpha/(6\beta)$ and α and β are physical constants given in the spatial KdV equation. It is known that finite gap solutions can approximate arbitrary periodic solutions. For small-amplitude surface elevations, they turn into Fourier series. The NFT of a finite gap solution consists of several parts, of which we will only need the constants E_i. These constitute the so-called main spectrum. For the computation of the main spectrum from a given spatial measurement $u_0(x)$, the second-order Schrödinger eigenvalue problem has to be solved. The Schrödinger eigenvalue problem is given by [6]

$$\psi_{xx} + [\lambda u(x,0) + k^2]\psi = 0, \quad \psi = \psi(x;k^2), \tag{1.33}$$

where k is the "nonlinear frequency" with $k^2 = E$. The monodromy matrix $\mathbf{M}(k^2)$ is a matrix-valued solution of (1.33), which is obtained by using the 2×2 identity matrix as an initial condition at an arbitrary point, and propagating it over one period of the waveform. The trace $\Delta(E)$ of the monodromy matrix $\mathbf{M}$ is the Floquet discriminant $\Delta(E) = \frac{1}{2}Tr\mathbf{M}$. The Floquet discriminant shows for which k^2 in Eq. (1.32) has quasi-periodic solutions [54, 97]. The main spectrum can be calculated by finding the solutions of $\Delta(E) = \pm 1$. The constants E_i in the main spectrum correspond to the k^2 for which (1.33) has periodic (if $\Delta(E) = +1$) and anti-periodic (-1) solutions ψ. Two adjacent eigenvalues determine an open band E_{2i}, E_{2i+1} when $|\Delta(E)| > 1$ for $E_{2i} < E < E_{2i+1}$. There is also an auxiliary spectrum, which consists of initial conditions $\mu_i(x_0,t_0)$ for the hyperelliptic modes. The nonlinear KdV spectrum is commonly decomposed into soliton and radiation components. The modulus m of the hyperelliptic functions is employed to distinguish between soliton and radiation waves:

$$m_i = \frac{E_{2i+1} - E_{2i}}{E_{2i+1} - E_{2i-1}}, \quad 0 < m_i < 1. \tag{1.34}$$

A modulus $m_i < 0.99$ indicates an oscillatory mode with $f_i = k_i/\pi$ [98]. For $m_i \geq 0.99$, we have solitons. The amplitude a_i of an hyperelliptic oscillation mode can be expressed as

$$a_i = \frac{E_{2i+1} - E_{2i}}{2\lambda}. \tag{1.35}$$

The soliton amplitudes η_n are given by

$$A_i = \frac{2(E_{\text{ref}} - E_{2n})}{\lambda}, \quad 1 \leq n \leq N_{\text{sol}}. \tag{1.36}$$

Here, the number of solitons N_{sol} is the largest N such that $m_i \geq 0.99$ for all $i = 1, 2, \ldots, N$. The reference level $E_{\text{ref}} = E_{2N_{\text{sol}}+1}$ corresponds to the level at which the solitons travel in periodic theory [6, 26, 99]. For visualization purposes, solitons are sometimes assigned the negative frequency [7, 17, 34],

$$f_i = -\frac{1}{2\pi}\sqrt{\frac{3A_i g}{4h^2}} \tag{1.37}$$

where h is the water depth.

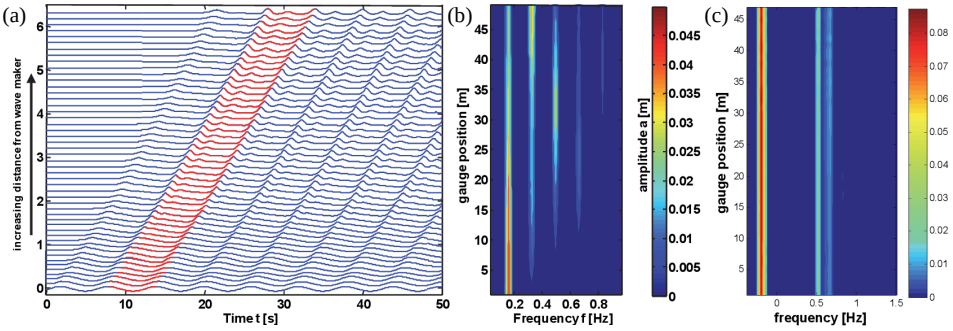


Figure 1.7: Comparison of conventional FFT and periodic KdV-NFT analyses. (a) Numerical simulation of an initially cosine-shaped wave with $H = 0.10$ m and $T = 6.0$ s propagating over a flat bottom with a constant water depth of $h = 0.56$ m. The red part indicates one period for better visualization. (b) Amplitude spectra calculated by conventional FFT. (c) Nonlinear spectra obtained by the KdV-NFT. Adapted from Brühl (2014), Dissertation, Technische Universität Braunschweig [100], https://doi.org/10.24355/dbbs.084-201411210916-0.

1.4.5. Comparison of FFT and Periodic KdV-NFT for Shallow Water Wave Evolution

To better understand how harmonic components are not well-suited to represent solitons under shallow water for conventional FFT and NFT, a numerical simulation

example from Brühl (2014) [100] using periodic KdV-NFT is presented. A numerical simulation was performed with the RNAS/VOF (Reynolds-averaged Navier-Stokes/volume of fuild) model COBRAS-UC [101]. This simulation provides dynamics of the nonlinear evolution of shallow water waves similar to the physical experiment shown in Fig. 1.2. More detailed descriptions can be found following in Brühl (2014) [100] or in Brühl et al. (2016) [17].

Here, an initial cosine wave with a wave height of $H = 0.10$ m and a wave period of $T = 6.0$ s was generated in a constant water depth of $h = 0.56$ m. The numerical domain was 50 m long, and the observed wave transformation occurred over a flat bottom. As shown in Fig. 1.7(a), the initial cosine wave does not retain its shape during propagation. The wave profile first becomes asymmetric, with a steeper front face, and subsequently develops higher wave crests. This change has been highlighted in red for one period for better visualization. Because the water depth remains constant, this transformation is not caused by bathymetric variation but by the both nonlinear and dispersive effects under the shallow water conditions.

The conventional FFT results in Fig. 1.7(b) initially show only one significant component at the fundamental frequency $f_0 = 0.167$ Hz, with an amplitude of approximately 0.05 m. As the wave propagates, as many as four additional components appear at the higher-harmonic frequencies $2f_0$, $3f_0$, $4f_0$, and $5f_0$. The amplitudes of these components are neither constant nor monotonically increasing with propagation distance. In the conventional Fourier interpretation, the appearance of these additional components is described as harmonic generation.

The nonlinear spectrum calculated using the periodic KdV-NFT is shown in Fig. 1.7(c). It can be seen that the nonlinear spectrum contains a total of four components. The largest component has an amplitude of approximately $a = 0.09$ m, representing a *soliton*. (As mentioned in Sec. 1.4.4, negative frequencies are utilized to visualize solitons in the nonlinear spectrum.) The other components correspond to oscillatory waves, with amplitudes of $a = 0.026$ m, $a = 0.01$ m, and $a = 0.001$ m, respectively. The type of the components, which is classified by the modulus m, is not shown here. The last component is nearly invisible in the figure owing to its small amplitude. An important feature of the NFT is that part of the nonlinear spectrum considered here remains invariant during propagation when the evolution is exactly governed by the corresponding integrable partial differential equation. This result is consistent with the conclusion of Osborne (2010) [6, p. 816], who stated that analytical, numerical and experimental results demonstrate that the nonlinear dynamics of the KdV equation show no resonances of additional spectral components under typical unidirectional shallow water propagation conditions. Here, the term *resonance* refers to the transfer of energy among spectral components from lower to higher. Indeed, no new nonlinear spectral components are generated as the shallow water wave propagates over the constant water depth in this simulation.

It should be noted that the periodic KdV-NFT is also capable of describing the dynamics represented by conventional Fourier modes. In the small-amplitude limit, the periodic KdV nonlinear spectrum reduces to the conventional linear Fourier representation [102]. Thus, the FFT may be regarded as the linear limiting description of the wave field, whereas the periodic KdV-NFT provides a nonlinear

spectral representation that remains applicable when finite amplitude effects become important. Although the FFT remains useful for quantifying the linear frequency content of a nonlinear wave profile, the periodic KdV-NFT provides a more physically consistent interpretation of shallow water wave evolution.

1.5. Research Questions

We have introduced how the nonlinear Fourier transform (NFT) is formulated based on the KdV and NLS equations under specific boundary conditions. Before applying the NFT to various wave fields obtained from numerical simulations and field measurements, we briefly revisit our motivation and establish the key research questions that guide this work. The main research questions can be formulated as follows:

1. Despite extensive research on rogue wave mechanisms, the application of NFTs to rogue wave data reveals nonlinear spectral characteristics of rogue wave events that remain poorly understood.

What are the characteristics of rogue waves in the nonlinear Fourier domain?

2. Open ocean wave fields are inherently non-integrable systems, with directional spreading representing a fundamental departure from the one-dimensional integrable equations underlying NFT theory. The effects of directionality on the nonlinear spectrum have rarely been investigated.

What are the effects of directional spreading on sea states with solitons?

3. Soliton gas, a collective ensemble of interacting solitons that dominates wave field dynamics, has been observed in laboratory experiments and land-locked lagoons. The presence of soliton gas in open ocean environments, where multiple non-integrable effects may suppress coherent structures, has not been established.

Do soliton gases actually occur in the open ocean?

1.6. Outline of the Dissertation

The focus of this dissertation is the application of the Nonlinear Fourier Transform (NFT) to water waves within the field of hydrodynamics. Due to the mathematical complexity of the NFT, only a limited number of studies have explored its application to water waves. In this study, we apply the NFT to both field measurement data and numerical simulation data to demonstrate its potential and to highlight some limitations in its use for analyzing water waves.

1.6.1. Chapter 2: Nonlinear Fourier Classification of 663 Rogue Waves Measured in the Philippine Sea

The nonlinear Schrödinger (NLS) equation is used to describe the propagation of deep water waves. Some highly nonlinear components, such as breathers and solitons from the NLS solutions, are regarded as possible generation mechanisms

of rogue waves. In Chapter 2, we apply the NFT based on the NLS equation to rogue wave data from field measurements in deep water. It is demonstrated that the presented method can successfully be applied to field measurement data as a signal processing tool. The statistical results also provide valuable insights regarding rogue wave characteristics.

The content in this chapter is adapted from "Lee, Y. C., Brühl, M., Doong, D. J., & Wahls, S. (2024). Nonlinear Fourier classification of 663 rogue waves measured in the Philippine Sea. PloS one, 19(5), e0301709." [3], which I authored, and is reproduced with permission from PLOS ONE.

1.6.2. Chapter 3: Evaluation of Nonlinear Fourier-based Maximum Wave Height Predictors under the Nonlinear Schrödinger Equation

The nonlinear Fourier transform can be a useful tool for predicting waves after they propagate a certain distance. This prediction is accurate if the nonlinear dynamics are fully governed by a specific nonlinear differential equation. As we know, rogue waves are extreme ocean waves that appear suddenly and vanish without a trace. Therefore, the objective here is to predict the occurrence of these rogue waves by the NFT-based criteria. The data is simulated using the JONSWAP spectrum with random phases. The spatial evolution of the JONSWAP time series is simulated through the one-dimensional NLS equation. Several parameters extracted from the NFT spectra of the initial time series will be investigated as predictors for the maximum wave height during the evolution.

The content in this chapter is adapted from "Lee, Y. C., Wahls, S., & Brühl, M. (2022). Evaluation of Nonlinear Fourier-Based Maximum Wave Height Predictors Under the Nonlinear Schrödinger Equation. In International Conference on Offshore Mechanics and Arctic Engineering (Vol. 85901, p. V05BT06A060). American Society of Mechanical Engineers." [1], which I authored, and is reproduced with permission from ASME.

1.6.3. Chapter 4: Impact of Directional Spreading on Nonlinear KdV-Soliton Spectra in Intermediate Water

We have analyzed data from both numerical simulations and field measurements. For nonlinear analysis of field measurement data, it is still uncertain how the nonlinear spectrum can be represented due to deviations from assumptions of the NLS equation under real conditions, such as narrow-banded and unidirectional propagation. The nonlinear spectrum will change if wave evolution is not fully governed by the corresponding nonlinear partial differential equation. Recent studies have demonstrated how long NLS solitons can maintain their amplitude under directional spreading. Similar to the NLS equation, the KdV equation assumes unidirectional conditions. However, it remains uncertain how representative the nonlinear spectrum of KdV-type equations is during evolution. The objective of

this study is to assess the effectiveness of the KdV-NFT in representing water wave dynamics under non-ideal conditions, particularly in wave fields with directionality.

The content in this chapter is adapted from "Lee, Y. C., & Wahls, S. (2025). Impact of directional spreading on nonlinear KdV-soliton spectra in intermediate water. Wave Motion, 137, 103542." [4], which I authored, and is reproduced with permission from Elsevier.

1.6.4. Chapter 5: When Do JONSWAP Spectra Lead To Soliton Gases In Deep Water Conditions?

Traditionally, ocean waves are analyzed using the linear Fast Fourier Transform, which assumes that they can be represented as a superposition of linear sine and cosine waves. However, many sea states exhibit significant nonlinearity. It remains unclear which specific sea states are predominantly characterized by nonlinear solutions such as breathers and solitons. When a large number of solitons dominates the dynamics of a system, scientists describe this collective behaviour of solitons as a soliton gas. Soliton gases are currently the subject of intense practical and theoretical investigations. The existence of soliton gases has been confirmed in experiments, but is not clear what kind of sea states might lead to soliton gases. Therefore, in order to determine the wave parameters for sea states in deep water that lead to soliton gases, large numbers of surface wave elevations are generated by the well-known JOSNWAP model. We investigate which JONSWAP parameters result in sea states in deep water that can be characterized as NLS soliton gases.

The content in this chapter is adapted from "Lee, Y. C., Brühl, M., & Wahls, S. (2023). When Do JONSWAP Spectra Lead to Soliton Gases in Deep Water Conditions?. In International Conference on Offshore Mechanics and Arctic Engineering (Vol. 86878, p. V005T06A101). American Society of Mechanical Engineers." [2], which I authored, and is reproduced with permission from ASME.

1.6.5. Chapter 6: Interpretation of Soliton Energy Ratios Measured in Directional Wave Fields

While the nonlinear Schrödinger equation assumes unidirectional wave propagation, recent studies demonstrate that solitons can persist under moderate directional spreading conditions, maintaining stability over several wave periods during their evolution. To bridge the gap between idealized NLS theory and realistic oceanic conditions, this study investigates how directional spreading affects soliton energy ratios derived from the nonlinear Fourier spectrum by constraining analysis to waves propagating within specific directional ranges, thereby approximating NLS validity while examining how soliton signatures evolve when directional energy is systematically removed from measured wave fields.

The content in this chapter is adapted from "Lee, Y. C. & Wahls, S. (2025). "Interpretation of Soliton Energy Ratios Measured in Directional Wave Fields, Applied

Ocean Research (under review)", which I authored, and is reproduced with permission from Elsevier.

1.6.6. Chapter 7: Observation of Suppressed Soliton Gases in the Open Ocean

Soliton gases are unique sea-state regimes characterized by collective behaviors of solitons and their mutual interactions, whose dynamics differ fundamentally from the linear Gaussian nature of conventional sea states. This distinct nonlinearity has attracted increasing scientific interest. We therefore investigate a highly nonlinear soliton-dominated sea state in deep water based on field measurements in Taiwan waters, using soliton energy ratios calculated via the nonlinear Fourier transform. Our findings successfully observed an extremely rare soliton gas-like condition, demonstrating its statistical characteristics. To our knowledge, this is the first field evidence of NLS soliton gas–like seas in deep waters. Additionally, we provide an interpretation of directional effects on the soliton gas–like seas.

The content in this chapter is adapted from "Lee, Y. C. & Wahls, S. (2026). Field observation of soliton gases in the deep open ocean. Results in Physics, 108726 [103], which I authored, and is reproduced with permission from Elsevier.

1.7. Data availability statement

Research data and code supporting the findings described in this thesis are available at https://data.4tu.nl/private_datasets/ltj6W-uL7rOFLHH9kX742YE5qi7xOBoeyB6_HzBLYNE.

2

NONLINEAR FOURIER CLASSIFICATION OF 663 ROGUE WAVES MEASURED IN THE PHILIPPINE SEA

CHAPTER ABSTRACT

Rogue waves are sudden and extreme occurrences, with heights that exceed twice the significant wave height of their neighboring waves. The formation of rogue waves has been attributed to several possible mechanisms such as linear superposition of random waves, dispersive focusing, and modulational instability. Recently, nonlinear Fourier transforms (NFTs), which generalize the usual Fourier transform, have been leveraged to analyze oceanic rogue waves. Next to the usual linear Fourier modes, NFTs can additionally uncover nonlinear Fourier modes in time series that are usually hidden. However, so far only individual oceanic rogue waves have been analyzed using NFTs in the literature. Moreover, the completely different types of nonlinear Fourier modes have been observed in these studies. Exploiting twelve years of field measurement data from an ocean buoy, we apply the nonlinear Fourier transform (NFT) for the nonlinear Schrödinger equation (NLSE) (referred to NLSE-NFT) to a large dataset of measured rogue waves. While the NLSE-NFT has been used to analyze rogue waves before, this is the first time that it is systematically applied to a large real-world dataset of deep-water rogue waves. We categorize the measured rogue waves into four types based on the characteristics of the largest nonlinear mode: stable, small breather, large breather and (envelope) soliton. We find that all types can occur at a single site, and investigate which conditions are dominated by a single type at the

measurement site. The one and two-dimensional Benjamin-Feir indices (BFIs) are employed to examine the four types of nonlinear spectra. Furthermore, we verify on a part of the data set that for the localized types, the largest nonlinear Fourier mode can be attributed directly to the rogue wave, and investigate the relation between the height of the rogue waves and that of the dominant nonlinear Fourier mode. While the dominant nonlinear Fourier mode in general only contributes a small fraction of the rogue wave, we find that soliton modes can contribute up to half of the rogue wave. Since the NLSE does not account for directional spreading, the classification is repeated for the first quartile with the lowest directional spreading for each type. Similar results are obtained.

The text in this chapter has previously appeared in modified form in the article "Lee, Y. C., Brühl, M., Doong, D. J., & Wahls, S. (2024). Nonlinear Fourier classification of 663 rogue waves measured in the Philippine Sea. PloS one, 19(5), e0301709." [3]. This is an open access article distributed under the terms of the Creative Commons Attribution License, which permits unrestricted use, distribution, and reproduction in any medium.

2.1. INTRODUCTION

Rogue waves are rare, suddenly emerging extreme waves with heights of at least twice the significant wave height. They are a danger for ships and offshore structures [104]. There are many different possible mechanisms that can potentially lead to the formation of oceanic rogue waves, such as the random superposition of Stokes waves [105], nonlinear four-wave interactions [16] and modulational instability (MI) [106–108], currents [109], crossing sea states [108, 110] and inhomogeneous sea floors [111–114]. The practical relevance of these individual mechanisms for rogue waves in the actual ocean is still under discussion [115–118].

Rogue waves are usually investigated from a statistical point of view, which makes it possible to estimate how likely rogue waves occur in random seas. Probability distributions for the significant and maximum wave heights have been derived for linear [5, 119, 120] and nonlinear cases [15, 121], assuming uni-directionality and narrow-bandedness. The effect of directional spreading and/or larger bandwidths has been investigated as well [122, 123]. There are also empirical distributions that are directly fit to data [124]. See the following papers for a discussion of further literature [125–129].

The statistical approach to rogue waves is widely applied for tasks like the design of ships and offshore structures [130, 131], but it is less useful for forecasting if a rogue wave is actually about to occur soon. This question is essential for the safe operation of ships and offshore structures after they have been deployed [104]. Many different indicators for the forthcoming occurrence of rogue waves, with varying predictive value and computational cost, have been proposed in the literature. Simple standard wave parameters such as the significant wave height or peak period only have value if they are employed in a region-specific manner [132]. The Benjamin-Feir index (BFI), which is obtained by dividing steepness by bandwidth and is related to the onset of the modulational instability, has been found to correlate with enhanced rogue wave occurrence [16, 106, 133], at least for long-crested waves [134]. The BFI has been integrated into the ECMWF freak wave warning system [135], but was found to perform badly on observational data in other works, so that crest-trough correlation has been proposed an alternative [105, 118]. Another indicator for specific analytic unidirectional rogue waves known as Peregrine breathers comes in the form a triangular spectrum that is present during all times of their evolution [136]. Next to simulations [137, 138], the triangular spectrum could also be observed in wave tank experiments [139]. As an alternative to the usual Fourier transform, wavelets have been considered as well [140, 141]. Yet another approach is to propagate measured time series numerically using either physical models or data-driven approaches to predict upcoming rogue waves [142, 143]. Finally, nonlinear Fourier transforms (NFTs; a.k.a. scattering transforms) have been used to investigate and predict rogue waves as well [1, 24, 25].

NFTs were invented in the context of the inverse scattering method for solving integrable partial differential equations [13], but they can also be used as signal processing tools [6, 91]. Their unique capabilities include the detection of possibly hidden solitons [7, 17, 99, 144], breather components [28, 145] and nonlinear instabilities [24, 146]. This makes them very interesting candidates for the analysis of

rogue waves. Different types of NFTs exist for different types of nonlinear dynamics. Recently, the NFT for the Korteweg-de Vries (KdV) equation with vanishing boundary conditions has been applied to a large data set of measurements from a shallow water site in the southern North Sea [34], at which rogue waves occurred more often than expected [147]. Strongly outstanding solitons in the nonlinear spectrum were found to indicate a rogue wave with high probability[1]. In this study, we use the NFT for the periodic nonlinear Schrödinger equation (NLSE) to analyze ocean wave data from a deep water site. Consequently, we denote this method the (periodic) NLSE-NFT.

The NLSE is a classical model for the propagation of weakly nonlinear narrow-banded wave envelopes in deep water in one dimension. The MI of the NLSE manifests itself in that even very small perturbations of simple initial conditions such as sufficiently large plane waves initially grow exponentially [76]. After the initial stage of exponential growth, the nonlinear dynamics damp the growth and lead to the generation of localized structures which can be described by breather solutions of the NLSE [148, 149]. As the name indicates, a breather is a wave packet which "breathes" up and down in space-time domain and propagates with a particular group velocity within a cycle. Some breathe only once. Breathers describe the growth-decay cycle of the MI and are sometimes considered prototypical rogue waves [71, 150–152].

The periodic NLSE-NFT was first developed to construct explicit formulas for periodic solutions of NLSE [93, 153]. To compute it, the linear spectrum of the so-called Zakharov-Shabat operator has to be determined. The periodic NLSE-NFT is then obtained by considering different types of eigenvalues (e.g., with periodic or anti-periodic eigenfunctions). For data that is actually governed by the NLSE, the NLSE-NFT has the interesting property that the evolution of the nonlinear spectrum can be performed analytically. The nonlinear Fourier modes provide information about the spectral signatures in nonlinear spectrum and behavior of the nonlinear system. The most important part of the nonlinear spectrum (i.e., the main spectrum that consists of periodic and anti-periodic eigenvalues) is even a constant of motion, i.e., it does not change at all during propagation with respect to the NLSE. In practice, the nonlinear spectrum will change, at least to some degree, as real ocean waves are often broad-banded and directional. This violates the narrow-band spectrum and uni-directionality assumptions behind the NLSE. However, these assumptions are not uncommon. Many classic wave height distributions are e.g. derived under the same assumptions, yet they are widely applied to real-world data [125]. Similarly, the conventional linear Fourier transform, which only solves linear systems exactly, is widely used to analyze nonlinear processes. We therefore argue that the NLSE-NFT can also be used to analyze processes that are not governed by the NLSE, if the results are interpreted with care. Indeed, the NLSE-NFT has successfully been used in this way both in optics [20–23] and in ocean engineering [28, 29, 154]. The evolution of the nonlinear spectrum is no longer trivial in such cases, but one may expect that it is still a better representation than the conventional linear Fourier spectrum,

[1] Note that the detected solitons were too small to explain the rogue waves on their own. The solitons instead made other, already large waves even larger, turning them into rogue waves.

because it accounts for certain nonlinear effects. It is worth mentioning that recent findings from a physical experiment demonstrate that breathers and solitons based on NLSE can propagate under short-crested and directional conditions [155]. A similar nonlinear directional wave group has been found based on a numerical wave model constrained by stereo images [156]. The propagation of rogue waves within envelope solitons through broad-banded water waves has been observed [154]. One experimental result also shows that the breather solution of NLSE can survive in an oppositely propagating regular wave train [157]. These further increase the feasibility of applying this method, and may not be limited by the aforementioned conditions.

In the literature, the periodic NLSE-NFT has been applied to simulated and wave tank data in many studies, e.g. [24, 25, 27]. However, only a very few studies have applied the periodic NLSE-NFT to experimental and measured oceanic rogue waves so far. In Ref. [28], a storm event in the Currituck Sound that included rogue waves was analyzed and found to be dominated by breather components in the nonlinear spectrum. On the other hand, a giant rogue wave measured in the Bay of Biscay during a storm was dominated by stable "Stokes" modes [29], which will be introduced in Sec. 2.4. In light of these contrasting results, the question arises if rogue waves in the ocean have typical nonlinear spectral signatures.[2]

In this study, we therefore apply the periodic NLSE-NFT to 663 10-minutes samples containing rogue waves from in-situ measurements in the Philippine Sea, which is a section of the western North Pacific Ocean. Our goal is to investigate if the rogue waves at this site exhibit typical nonlinear spectral signatures. We first categorize the nonlinear spectra based on the characteristics of the largest nonlinear Fourier mode. We then investigate if particular characteristics are more common for rogue waves than others, and compare the occurrence of different types of nonlinear spectra for rogue-wave and non-rogue samples. We investigate the relationship between rogue waves in time series and the largest nonlinear Fourier mode using a new approach. Finally, the results are discussed.

2.2. Rogue wave Definition

In this study, each 10 min time series has been analysed in time domain by the downward zero-crossing method [159]. This method can extract individual wave heights and wave periods by identification of the water surface crossing the mean water level in an downward direction. Subsequently, each individual wave was ranked and the mean wave height of the one-third largest waves is defined as the significant wave height $H_{1/3}$. The wave are classified as rogue waves if

$$\mathrm{AI} = \frac{H}{H_{1/3}} \geq 2, \tag{2.1}$$

where the ratio AI is called the abnormality index [160].

[2] We also mention that using the vanishing instead of the periodic NLSE-NFT, several measured rogue waves were found on top of large soliton groups [154, 158]. Breathers can be interpreted as solitons that interact with a specific background, but solitons that interact with a background do not have to be breathers. Therefore, it is not clear what the periodic NLSE-NFT of these rogue waves would look like.

To characterize the sea states in which rogue waves occur, we now introduce several parameters. Following [161, 162], the directional spreading is calculated as

$$\sigma_\theta = \left[2 \left\{ 1 - \left(\frac{p^2 + q^2}{m_0^2} \right)^{\frac{1}{2}} \right\} \right]^{\frac{1}{2}}, \tag{2.2}$$

where $p = \int_0^{2\pi} \int_0^{\infty} \cos(\theta) S(\omega,\theta) d\omega d\theta$, $q = \int_0^{2\pi} \int_0^{\infty} \sin(\theta) S(\omega,\theta) d\omega d\theta$, and $m_0 = \int_0^{2\pi} \int_0^{\infty} S(\omega,\theta) d\sigma d\theta$ is the zeroth spectral moment. $S(\omega,\theta)$ is the directional spectrum.

The Benjamin–Feir index (BFI) is a parameter used to describe kurtosis in water waves that can be related to the modulational instability [16]. It is given by the ratio of the spectral steepness ϵ and the spectral width δ_ω for one-dimensional wave spectra,

$$BFI_{1D} = \frac{\sqrt{2}\epsilon}{\delta_\omega}. \tag{2.3}$$

The spectral width δ_ω can be calculated from Goda's peakedness parameter Q_p [163], which is related to half-width at half-maximum of the spectrum:

$$\delta_\omega = \frac{1}{Q_p \sqrt{\pi}}, \tag{2.4}$$

$$Q_p = \frac{2}{m_0^2} \int \omega S^2(\omega) d\omega. \tag{2.5}$$

The one-dimensional BFI does not account for directionality. Mori et al. (2011) investigated the relationship between wave height distribution and kurtosis in directional seas and introduced a two-dimensional BFI to assess kurtosis behavior within directional sea states [164]. The proposed two-dimensional BFI is given by

$$BFI_{2D}^2 = \frac{BFI_{1D}^2}{1 + \alpha_2 R}, \tag{2.6}$$

where α_2 is an empirical constant equal to 7.1, and

$$R = \frac{1}{2} \frac{\delta_\theta^2}{\delta_\omega^2} \tag{2.7}$$

is the ratio of the directional bandwidth δ_θ and the frequency width δ_ω. Here, the directional bandwidth δ_θ is calculated as[135]

$$\delta_\theta = \sqrt{2(1 - M_1)}, \tag{2.8}$$

$$M_1 = \frac{1}{m_0} \int \int \cos\left(\theta - \theta_p(\omega)\right) S(\omega,\theta) d\omega d\theta, \tag{2.9}$$

$$\theta_p(\omega) = \arctan\left(\frac{\int \sin(\theta) S(\omega,\theta) d\theta}{\int \cos(\theta) S(\omega,\theta) d\theta} \right) \tag{2.10}$$

with θ_p denoting the peak direction.

2.3. ROGUE WAVE DATA ACQUISITION AND PRE-PROCESSING

2.3.1. DESCRIPTION OF ROGUE WAVE DATA

Surface wave data was derived from a buoy operated by the Coastal Ocean Monitoring Center (COMC), National Cheng Kung University (NCKU), Taiwan [165, 166]. The in-situ measurement device is shown in Fig. 2.1a. It is a discus buoy equipped with an accelerometer-tilt-compass (ATC) sensor that was moored at 21.75°N, 124.12°E in a water depth of around 5000 m in the Philippine Sea, in the margin of the western North Pacific Ocean. Compared to the relative position of Taiwan, it is located in the southeast of Taitung county. The buoy is called the Taitung Open Ocean buoy. The buoy is 2.5 meters in diameter and 1310 kg in weight, and its power is supplied by batteries and solar panels. Two anemometers are installed on the top of the buoy about 3 meters above the sea level to measure the wind information including wind speed and wind direction. Navigation assistance is provided by radar reflector. Barometers and temperature sensors measure the atmospheric pressure and air temperature, respectively. Acoustic Doppler current profilers (ADCP) are widely used for measuring ocean currents. The ATC sensor measures buoy accelerations, inclinations, and the azimuth at a frequency of 2 Hz. The measurements of accelerations of buoys are well consistent with the surface wave motions.

As shown in Fig. 2.1b, the buoy motions include six degrees of freedom, which are the translational motions (heave, sway and surge) and rotational motions (roll, pitch, and yaw). Each hour, a time series with a length of 10 min (600 s) is recorded. Exemplary time series of the buoy accelerations and corresponding motions of pitch, roll, and azimuth are shown in Fig. 2.2a. The vertical acceleration is used to calculate one-dimensional spectra, where the power spectral density (Fig. 2.2b) is calculated by Fourier transform of the time series of buoy accelerations. Finally, the surface wave elevation (Fig. 2.2c) is obtained by filtering the low-frequency noise generated during the transformation between acceleration and spectrum [167, 168]. Note that the influence of wave transformation over bathymetry and the effects of refraction can be neglected in our data due to the deep water depth of 5000 m.

To give an idea of what the surface waves in our measurements look like, we provide histograms of basic wave parameters for both rogue and non-rogue waves samples in Fig. 2.3. The wave parameters include significant wave height $H_{1/3}$, maximum wave height $H_{\max}$, peak period T_p and directional spreading σ_θ. The samples have a wide range of significant wave height $H_{1/3}$ from 0.04 m to 15.28 m, maximum wave height $H_{\max}$ from 0.1 m to 28.83 m and peak period T_p from 4.62 s to 21.43 s. This data set covers most of the local environmental conditions and contains most types of waves. The directional spreading is calculated based on the Ref. [161]. Our buoy is located in the open sea, where the waves can come from any direction. The directional spreading of both rogue and non-rogue samples consequently ranges from 52° to 83° and is therefore quite large.

2.3.2. Reconstruction of Surface Wave Elevation

An ATC sensor consists of three accelerometers and three magnetometers, which measure the motion and orientation of the buoy. In order to apply the NLSE-NFT, the surface elevation must be reconstructed from this data. For the reconstruction of the time series of surface elevation, only the nearly vertical acceleration, denoted by a_Z, was used. The horizontal acceleration and rotational measurements were retained for the characterization of buoy motion and directional wave properties.

We now summarize the procedure outlined in Appendix A of Ref. [169]. The vertical acceleration in discrete form, $a_Z[j] = a_Z(j\Delta t)$, with $j = 0, 1, \ldots, N-1$, is transformed into the frequency domain using the FFT, which is given by

$$A_Z[n] = \frac{1}{N}\sum_{j=0}^{N-1} a_Z[j]\exp\left(-\mathrm{i}\frac{2\pi n j}{N}\right), \tag{2.11}$$

where Δt is the sampling interval and N is the number of samples. $A_Z[n]$ is the complex Fourier coefficient of the vertical acceleration with the n-th frequency bin.

The real and imaginary part of the Fourier coefficient, the power spectral density (PSD), and the phase spectrum of the acceleration are given by

$$A_Z[n] = G_n + \mathrm{i}H_n, \tag{2.12}$$

$$S_a[n] = \frac{|A_Z[n]|^2}{\Delta f}. \tag{2.13}$$

$$\epsilon_a[n] = \tan^{-1}\left(\frac{H_n}{G_n}\right), \tag{2.14}$$

where $\Delta f = 1/(N\Delta t)$ is the frequency resolution with $N = 512$ s and $\Delta t = 1$ s. For an even number of samples N, the frequencies are $f_n = n\Delta f$ for $0 \le n \le N/2-1$ and $f_n = (n-N)\Delta f$ for $N/2 \le n \le N-1$.

Now we explain why the phase spectrum of acceleration and surface elevation differ in phase by π. According to linear wave theory, the vertical acceleration is related to the surface elevation through the second time derivative. For a harmonic surface elevation $\eta(t) = \eta_a\cos(\omega t + \phi)$, the corresponding vertical acceleration is

$$a_Z(t) = \frac{\mathrm{d}^2\eta(t)}{\mathrm{d}t^2} = -\omega^2\eta_a\cos(\omega t+\phi) = \omega^2\eta_a\cos(\omega t+\phi+\pi). \tag{2.15}$$

Taking the second time derivative introduces a factor of $-\omega^2$, which corresponds to a phase shift of π between the acceleration and surface elevation. Therefore, the phase spectrum of the surface elevation is given by

$$\epsilon_\eta(f_n) = \epsilon_a(f_n) + \pi. \tag{2.16}$$

The acceleration signals measured by the buoys are usually contaminated by low-frequency noise [168–170]. This noise was corrected using an empirical noise correction function. The corrected acceleration PSD was defined as

$$S'_a(f_n) = \begin{cases} S_a(f_n) - NC\left(f_n\right), & \text{for} \quad |f_n| \ge 0.03 \text{ Hz}, \\ 0, & \text{for} \quad |f_n| < 0.03 \text{ Hz}. \end{cases} \tag{2.17}$$

By applying the noise correction function $NC(f_n)$, the low-frequency noise was removed from the acceleration PSD. In the present study, the correction function, following [170], was given by

$$NC(f_n) = \frac{\max\left[C_{11M}(|f_n| < 0.03)\right]}{0.15 - f_{\mathrm{Max}C_{11M}}}(0.15 - |f_n|), \tag{2.18}$$

where $\max[C_{11M}(|f_n| < 0.03)]$ is the maximum acceleration PSD within the frequency range from -0.03 to 0.03 Hz, and $f_{\mathrm{Max}C_{11M}}$ is the frequency at which this maximum occurs. Signals with absolute frequencies $|f_n|$ below 0.03 Hz corresponding to periods longer than approximately 33.3 s were ignored. This is reasonable because the periods of typical ocean surface waves are generally shorter than 20 s.

Because the conversion from acceleration to surface elevation involves a factor of ω^{-2}, low-frequency noise in the acceleration signal can be strongly amplified. The acceleration spectrum was therefore corrected before the surface elevation spectrum was calculated. The corrected acceleration PSD, $S'_a(f_n)$, was converted into the surface elevation PSD according to [169, 170]

$$S_\eta(f_n) = \frac{S'_a(f_n)}{\omega^4} = \frac{S'_a(f_n)}{(2\pi f_n)^4}. \tag{2.19}$$

The surface elevation PSD had a frequency bin width of $\Delta f = 0.001953$ Hz. It was subsequently smoothed using convolution with a 15-point Bartlett window.

Based on the definition of the power spectral density, the magnitude of the surface elevation Fourier coefficient was obtained as

$$\left|\widetilde{\eta}(f_n)\right| = \sqrt{S_\eta(f_n)\Delta f}, \tag{2.20}$$

where $\widetilde{\eta}(f_n)$ denotes the complex Fourier spectrum of the surface elevation and Δf is the frequency resolution. The complex Fourier coefficients of the surface elevation were then reconstructed by combining the spectral magnitude with the corresponding surface elevation phase spectrum

$$\widetilde{\eta}(f_n) = \left|\widetilde{\eta}(f_n)\right| \exp\left[\mathrm{i}\epsilon_\eta(f_n)\right], \tag{2.21}$$

The time series of surface wave elevation was subsequently obtained using the inverse FFT.

2.4. Interpretation of the nonlinear Fourier spectrum by the NLSE-NFT

Before we introduce the four classes of nonlinear spectra mentioned in the abstract, we start with a more fundamental study of different characteristic solutions of the NLSE using numerical simulations. The main spectrum and spines in the nonlinear spectrum stay invariant during the evolution with respect to the NLSE. This distinctive feature enables the detection of hidden characteristics such as e.g. envelope solitons (when the NLSE holds). This is the key advantage of the NFT:

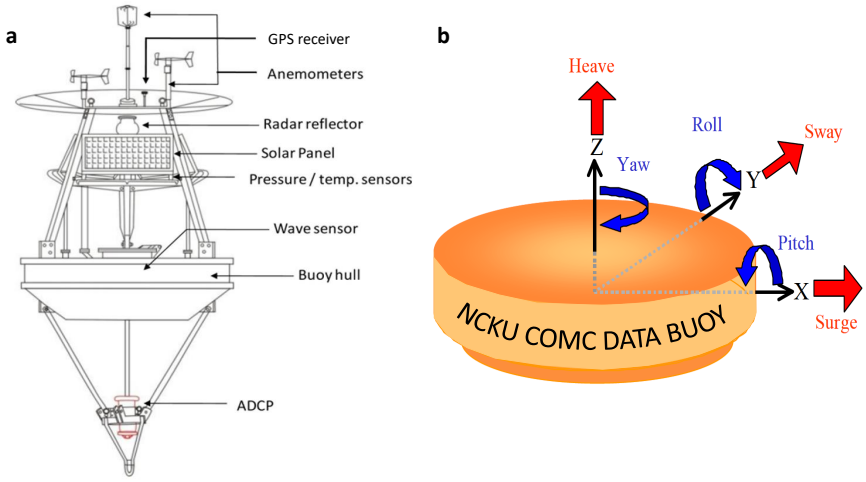


Figure 2.1: **Measurements of surface waves by wave buoys operated by Coastal Ocean Monitoring Center (COMC), National Cheng Kung University (NCKU), Taiwan.** (a) The discus buoy is equipped with an GPS receiver, anemometers, radar reflector, temperature sensors, accelerometer-tilt-compass (ATC) sensor and acoustic Doppler current profiler (ADCP). (b) The buoy motions by six degrees of freedom are heave, sway and surge, roll, pitch, and yaw.

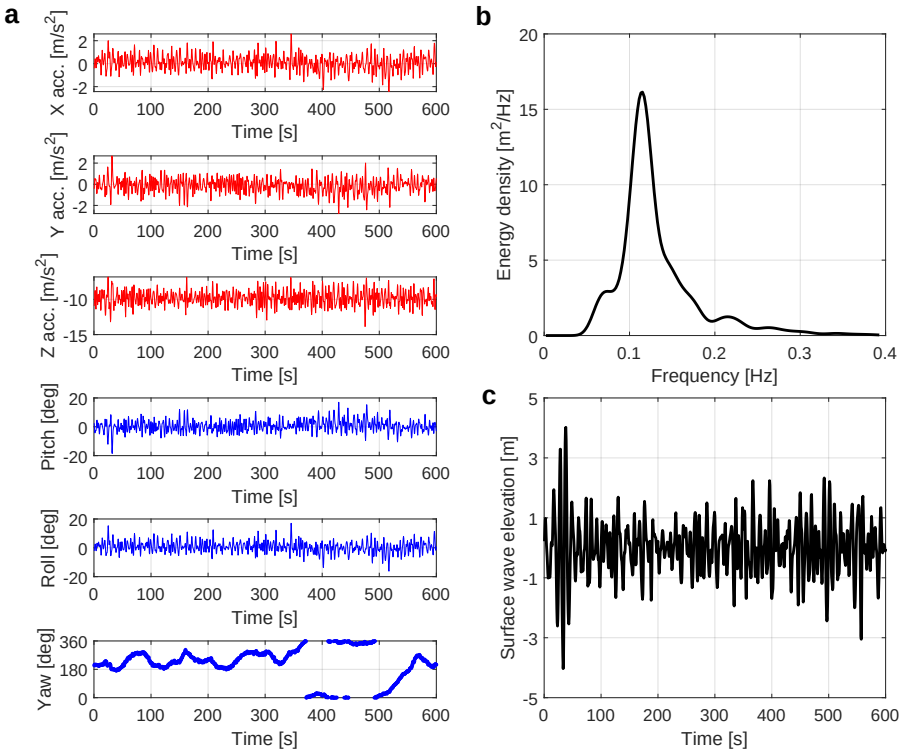


Figure 2.2: **Signals from measurements.** (a) The time series of buoy accelerations and corresponding motions of pitch, roll, and yaw. (b) The power-density spectrum determined by heave acceleration.(c) The time series of surface-wave elevation determined by wave spectrum.

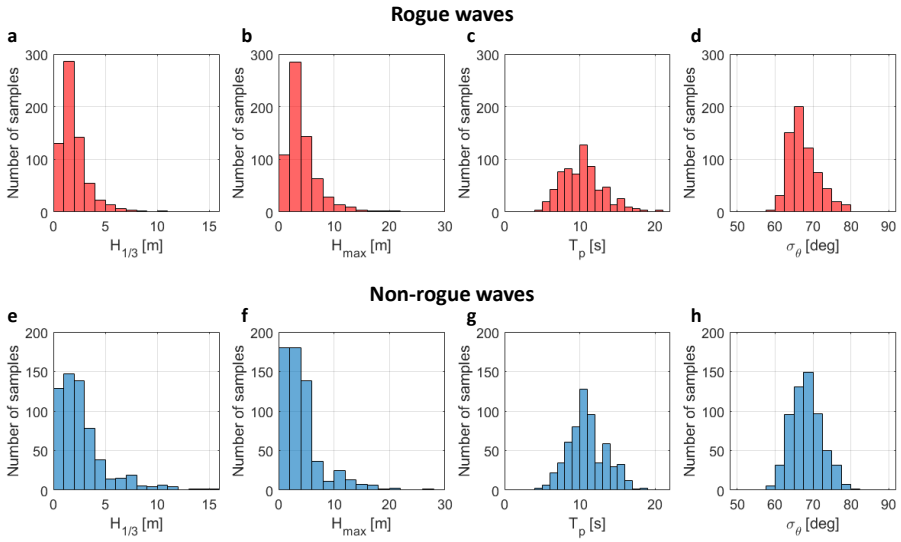


Figure 2.3: **Histograms of basic wave parameters of measured surface waves.** (a-d) Histograms of rogue wave samples of the significant wave height $H_{1/3}$, maximum wave height $H_{\max}$, peak period T_p and directional spreading σ_θ, respectively. (e-h) Histograms of non-rogue wave samples of significant wave height $H_{1/3}$, maximum wave height $H_{\max}$, peak period T_p and directional spreading σ_θ, respectively. There are 663 samples for rogue waves and 600 samples for non-rogue waves, respectively.

it describes solutions of NLSE in terms of analytically evolving nonlinear spectral components.

The well-known breather solutions of the NLSE include Akhmediev breathers, Peregrine breathers and Kuznetsov-Ma breathers. These solutions stand as exemplary prototypes for the modeling of rogue waves in various nonlinear media. Recently, large families of breathers that contain these solutions as special cases were investigated in the Refs. [171, 172]. There are two kinds of doubly periodic solutions, A-type and B-type, which differ by the phase shift of their consecutive maxima. The local maxima of A-type breathers occur periodically with a shift of half the temporal period after propagating half the spatial period. B-type breathers exhibit local maxima that occur periodically without a shift in the temporal period. A- and B-type breathers are specified by parameters known as α_3, ρ, and η, and α_1, α_2, and α_3, respectively.

Fig. 2.4 shows four characteristic wave structures in the spatial-temporal domain and in the nonlinear Fourier domain: a constant envelope (first row), a soliton (second row), an A-type breather with parameters $\alpha_3 = 1, \rho = 3, \eta = 0.4$ (third row) and a B-type breather with parameters $\alpha_1 = 0.1, \alpha_2 = 0.5, \alpha_3 = 1$ (fourth row). Note that $u(X,T)$ refers to the complex envelope of the surface elevation with X and T denoting normalized space and moving time variables. We compute the nonlinear spectra of these general wave structures using the periodic NLSE-NFT. The corresponding nonlinear spectra of the four characteristic waveforms are shown in the Figs. 2.4b,e,h and k. Note that the nonlinear spectra are symmetric with respect to the real axis. The complex points marked with blue circles in the plots indicate the main spectrum. The red curves connecting pairs of main spectrum points are the spines.

We now discuss the connection between spines and linear stability. It can happen that one spine ends exactly where another begins, so that two points in the main spectrum share the same position. Such points are then called *double points*. For the constant envelope in Fig. 2.4b, a double point occurs at $\lambda = \pm 0.81i$ because two spines touch. For the soliton in Fig. 2.4e, $\lambda = \pm 0.5i$ appears to be a double point, but we know from theoretical results that the spine is just very short. If a double point traps a point in the auxiliary spectrum, it is called *degenerate* [173]. The point $\lambda = 0.86i$ in Fig. 2.4b is an example for a degenerate point. This can be seen in Fig. 2.4c, where the values of the hyperelliptic modes $\mu_k(0,T)$ have been marked with small black dots for $0 \leq T \leq l$. We see that a single black point is stuck at the double main spectrum point at $\lambda = 0.86i$. This shows that the corresponding auxiliary spectrum cannot move away and is thus trapped: $\mu_k(0,0) = \mu_k(0,T)$ for $0 \leq T \leq l$. Therefore, we conclude that $\lambda = 0.86i$ is degenerate. We can also see that the point $\lambda = 0.5i$ in Fig. 2.4e is not a degenerate double point, because the corresponding hyperelliptic mode in Fig. 2.4f is moving around. It is therefore not degenerate. The A-type breather has double points at the centers of the horizontal spines in Fig. 2.4h. From Fig. 2.4i, we see that they are not degenerate either. The B-type breather also has no degenerate points in Fig. 2.4k. We know this because degenerate points can only occur on spines or on the real axis [146, p. 825].

Degenerate double points in the main spectrum are known to play a fundamental

role for the modulational instability [146, 174]. Any double point in the main spectrum will, except in very special cases, split into two single points when the solution is perturbed. If a hyperelliptic mode is trapped by a degenerate double point, it can thus be freed by arbitrarily small perturbations. The freed hyperelliptic mode will sometimes grow rapidly as the waveform evolves and then significantly change the solution via Eq. (1.27). In such cases, the solution turns out to be linearly unstable [146]. The plane wave in Fig. 2.4a is for example known to be linearly unstable [76], which is caused by the degenerate points on the spine [146, 174]. Degenerate points are thus indicators for potential linear instabilities. However, not all degenerate points give rise to instabilities. For example, there are infinitely many degenerate points on the real axis (not shown in Fig. 2.4) that are known not to cause instability [146]. The most useful consequence of this discussion probably is that finite genus solutions of the NLSE without non-real main points in the main spectrum that are located on spines are linearly stable [146].

Following the terminology in [6], spines in the nonlinear spectrum are also called nonlinear Fourier modes. A spine that crosses the real axis (such as the central spines in the Figs. 2.4b,h,k) is called a stable mode. Stable modes correspond to sine or Stokes waves [6]. (The Stokes waves turn into sine waves for small amplitudes. The spines become vertical lines in that case. See e.g. [28, Fig. 13] or compare Figs. 3 and 4 in [63].) A spine that does not cross the real axis (such as the nearly overlapping double points with invisible spines in Fig. 2.4d, the two horizontal spines in Fig. 2.4f and the two vertical spines in Fig. 2.4h that do not cross the real axis) is called an unstable mode [6, 28]. When an unstable mode interacts with a stable mode as in the Fig. 2.4h and k, it corresponds to a breather [6]. An unstable mode is considered to be a soliton when, as in Fig. 2.4e, it visually appears to be a double point with a spine of length zero. In that case, no interacting stable mode is needed. Unstable modes are called unstable because they describe the *nonlinear* stage of the modulational instability, which is known to be dominated by breathers [6, p. 276], [173]. Solitons are also counted in this class as they can be obtained by taking the appropriate limits for breather solutions. Technically, the solitons in the periodic NLSE-NFT spectrum are just breathers whose parameters are very close to this limit.

2.5. Four types of nonlinear spectra of rogue wave samples in the ocean

We are now ready to introduce the four different types of nonlinear spectra used in our classification. To illustrate them, we selected four rogue wave records with similar significant wave height $H_{1/3} \cong 3.5$ m. They were measured during storm events with extreme environmental conditions. The four time series with rogue waves have similar significant wave heights $H_{1/3}$ equal to 3.24 m, 3.44 m, 3.62 m and 3.56 m, but different maximum wave heights H_{max} equal to 6.67 m, 6.96 m, 7.53 m, and 8.05 m, respectively. They are shown in Fig. 2.5a to Fig. 2.5d (black lines). The abnormality index (AI) is calculated as the ratio of maximum wave height H_{max} to significant wave height $H_{1/3}$ and equals 2.06, 2.02, 2.08 and 2.26, respectively. This qualifies them as rogue waves. We have labelled plus/minus the significant wave

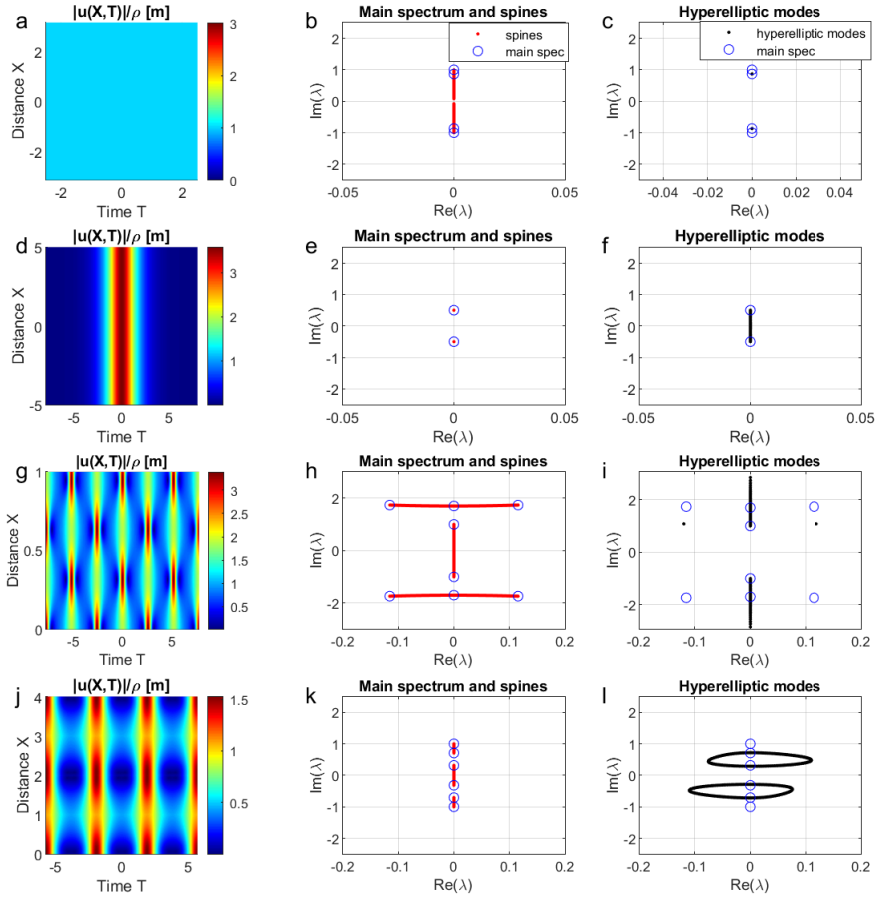


Figure 2.4: **Characteristic wave structures in the spatial-temporal domain and their analytical results from the nonlinear Fourier transform.** (a) Spatial-temporal evolution of the constant envelope. (b) Main spectrum and spines of the constant envelope. The small gap in the spine at zero is a numerical artifact. (c) Hyperelliptic modes of the constant envelope. (d) Spatial-temporal evolution of the fundamental soliton. (e) Main spectrum and spines of the fundamental soliton. (f) Hyperelliptic modes of the fundamental soliton. (g) Spatial-temporal evolution of the A-type doubly periodic solutions of the NLSE with the parameters $\alpha_3 = 1, \rho = 3, \eta = 0.4$. (h) Main spectrum and spines of the A-type doubly periodic solutions of the NLSE. (i) Hyperelliptic modes of the A-type doubly periodic solutions. The two individual black points in the upper left and right are numerical artifacts. (j) Evolution of the B-type doubly periodic solutions of the NLSE with the parameters $\alpha_1 = 0.1, \alpha_2 = 0.5, \alpha_3 = 1$. (k) Main spectrum and spines of the B-type doubly periodic solutions of the NLSE. (l) Hyperelliptic modes of the B-type doubly periodic solutions

height $H_{1/3}$ on the right y-axis, and indeed found the wave elevation range larger than twice of the significant wave height $H_{1/3}$. The red lines in Fig. 2.5 represent the magnitudes of the complex envelopes obtained from the Hilbert transform.

Subsequently, we show the nonlinear spectra of the four rogue wave time series data obtained by using the NLSE-NFT. The nonlinear spectra are presented in Fig. 2.6, where the horizontal axis is the wave frequency in Hz and the vertical axis is the spectral amplitude. Note that the units of the nonlinear spectra in Fig. 2.6 have been chosen such that the NFT reduces to the usual Fourier transform for low amplitude signals. Nonlinear modes however have no interpretation in terms of frequency. In the following, we classify the nonlinear spectra with rogue waves into four types according to their spectral portraits.

All spectral modes of the spectrum in Fig. 2.6a are connected to the real axis. This means we consider them stable modes, which correspond to be either sine or Stokes waves [6]. The difference between the spectral components of sine waves and Stokes waves is that the main spectrum points of sine waves are connected by vertical spines, and the main spectrum points of Stokes waves are connected by distorted spines. In this case, the rogue wave is generated by nonlinear interactions of sine-wave or Stokes-wave components [6]. We categorize this spectrum as type 1, i.e. a stable-mode spectrum.

In Fig. 2.6b, the two points at the coordinates (0.102 Hz, 0.329 m) and (0.103 Hz, 0.383 m) are connected by a spine that does not cross the real axis. Together with the closest stable mode, it represents a breather, which is a combination of a stable and an unstable mode (see Fig. 2.4h and k). It indicates some nonlinear effects in the sea state. Here, the unstable mode has an amplitude similar to the stable modes. Since the maximum amplitude of the unstable mode does not exceed 120% of the maximum amplitude of the stable modes, we categorize this spectrum as type 2, i.e. a small-breather spectrum. This threshold is determined through empirical evaluation, which relies on comparing the amplitudes of stable modes and small breathers.

The nonlinear spectrum in Fig. 2.6c has one large breather in the peak center of the spectrum and three small breathers. The largest unstable mode consists of two main spectral points at (0.096 Hz, 0.610 m) and (0.096 Hz, 0.625 m) at the peak of the spectrum. Since the maximum amplitude of the unstable mode is larger than 120% of the maximum amplitude of the stable modes, we categorize this spectrum as type 3, i.e. a large-breather spectrum. The nonlinear spectrum in Fig. 2.6c indicates that the time series of Fig. 2.5c is generated by the nonlinear interactions of one larger breather, three small breathers and other small-amplitude stable modes.

In the nonlinear spectrum in Fig. 2.6d, there is one large breather with two points of main spectrum very close to each other such that the spine reduces to a single red dot in the figure. This constellation corresponds to a periodicized soliton (see Fig. 2.4e). An unstable mode was considered a soliton if, based on visual inspection, the spine reduced to a single point in the nonlinear spectrum. The spectrum thus contains one soliton with two main spectral points around the coordinates (0.091 Hz, 0.778 m), and two small breathers to the right of the soliton. Since the nonlinear mode with the highest amplitude is a soliton, we categorize the nonlinear spectrum

as type 4, i.e. a soliton spectrum.

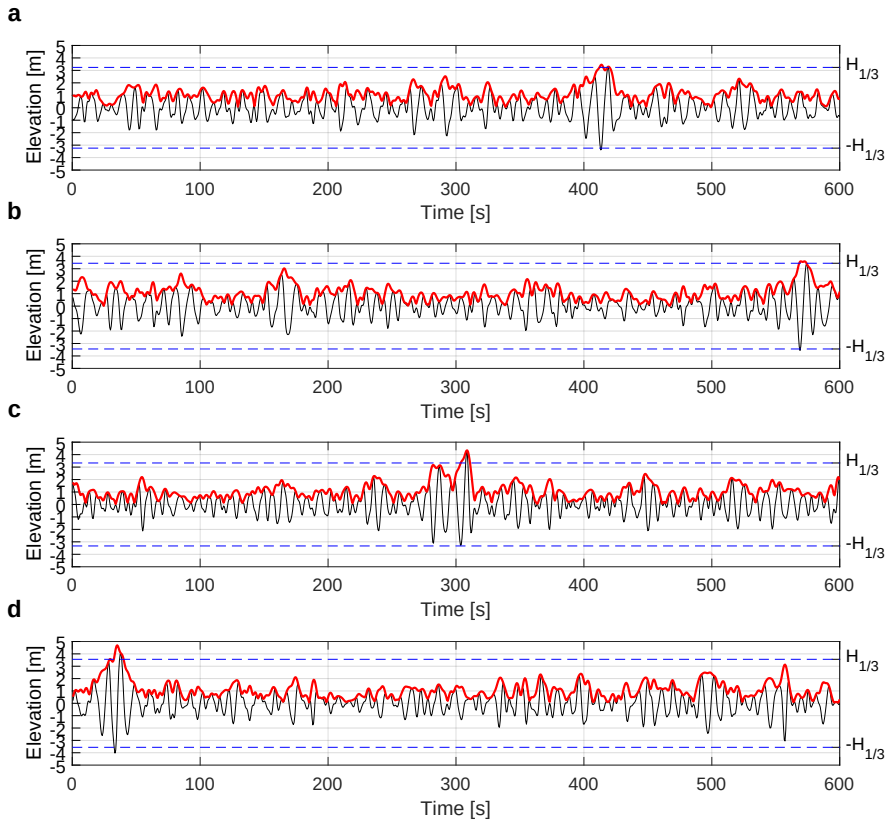


Figure 2.5: **Time series of rogue wave records from Taitung Open Ocean buoy.** The surface-wave elevation is shown as the black line and the magnitude of the complex envelope calculated by Hilbert transform is shown as red line. The blue dashed lines refer to $\pm H_{1/3}$. (a) The rogue-wave data measured from 20:00h on 18 January 2013 with $H_{\max} = 6.67$ m, $H_{1/3} = 3.24$ m, and AI = 2.06. (b) The rogue-wave data measured from 22:00h on 4 October 2014 with $H_{\max} = 6.96$ m, $H_{1/3} = 3.44$ m, and AI = 2.02. (c) The rogue-wave data measured from 08:00h on 4 December 2015 with $H_{\max} = 7.53$ m, $H_{1/3} = 3.62$ m, and AI = 2.08. (d) The rogue-wave data measured from 20:00h on 25 September 2012 with $H_{\max} = 8.05$ m, $H_{1/3} = 3.56$ m, and AI = 2.26.

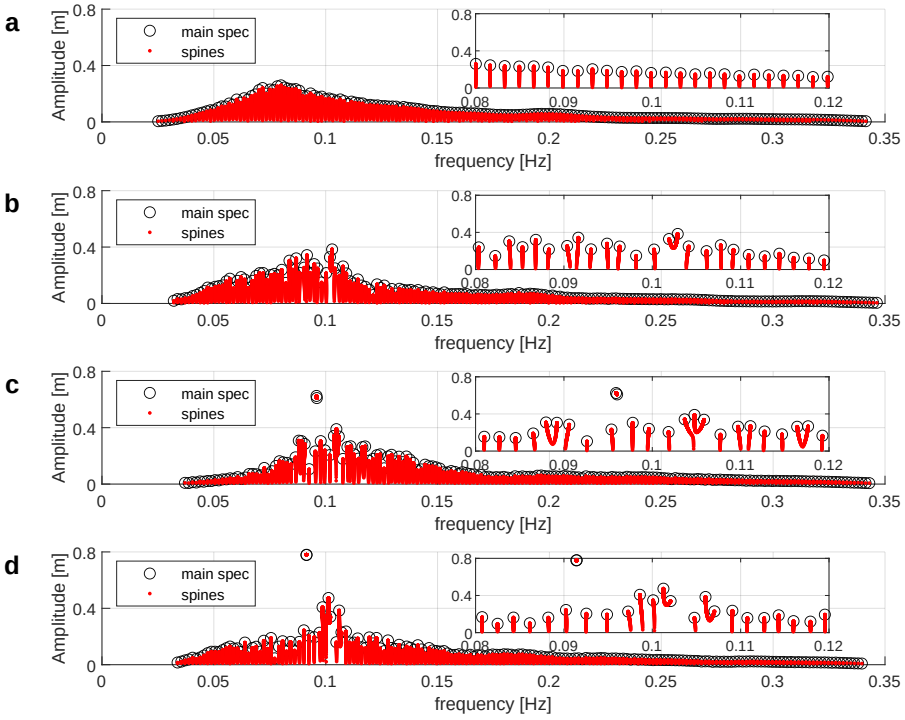


Figure 2.6: **Nonlinear spectra with envelope amplitudes on the vertical axis and carrier wave frequencies on the horizontal axis.** (a) Spectrum of the time series of complex envelope from Fig. 2.5a is classified as type 1: stable mode. (b) Spectrum of the time series of complex envelope from Fig. 2.5b is classified as type 2: small breather. (c) Spectrum of the time series of complex envelope from Fig. 2.5c is classified as type 3: large breather. (d) Spectrum of the time series of complex envelope from Fig. 2.5d is classified as type 4: soliton.

2.6. DATA ANALYSIS OF WAVE SAMPLES WITH FOUR TYPES OF NONLINEAR SPECTRA: STABLE, SMALL AND LARGE BREATHER, SOLITON

The surface wave data discussed in this study were measured by the Taitung Open Ocean buoy. There are in total 43018 samples (i.e. time series) in the period from 2006 to 2017. Among these, 663 samples contained rogue waves. In Fig. 2.7a, we plot the peak period T_p obtained via conventional frequency-domain analysis over the maximum wave height $H_{\max}$ for all 663 samples with rogue-wave events. The peak period T_p is defined as the dominant wave period in the wave-energy spectrum. The rogue-wave events in the plot have thereby been classified based on the four types of nonlinear spectra as discussed in the previous subsection. The four types of nonlinear spectra from stable-modes type to soliton type account for 75.1%, 6.3%, 12.2% and 6.3% of the rogue-wave samples, respectively.

Our results show that most of the rogue-wave samples are of the stable-mode type. Under the assumption that the NLSE describes the evolution of the time series at least approximately, this implies that the nonlinear superposition of sine waves or Stokes waves is the main generation mechanism in the real ocean, in accordance with the findings from Ref. [175]. In any case, it does not suggest that breather solutions of the NLSE are prototypical rogue waves in our samples. However, 24.9% of the nonlinear spectra of rogue waves contain unstable modes such as breathers or solitons. This is especially for rogue-wave samples with maximum wave heights larger than 15 m. The results show that the nonlinear spectra of samples with larger maximum wave height almost certainly contain unstable modes. A large portion (90.9%) of the samples with maximum wave height higher than 15 meters is strongly linked to type 3 (large breather spectra) and type 4 (soliton spectra).

Another feature of the four types of rogue-wave spectra can be observed from their peak periods. In general, the larger amplitudes of extreme waves require a large enough wave period to evolve in the ocean. Otherwise, the waves will break when the ratio of wave height to wavelength exceeds $H/L \geq 1/7$ [176]. However, it is noteworthy that for any given maximum wave height below 15 m, the nonlinear spectra with breathers or solitons show relatively low peak periods compared with those spectra with stable modes.

To investigate how specific these results are for rogue waves, a second data set of 600 selected non-rogue samples is analyzed as well. For the non-rogue data set, we first selected all samples from 2012 and then removed all rogue waves samples. In 2012, there were 4672 non-rogue samples. From those, we keep all non-rogue samples with a maximum wave height $H_{\max} \geq 5$ m. There were 130 such samples. Additionally, 470 non-rogue samples were selected randomly among the remaining samples with a maximum wave height smaller than 5 m. In total, there are thus 600 non-rogue wave samples to be analysed with NLSE-NFT. The nonlinear spectra of the non-rogue samples are also classified using the four types of spectra (stable modes, small breathers, larger breathers and solitons). The results of the classification are shown in Fig. 2.7b. The distribution of the four types has similar features for the non-rogue samples than for the rogue wave samples. The four

types of spectra from the stable mode type to the soliton type account for 79.7%, 7.8%, 9.2% and 3.3% of the samples, respectively. The sample proportion is likely not completely representative because it is not completely randomly selected. But it is noteworthy that all non-rogue spectra with maximum wave heights larger than 14 m are type 2, type 3 or type 4 spectra with unstable modes. This suggests that the existence of unstable modes in nonlinear spectra is related to large waves in real ocean no matter if they are rogue or non-rogue waves.

In Fig. 2.7c, we show a scatter plot of the abnormality index (AI) over the maximum wave height $H_{\max}$ with respect to the four types of nonlinear spectra for the rogue-wave data. We expected that the nonlinear spectra with breathers or solitons may cluster at higher values of the AI. However, we found that there are no clear differences for the four types of spectra in this representation. Fig. 2.7d shows a similar scatter plot for the non-rogue wave data. Also here there is no clear evidence for the four types of spectra. The non-rogue samples with maximum wave height larger then 15 m ranging between an AI of 1.32 and 1.88 are identified as breathers and solitons. This suggests that the existence of unstable modes in nonlinear spectra contributes to the formation of large waves in general, instead of only rogue waves.

The relationship between $H_{\max}$ and T_p in Fig. 2.7a and b appears to be similar to a square root for large breathers and solitons. Motivated by that wave steepness is proportional to the ratio of wave height and squared period, we plot the square of the peak period over the maximum wave height in Fig. 2.8. There is no apparent correlation for stable mode types. For spectra of unstable types, the squared peak period however does increase approximately linearly with the maximum wave height, where the slope of the linear fit depends on the exact type (small breather, large breather or soliton). Similar findings are made in the non-rogue wave case. However, the slopes of the linear fits are slightly different. Since most stable type samples are located far above the unstable type samples, the presence of a unstable dominant mode in the nonlinear spectrum is found to indicate increased wave steepness.

It was already mentioned in the introduction that the nonlinear spectrum will likely not stay constant during propagation at the site due to unaccounted factors such as directional spreading, which is present in our data (see Fig. 2.3d and h). To see if directional spreading influences the classification, we have repeated the classification using only the first quartile with the lowest directional spreading for each class. The results are shown in Fig. 2.9. When comparing Fig. 2.7 and 2.9, we find that the overall distributions appear to be quite similar.

We furthermore investigated the correlation of the one- and two-dimensional Benjamin-Feir indices with the maximum wave height for the four types of nonlinear spectra. The results are shown in Fig. 2.10. In Fig. 2.10a, we plot BFI_{1D} over the maximum wave height for the rogue wave samples of each type. All stable mode spectra have BFI_{1D} values below 0.3. The small breather and large breather rogue wave samples exhibit higher BFI_{1D} values in the range from 0.1 to 0.4. The soliton spectra can reach the highest BFI_{1D}, with values up to 0.55. The four types of nonlinear spectra are somewhat separated on the scatter plot. Similar findings are however also observed for the non-rogue wave samples in Fig. 2.10b. Since the BFI_{1D} values of non-rogue wave samples appear to be even slightly larger, high values of

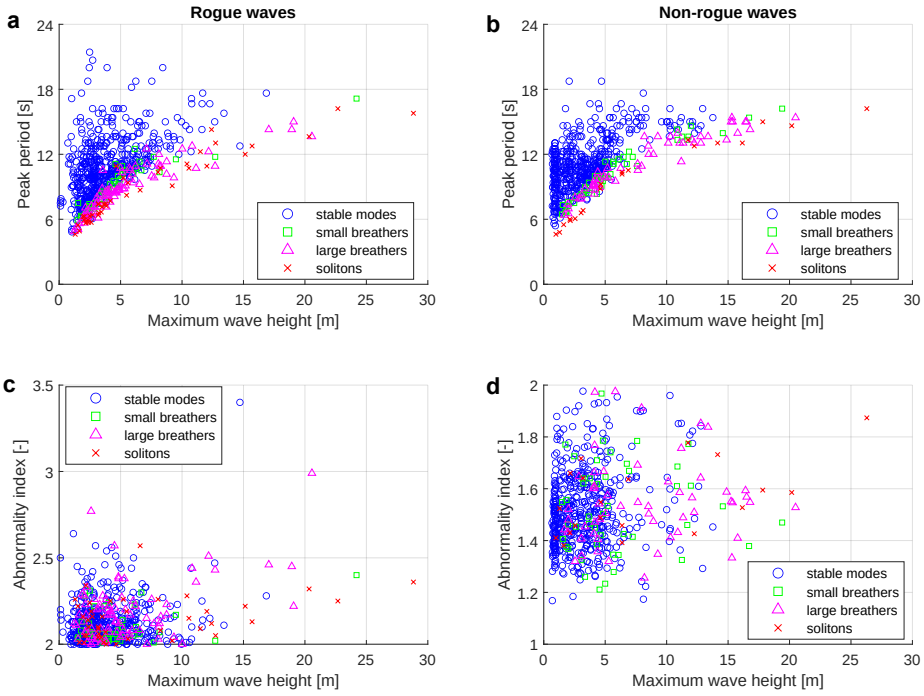


Figure 2.7: **Classification results of rogue and non-rogue waves based on the four types of nonlinear spectra.** (a) Scatter plot of rogue-wave samples of peak period T_p over maximum wave height $H_{\max}$ based on the four types of spectra. (b) Scatter plot of non-rogue wave samples of peak period T_p over maximum wave height $H_{\max}$ based on the four types of spectra.(c) Scatter plot of rogue-wave samples of abnormality index AI over maximum wave height $H_{\max}$ based on the four types of spectra.(d) Scatter plot of non-rogue wave samples of abnormality index AI over maximum wave height $H_{\max}$ based on the four types of spectra. The four types of spectra are stable-mode type, small-breather type, large-breather type and soliton type shown as blue circles, green squares, purple triangles and red crosses, respectively.

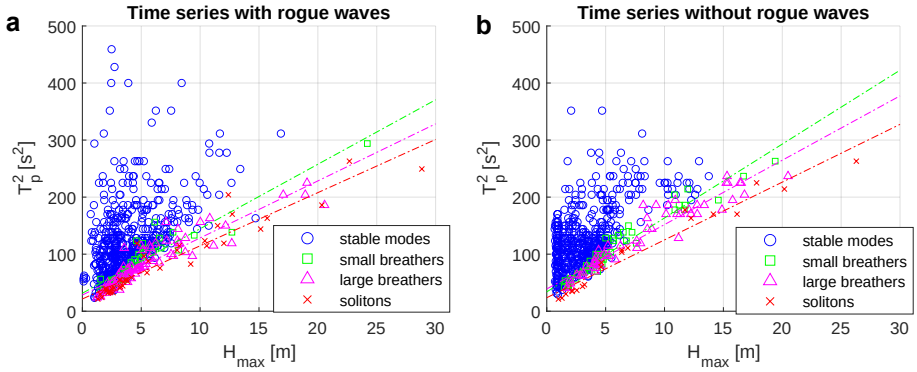


Figure 2.8: **Squared peak period vs maximum wave height for nonlinear spectra of the four types.** (a) Time series with rogue waves (b) Time series without rogue waves

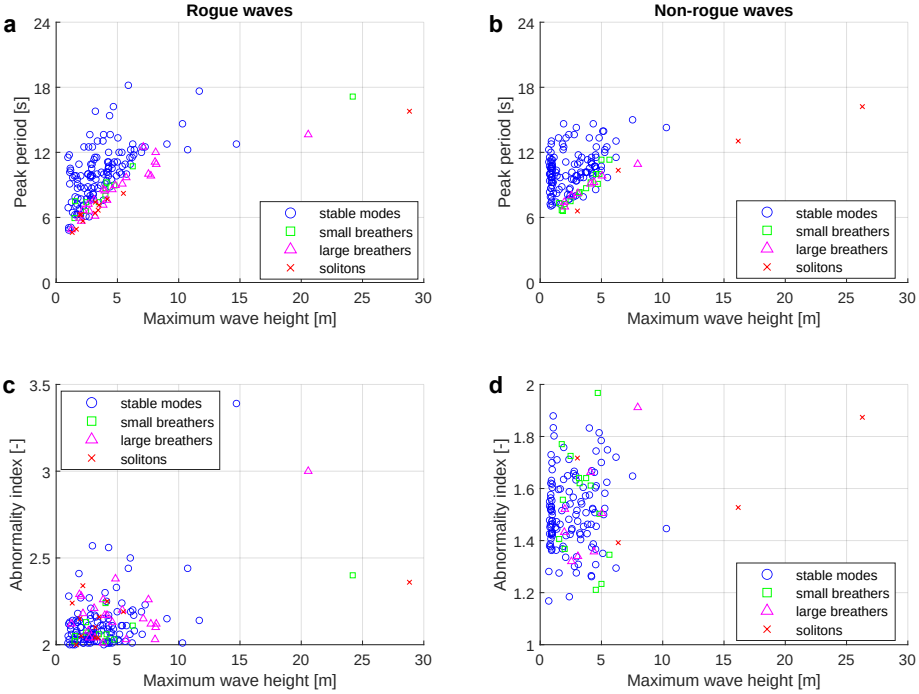


Figure 2.9: **Classification results of rogue and non-rogue waves with low directional spreading.** This figure presents the same information as Fig. 2.7, but only the first quartile of the rogue waves with the lowest directional spreading have been kept for each class.

BFI_{1D} do not indicate rogue waves at the measurement site. It is also consistent with the findings in [118], where for another data set of real-world it was found that BFI_{1D} is only a weak predictor for rogue waves. The mean BFI_{1D} values presented in Table 2.1 confirm the visual impression that BFI_{1D} is slightly larger for non-rogue samples with unstable types (small or larger breather, soliton). For stable mode spectra, BFI_{1D} is almost identical for rogue and non-rogue samples. We furthermore observe that the mean BFI_{1D} is increasing with the type of nonlinear spectrum for both rogue and non-rogue waves. That is, the mean BFI_{1D} value is increasing as we proceed from stable modes to small breathers, larger breathers and finally solitons.

We repeated the analysis with the two-dimensional BFI_{2D}. The results are shown in Fig. 2.10c and Fig. 2.10d. While the absolute BFI_{2D} values are lower than the corresponding BFI_{1D} values because of the denominator in Eq. (2.6), we still observe that the BFI_{2D} values of stable modes are on average smaller than those of unstable modes (small and large breathers, solitons) in the rogue wave case. The stable mode spectra exhibit lower BFI_{2D}'s in the range of 0 to 0.036, while the BFI_{2D} values for small breathers, large breathers, and soliton spectra fall within the range of 0.01 to 0.05. Within the group of unstable modes, small breathers, large breathers, and soliton spectra can no longer be clearly distinguished. The mean values of BFI_{2D} in Table 2.1 however reveal that the mean values of BFI_{2D} are still increasing as we progress from stable modes to small breathers, large breathers and solitons. Similar findings are observed for the non-rogue wave samples, as depicted in Fig. 2.10d. Large BFI_{2D} values therefore again do not indicate the existence of rogue waves.

To see if directional spreading influences the relation between the BFI's for the four types of nonlinear spectra, we finally repeated the analysis using only the first quartile with the lowest directional spreading for each class, as shown in Fig. 2.11. When comparing Fig. 2.10 and 2.11, we observe that the two figures exhibit a considerable degree of similarity. The directional spreading does not alter the distribution of the four types of spectra significantly.

Table 2.1: **Comparison of the mean one- and two-dimensional BFI between time series of rogue waves and non-rogue waves for the four types of nonlinear spectra.**

Rogue waves		
Types	Mean of BFI_{1D}	Mean of BFI_{2D}
Stable mode	0.1175	0.0143
Small breather	0.2053	0.0235
Large breather	0.2448	0.0266
Soliton	0.2997	0.0306
Non-rogue waves		
Types	Mean of BFI_{1D}	Mean of BFI_{2D}
Stable mode	0.1161	0.0145
Small breather	0.2431	0.0285
Large breather	0.3077	0.0323
Soliton	0.3559	0.0360

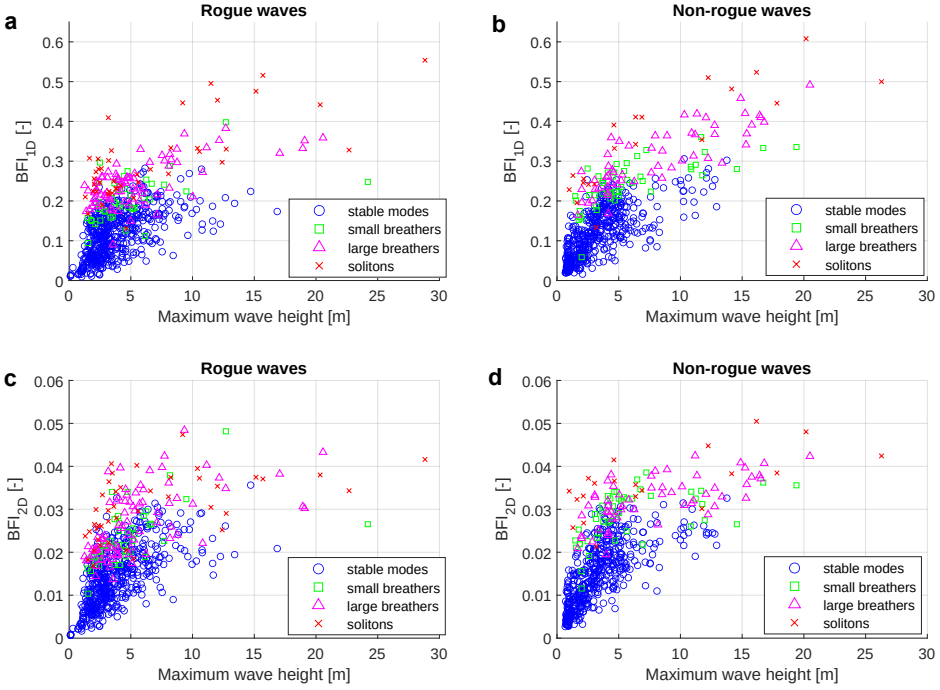


Figure 2.10: **Four types of nonlinear spectra and their Benjamin-Feir index.** (a) Scatter plot of rogue-wave samples of one-dimensional Benjamin-Feir index BFI_{1D} over maximum wave height $H_{\max}$ based on the four types of spectra. (b) Scatter plot of non-rogue wave samples of two-dimensional Benjamin-Feir index BFI_{2D} over maximum wave height $H_{\max}$ based on the four types of spectra. (c) Scatter plot of rogue-wave samples of one-dimensional Benjamin-Feir index BFI_{1D} over maximum wave height $H_{\max}$ based on the four types of spectra.(d) Scatter plot of non-rogue wave samples of two-dimensional Benjamin-Feir index BFI_{2D} over maximum wave height $H_{\max}$ based on the four types of spectra.

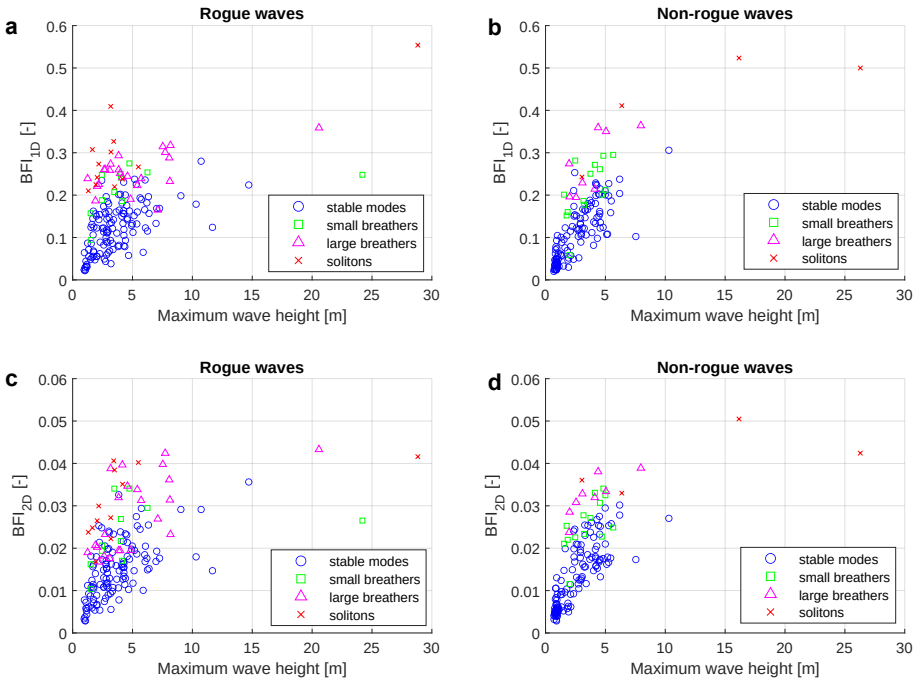


Figure 2.11: **Four types of nonlinear spectra and their Benjamin-Feir index with low directional spread.** This figure presents the same information as Fig. 2.10, but only the first quartile of the rogue waves with the lowest directional spreading have been kept for each class.

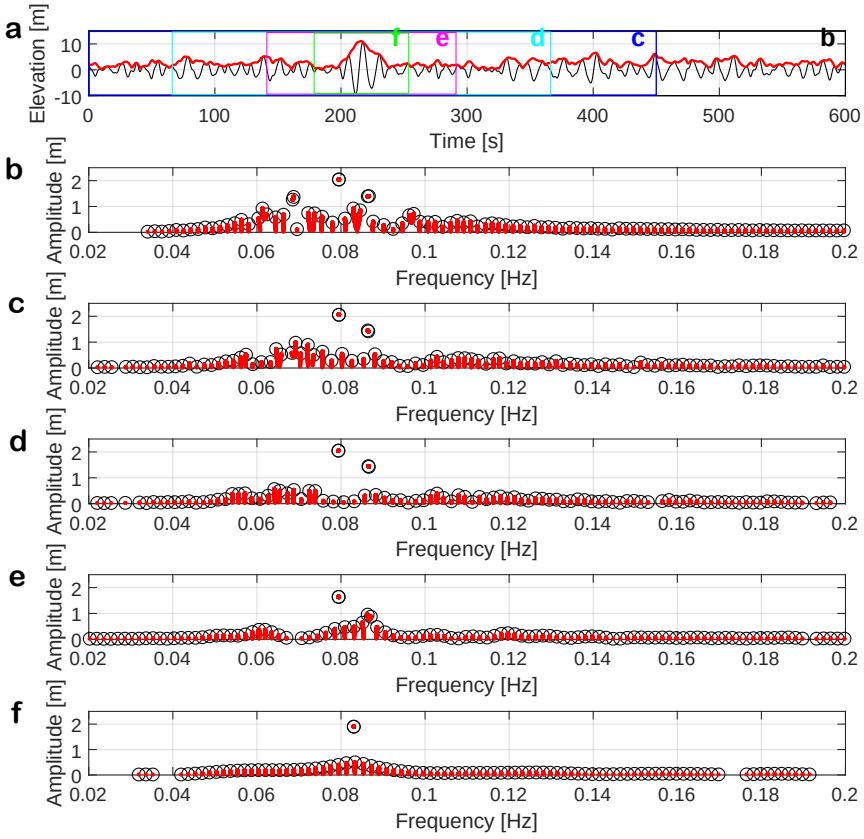


Figure 2.12: **Relationship of unstable modes to rogue waves**. (a) The rogue-wave data is measured from 06:00h to 06:10h on 29 July 2017 with the maximum wave height $H_{\max} = 20.34\,\text{m}$, the significant wave height $H_s = 8.76\,\text{m}$, the peak wave period $T_p = 13.64\,\text{s}$, and the abnormality index $AI = 2.32$. The surface-wave elevation is shown as the black line and the magnitude of the complex envelope calculated by Hilbert transform is shown as red line. The original signal is cut into different time lengths of 600 s, 450 s, 300 s, 150 s, and 75 s, which are labelled from b to f. (b-f) Nonlinear spectra corresponding to the time series from b to f.

2.7. Relationship of unstable modes in nonlinear spectra to rogue waves

In this section, we investigate whether the unstable mode (i.e., small breather, large breather, or soliton) with the largest amplitude in the nonlinear spectrum can be attributed to rogue waves in time series. We select the time series with a rogue wave shown in Fig. 2.12a as an example. The time series was measured from 06:00h to 06:10h on 29 July 2017 during an extreme sea state. The maximum wave height is $H_{\max} = 20.34$ m, the significant wave height is $H_{1/3} = 8.76$ m, the peak wave period is $T_p = 13.64$ s, and the abnormality index is $AI = 2.32$. In order to determine which nonlinear modes contribute to the rogue wave, we propose a new windowing approach. We cut the localized structures of rogue wave with 450 s, 300 s, 150 s and 75 s (see Fig. 2.12a). Outside these time frames, the elevation of the time series is set to zero. The entire duration of the sample keeps 600 s. The window is initially positioned at the center of the rogue wave. If the window extends beyond the bounds of the time series, it is subsequently adjusted by moving it left and right within the time series. Similar to zero-padding for the conventional FFT, this approach ensures that the nonlinear frequency resolution stays the same when the NLSE-NFT is computed. We remark that the popular approach of cutting out short parts of the time series and analyzing them with a shorter signal period [92] did not allow us to localize nonlinear modes. Note that in our approach, the period of the signal is not reduced.

Fig. 2.12a shows the localized structures b to f outside which the time series in Fig 2.12a was set to zero before computing the nonlinear spectra, which are presented in Fig. 2.12b-f. These plots only show the center part of the spectra with frequencies from 0.02 Hz to 0.2 Hz, including the dominant frequencies. The nonlinear spectrum of the original time series is shown in Fig. 2.12b. There are five unstable modes: one soliton with coordinates (0.079 Hz, 2.05 m) and four breathers. Two unstable modes have larger amplitudes with coordinates (0.068 Hz, 1.27m), (0.069 Hz, 1.37 m) and (0.086 Hz, 1.4 m), (0.087 Hz, 1.4 m) that satisfied the criterion of being larger than 120% than the maximum amplitude of the stable modes. The other two smaller breathers are at the coordinates (0.061 Hz, 0.92 m), (0.062 Hz, 0.7 m) and (0.096 Hz, 0.66 m), (0.097 Hz, 0.72m).

The nonlinear spectra of the partially zeroed time-series in the Figs. 2.12c-f show that most of the spectral amplitudes reduce. The number of unstable modes in the nonlinear spectrum in Fig. 2.12c is already reduced. While the soliton and the large breather with the higher frequencies still exist, the large breather with the smaller frequency changed into a small breather. Two smaller breathers from the original spectrum of Fig. 2.12b turn into small stable modes. A remarkable finding here is that the soliton in Fig. 2.12c keeps nearly the same frequency and amplitude as in Fig. 2.12b, indicating that the cut-off fragment from 450 s to 600 s in the original time series does not contain wave components that correspond to this soliton. In other words, this soliton exists in both time series.

Similarly, this soliton is still retained in the spectra of Fig. 2.12d and Fig. 2.12e, whereas the other spectral components change owing to the reduced window length

of 300 s and 150 s, respectively, outside which the time series is set to zero. When the window length is 75 s, it only contains a part of the rogue wave. The corresponding nonlinear spectrum in Fig. 2.12f is dominated by the soliton with nearly the same amplitude as in the previous spectra, but with a slightly shifted frequency. This shows that the largest soliton amplitude in the nonlinear spectrum is related to the rogue wave at 218 s in the time series of Fig. 2.12a.

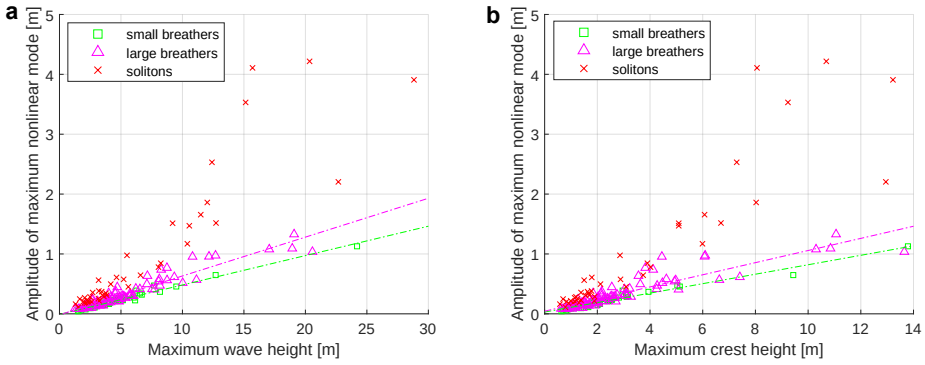


Figure 2.13: **Relationship of the largest nonlinear mode to wave parameters.** (a) Scatter plot of the largest nonlinear mode over maximum wave height. (b) Scatter plot of the largest nonlinear mode over maximum crest height.

Now that we know that the dominant nonlinear modes of the breather and soliton types are located at the rogue waves, the question of how much they contribute to the rogue waves arises. We therefore relate the amplitude of the largest nonlinear mode to the maximum wave height and maximum crest height of the time series with rogue waves in a scatter plot in Fig. 2.13. The comparison does not contain stable modes, as those were not found to be localized. We observe that for both small and large breather modes, the relation between their amplitudes and the rogue wave height and crest height is approximately linear. The amplitudes of the dominant mode are in the range of roughly 2.5% to 10% of the maximum wave height, and roughly 5% to 20% of the maximum crest height in these cases. The picture is different when the dominant mode is of the soliton type, with the amplitudes of maximum soliton ranging from approximately 7% to 27% of the maximum wave height, and approximately 14% to 51% of the maximum crest height in these cases. Notably, for maximum wave heights larger than 15 m, the amplitude of dominant modes of the soliton type can arrive up to one quarter of the maximum wave height. For crest heights larger than 8 m, the amplitude dominant modes of the soliton type can account for half of the maximum crest height. The two figures illustrate similar results. It is worth noting that the amplitudes of the maximum unstable modes are represented by the envelope, which is entirely above the sea surface. This characteristic facilitates a more straightforward comparison with crest height.

2.8. SUMMARY AND DISCUSSION

In the results section, we have classified the nonlinear spectral portraits of 663 rogue wave samples that were measured by the Taitung Open Ocean buoy in the Philippine Sea from 2006 to 2017, using the periodic NLSE-NFT. For comparison, we also analyzed 600 selected non-rogue wave samples from 2012. The four different types of spectra were stable modes (i.e., sine or Stokes waves), small breathers, large breathers and solitons. We found that the majority of the rogue wave samples (75.1%) were stable mode spectra.

This finding is in line with with other studies such as[118, 175], where the majority of rogue waves were found to be generated from linear mechanisms. Furthermore, it complements the different observations in [29] and [28], where dominant modes of the stable and breather type, respectively, were attributed to rogue waves.

Another interesting finding is that a large portion (90.9%) of the rogue wave samples with maximum wave heights larger than 15 m are of the breather or soliton type. When analyzing the non-rogue samples a similar picture was found. All non-rogue wave samples with maximum wave heights larger than 14 m were again of breather and soliton types. This suggests that dominant breather and soliton components in the nonlinear spectrum are in general representative for (the complex envelopes of) time series with large maximum wave heights. Furthermore, we found that they can also be associated with increased wave steepness.

By studying the relations between the one- and two-dimensional BFIs and the maximum wave height, we found that unstable modes have higher BFI's than stable modes in all cases (1D and 2D, rogue and non-rogue). This seems plausible because both BFIs can be linked to kurtosis under certain assumptions (i.a. narrowbandedness), which in turn is linked to nonlinear interactions [16, 164]. Therefore, our results seem to confirm that sea states with an unstable dominant mode are more nonlinear than sea states with a stable dominant mode. Moreover, we found that the distributions of the BFIs are similar for rogue and non-rogue waves. If the BFIs were correlated with the rogue wave probability, one would expect higher BFIs for the rogue wave data. Since that does not appear to be the case here, our results do *not* suggest a connection between the BFIs and the rogue wave probability. This is contrast to the unidirectional case, where BFI_{1D} is known to correlate with the rogue wave probability [16, 107, 133]. The finding is however in line with other field measurements [118].

The one-dimensional BFI can also be related to the modulational instability, both from a stochastic and a deterministic point of view. For random waves, Alber [177] has shown that narrowband Gaussian random deep-water wavetrains can be modulationally unstable if $BFI_{1D} > 1$. Numerical simulations indicate that modulational instability can also occur for $BFI_{1D} < 1$, where the effect is gradually decreasing [16, p. 866]. The largest BFI_{1D}'s in our data set are smaller than 0.6, while the large majority of rogue wave events occurred in the regime $BFI_{1D} < 0.4$. It is also known that the modulational instability is weakened in directional wave fields [164]. Since the directional spreading is strong in our data (see Fig. 2.3d,h), it seems unlikely that the modulational instability played a significant role for the formation of rogue waves. From a deterministic point of view, we know that modulational

instability is only possible if the nonlinear spectrum has a degenerate double point in the main spectrum [146]. Due to the large water depth, all our rogue waves occurred in the focusing regime of the NLSE, in which the modulational instability can occur. However, since any small random perturbation will split up the double points, the probability of actually measuring a modulationally unstable wave train (in the deterministic sense) is zero. Consequently, no degenerate points were observed in our data. As an alternative, the so-called splitting distance has been proposed in order to instead estimate how close a generic nonlinear spectrum is to one with a degenerate point [24, 25]. To the best of our knowledge, the splitting distance has not yet been evaluated on real-world measured rogue waves. However, in simulations of the NLSE it was found that it does not correlate with maximum wave height, while the amplitude of the dominant nonlinear mode considered in this work does [1].

Using a new procedure to localize nonlinear modes, the largest nonlinear mode of exemplary rogue wave samples of the soliton type were shown to be localized in the rogue wave. This is an interesting difference to conventional Fourier analysis, where individual modes (i.e. sinusoidal waves) in themselves are never localized and thus always have an impact on the complete time series. We were not able to localize the largest modes of exemplary rogue wave samples of the small breather and stable mode types in the corresponding rogue waves. The results for large breather modes were mixed. We suspect that smaller breathers are less localized. Stable modes (i.e. sine or Stokes waves) are furthermore not localized at all. Hence, this finding seems plausible.

By relating the amplitude of the dominant modes to the height of the corresponding rogue waves, we found that the dominant nonlinear modes of the localized breather and soliton types in general only contribute a small fraction of the rogue waves total wave height. This overall picture is consistent with other studies such as [28, 34], where the dominant nonlinear mode had to interact with other wave components to form the rogue wave. It often seems to push already large waves over the rogue wave threshold. Our data however includes a noteworthy exception to this general pattern, for rogue waves of the soliton type with large wave heights. In those cases, the dominant soliton component could contribute more than half of the total height of the rogue wave in extreme cases. Here, it is important to keep in mind that the soliton components are envelope solitons (because the NLSE is a envelope equation). Through the lens of surface elevations, they actually correspond to travelling wave groups. The strong contribution of solitons (in the complex envelope) to rogue waves has also been observed in the literature [158], where an (vanishing) NLSE-NFT-based analysis showed the same pattern for two measured rogue waves.

Finally, we also observed that rogue wave samples with unstable modes have low peak periods when compared to stable mode samples with the same maximum wave heights. Furthermore, there is no clear relation between the abnormality index (AI) and four types of nonlinear spectra. The relation between the squared peak period and the maximum wave height has however been found to be approximately linear for nonlinear spectra of the breather and soliton types.

In conclusion, this study applied the NLSE-NFT to classify rogue waves that were measured in the Philipine sea under deep water conditions. It is the first time that

the NLSE-NFT has been systematically applied to study a large number of real-world rogue waves in deep water. Prior NLSE-NFT-based studies of individual rogue wave events had resulted in very different nonlinear spectra, ranging from dominating stable modes over breather to soliton modes. Our study shows that all three cases can occur at a single measurement site. We found stable modes are most typical for rogue waves in general, but that rogue waves with large wave heights are mostly of the large breather or soliton type. We furthermore found that while the contribution of the dominant nonlinear mode to the rogue wave is in general small, it can contribute up to 50% for large rogue waves of the soliton type.

While the classification results for non-rogue waves show no significant differences to the rogue wave samples, we point out that the difference between nonlinear rogue and non-rogue spectra might be qualitative instead of quantitative. We only classified the type of spectrum, but the difference could also be in the arrangement of the components. The sizes of certain gaps have been found to relate to the probability of seeing a rogue wave under certain circumstances in simulations of the NLSE in Ref. [24, 25]. A similar observation has been made recently in the analysis of rogue waves that were measured under shallow water conditions in the north sea [34].

We finally remark again that in particular due to the presence of directional spreading the nonlinear spectra most likely would change under propagation at the measurement site. While our classification results did not change noticeably when only the lowest quartile with the least directional spreading was considered for each type of rogue waves, the impact of directionality on nonlinear spectra remains not well understood.

3

Evaluation of Nonlinear Fourier-based Maximum Wave Height Predictors under the Nonlinear Schrödinger Equation

CHAPTER ABSTRACT

Rogue waves are extreme waves in the ocean that appear from nowhere and disappear without a trace. They are usually modelled by the nonlinear Schrödinger equation (NLS), which describes nonlinear phenomena such as modulational instability and solitons on finite backgrounds. In this study, the periodic nonlinear Fourier transform (NFT) for the NLS equation is applied to simulate ocean surface waves in deep water. The temporal and spatial structures of surface waves are obtained by evolving JONSWAP time series using the NLS equation. Several parameters extracted from the NFT spectra of the initial time series are investigated as predictors for the maximum wave height during evolution. We investigate several parameters from the literature, and find that with suitably optimized coefficients, a NFT-based parameter based on the largest unstable mode has a good correlation with the overall maximum wave amplitude. This new spectral criterion can contribute to rogue wave forecasting under extreme sea states.

The text in this chapter has previously appeared in modified form in the article "Lee, Yu-Chen, Sander Wahls, and Markus Brühl. "Evaluation of Nonlinear Fourier-Based Maximum Wave Height Predictors Under the Nonlinear Schrödinger Equation." International Conference on Offshore Mechanics and Arctic Engineering. Vol. 85901. American Society of Mechanical Engineers, 2022." [1]. https://doi.org/10.1115/OMAE2022-79838. Reproduced from Proceedings of Paper No: OMAE2022-79838, V05BT06A060, with permission.

3.1. Introduction

Traditionally, the analysis of free surface gravity waves using the fast Fourier transform (FFT) assumes linear superposition of regular waves. This model is also commonly used in offshore engineering to predict extreme sea states for design and safety in construction. However, it looses accuracy when applies to nonlinear waves. In contrast to the traditional linear Fourier transform, which is restricted to superposition of linear waves such as sinusoidal waves, here we utilize a useful tool called the nonlinear Fourier transform (NFT). The term nonlinear Fourier transform (NFT) generally refers to a transform that decomposes a signal in time domain into nonlinearly interacting wave components that have a simple representation in a suitable nonlinear spectral domain [9]. The NFT simplifies the description of nonlinear systems because it transforms the nonlinear and dispersive time-domain behavior into linearly evolving nonlinear spectral components. The distinctive capabilities of NFT furthermore enable the detection of solitons and modulation instability, which are of interest for fundamental nonlinear phenomena such as rogue waves [6, 146].

Rogue waves are rare events with extreme wave heights whose heights are larger than two times the significant wave height. Due to their large amplitudes, these waves can cause significant damage to ships and offshore structures [178]. Nowadays, many in-situ measurements of rogue waves are available. The most famous rogue waves were recorded in the North Sea and include the Draupner wave [179], the Andrea wave [180] and the Gorm wave [181]. There are several studies on the physical mechanisms behind the formation of rogue waves, and the modulational instability and solitons on finite background are two possible causes for large rogue waves that have been discussed in the literature [70, 72, 182, 183]. Both phenomena can only occur under nonlinear dynamics. Meanwhile, the nonlinear Schrödinger (NLS) equation is the simplest model for deep-water ocean waves ($k_0 h > 1.363$) that incorporates these nonlinear effects. The NLS equation describes the spatio-temporal evolution of the complex envelope for narrow-banded waves and constant water depth. The NLS equation can be solved in the spectral domain by applying a suitable NFT [93]. Using the inverse NFT, exact solutions for different types of breathers, solitons on finite backgrounds such as Akhmediev breathers (ABs), Kuznetsov-Ma (KM) solitons, the Peregrine soliton, A-type breathers and B-type breathers can be constructed [184]. These solutions allow analytical studies of the conditions under which high amplitude events such as the occurrence of rogue waves. Another possible explanation for formation of rogue waves is dispersive focusing of second-order bound harmonic waves based on the dataset of field measurements [175, 185]. At this point, there is no clear conclusion about the dominant mechanism behind rogue wave generation in the real ocean. Further investigations of the generation mechanisms of rogue waves are needed.

The nonlinear Fourier transform (NFT) for the nonlinear Schrödinger (NLS) equation, which describes unidirectional surface waves in deep water, will be briefly called NLS-NFT from here on. The evolution of the nonlinear spectrum becomes trivial if the evolution in the time domain follows the NLS equation exactly. While this is rarely the case in practice, one would nevertheless expect the nonlinear

spectrum to provide a better characterization of the evolution than e.g. a linear Fourier transform of the same time series. Consequently, it seems reasonable that the NFT-based data analysis methods could replace conventional linear method. In recent years, the NLS-NFT has been applied to analysis of rogue waves in different application areas such as laser radiation [22], optical fiber [92, 186, 187], and ocean waves [154, 188]. Nonlinear phenomena such as the modulational instability and solitons can be clearly observed in the nonlinear Fourier domain due to their distinctive spectral portraits [92, 146]. As the most parts of the NFT spectrum are invariant when the wave propagation is described by the NLS equation, currently hidden structures in a time series can be identified.

The objective of this study is to investigate several criteria for the prediction of rogue waves from nonlinear spectral domain based on the works of Schober et al. [24, 25, 189] and Osborne et al. [6, 28]. Most parts of NFT spectra stay, as already mentioned above, invariant under the NLS equation. Hence, such criteria might help to reveal rogue waves that are not yet visible. The setup will be similar to the works discussed above, which in turn were inspired by a paper of Oronato et al. [133]. We generate random time series from JONSWAP spectra, which represents various sea conditions including storm events. The time series are propagated using the narrow-band NLS equation. Finally, we correlate the maximum rogue wave heights over time and space with several NFT-based criteria obtained from the initial time series. Note that we thus evaluate these criteria under optimal conditions. The evaluation under more realistic conditions requires additional studies.

The novel aspects of this work are as follows: First, we evaluate the so-called splitting distance from the works of Schober et al.[24, 25, 189] for longer and thus more complicated random time series. Second, we investigate the correlation for criteria based on the work of Osborne et al.[6, 28]. that have not been applied in such a setup before. Third, this is the first time that these criteria by Schober et al.[24, 25, 189] and Osborne et al.[6, 28]. are compared against each other. Finally, we find a better correlation of revised formula according to the simulated data used in this study.

3.2. Example of NLS-NFT spectrum

The NLS-NFT requires the complex envelope of the surface elevation, which can be obtained from the surface elevation with the help of the Hilbert transform [190]. The magnitude of the complex envelope of an exemplary time series is shown in Fig. 3.1a with a red line. In this paper, we used the open source software library FNFT by Wahls et al.[63, 191] to compute NFT spectra. The periodic NLS-NFT spectrum of the examplary time series in Fig. 3.1a is shown in Fig. 3.1b. The main spectrum points E_k are shown as circles in the complex plane. The main spectrum is symmetric with respect to the real axis. Therefore, we here only show the upper part of the spectrum. The initial conditions $\mu_k(X_0, T_0)$ for the hyperelliptic modes and the Riemann sheet indices $\vartheta(X_0, T_0)$ are less informative since the μ_k and ϑ_k vary with time and space and therefore are not shown. More information about the spectra of finite gap potentials can be found in Refs. [192–194].

Another important aspect of the spectral portraits is that the main spectrum points form pairs that are connected by red curves called spines. The spines provide additional information about the nature of the spectral modes in the spectrum [6, 28]. When two main spectrum points are connected by a spine that crosses the real axis, these spectral components are called stable modes. When considered in isolation (i.e., with the other components removed from the spectrum), they correspond to sine wave or Stokes wave components in the time domain. On the contrary, if two main spectrum points are connected by a spine that does not cross the real axis, these spectral components are called unstable modes. In isolation, they correspond to breather solutions of the NLS equation. A very short unstable breather that looks like an isolated single point in particular corresponds to a soliton(-like) component. It might also happen that two points in the main spectrum overlap and lead to a double point on a spine. Such points are indicators for potential modulational instabilities [146]. In Fig. 3.1b, there is one soliton at $\lambda \approx -0.0054 + 0.0224i$ and two breathers connection $\lambda \approx 0.0189 + 0.0111i$ and $\lambda \approx 0.0195 + 0.0104i$ with $\lambda \approx 0.0032 + 0.0114i$ and $\lambda \approx 0.0029 + 0.0106i$, respectively.

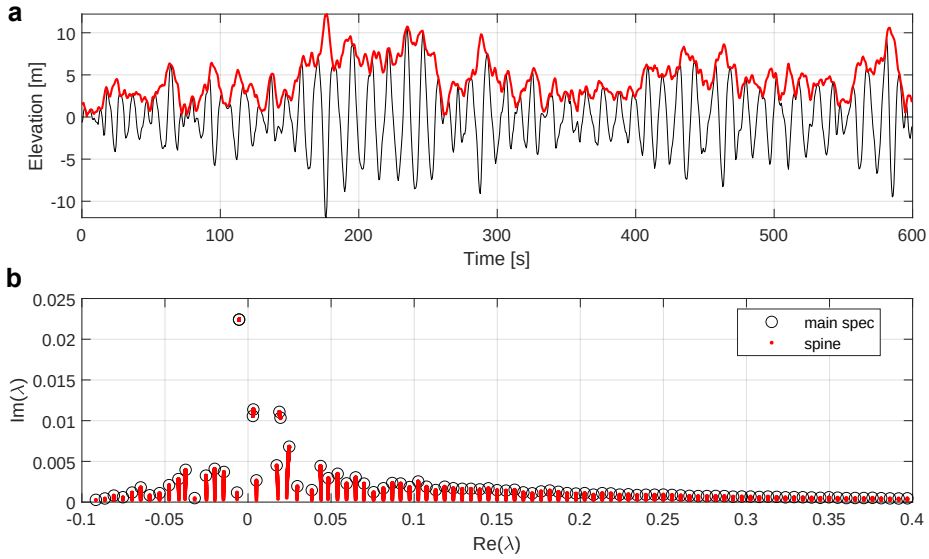


Figure 3.1: **a** The time series of surface elevation simulated by JONSWAP model with $f_0 = 1/12.5, \alpha = 0.02, \gamma = 6.6$. The black line is the surface wave elevation and the red line is the magnitude of complex envelope. **b** The NFT spectrum for the complex envelope of the surface elevation. The black circles are the main spectrum points and the red lines are the spines connecting two points.

3.3. SIMULATION SETUP

Measurements of ocean surface waves provide us with information about local sea states, which may consist of multiple wave systems generated by different atmospheric systems. The sea states are usually represented by empirical and statistical models, where the most famous one is the Joint North Sea Wave Observation Project (JONSWAP) [195]. JONSWAP spectra cover most of the typical sea states in the North Sea and have been widely used for determination of wave parameters in coastal and offshore engineering for structure design. The JONSWAP spectrum can be expressed as

$$S(f) = \frac{\alpha g^2}{(2\pi f)^5} e^{-\frac{5}{4}\left(\frac{f_0}{f}\right)^4} \gamma^r, \quad \sigma = \begin{cases} 0.07 & f \le f_0 \\ 0.09 & f > f_0 \end{cases}, \tag{3.1}$$

where $r = \exp\left[-\frac{1}{2}\left(\frac{f-f_0}{\sigma f_0}\right)^2\right]$, f is frequency, g is gravity, f_0 is the dominant frequency, γ is the enhancement factor and α is the Phillip's parameter. The parameter γ influences the peak shape. If $\gamma > 1$, the sea states are undeveloped and do not arrive at steady conditions due to the nonlinear wave-wave interactions. As the enhancement factor increases, the JONSWAP spectrum becomes higher and narrower in the center of the spectral peak. Meanwhile, a higher Phillip's constant indicates that the JONSWAP spectrum has a lower decay rate for both high and low frequency ranges. The range of validity of the peak enhancement factor for studying rogue waves is $2.5 < \gamma < 8$ [133].

We generated different surface wave data with the relevant parameters of JONSWAP with cases in this study, and the corresponding JONSWAP spectra areas shown in Fig. 3.2. The values of these parameters refer to Ref. [196], which investigated the sea states in North Sea with regard to the likelihood of rogue wave development. These conditions were observed during strong storms, which have long peak periods and high values of gamma. Fig. 3.2 shows variations of JONSWAP spectra with peak frequency, alpha and gamma. It can be found that longer peak periods correspond to higher energy densities, larger αs correspond to higher energy in the side band, and larger γs correspond to higher peaks. For this study, we generated 80 surface wave time series using JONSWAP spectra with $f_0 = 1/11$ and $1/12.5$ Hz, $\alpha = 0.01$ and 0.02, and $\gamma = 3.3$ and 6.6, as shown in Fig. 3.2. For each spectrum, ten samples with different sets of random phase were generated. The initial time series of 600 s has the sampling frequency with 1.7 Hz. In the next section, indicators extracted from these time series will be correlated with the maximum wave height after evolution. In this study, we use the NLS equation with focusing nonlinearity to simulate the evolution of complex envelope. The chosen propagation distance is $x = 50000\,m$, which is long enough to excite rogue waves.

3.4. COMPARISON WITH LINEAR PROPAGATION

An exemplary numerical simulation of the solution of the focusing NLS with the initial JONSWAP data is presented in Fig. 3.3b. Next to the evolution according to the NLS equation, Fig. 3.3a shows the corresponding evolution with respect

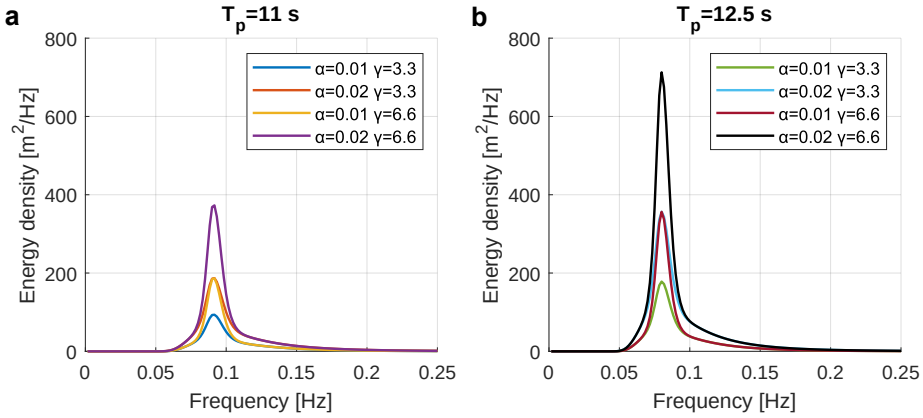


Figure 3.2: Variation of the JONSWAP spectra for different parameters. **a** Spectra with $f_0 = 1/11Hz$, $\alpha = 0.01$ and 0.02, $\gamma = 3.3$ and 6.6. **b** Spectra with $f_0 = 1/12.5Hz$, $\alpha = 0.01$ and 0.02, $\gamma = 3.3$ and 6.6.

to the linear Schrödinger equation, which is obtained when the nonlinear term is dropped. The maximum wave height and significant wave height are 19.1 m and 14.4 m, respectively. The significant wave height is here defined by four times the standard deviation of the surface elevation. In the studies related to rogue waves, the abnormality index (AI), which is the ratio between the maximum wave height and significant wave height. This ratio is used to define rogue waves, which value should be larger than two. In this example, the AI value of initial surface wave is 1.33. Consequently, it does not satisfy the rogue wave definition. By comparing the results for linear and nonlinear evolution, we find that the maximum complex amplitude is larger for nonlinear evolution than for linear evolution. The maximum amplitude of two cases are 16.3 m and 18.7 m, and the maximum wave height are 28.4 m and 32.8 m, respectively. They occur at distance of around 1750 m. This result illustrates that rogue waves occur with higher probability under the nonlinear wave evolution governed by the NLS equation, which was already observed in [133].

Next, we analyze the relation between basic wave parameters for linear and nonlinear evolution in order to enhance the understanding of the simulated data. Fig. 3.4 relates the abnormality indices of the initial time series against the maximum abnormality index for both linear and nonlinear evolution in scatter plots. The range of the abnormality index of the original time series is $1.1 < AI_0 < 2.1$, which shows that most of the initial time series do not contain rogue waves. Fig. 3.4a shows the maximum abnormality index after linear evolution. Its range is $1.8 < AI_{linear} < 2.4$. The red line with $AI = 2$ is the rogue wave criterion. The results show that 82% of data changing into rogue waves under linear evolution. Fig. 3.4b shows the maximum abnormality index with the range $1.9 < AI_{NLS} < 3$ after nonlinear evolution, indicating that 98% of data change into rogue waves under the

nonlinear evolution. The NLS equation thus leads to higher amplitude rogue waves than the linear method after propagation. To sum up, in this section, we provide the quantitative analysis on the evolution process of complex envelope. Our simulations are consistent with previous results in Ref.[133]. Meanwhile, it is plausible that the assumption of a narrow-banded process might have influenced the overestimation of the maximum wave height during the evolution of the NLS equation. Nevertheless, these simulations illustrate that nonlinear effects might play an important role in the generation of rogue waves.

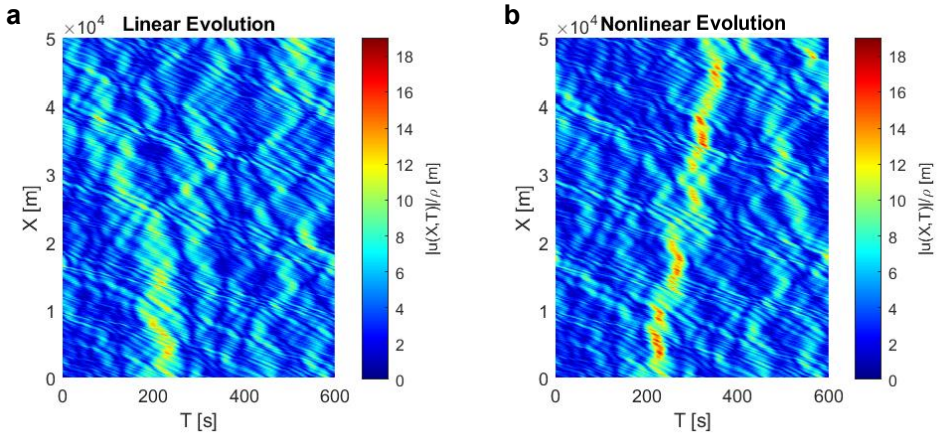


Figure 3.3: The numerical simulation of the time-space evolution with the initial surface wave data generated by JONSWAP, where $f_0 = 1/12.5Hz, \alpha = 0.02, \gamma = 6.6$. **a** Linear evolution by linear Fourier transform **b** Nonlinear evolution by the focusing NLS equation.

3.5. Advantages and Limitations of the NLS Equation

Recently, there has been increasing interest in deterministic wave prediction methods in order to predict the rogue waves before they occur. The most commonly used methods are based on the linear theory, which has been applied to ocean surface waves and proved by field measurements such as X-Band rader [197, 198]. Hilmer et al.[199] showed that linear wave prediction is accurate under the sea states with small or moderate wave steepness. Meanwhile, several linear wave prediction models are developed such as FutureWaves [200] and NextOcean because it is simple, effective and robust. However, these linear models do not contain nonlinear effects, and will lose accuracy with increasing nonlinearity in sea states of large wave steepness.

The NLS equation is one of the simplest models for unidirectional nonlinear wave evolution. It has been validated in numerical simulations and physical experiments, but note that the assumption of the unidirectionality causes deviations between the

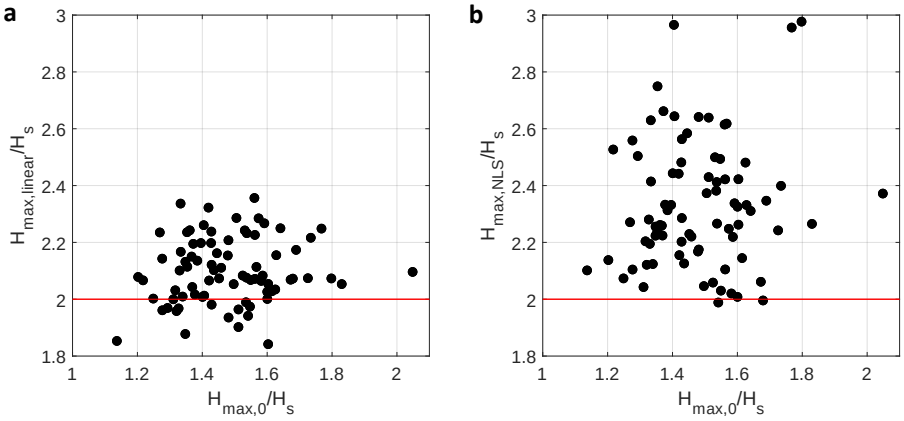


Figure 3.4: **a** The scatter plot of abnormality index of original time series against the abnormality index in linear evolution. **b** The scatter plot of abnormality index of original time series against the abnormality index in nonlinear evolution.

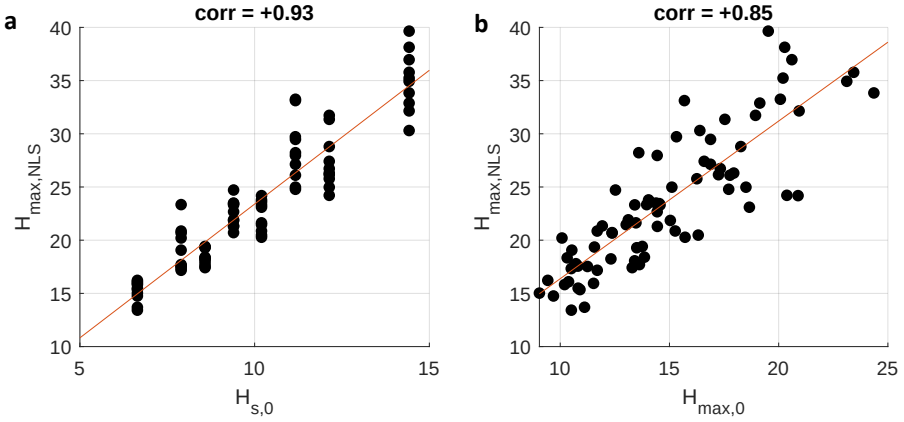


Figure 3.5: **a** The scatter plot of significant wave height of original time series against the maximum wave height in nonlinear evolution **b** The scatter plot of maximum wave height of original time series against the maximum wave height in nonlinear evolution

numerical simulations and the real situations. Shemer et al.[201, 202] generated nonlinear wave groups in a wave tank and found that the evolution of nonlinear groups is consistent with numerical results from the NLS equation under different water depth conditions. Furthermore, extensions of the NLS equation have been investigated as well. Several tank experiments [203, 204] showed the modified NLS equation can predict both the evolution of individual wave crests and the modulation of the envelope. The 1+2 dimensional NLS equation is also suitable to predict rogue waves by description of process of nonlinear spatial-temporal focusing [205]. On the other hand, the modified NLS equation provides better agreement to capture nonlinear phenomena without the restriction of narrow bandwidth spectra [206]. Another widely used method for wave prediction is the high-order spectral method (HOSM) [207–209]. The HOSM enables the simulation of the evolution of short-crest wave trains under the consideration of nonlinear interactions, resonant and non-resonant, wave-current interactions, and wave-bottom interactions. Klein et al. [210] showed that the HOSM has a high accuracy for wave prediction in steeper investigated sea states than linear wave equations and the NLS equation.

3.6. Review of NFT-based Criteria for Rogue Wave Prediction

There are several studies on the prediction of rogue waves based on indicators from the NFT spectrum as main spectrum has the distinctive features of being invariant under NLS wave propagation. Schober et al. [24, 25, 189] provided a simple indicator, the splitting distance, that was found to correlate with the AI. The exact definition of the splitting distance is not straight-forward. The time series in [24] were relatively short, resulting in simple NFT spectra that had one clear gap. The time series in this paper are longer and have therefore more complicated NFT spectra. We define the splitting distance as the smallest distance between the main spectrum points λ_+ associated to unstable modes and main spectrum points λ_- associated to stable modes, as illustrated in Fig. 7.2. The splitting distance used in this paper can thus be written as

$$\delta = \min_{\lambda_+,\lambda_- \text{ as above}} |\lambda_+ - \lambda_-|. \tag{3.2}$$

The splitting distance δ measures how close the spectrum is to having a double point on a spine, which corresponds to potential instabilities. Here, $\delta = 0$ would indicate an exact double point on a spine. As the splitting distance δ decreases, the likelihood of obtaining rogue waves was found to increase in simulations of JONSWAP initial data.

Osborne et al. [28] proposed another criterion that estimates the AI of unstable modes in the NFT spectrum [28]:

$$\frac{H_{\max}}{H_{s,0}} = \sqrt{\frac{\pi}{8}}\left(1 + 2\frac{\lambda_I}{a_o}\right) \approx 0.62666\left(1 + 2\frac{\lambda_I}{a_o}\right) \tag{3.3}$$

where $a_0 = \sqrt{\pi/2}H_{s,0}/4 \approx 0.31333 H_{s,0}$ and λ_I is the mean value of two main spectral points. In this study, considering the prediction of the maximum rogue wave in time

series, we utilize the maximum λ_I corresponding to large spectral components can be directly seen in the time series. As shown in the examplary NFT spectrum in Fig. 7.2, λ_I is the maximum two spectral points, which share the same location in the complex plane.

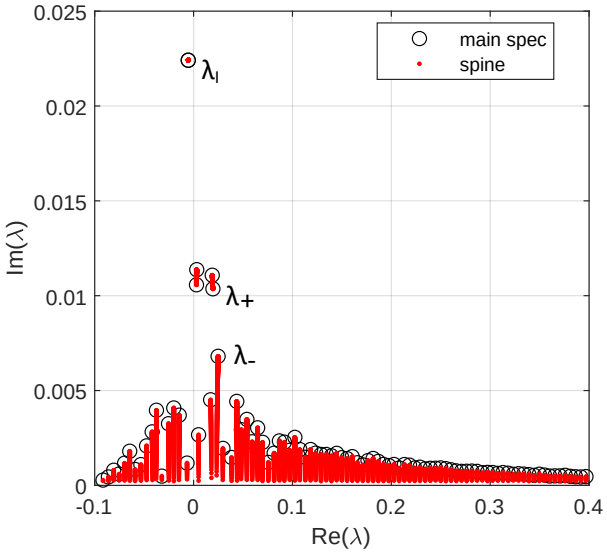


Figure 3.6: The NFT spectrum of the complex envelope. The splitting distance is the distance between eigenvalue $\lambda_+$and eigenvalue λ_- shown in Eqs(3.2). Here, λ_I is the mean value of two main spectrum points. In order to compute the maximum wave height of the time series, λ_I is the mean eigenvalues of the maximum unstable modes.

3.7. Evaluation of NFT-based Criteria for Predicting Maximum Wave Height

In this section, we investigate how well various criteria based on the initial time series predict the maximum wave height after propagation for the data described in Sec.3.3. Note that we chose to predict the maximum wave height instead of the commonly used AI because the AI is normalized and therefore contains no information about how relevant nonlinear effects are for a time series. However, this information is contained in normal, un-normalized wave heights. The quality of the predictions will be assessed using two indications, Pearson's linear correlation coefficient and mutual information (MI). MI is a dimensionless quantity that can be regarded as the reduction in uncertainty. A high MI indicates a large reduction in uncertainty, while a zero MI means the two variables are independent. The advantage of MI over linear correlation is that it also takes nonlinear relationships

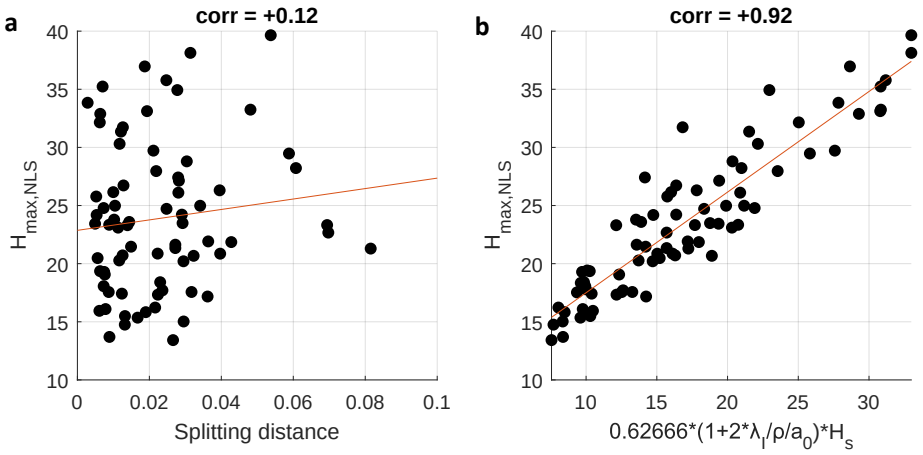


Figure 3.7: Prediction analysis on the JONSWAP simulation data. **a** The scatter plot of formula of rogue wave prediction by Schober. **b** The scatter plot of formula of rogue wave prediction by Osborne.

into account. The disadvantage is that it is not easy to estimate. For our analysis, we used the `mutual_info_regression` routine from the popular scikit-learn package [211] for Python.

To establish a baseline, Fig. 3.5 shows two scatter plots of the maximum wave height after the nonlinear evolution and the significant wave height and maximum wave height of initial data, respectively. The waves will arrive its maximal amplitude after propagating with certain distance with certain choices of the phases. Since we consider eight different JONSWAP spectra, there are eight significant wave heights for the initial data with $6 < H_{s,0} < 15$. The maximum wave height of initial time series satisfies $9 < H_{max,0} < 25$, and reaches its maximum of $13 < H_{max,NLS} < 40$ during the nonlinear evolution. The correlation and mutual information between significant wave height of initial data and maximum wave height in nonlinear evolution are equal to $corr = +0.92$ and $MI = 1.27$. The correlation and mutual information between maximum wave height of initial data and maximum wave height in nonlinear evolution are equal to $corr = +0.85$ and $MI = 0.87$.

Fig. 3.7 contains two scatter plots that show the maximum wave height over the NFT-based spectral parameters from Sec. 3.6. We see that there is no clear relation between the maximum wave height and the splitting distance. The correlation is only 0.12, while the mutual information is estimated as 0.00. There are several potential reasons for this somewhat surprising result. The time series in this paper are longer than in earlier works. This leads to more nonlinear modes, which are more difficult to analyze. As already discussed in Sec. 3.6, finding the "right" gap becomes difficult, and our chosen definition for the splitting distance might not be optimal. Another potential issue is that the splitting distance was originally used to

predict the maximum AI, and not maximum wave height as is done here. Meanwhile, the correlation for the formula in Eq. (3.3) is equal to 0.93. The corresponding MI is 0.99. While a relation is clearly visible in the plot, we note that the correlation and MI are not better than for the simple baseline indicators studied above.

In order to obtain better predictions, we now optimize the coefficients in Eq. (3.4) for our specific data set. With generic constants, the formula becomes

$$H_{\max} = C_1 H_{s,0} + C_2 \lambda_I / \rho. \tag{3.4}$$

Using linear regression, the following coefficients were obtained: $C_1 = 1.87$ and $C_2 = 1.74$. The results for this indicator are shown in Fig. 3.8. It has the strongest correlation ($corr = 0.97$) and largest mutual information ($MI = 1.47$) among all indicators. This shows that simple spectral parameters based on NFT spectra are useful for the prediction of maximum wave height.

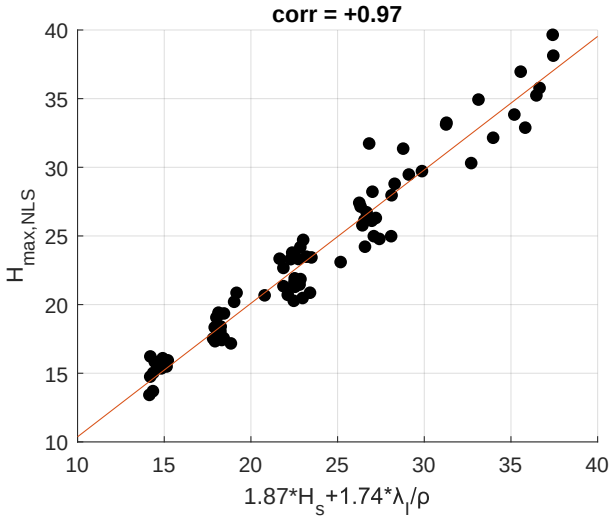


Figure 3.8: Prediction analysis on the JONSWAP simulation data. The scatter plot of formula of rogue wave prediction proposed by this study.

3.8. Conclusions

Nonlinear fourier transforms (NFTs) are powerful tools for the analysis of nonlinear systems, which can detect nonlinear properties such as hidden solitons and modulational instability. Approximately unidirectional narrow-banded ocean surface waves under the deep water condition are governed by the nonlinear Schrödinger equation (NLS). In this study, initial time series of surface waves are generated using JONSWAP spectra for extreme storm conditions. We propagated these initial time series numerically using the NLS equation, and investigated predictors for the

maximum wave height based on the NSE-NFT of the initial time series. While existing predictors did not result in better correlations than a simple baseline, we were able to outperform the baseline by optimizing the weights in an NFT-based predictor. For future research, it would be interesting to assess the new criterion using a more realistic propagation model.

4

IMPACT OF DIRECTIONAL SPREADING ON NONLINEAR KDV-SOLITON SPECTRA IN INTERMEDIATE WATER

CHAPTER ABSTRACT

The Korteweg–De Vries (KdV) equation is a partial differential equation used to describe the dynamics of water waves under the assumptions of shallow water, unidirectionality, weak nonlinearity and constant depth. It can be solved analytically with a suitable nonlinear Fourier transform (NFT). The NFT for the KdV equation is subsequently referred to as the KdV-NFT. The soliton part of the nonlinear Fourier spectrum provides valuable insights into the nonlinear evolution of waveforms by exposing the amplitudes and velocities of potentially hidden solitonic components. Under the KdV equation, the nonlinear spectrum evolves trivially according to simple analytic rules. This in particular reflects that solitons are conserved by the KdV equation. However, in reality, the nonlinear spectrum will change during evolution due to deviations from the KdV equation. For example, waves in the ocean are typically multi-directional. Furthermore, the water depth may range into the intermediate regime, e.g. depending on tides and peak periods. It is therefore uncertain how long the nonlinear spectrum of real-world data remains representative. In particular, it is unclear how stable the detected soliton components are during evolution. To assess the effectiveness of the KdV-NFT in representing water wave dynamics under non-ideal conditions, we generated numerical sea states with varying directional spreading in intermediate water ($kh = 1.036$) using the High-Order Spectral Ocean (HOS-Ocean)

model for nonlinear evolution. After applying the NFT to space series extracted from these evolving directional wave fields, we observe that the KdV-soliton spectra from the NFT are quite stable for cases with small directional spreading. We in particular observe that the largest soliton amplitude is (sometimes dramatically) more stable than the amplitude of the largest linear mode. For large directional spreading, the applicability is limited to short propagation times and distances, respectively.

The text in this chapter has previously appeared in modified form in the article "Lee, Y. C., & Wahls, S. (2025). Impact of directional spreading on nonlinear KdV-soliton spectra in intermediate water. Wave Motion, 137, 103542." [4]. https://doi.org/10.1016/j.wavemoti.2025.103542. This article is distributed under the terms of the Creative Commons Attribution 4.0 International License (CC BY 4.0), which permits unrestricted use, distribution, and reproduction in any medium, provided the original author and source are credited.

4.1. Introduction

Solitons have been recognized as fundamental building blocks in the field of nonlinear dynamics. Their initial discovery dates back to the experiments by John Scott Russell in 1844 [212]. They were subsequently described mathematically by the Korteweg–De Vries (KdV) equation [10]. The KdV equation provides a mathematical framework for the evolution of weakly nonlinear and dispersive progressive unidirectional free-surface waves in shallow water with a constant water depth.

The Nonlinear Fourier Transform (NFT)[1] is as a powerful mathematical tool capable of effectively solving the KdV equation [11]. By employing the NFT, we obtain a nonlinear spectrum that reveals physically meaningful nonlinear components with respect to the KdV equation. The solitonic part of the nonlinear spectrum provides amplitudes, velocities, and phases of solitons, offering essential information for understanding the behavior of systems affected by (potentially hidden) solitons. The nonlinear spectrum evolves trivially when the wave propagation is governed by the KdV equation. As there are also NFTs for other (so-called integrable) equations than the KdV, we refer to the KdV-NFT. The KdV-NFT can be used as a signal processing tool [6], and has been utilized to analyze both experimental [7, 17, 26, 144, 213] and field measurements [34, 36, 55, 98, 214]. Especially in field measurements, the KdV equation can only be an approximate model for wave propagation. In [34], where the measurement site was not specifically chosen to demonstrate the KdV-NFT, non-negligible directional spreading was present and some of the data ventured into intermediate water depths. At the moment, it is not clear what the lifetime of the detected soliton components is. The goal of this paper is to shed some light into this question.

Recently, the paper [215] has explored the impact of directional spreading on the nonlinear Fourier spectrum with respect to the nonlinear Schrödinger equation, which applies to the deep water case. However, there currently is no study that investigates the distance for which KdV solitons can maintain stability during non-ideal evolution. In this paper, we therefore investigate the effects of directional spreading on the solitonic part of KdV-NFT spectra in intermediate water using numerical simulations, and estimate the propagation distances of the soliton components in various scenarios.

To perform the simulations, we utilize a nonlinear phase-resolving wave model based on the High-Order Spectral (HOS) method in order to generate the spatio-temporal evolution of surface wave elevation. We employ the open-source model HOS-Ocean by Ducrozet et al. [216]. HOS-Ocean is based on the Zakharov equation [49], which describes the dynamics of weakly nonlinear and dispersive surface gravity waves in arbitrary constant depths (see the HOS-Ocean repository on GitLab `https://gitlab.com/lheea/HOS-Ocean`). The HOS-Ocean model has been employed in numerous investigations focused on extreme wave phenomena and rogue waves [217–222]. Simulating nonlinear waves numerically poses a challenge due to the issue of wave breaking [223]. The applicability of the HOS-Ocean model is constrained to non-breaking waves propagating within a uniform water depth.

[1] The NFT is also known as the forward transform of the inverse scattering method.

Therefore, wave-breaking conditions should be avoided as discussed in [224, 225]. (More details on this aspect are provided in subsequent sections.)

In this study, we show the first results on the impact of directionality on the NFT based on the (uni-directional) KdV equation. The theoretical background of the methods is introduced. Then we present the simulation set-up. Based on the simulation, the fundamental statistical results for the HOS-Ocean model are shown. These results will be used to make a comparison with the KdV evolution under unidirectional conditions. Subquently, we applied the NFT on the wave fields from the HOS-Ocean model. Two evaluation indices will be used to assess the impact of directional spreading on the evolution of the soliton spectrum. Finally, we discuss the results and provide a summary.

4.2. Methods

4.2.1. The High-Order Spectral method

Simulations of the random surface waves were performed using the open-source model HOS-Ocean [216]. It is based on the High-Order spectral (HOS) method first proposed by [207, 208]. HOS-Ocean demonstrates superior efficiency and accuracy in wave propagation when compared to other advanced methods [217, 226, 227]. It has been widely used to investigate the simulation of rogue waves [217, 218, 228, 229], wave-structure interaction [230], and the effects of ship motion [231].

The model is based on the potential flow formalism, assuming an incompressible, inviscid fluid, and irrotational flow. The Laplace equation for the velocity potential ϕ is solved with boundary conditions. The Laplace equation can be written as

$$\nabla^2\phi + \frac{\partial^2\phi}{\partial z^2} = 0, \tag{4.1}$$

where ∇ is the gradient operator. The kinematic and dynamic free surface boundary conditions, involving the free surface elevation η and the free surface velocity potential $\widetilde{\phi}(x,t) = \phi(x, z = \eta(x,t), t)$, satisfy

$$\begin{aligned} \frac{\partial\eta}{\partial t} &= \left(1 + |\nabla\eta|^2\right) W - \nabla\widetilde{\phi}\cdot\nabla\eta, \\ \frac{\partial\widetilde{\phi}}{\partial t} &= -g\eta - \frac{1}{2}|\nabla\widetilde{\phi}|^2 + \frac{1}{2}\left(1 + |\nabla\eta|^2\right) W^2, \end{aligned} \tag{4.2}$$

where W is the vertical velocity at the free surface elevation. It solves the fully nonlinear boundary value problem for two unknowns which are the surface elevation η and velocity potential $\widetilde{\phi}$. HOS-Ocean considers periodic boundary conditions:

$$(\eta, \widetilde{\phi}, W)(x = 0, t) = (\eta, \widetilde{\phi}, W)(x = L_x, t). \tag{4.3}$$

The HOS-Ocean model evaluates the vertical velocity W with the HOS nonlinear order M,

$$\phi(x,z,t) = \sum_{m=1}^{M} \phi^{(m)}(x,z,t), \tag{4.4}$$

where $\phi^{(m)}(x,z,t)$ is assumed to be of order $O(\epsilon^m)$, and ϵ is a measure of the wave steepness. The HOS nonlinear order M enables considering up to $M+1$ nonlinear wave interactions. The nonlinear order M=2 thus considers the three-wave nonlinear process, while M=3 considers the four-wave quasi-resonant interactions.

From the mean water level of $z=0$, the velocity potential ϕ can be expanded to other water levels using Taylor series:

$$\begin{aligned}\phi^{(1)}(x,0,t) &= \widetilde{\phi}(x,t),\\ \phi^{(m)}(x,0,t) &= -\sum_{k=1}^{m-1}\frac{\eta^k}{k!}\frac{\partial^k\phi^{(m-k)}}{\partial z^k}(x,0,t) \quad \text{for } m>1.\end{aligned} \tag{4.5}$$

Once the individual orders of velocity potential $\phi^{(m)}$ are obtained, the vertical velocity W can also be calculated using the Taylor expansion:

$$\begin{aligned}W(x,t) &= \sum_{m=1}^{M} W^{(m)}(x,z,t),\\ W^{(m)}(x,t) &= \sum_{k=0}^{m-1}\frac{\eta^k}{k!}\frac{\partial^{k+1}\phi^{(m-k)}}{\partial z^{k+1}}(x,0,t).\end{aligned} \tag{4.6}$$

The HOS-Ocean model utilizes a pseudo-spectral method in order to achieve a balance between the high accuracy of spectral methods and the computational efficiency of real-space calculations [216]. This methodology involves representing the solution using a series of basis functions, typically Fourier series, enabling the application of Fast Fourier Transforms (FFTs) for efficient conversion between real and spectral domains. In terms of temporal evolution, HOS-Ocean model commonly employs an efficient 4th order Runge-Kutta Cash-Karp scheme renowned for their precision and stability in integrating equations over time [232]. These methods iteratively propagate the solution forward by computing intermediate steps within each time increment.

4.2.2. EXAMPLE OF PERIODIC KDV-NFT SPECTRUM

To illustrate the periodic KdV-NFT, we now show one example from the HOS-Ocean model. Using basic settings of $H_s=6$ m, $T_p=10$ s and $\Theta=0$, a unidirectional wave field is generated. The space series extracted from the middle of the wave field with respect to the y-direction is shown in Fig. 4.1(a). After applying the NFT on the space series, the associated Floquet spectrum shown in Fig. 4.1(b) is found. It consists of the Floquet discriminant $\Delta(E)$ (blue line), main spectrum points (red dots), reference level E_{ref} (pink line) and open bands (red lines). The main spectrum points are located at the intersections of $\Delta(E)$ with ±1. The reference level is used to distinguish between the soliton components and the radiation components. Solitons are calculated by the Floquet discriminant to the left of reference level, while radiation waves are to the right of reference level. An open band refers to intervals of E (as illustrated in Fig. 15.1 and 17.3-17.5 in Osborne's book [6]). In Fig 4.1(c), the hyperelliptic modes are described by their amplitude (blue line) and modulus (red line). One soliton can be found in spectrum with modulus larger

than 0.99. The other components are oscillatory waves. A feature of the nonlinear Fourier spectrum is that it can be represented by the linear superposition of cnoidal waves and their interactions with each other [233]. Note that the calculated wave number of the soliton is negative by convention, to separate it from the oscillatory part. For a detailed interpretation of the nonlinear Fourier spectrum obtained from the periodic NFTs based on the KdV equation, see [6, 17].

For this paper, the main spectrum part of the periodic KdV-NFT (i.e., the E_i) was computed using a development version of the open source software library FNFT (commit 7bd10db) [191], which has already been applied to various problem in the context of optical fiber [234–236] and hydrodynamics [1, 3, 34, 63]. More information about FNFT can be obtained online at https://github.com/FastNFT/FNFT. The moduli, reference level and soliton amplitudes were computed from the main spectrum in a custom Matlab function, which implemented the formulas given above.

4.3. Simulation Setup

The HOS-Ocean model utilizes a directional spectrum of the form $S(\omega,\theta) = F(\omega)G(\theta)$, where $F(\omega)$ is a JONSWAP spectrum and $G(\theta)$ is a directional spreading function. The JONSWAP spectrum is a widely recognized empirical model extensively used for characterizing irregular waves [216]. It takes into account the significant wave height (H_s), angular peak frequency (ω_p), peak enhancement factor (γ), and angular spreading parameter (α):

$$F(\omega) = \alpha_J H_s^2 \omega_p^4 \omega^{-5} \exp\left[-\frac{5}{4}\left(\frac{\omega}{\omega_p}\right)^{-4}\right] \gamma^{\exp\left(-\frac{(\omega-\omega_p)^2}{2\sigma^2\omega_p^2}\right)} \tag{4.7}$$

with $\sigma = \begin{cases} 0.07 & \text{for} \quad \omega < \omega_p \\ 0.09 & \text{for} \quad \omega \geq \omega_p \end{cases}$, where α_J is a constant to obtain the correct significant wave height. The directional spreading function $G(\theta)$ is defined as [216, 237, 238]

$$G(\theta) = \frac{1}{\beta}\left[\cos\left(\frac{\pi\theta}{2\beta}\right)\right]^2, \quad \left|\frac{\pi\theta}{2\beta}\right| \leq \frac{\pi}{2}, \tag{4.8}$$

where β is a measure of the directional spreading. We introduce $\Theta = 2\beta$ in degrees, which represents the range of the directional distribution. The parameter β is suggested to be in the range [0, 0.6], where $\beta = 0.6$ represents a short-crested sea state with very large spreading [224]. In this study, we set the parameter β to 0, 0.0872, 0.1309, 0.1745, 0.2618, 0.5236, which corresponds to $\Theta = 0°$, 10°, 15°, 20°, 30°, and 60°, respectively. Fig. 4.2 (a) depicts the corresponding spreading functions.

The HOS-Ocean model is unable to explicitly describe wave breaking. Guidelines for ensuring the applicability of the model for directional irregular sea states with different water depths have been developed in [224]. In this study, we consider a water depth of 20 m. The threshold for wave breaking in different water depths is, based on the reference [239], given by

$$H_b = \kappa \lambda_p \tanh(K_p h), \tag{4.9}$$

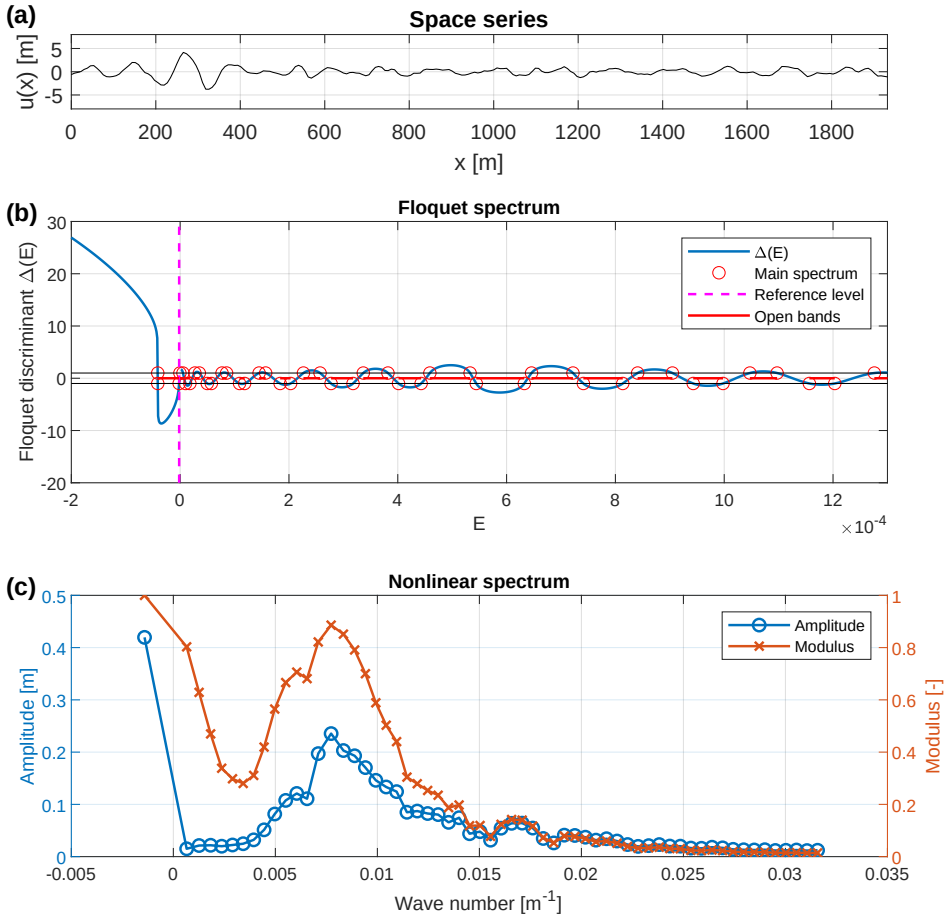


Figure 4.1: (a) Example of simulated space series (b) The Floquet spectrum of simulated space series contains the Floquet discriminant $\Delta(E)$ (blue line), main spectrum points (red dots), reference level E_{ref} (pink line) and open bands (red lines). (c) The nonlinear Fourier spectrum of simulated space series. The nonlinear modes are represented by amplitudes (blue circle line) and modulus (red cross line).

where H_b is the breaking wave height, κ is a coefficient, λ_p is the wave length based on the peak period, k_p is the peak wave number, and h is the water depth. The value of κ varies across locations, depending on the local water depth and environments [240–242]. We use $\kappa \in [0.067; 0.076]$, which is considered suitable for the HOS-ocean model according to [224]. Fig. 4.2 (b) shows the applicability range for the highest possible irregular wave field at different water depths. Under consideration of the non-breaking wave conditions, the wave fields are generated

with significant wave heights of $H_s = 4,5,6$ m and a peak period of $T_p = 10$ s. The relative water depth kh is equal to 1.036 in our case, which corresponds to an intermediate water depth ($0.1\pi < kh < \pi$) [243, 244]. It is nevertheless below the two KdV applicability thresholds discussed earier, $kh < 1.14$ [55] and $kh < 1.36$ [54].

In this study, we have simulated the evolution of in total 36 wave fields corresponding to different input conditions, as shown in Table 4.1. We adopted a spatial discretization of $N_x = 256$ and $N_y = 64$ grid points for all simulations, with computational domain lengths of $L_x = 16\lambda_p \simeq 1932.21$ m and $L_y = 8\lambda_p \simeq 954.74$ m, where $\lambda_p = 2\pi/k_p$ is the peak wavelength. The mesh resolution is $\Delta x = L_x/(N_x - 1) \simeq 7.58$ m and $\Delta y = L_y/(N_y - 1) \simeq 15.15$ m. The nonlinear order M is either $M = 2$ or $M = 3$. The input parameters for the JONSWAP spectrum are set to $H_s = 4,5,6$ m, $T_p = 10$ s and $\gamma = 3.3$. The random phases were fixed by using the same initial seed for the random number generator. The wave fields are evolved for 1200 s. We show an example of nonlinear wave fields at $t = 201$ s with the settings $H_s = 4$ m, $T_p = 10$ s and M=3 with $\Theta = 0°, 10°, 15°, 20°, 30°, 60°$ in Fig. 4.3. It should be noted that in HOS-Ocean simulation, the initial wave field is generated using linear solutions. An adjustment period is necessary to manage the transition from linear initial conditions to a nonlinear surface wave field [245, 246]. The adjustment duration is recommended for the first 20 wave periods, which in our cases, with a peak wave period of $T_p = 10$ s, amounts to 200 s.

In Fig. 4.4, we present the spectral evolution of the two-dimensional linear spectrum for a directional spreading of 60° (initial wave field in Fig. 4.3 (f)). The proper wavenumber-domain bandwidth ensures accurate representation of the wave field and efficient numerical computation. The wavenumbers are distributed in the range between $k_{\min}$ and $k_{\max}$. As suggested in [224, 247], we select $k_{\max} = 8k_p$ with the peak wave number $k_p = 2\pi/\lambda_p$ as the bandwidth of the reconstructed wave field.

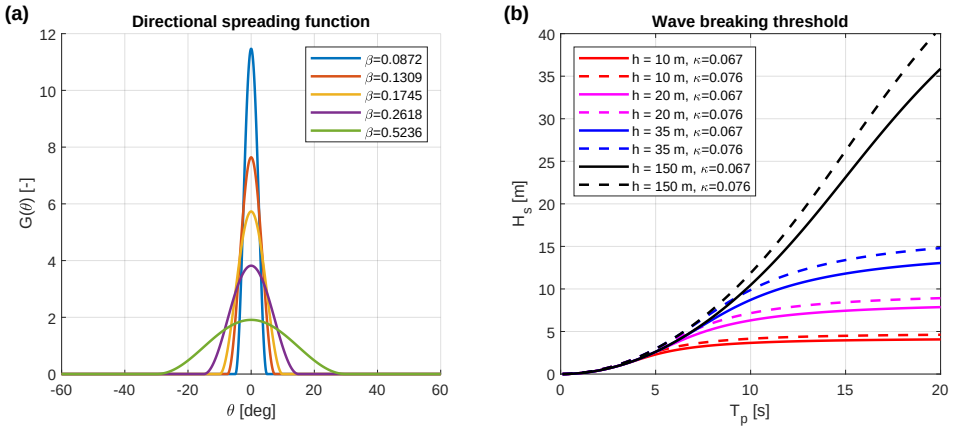


Figure 4.2: (a) Directional spreading function $G(\theta)$ of angle θ for different directional spreadings. (b) Applicability limits for HOS simulation with water depths of $h = 10$ m (red lines), $h = 20$ m (purple lines), $h = 35$ m (blue lines) and $h = 150$ m (black lines) with coefficient κ varying from local sites.

Table 4.1: Input wave parameters of directional seas for the HOS-Ocean simulation.

Case	H_s [m]	T_p [s]	Θ [°]	M	Case	H_s [m]	T_p [s]	Θ [°]	M
1	4.0	10.0	0°	2	19	4.0	10.0	0°	3
2	5.0	10.0	0°	2	20	5.0	10.0	0°	3
3	6.0	10.0	0°	2	21	6.0	10.0	0°	3
4	4.0	10.0	10°	2	22	4.0	10.0	10°	3
5	5.0	10.0	10°	2	23	5.0	10.0	10°	3
6	6.0	10.0	10°	2	24	6.0	10.0	10°	3
7	4.0	10.0	15°	2	25	4.0	10.0	15°	3
8	5.0	10.0	15°	2	26	5.0	10.0	15°	3
9	6.0	10.0	15°	2	27	6.0	10.0	15°	3
10	4.0	10.0	20°	2	28	4.0	10.0	20°	3
11	5.0	10.0	20°	2	29	5.0	10.0	20°	3
12	6.0	10.0	20°	2	30	6.0	10.0	20°	3
13	4.0	10.0	30°	2	31	4.0	10.0	30°	3
14	5.0	10.0	30°	2	32	5.0	10.0	30°	3
15	6.0	10.0	30°	2	33	6.0	10.0	30°	3
16	4.0	10.0	60°	2	34	4.0	10.0	60°	3
17	5.0	10.0	60°	2	35	5.0	10.0	60°	3
18	6.0	10.0	60°	2	36	6.0	10.0	60°	3

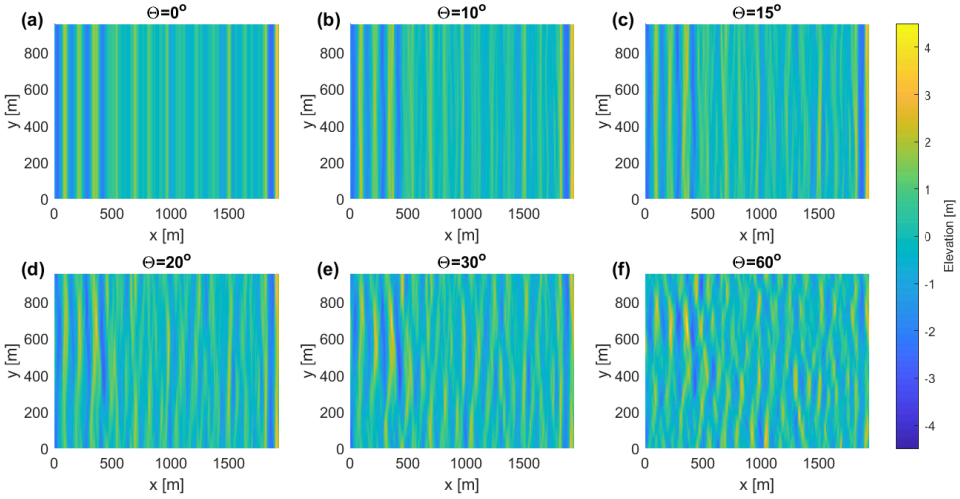


Figure 4.3: Simulated wave fields by HOS-Ocean model with conditions of $H_s = 4$ m and $T_p = 10$ s at $t = 201$ s by HOS-Ocean model under different directional spreading conditions: (a) $\Theta = 0°$ (b) $\Theta = 10°$ (c) $\Theta = 15°$ (d) $\Theta = 20°$ (e) $\Theta = 30°$ (f) $\Theta = 60°$

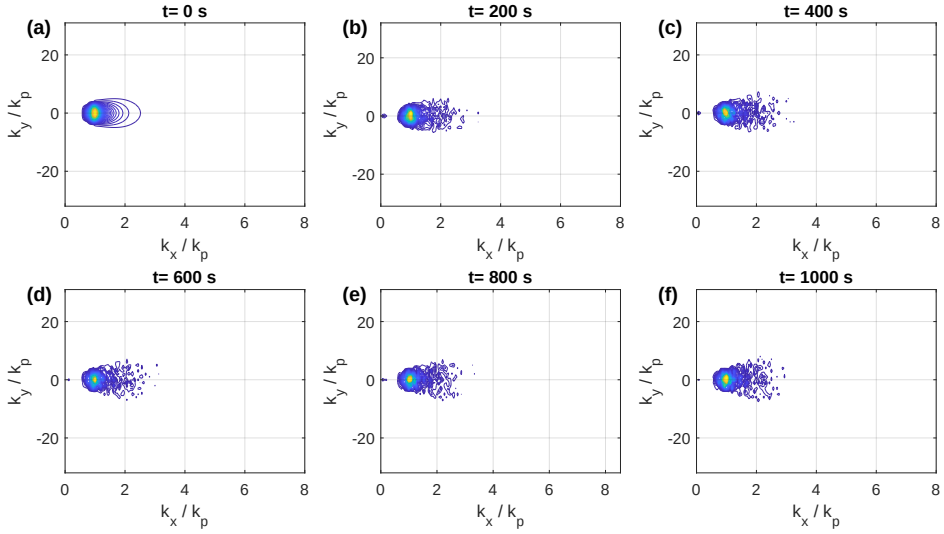


Figure 4.4: Evolution of wave spectrum with $H_s = 4$ m, $T_p = 10$ s, and $\Theta = 30°$ by the HOS-Ocean model uring nonlinear propagation at (a) $t = 0$ s (b) $t = 200$ s (c) $t = 400$ s (d) $t = 600$ s (e) $t = 800$ s (f) $t = 1000$ s.

4.4. Results

Utilizing the HOS-Ocean model with the aforementioned settings, we discuss the nonlinear spectral characteristics of the wave field under different directional spreading. We first present conventional statistical results for the simulated wave fields in Sec. 4.4.1 to characterize the simulation setup, and contrast these results with a KdV-based evolution in Sec. 4.4.2. The temporal evolution of the nonlinear KdV-type soliton spectrum under the HOS model is presented in Sec. 4.4.3 to assess the impact of directional spreading and intermediate water conditions. in In Sec. 4.4.4, we then quantify the impact of directional spreading on the KdV-NFT soliton spectra. Finally, in Sec. 4.4.5, the evolution of the largest soliton is compared to that of the largest linear mode.

4.4.1. Statistical characteristics during nonlinear evolution

The simulated wave fields correspond to two conditions with nonlinear order M: $M = 2$ and $M = 3$. Three parameters including maximum wave height, kurtosis, and skewness are used to represent spectral characteristics. Kurtosis measures wave height concentration around the mean, with high values indicating intense, steep waves and low values suggesting uniform distribution [16, 126]. Skewness assesses distribution asymmetry, with positive values implying a prevalence of taller, sharper crests and shallower, more rounded troughs [16]. The skewness and kurtosis can be

expressed as

$$\text{Skewness} = \frac{\overline{\eta^3}}{\sigma^3}, \tag{4.10}$$

$$\text{Kurtosis} = \frac{\overline{\eta^4}}{\sigma^4}, \tag{4.11}$$

where σ is the standard deviation of the surface elevation η, and the overbar indicates the time average operator.

In Fig. 4.5 and Fig. 4.6, we show exemplary statistical results for the wave field with $H_s = 4$ m and $T_p = 10$ s for two conditions, where $M = 2$ and $M = 3$. We first focus on the $M = 2$ case. For directional spreading $\Theta = 0°$ (Fig. 4.5 (a)-(c)), the wave field is long-crested and aligned in the x-direction. As mentioned in section 6.3, the first 20 periods represent the transition from linear solutions to nonlinear behavior. The statistical and spectral wave characteristics become stationary after the transition stage. This characteristic can also be observed in both Fig. 4.5 and Fig. 4.6. The maximum wave height of the initial space series is 8 meters. During the transition stage, the maximum wave height decreases and settles at around 5 meters afterward. A similar trend can also be observed in the kurtosis, which starts at 6.6, decreases during the transition, and finally stabilizes at around 2.5. The skewness is also unstable during the first 20 periods, thereafter, it mostly maintains values above 0. The maximum value of skewness observed throughout the evolution is 0.53. A normal distribution has a kurtosis of 3, whereas our simulation's kurtosis of 2.5 is slightly lower than that of a normal distribution, indicating that extreme values of wave elevation are slightly less common than in a normal distribution. Additionally, the positive skewness during the evolution suggests a noticeable asymmetry in our simulation.

When directionality is introduced to a long-crested wave field (starting from Fig. 4.5 (d)), it leads to a transition to short-crested waves, which exhibit a more chaotic pattern. The wave energy is distributed spatially across a range of directions based on the directional spreading. The directionality alters the wave pattern along the y-direction. The statistical parameters such as the maximum (upper line), minimum (lower line), and mean (middle line) values are computed across all spatial series in the y-direction. The statistical parameters of the HOS wave fields under different directional spreading with $\Theta = 10°$, $15°$, $20°$, $30°$, and $60°$ are depicted in Fig. 4.5 (c)-(r). With increasing directional spreading, it is evident that the statistical parameters including maximum wave height, kurtosis, and skewness exhibit a wider variation range from minimum to maximum values. If we compare the maximum wave height under directional spreading with $\Theta = 60°$ (Fig. 4.5 (p)) with the unidirectional case (Fig. 4.5 (a)) after the transition stage ($t > 200$) s, it is observed that as waves are distributed in the y-direction in the multi-directional case, the interaction among waves results in larger waves compared to the unidirectional case. The largest maximum wave height of $H_{\max} = 8.42$ m is detected at $t = 930$ s. Similar results are observed in kurtosis (Fig. 4.5 (q)) and skewness (Fig. 4.5 (r)). The largest kurtosis value is Kurtosis = 6.09 at $t = 225$ s, while the largest skewness value is Skewness = 0.96 at $t = 582$ s.

Subsequently, we compare the nonlinear orders $M = 2$ (Fig. 4.5) and $M = 3$ (Fig. 4.6). The overall results are very similar; however, there are more extreme values of the statistical parameters are observed in the $M = 3$ cases. Considering that third-order nonlinearity is typically more pronounced in deep water conditions, and our simulations are conducted under intermediate water conditions, the third-order effects are not as prominent in our cases. Nonetheless, they still contribute slightly to enhancing the statistical parameters. The statistical results here are quite similar to the simulations of two-dimensional shallow water waves using the Kadomtsev–Petviashvili equation by Toffoli et al. (2008) [248], suggesting that the interaction of two crossing wave trains in shallow water may increase skewness and kurtosis under certain crossing angles.

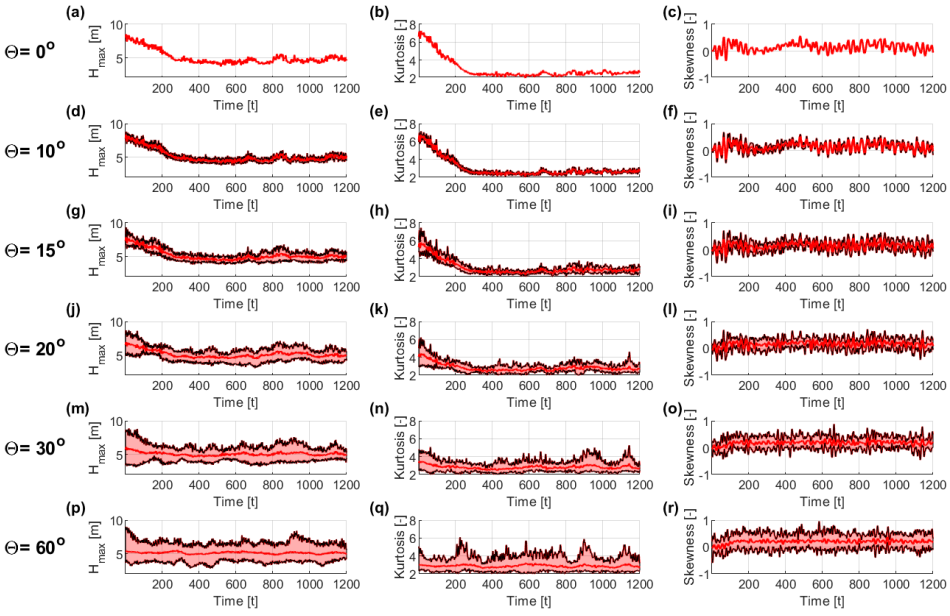


Figure 4.5: Statistical results of maximum wave height, kurtosis and skewness of wave fields with $H_s = 4$ m, $T_p = 10$ s, and M=2 under nonlinear wave evolution with different directional spreadings. The results are presented with the maximum shown by the upper black line, the minimum by the lower black line, and the mean by the middle red line.

4.4.2. Comparison with spectral characteristics obtained from KdV-dynamics

Similarly to the HOS model considered in the previous subsection, the nonlinear dynamics of random wave fields governed by the KdV equation exhibits different behavior compared to wave evolution by linear wave theory. As nonlinearity

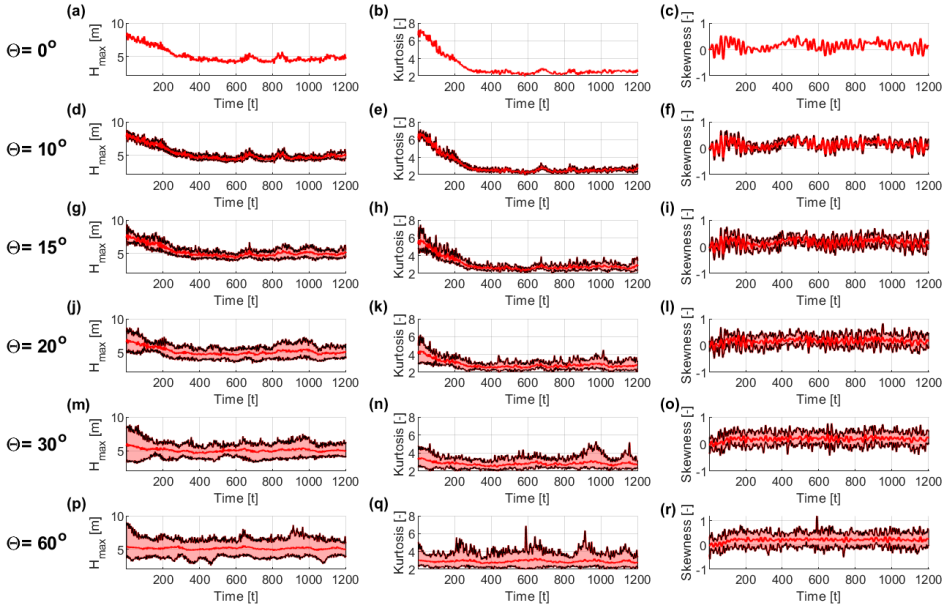


Figure 4.6: Statistical results of maximum wave height, kurtosis and skewness of wave fields with $H_s = 4$ m, $T_p = 10$ s, and M=3 under nonlinear wave evolution with different directional spreadings. The results are presented with the maximum shown by the upper black line, the minimum by the lower black line, and the mean by the middle red line.

increases in the system, the wave fields deviate from a near-Gaussian distribution towards greater asymmetry, characterized by increased kurtosis and positive skewness [249]. This could occur under the interaction of two crossing wave trains in a two-dimensional wave field [248].

In the previous section, we showed the statistical results of the HOS simulation during temporal evolution. The question here is whether the temporal evolution of the HOS wave field under unidirectional conditions resembles that of the KdV equation. The statistical comparison of nonlinear wave fields under unidirectional conditions by the HOS-Ocean model and the KdV equation is illustrated in Fig. 4.7 for $M = 2$ and 4.8 for $M = 3$. For applying the HOS-Ocean model, the first 20 periods of the simulation should be neglected to avoid the transition stage as it becomes nonlinear (as mentioned in Sec. 6.3). The spatial series at $t = 201$ s is chosen as the initial input for the Korteweg-de Vries (KdV) equation. The temporal evolution will be simulated for 1000 s to compare the statistics of the propagated waveform with the HOS-Ocean model. The temporal evolution using the KdV equation is performed using the spin command of the Matlab package Chebfun [250]. The numerical settings for Chebfun include 10,000 grid points and a time step of $dt = 0.1$ s. The propagation time is set as 1000 s with an interval of 1 s, which allows a comparison

with the HOS-Ocean simulation. In Fig. 4.7 (a) with the condition of $H_s = 4$ m, it is observed that the maximum wave height $H_{\max}$ of KdV evolution can exceed that of the HOS-Ocean model. Similar results can be found in Fig. 4.7 (d) with $H_s = 5$ m and (g) $H_s = 6$ m. Similar to maximum wave height, kurtosis in the KdV evolution tend to be larger than those obtained from the HOS-Ocean model, as shown in Fig 4.7 (b,e,h). Regarding skewness, depicted in Fig. 4.7 (c, f, i), the skewness has more positive and larger values in the HOS simulation than in the KdV equation during temporal evolution. This suggests that the HOS-Ocean model generates wave fields with greater asymmetry during evolution, whereas the KdV equation produces more symmetrical wave fields.

Considering the nonlinear order $M = 3$, Fig. 4.8 depicts the temporal evolution of statistical parameters for the HOS wave field including third-order nonlinearity. We had observed that the evolution of maximum wave heights for the three different conditions with $M = 3$ is slightly larger than the corresponding conditions for $M = 2$. However, the KdV equation evolution does not exhibit this trend of $M = 3$ cases exceeding the corresponding $M = 2$ conditions. (The KdV equation itself is of course not influenced by the nonlinear order parameter M of the HOS model. Only its initial conditions, which are extracted from the HOS model at $t = 201$s, change.) As shown in Fig. 4.8 (g), the maximum wave height of the HOS-Ocean model can be larger than that of the KdV equation during evolution. Similar results are observed for kurtosis and skewness, where $M = 3$ cases are larger than $M = 2$, but this trend is not observed in the KdV evolution. Our results show that both methods exhibit different nonlinear evolution properties even under unidirectional conditions. This difference can be attributed to two main factors. First, the applicability of the KdV equation is more suitable for shallow water conditions, whereas the wave fields by HOS-ocean are modeled under intermediate water condition in this study. Second, the KdV equation is, in constrast to HOS-Ocean, only a weakly nonlinear model.

4.4.3. Change of the nonlinear KdV-soliton spectrum under HOS dynamics

In this section, we show the results of the nonlinear Fourier analysis of the wave fields simulated using the HOS-Ocean model. The space series required by the NFT are extracted from the wave fields by considering only the center with respect to the y-direction. By applying the NFT with periodic boundary conditions to a specific space series (i.e., for some fixed time $t = t_0$), the nonlinear Fourier spectra are obtained. In our simulations, the modulus of the first amplitude of hyperelliptic oscillation modes, A_1, is consistently greater than 0.99, indicating the presence of a soliton. In the following, we call A_1 the amplitude of the largest soliton. Similarly, when present, A_2 and A_3 denote the amplitudes of the second- and third-largest solitons, respectively.

Recall that soliton amplitudes are calculated using a reference level in the periodic KdV-NFT (1.36). The reference level is considered to be the propagation level of solitons. Typically, it differs from the still water level [99]. In practice, it is found by checking when the modulus of the hyperelliptic modes drops below the threshold of 0.99. When applying the NFT to wave fields generated by the HOS-Ocean model, we

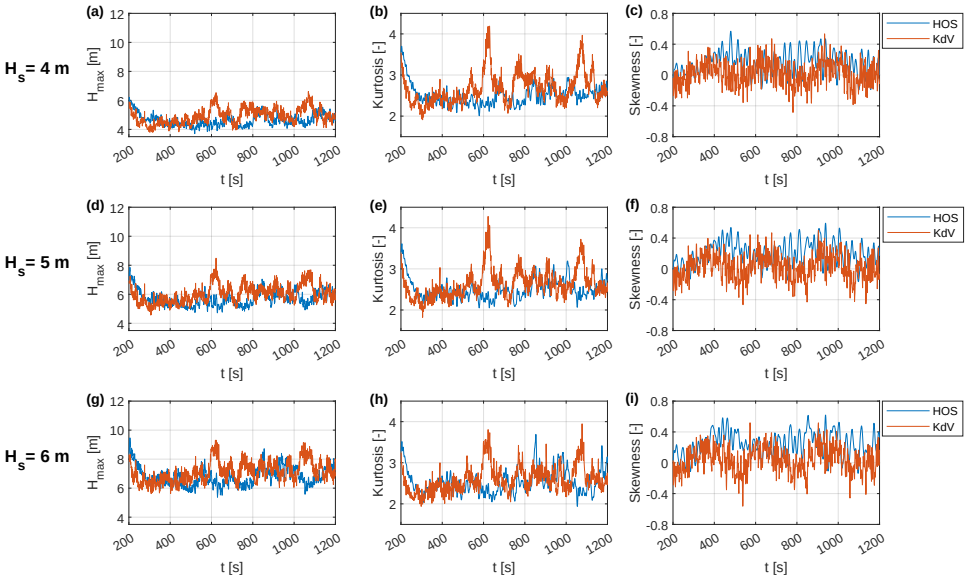


Figure 4.7: Comparison of the HOS-Ocean model with the KdV equation under unidirectional conditions. The nonlinear order M=2 is used. The parameters maximum wave height, kurtosis, and skewness are examined for $H_s = 4$ m, $H_s = 5$ m, and $H_s = 6$ m. The blue line represents the HOS-Ocean model, and the orange line represents the KdV evolution.

encountered a critical issue: the soliton amplitudes regularly made implausible large jumps. The discontinuities arise from the use of a fixed threshold. Under non-KdV evolution, the moduli of the hyperelliptic change during propagation. When a modulus passes the threshold, the reference level jumps suddenly due to the way it is computed. To address this issue, we use the maximum reference level seen throughout the temporal evolution as the reference level for each individual space series. With this revision, we obtain soliton amplitudes that change continuously over time.

Based on the above revision of the reference level, we first show that the solution amplitudes evolve continuously in our simulated wave fields with $M = 3$, $H_s = 6$ m, in Fig. 4.9. In this case, there are in total three soliton components, where the amplitudes of the largest soliton A_1 is represented by the blue line, second-largest soliton A_2 by the red line, and third-largest soliton A_3 by the yellow line. In unidirectional case with $\Theta = 0°$ in Fig 4.9(a), we can observe that amplitudes of the three soliton components are quite stable after the transition stage. This feature is also observed in the cases with directional spreading. Even at larger directional spreading ($\Theta = 60°$), A_1 consistently maintains a higher amplitude than A_2. Furthermore, there is no crossover between the amplitudes during temporal evolution, indicating that there is almost no energy exchange among them.

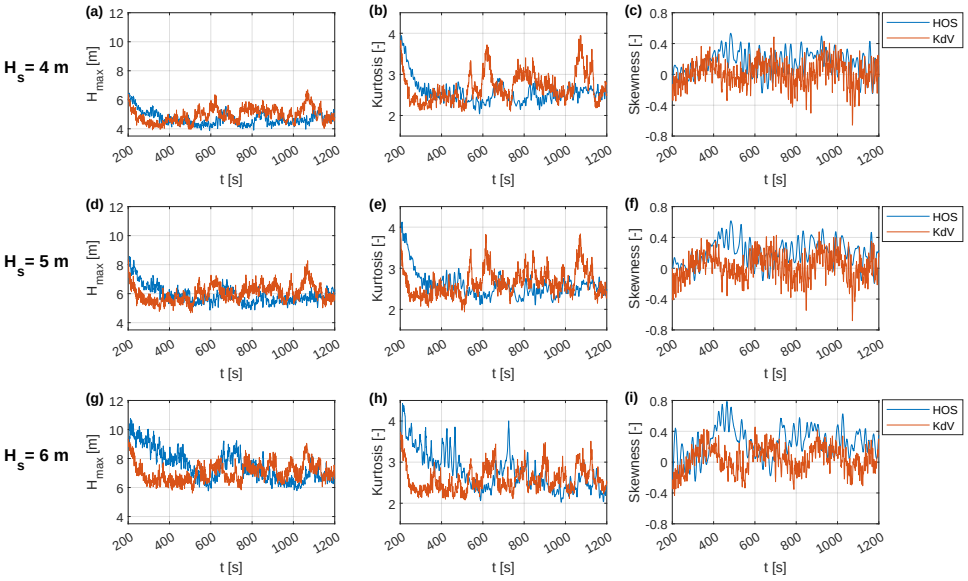


Figure 4.8: Comparison of the HOS-Ocean model with the KdV equation under unidirectional conditions. The nonlinear order M=3 is used. The parameters maximum wave height, kurtosis, and skewness are examined for $H_s = 4$ m, $H_s = 5$ m, and $H_s = 6$ m. The blue line represents the HOS-Ocean model, and the orange line represents the KdV evolution.

Subsequently, we focus on the amplitude of the largest soliton A_1 as the dominant representative of the soliton spectrum. In Fig. 4.10, we show how the amplitude of the largest soliton A_1 changes during temporal evolution of HOS-Ocean model with $M = 2$ under various significant wave heights (H_s = 4 ,5, and 6 m) and directional spreadings ($\Theta = 0°$, 10°, 15°, 20°, 30°, 60°). In Fig. 4.10 (a), it can be observed that A_1 changes most slowly and remains quite stable under unidirectional spreading. In ideally KdV-governed wave fields, the soliton amplitude would remain constant during evolution. Our results thus show that the non-ideal evolution conditions (from a KdV perspective) in the HOS-ocean simulations only have minor effects on the soliton spectrum under uni-directional spreading. Variations in the amplitudes of the soliton increase with greater directional spreading. According to Fig. 4.3, we see that wavelengths are quite short compared to the simulated wave fields in the y-direction, and thus wave groups can enter or leave the area where the space series is measured. When considering larger significant wave heights in Fig. 4.10 (b) and Fig. 4.10 (c), the variations of A_1 also increase due to higher nonlinearity in the system, which increasingly deviates from the weakly nonlinear assumption of the KdV equation. Nevertheless, for cases with comparatively small directional spreadings ($\Theta \leq 30°$), the variations of the soliton amplitudes hardly increases. Only for $\Theta = 60°$, a noticeable increase in the variation of A_1 is observed.

Fig. 4.11 shows the temporal evolution of the amplitude of the largest soliton A_1 in a nonlinear wave field modeled by the HOS-Ocean model with $M = 3$. The temporal evolution of A_1 is quite similar to the case $M = 2$ in Fig. 4.10, but A_1 in the $M = 3$ case is slightly larger than in the $M = 2$ case. This indicates that the third-order nonlinearity increases the amplitude of A_1, and it is more pronounced in wave fields with larger significant wave height. It also leads to somewhat larger variations of A_1 when the significant wave height is large ($H_s =$ 6m), compared to the cases with $M = 2$.

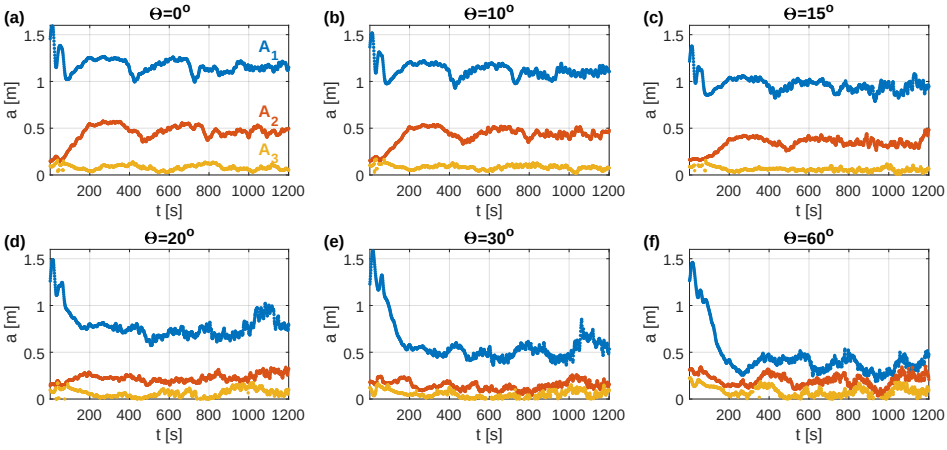


Figure 4.9: The amplitudes of solitons in soliton spectra of HOS wave fields with M=3 under the conditions of significant wave height $H_s = 6$ m. Different directional spreadings are considered $\Theta = 0°$, $\Theta = 10°$, $\Theta = 15°$, $\Theta = 20°$, $\Theta = 30°$, $\Theta = 60°$ from (a) to (f), respectively. The amplitudes of the largest soliton A_1 is represented by the blue line, second-largest soliton A_2 by the red line, and third-largest soliton A_3 by the yellow line.

4.4.4. QUANTIFICATION OF THE IMPACT OF DIRECTIONAL SPREADING ON NONLINEAR KDV-SOLITON SPECTRA IN INTERMEDIATE WATER CONDITIONS

We use the largest solitons as representatives of the nonlinear spectrum when describing the nonlinear evolution of shallow water waves. However, in the case of larger directional spreading, part of the soliton's energy may travel into other regions that our selected space series does not capture, causing a larger variation in soliton amplitude. In order to quantify the impact of directional spreading on nonlinear soliton spectra during temporal evolution, we consider the Relative Error (RE) and the Relative Deviation of the Mean (RDM). Denoting the amplitude of largest soliton at time t by $A_1(t)$, the relative error (RE) is the relative change in $A_1(t)$ compared to

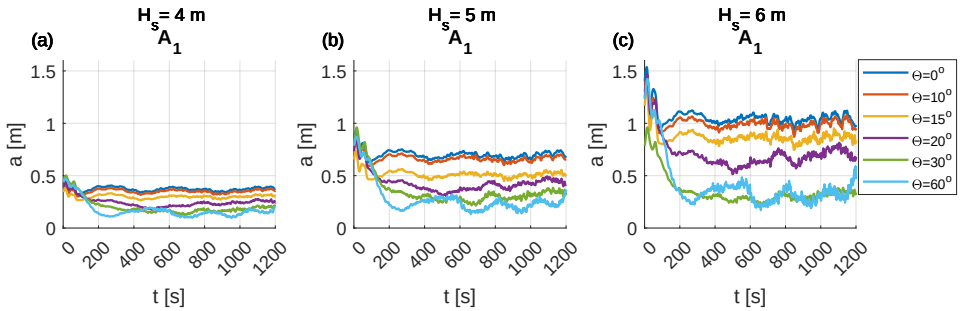


Figure 4.10: The amplitudes of the largest soliton A_1 in soliton spectra of HOS wave fields with M=2 under the conditions of significant wave height (a) $H_s = 4$ m, (b) $H_s = 5$ m and (c) $H_s = 6$ m with directional spreadings $\Theta = 0°$, $\Theta = 10°$, $\Theta = 15°$, $\Theta = 20°$, $\Theta = 30°$, $\Theta = 60°$.

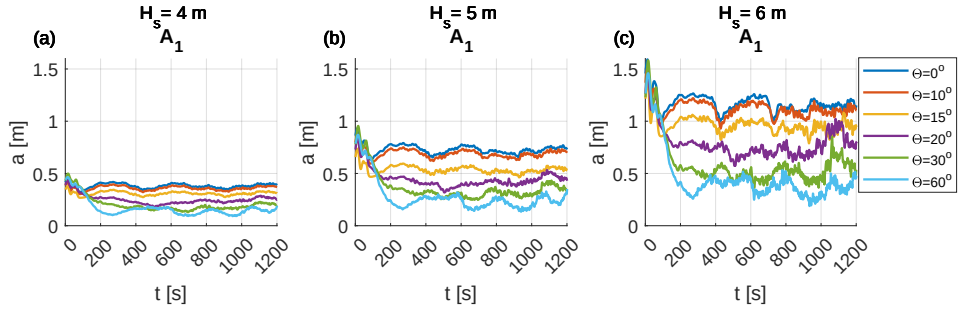


Figure 4.11: The amplitudes of the largest soliton A_1 in soliton spectra of HOS wave fields with M=3 under the conditions of significant wave height (a) $H_s = 4$ m, (b) $H_s = 5$ m and (c) $H_s = 6$ m with directional spreadings $\Theta = 0°$, $\Theta = 10°$, $\Theta = 15°$, $\Theta = 20°$, $\Theta = 30°$, $\Theta = 60°$.

its value at the end of the HOS-Ocean start-up phase after (i.e., at t =201 s):

$$\mathrm{RE}(t) = \frac{|A_1(t) - A_1(201)|}{A_1(201)}. \tag{4.12}$$

The second evaluation parameter, Relative Deviation of the Mean (RDM), focuses on the deviation of the average amplitude of the largest soliton over the time interval $[201, t]$ from the initial value:

$$\mathrm{RDM}(t) = \frac{\left| \frac{\sum_{201}^{t} A_1(t)}{t-200} - A_1(201) \right|}{A_1(201)}. \tag{4.13}$$

Due to the averaging, the RDM results in smoother curves than the RE. We use these two evaluation indices to assess the impact of directional spreading on nonlinear soliton spectra, as shown in Fig. 4.12 for $M = 2$ and Fig. 4.13 for $M = 3$.

Fig. 4.12 shows the temporal evolution of the RE and RDM of the soliton amplitude $A_1(t)$ for shallow water waves fields with $M = 2$ and significant wave heights of (a, d) $H_s = 4$ m, (b, e) $H_s = 5$ m, (c, f) $H_s = 6$ m. We focus on the practically relevant initial stage and observe when the RE and RDM, respectively, hit fixed thresholds for the first time. (Under ideal propagation according to the periodic KdV equation, this would never happen as both indicators would stay zero forever.) We use the unidirectional case with $\Theta = 0°$ as a baseline to determine these thresholds. In Fig. 4.12 (a), we first focus on the unidirectional case of $\Theta = 0°$ with $H_s = 4$ m, where the RE reaches a first major maximum of RE = 0.15 after 236 s before, and the RDM reaches a first major maximum of RDM = 0.065 after 346 s. Under unidirectional conditions, the RE never exceeds 0.15 and the RDM never exceeds 0.071. In the following, we therefore use the more stringent thresholds RE = 0.10 and RDM = 0.05.

We then calculate the propagation times required for the RE to reach 0.1 and the RDM to reach 0.05 for all directional spreadings ($\Theta = 0°$, 10°, 15°, 20°, 30°, 60°). The results show that the durations for these cases are 213 s, 202 s, 178 s, 112 s, 37 s and 16 s, respectively. We also evaluate the propagation time with the RDM shown in Fig. 4.12 (d). When it reaches 0.05, we obtain results of 268 s, 255 s, 246 s, 142 s, 24 s and 22 s for corresponding directional spreadings. The corresponding results for $H_s = 5$ m (see Fig. 4.12 (b,e)) and $H_s = 6$ m (shown in Fig. 4.12 (c,f)) are provided in Table 4.2. It can be observed that under smaller directional spreading conditions ($\Theta \leq 20°$), the representative propagating time can last more then 110 s. For larger directional spreading conditions ($\Theta \geq 30°$), the RE and RDM deviate significantly faster, resulting in a reduced representative propagation time. This finding is consistent for all significant wave heights.

The evaluation of the impact of directional spreading on the soliton amplitude for $M = 3$ is provided in Fig. 4.13 and Table 4.2. In Fig. 4.13, it can be observed that the RE and RDM with directional spreadings of $\Theta = 0°, 10°$ and 15° are almost the same. The RE and RDM start to increase when the directional spreading becomes larger ($\Theta \geq 20°$). The general behavior of the errors in case of $M = 3$ is quite similar to the results for $M = 2$. Based on Table 4.2, the representative propagation times for $M = 3$ closely resemble the case for $M = 2$.

To estimate a representative propagation distance for solitons, we consider a single solitary wave $u(x,t) = A\text{sech}^2[(x - ct)/l]$, where $c = \sqrt{g(h+A)}$ is the wave celerity and $l = \sqrt{4h^3/(3A)}$ is the characteristic length [6, 52, 251]. For a wave field with $M = 2$, $H_s = 4$ m and $h = 20$ m, a soliton amplitude of 0.4 m can be read off in Fig. 4.10(a). The corresponding wave celerity is calculated as 14.15 m/s. For small directional spreading ($\Theta \leq 15°$), propagation times of at least $t_{\text{prop}} = 178$ s can result in propagation distances larger than $c \times t_{\text{prop}} = 14.15\text{m/s} \times 178\text{s} \approx 2519$ m. Compared to the characteristic length of a soliton with amplitude 0.4 m, which equals 163.3 m, this propagation distance is about 15.4 times the characteristic length. In contrast, with large directional spreading ($\Theta = 60°$), a propagation time of 16 s yields a calculated propagation distance of only around 226 m. In this case, the nonlinear spectrum remains representative for approximately 1.4 times of characteristic lengths. This suggests that the NFT-based method can capture the nonlinear evolution of waves with directional spreading for limited propagation times or distances, which

decrease with increasing directional spreading and significant wave height.

4.4.5. Comparison with linear Fourier modes

To compare our results with the linear Fourier method, we also calculated the RE of the dominant linear Fourier mode during temporal evolution. Based on the HOS wave fields with $M = 3$ and $H_s = 6$ m, we show the results in Fig. 4.14. The RE of the largest linear Fourier mode obtained by the fast Fourier transform (FFT) and is marked by a blue line. The largest nonlinear mode (soliton) obtained by the NFT is marked with a red line. The RE of the largest linear mode increases faster than the RE of the largest soliton in the practically important initial phase for all cases except $\Theta = 60°$. For the cases with $\Theta \leq 20°$, the soliton RE even stays close to zero for a significant time, while the linear mode RE in contrast increases immediately. These results suggest that the nonlinear Fourier transform may be a more appropriate method for describing the nonlinear evolution of directional wave fields than the conventional linear FFT, even under non-ideal intermediate water and moderate directional spreading conditions.

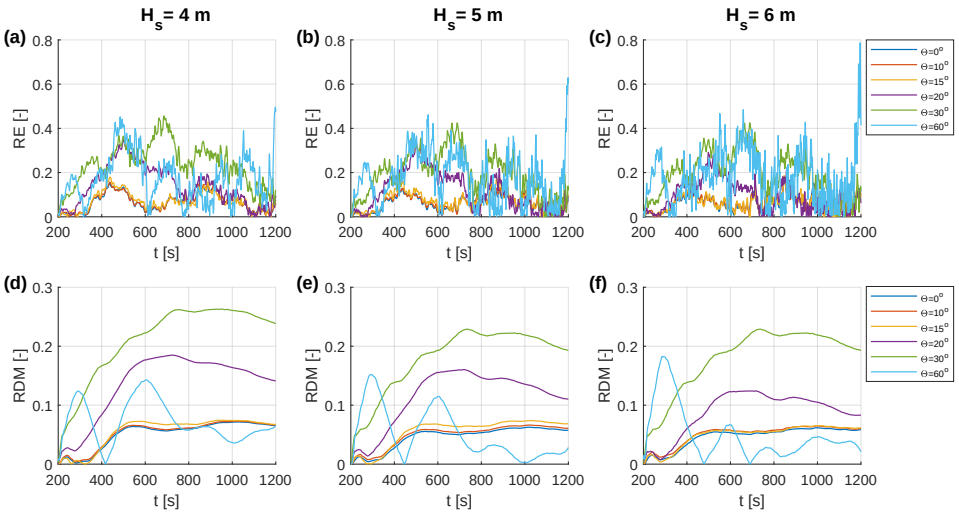


Figure 4.12: Evaluation of the amplitude of largest soliton A_1 by relative error (RE) and relative deviation of the mean (RDM) based on the HOS wave fields with M=2 under the conditions of significant wave heights $H_s = 4$ m, $H_s = 5$ m and $H_s = 6$ m, and directional spreading $\Theta = 0°$, $\Theta = 10°$, $\Theta = 15°$, $\Theta = 20°$, $\Theta = 30°$ and $\Theta = 60°$.

4.5. Discussion and Conclusions

This paper evaluated the impact of directional spreading and intermediate water conditions on soliton components detected using the nonlinear Fourier transform

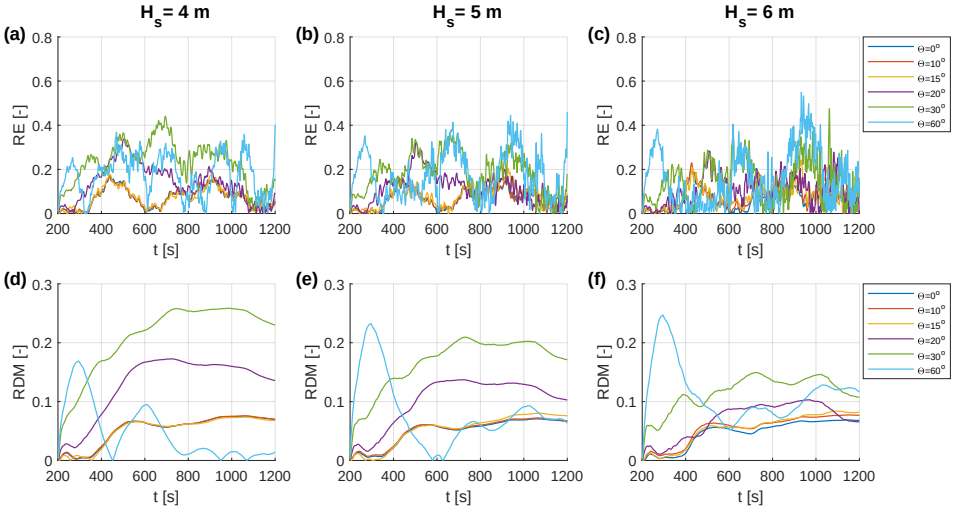


Figure 4.13: Evaluation of the amplitude of largest soliton A_1 by relative error (RE) and relative deviation of the mean (RDM) based on the HOS wave fields with M=3 under the conditions of significant wave heights $H_s = 4$ m, $H_s = 5$ m and $H_s = 6$ m, and directional spreading $\Theta = 0°$, $\Theta = 10°$, $\Theta = 15°$, $\Theta = 20°$, $\Theta = 30°$ and $\Theta = 60°$.

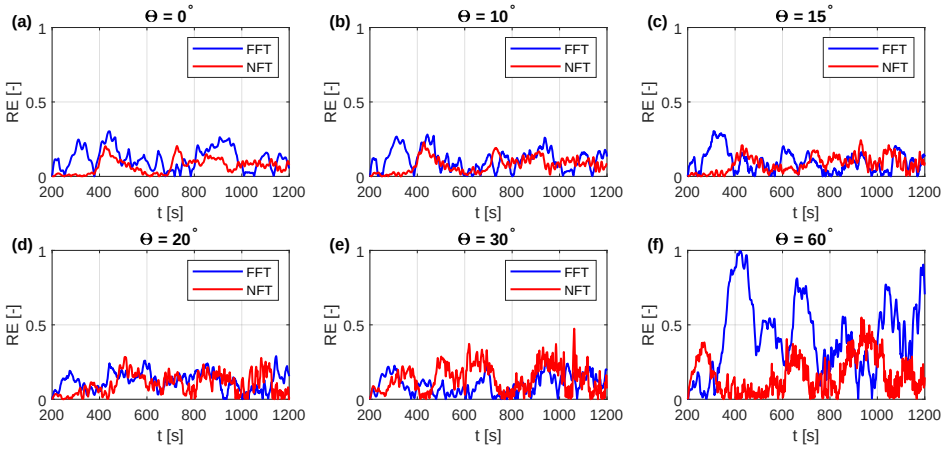


Figure 4.14: Evaluation of the amplitudes of dominant linear Fourier modes by relative error (RE) based on the HOS wave fields with M=3 under the conditions of significant wave heights $H_s = 6$ m, and directional spreading $\Theta = 0°$, $\Theta = 10°$, $\Theta = 15°$, $\Theta = 20°$, $\Theta = 30°$ and $\Theta = 60°$ from (a) to (f), respectively.

Table 4.2: Representative propagation time for the nonlinear spectra under different directional spreading conditions

M=2	$H_s = 4$ m		$H_s = 5$ m		$H_s = 6$ m	
0°	213 s	268 s	215 s	289 s	216 s	247 s
10°	202 s	255 s	216 s	262 s	198 s	243 s
15°	178 s	246 s	161 s	239 s	161 s	241 s
20°	112 s	142 s	131 s	161 s	137 s	180 s
30°	37 s	24 s	75 s	27 s	75 s	27 s
60°	16 s	22 s	14 s	21 s	13 s	16 s
M=3	$H_s = 4$ m		$H_s = 5$ m		$H_s = 6$ m	
0°	212 s	265 s	201 s	271 s	200 s	281 s
10°	202 s	259 s	202 s	265 s	200 s	249 s
15°	182 s	267 s	184 s	283 s	201 s	266 s
20°	133 s	150 s	135 s	171 s	161 s	289 s
30°	35 s	15 s	77 s	15 s	86 s	15 s
60°	11 s	10 s	8 s	6 s	9 s	9 s

(NFT) for the Korteweg-de Vries (KdV) equation. Under ideal KdV propagation, the soliton amplitudes would stay constant during propagation. Directional spreading and intermediate water conditions however violate the assumptions of the KdV equation, so that the soliton amplitudes are expected to change during propagation. We explored how long the soliton amplitudes remain representative for different directional spreading conditions. To this end, the nonlinear evolution of randomly generated wave fields was simulated using the HOS-Ocean model [216] for various directional spreadings under intermediate water conditions ($kh = 1.036$).

The nonlinear temporal evolution of wave fields was simulated using the HOS-Ocean model for sea states with significant wave heights $H_s = 4$ m, $H_s = 5$ m and $H_s = 6$ m, respectively. A statistical analysis of basic wave parameters during nonlinear evolution was then performed. The evolution of several statistical parameters was compared between the HOS-Ocean model and the KdV equation. This confirmed that the two methods exhibit different nonlinear evolution. Although the KdV equation has limitations in its applicability, we found that the soliton amplitudes obtained from the KdV-NFT nevertheless may vary only slightly during the nonlinear evolution of directional intermediate water waves for certain propagation times or distances, depending on the directional spreading conditions. Moreover, we observed that except for strong spreading conditions, the largest soliton is more stable than the largest linear Fourier mode.

We also observed that the soliton amplitude remains stable during temporal evolution in the unidirectional case although the wavefields were propagated using the HOS method instead of the KdV equation, and intermediate waters were considered. Under increasingly directional spreading conditions, the soliton amplitude exhibits larger and larger variations during temporal evolution. Using

two evaluation metrics, the Relative Error (RE) and the Relative Deviation of the Mean (RDM), we determined representative propagation times for the soliton wave heights for various significant wave heights and directional spreading conditions (see Table 4.2). Our results show that the largest soliton in the nonlinear spectrum is quite stable for the small directional spreading cases. However, even in cases with large directional spreading, the soliton amplitudes provided by the KdV-NFT can still retain their representative character for short propagation times or distances. These findings indicate that NFT-based analyses can be physically meaningful even under physical propagation conditions different from the integrable equation that is solved exactly by the NFT. Similar results have also been reported only recently for the deep water case, where the NFT for the nonlinear Schödinger equation is used [215].

From a practical point of view, this study provides the first attempt to quantify in particular of impact of directional spreading on nonlinear Fourier spectra obtained by applying the KdV-NFT to space series extracted from multidirectional seas. Such results are important to further interpret the results of real-world studies based on the KdV-NFT such as [34, 36, 55, 98, 214]. For the sea states with moderate directional spreading, the nonlinear soliton spectrum varied only moderately during evolution when considered for short enough periods of time. Since surface waves in shallow water regions are expected to experience reduced spreading compared to deep water locations due to the shallow water effects [55, 161], this further enhances the potential of the KdV-NFT for field measurements. We finally remind the reader that these results are based on the nonlinear temporal evolution of wave fields by the HOS-Ocean model. While HOS-Ocean is a powerful model, numerical models cannot always describe the nonlinear evolution of realistic wave fields accurately. High-quality field data is therefore essential for future investigations about the practical applicability of the KdV-NFT.

5

When Do JONSWAP Spectra Lead To Soliton Gases In Deep Water Conditions?

CHAPTER ABSTRACT

When a large number of solitons dominates the dynamics of a system, scientists describe this collective behaviour of solitons as a soliton gas. Soliton gases are currently the subject of intense practical and theoretical investigations. The existence of soliton gases has been confirmed in experiments, but is not clear what kind of sea states might lead to soliton gases. Therefore, in order to determine the wave parameters for sea states that lead to soliton gases, large numbers of surface wave elevations are generated by the well-known JOSNWAP model in this paper. Here, we only discuss soliton gases in deep water governed by the nonlinear Schrödinger (NLS) equation. The nonlinear Fourier transform (NFT) with vanishing boundary conditions is applied to the simulated ocean surface waves. The resulting nonlinear Fourier spectrum is used to calculate the energy of radiation waves and solitons. We investigate which JONSWAP parameters result in sea states that can be characterized as soliton gases, and find that a large Phillip's parameter α, a large peak enhancement parameter γ and a short peak period T_p are important factors for soliton gas conditions. The results allow allows researchers to estimate how likely soliton gases are in deep waters. Furthermore, we find that the appearance of rogue waves is more likely in highly nonlinear sea states with soliton gas-like conditions.

The text in this chapter has previously appeared in modified form in the article "Yu-Chen Lee, Markus Brühl, and Sander Wahls. "When Do JONSWAP Spectra Lead to Soliton Gases in Deep Water Conditions?." International Conference on Offshore Mechanics and Arctic Engineering. Vol. 86878. American Society of Mechanical Engineers, 2023." [2]. https://doi.org/10.1115/OMAE2023-104326. Reproduced from Proceedings of OMAE 2023, Paper No: OMAE2023-104326, V005T06A101, with permission.

5.1. Introduction

Long cosine waves and undular bore-shaped waves in shallow water change into trains of solitons after travelling to the far field under certain conditions, e.g., [7, 17]. Such unsuspicious wave profiles can thus be generated by nonlinear interacting solitons. When solitons dominate the dynamics, the properties of the nonlinear wave field are characterised by interacting solitons. This scenario is known as a soliton gas in the literature.

Soliton often occur in nonlinear integrable partial differential equations (PDEs) such as the Korteweg–de Vries (KdV) equation for shallow water waves and the nonlinear Schrödinger (NLS) equation for deep water waves. The term "soliton" was first coined by Zabusky and Kruskal [10] based on numerical solutions of the KdV equation. The integrability of nonlinear PDEs enables their complete analytical solution. S-integrable PDEs can be solved by scattering transforms, which are also known as nonlinear Fourier transforms (NFTs) [252]. The solution of the KdV equation was first developed by Gardner et al [11]. Later, the NLS equation was solved by Zakharov and Shabat [12]. An extension of the NFT method to more PDEs was given by Ablowitz et al. [9]. Using NFTs for vanishing boundary conditions, the initial condition is transformed into a nonlinear spectrum (also called scattering data), which is composed of a continuous spectrum and a discrete spectrum. The continuous spectrum is associated with dispersive radiation waves, while the solitons are linked to the discrete spectrum. The soliton solutions for the NLS equation are envelope solitons in deep water [253]. Note that the eigenvalues in the nonlinear spectrum, which indicate the height and velocity of solitons, remain invariant during the evolution. This feature allows us to find hidden solitons in the initial condition. The collisions of NLS solitons sometimes lead to the emergence of rogue waves after propagating a certain distance [254].

Soliton gases can be described with a soliton density function. Kinetic equations describe the evolution of the soliton density function under consideration of soliton-soliton collisions, which provides a reasonable description of a soliton gas. The first kinetic equation for a rarefied soliton gas based on the KdV equation for shallow water conditions was derived by Zakharov [30]. Here, an infinite statistical ensemble of weakly interacting solitons typified by a small density of states is called a rarefied soliton gas, in contrast to the notion of a dense soliton gas. Later, the kinetic equations for a dense soliton gas for the KdV as well as for the NLS equation were obtained by El and Kamchatnov [31]. The critical density of a soliton gas was discussed by El to obtain a quantitative criterion for a dense soliton gas [255].

Recent numerical simulations, laboratory experiments and field measurements provide further support for the existence of soliton gases in different physical systems. Sea states that resemble a KdV-soliton gas have been measured under wind wave conditions in the Currituck Sound, North Caralina, by Costa et al. [36]. An experimental demonstration of a soliton gas in an one-dimensional wave flume has been achieved for the KdV type by Redor et al. [86] and for the NLS type by Suret et al. [65]. From the above studies, the existence of soliton gases has been confirmed in both experiments and in-situ measurements of free surface gravity waves. However, to our knowledge, there are no studies on what kind of sea states might lead to

soliton gases.

In the present paper, we therefore investigate the occurrence of NLS soliton gases for unidirectional random sea states with JONSWAP spectra under deep water conditions using the NLS equation. Random realizations of specific JONSWAP spectra are generated with different values of decisive parameters, which are the peak period T_p, the Phillip's parameter α and peak enhancement parameter γ. Using the NFT for the NLS equation with vanishing boundary conditions, our analysis allows us to determine the ratio of soliton energy to total energy for each realization. From this data, we can determine how likely specific JONSWAP parameters lead to soliton gases.

5.2. SIMULATION SETUP

The most commonly used model to describe random sea states for academic research and engineering design is according to the Joint North Sea Wave Observation Project (JONSWAP) [195]. The JONSWAP spectrum can be expressed as

$$S(f) = \frac{\alpha g^2}{(2\pi f)^5} \mathrm{e}^{-\frac{5}{4}\left(\frac{f_p}{f}\right)^4} \gamma^r, \quad \sigma = \begin{cases} 0.07 & f \le f_p \\ 0.09 & f > f_p \end{cases}, \tag{5.1}$$

where $r = \exp\left[-\frac{1}{2}\left(\frac{f-f_p}{\sigma f_p}\right)^2\right]$, f is frequency, g is gravity, f_p is the dominant frequency, σ is the narrowness of the peak parameter, γ is the enhancement factor and α is the Phillip's parameter. The parameter γ influences the peak shape. If $\gamma > 1$, the sea states are undeveloped, due to nonlinear wave-wave interactions, do not arrive at steady conditions. The higher values of enhancement factor γ represent higher and narrower in the center of the spectral peak of JONSWAP spectrum. The values of Phillip's parameter α determine the energy scale of JONSWAP spectrum.

In this study, we generated various JONSWAP spectra based on the basic JONSWAP spectral parameters α, γ and peak period T_p. The selected range of JONSWAP parameters for α is from 0.001 to 0.03 with an interval of 0.001, for γ is from 1 to 6 with an interval of 0.1, and for T_p is from 5 s to 15 s with an interval of 2 s. There are totally 9180 JONSWAP spectra in our simulation. After generating JONSWAP spectra with selected JONSWAP parameters, the significant wave height H_s can be calculated from $4\sqrt{m_0}$, where m_0 is zeroth-order spectral moment. Fig. 5.1 shows the plots of H_s over the JONSWAP parameters α and γ. Spectra with different peak periods from 5 s to 15 s are shown from Fig. 5.1a to Fig. 5.1f. With regards to higher values of α and γ, the spectra have larger H_s due to the larger amplitude scale and sharper spectral peak.

For each JONSWAP spectrum, we generate 10 surface wave elevations with random phases. The time series have a duration of length with 600 s. The sampling frequency is 1.7 Hz. The complex envelope, which is what the NSE actually describes, can be calculated from the surface wave elevation with the help of the Hilbert transform [60]. The NLS-NFT analysis of the complex envelope is shown in the next section. The water depth is set to 1000 m. All simulated surface waves satisfy the critical depth $k_0 h > 1.363$ that is required for the NLS equation to be in the soliton-supporting focusing regime.

Before we start on our analysis, we would like to emphasize that our dataset of the simulated JONSWAP sea states differs from realistic sea states. Real-world spectra are complex and change from site to site with the meteorological and oceanographic conditions. However, long-term measurements of in-situ data are rare and costly. JONSWAP spectrum is commonly used to calculate the basic wave parameters for engineering design. Our data cover a wide range of JOSNWAP parameters containing most of possible JOSNWAP sea states.

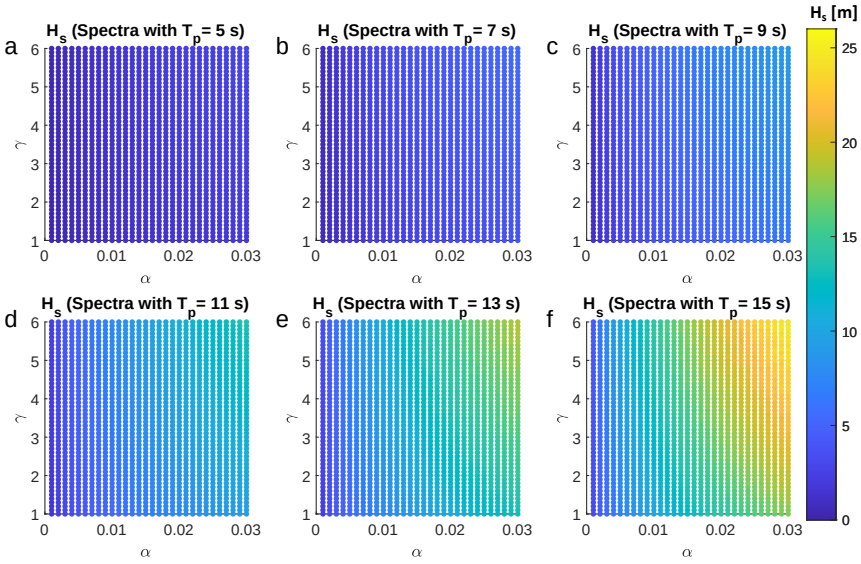


Figure 5.1: Scatter plots of α and γ for significant wave height of all JONSWAP spectra. **a**. Spectra with peak period T_p equal to 5 s. **b**. Spectra with peak period T_p equal to 7 s. **c**. Spectra with peak period T_p equal to 9 s. **d**. Spectra with peak period T_p equal to 11 s. **e**. Spectra with peak period T_p equal to 13 s. **f**. Spectra with peak period T_p equal to 15 s.

5.3. Soliton Energy Ratio

The energy of solitons and radiation waves can be calculated by discrete spectra and continuous spectra [13]. First, the total energy of the time series is

$$E_{\text{total}} = E_{\text{sol}} + E_{\text{rad}} = \int_{-\infty}^{\infty} |u|^2 dt \tag{5.2}$$

where E_{sol} is the energy of the solitons

$$E_{\text{sol}} = 4 \sum_{k=1}^{N} \text{Im}(\zeta_k) \tag{5.3}$$

and E_{rad} is the energy of the radiation waves

$$E_{\text{rad}} = 4\int_{-\infty}^{\infty} \log(1+|r(\zeta)|^2) \tag{5.4}$$

The soliton energy ratio is

$$E_{\text{sol_ratio}} = E_{\text{sol}}/E_{\text{total}} = (E_{\text{total}} - E_{\text{rad}})/E_{\text{total}} \tag{5.5}$$

If the energy ratio is high, the solitons are the dominant components in the time series. We use the formula that utilizes the radiation energy to compute the energy ratio because it is easier to compute the continuous spectrum numerically.

Based on the soliton energy ratio, we classify the sea states into four types, as shown in Table 5.1: (1) If $E_{\text{sol_ratio}} < 40\%$, the sea state is considered to be dominated by radiation waves. (2) If $40\% \le E_{\text{sol_ratio}} < 60\%$, the sea state is considered to be equally influenced by radiation waves and solitons. (3) If $60\% \le E_{\text{sol_ratio}} < 90\%$, the sea state is considered to be dominated by solitons. (4) If $90\% \le E_{\text{sol_ratio}} < 100\%$, the sea state is considered to be soliton gas-like.

Table 5.1: Definition of four classes

Class	Range
Radiation wave dominance	$E_{\text{sol_ratio}} < 40\%$
Radiation wave and soliton combination	$40\% \le E_{\text{sol_ratio}} < 60\%$
Soliton dominance	$60\% \le E_{\text{sol_ratio}} < 90\%$
Soliton gas-like	$90\% \le E_{\text{sol_ratio}} < 100\%$

5.4. An example of nonlinear Fourier analysis

We provide an example of a surface wave elevation generated by JONSWAP spectrum with $\alpha = 0.02$, $\gamma = 3.3$, $f_p = 1/7$Hz and complex envelope, as shown in Fig. 5.2a and Fig. 5.2b, respectively. The blue line is the complex envelope calculated from the Hilbert transform. You can find a more detailed view of the elevation and envelope that is obtained by zooming in from 200 s to 400 s in Fig. 5.2c. The complex envelope will be analyzed by the nonlinear Fourier transform with vanishing boundary conditions. The nonlinear Fourier spectrum is shown in Fig. 5.3. Fig. 5.3a shows the continuous spectrum with ζ on the x-axis and the reflection coefficient on the y-axis. Fig. 5.3b shows the discrete spectrum with the real part of the eigenvalue on the x-axis representing soliton velocity and the imaginary part on the y-axis representing soliton amplitude. The number of solitons N is 64 in this case. Note that the soliton of the NLS equation is in the envelope instead of the surface elevation.

Figure 5.4 shows the magnitude of the initial complex envelope and the magnitude of envelope of nonlinear spectral components reconstructed by the iNFT. We see that the envelope reconstructed from the full (i.e., continuous and discrete) nonlinear

spectrum (orange line) is identical to the initial magnitude of complex envelope (blue line), as shown in Fig. 5.4a. Figure 5.4b and c show the magnitude recovered from only the continuous spectrum (radiation part) and only the discrete spectrum (soliton part), respectively. It is clear that the soliton components dominante the wave field, as most envelope peaks in the time series match the peaks of the initial complex envelope. Meanwhile, Fig. 5.4d shows the linear sum of time series that correspond to only the continuous spectrum and only the discrete spectrum. It is found that the linear sum of soliton and radiation waves is different from the inverse of the full nonlinear spectrum. This reveals that the nonlinear interaction between continuous spectrum and discrete spectrum cannot be neglected in this case. The soliton energy ratio is 91% in this case, indicating a sea state in a soliton gas-like condition.

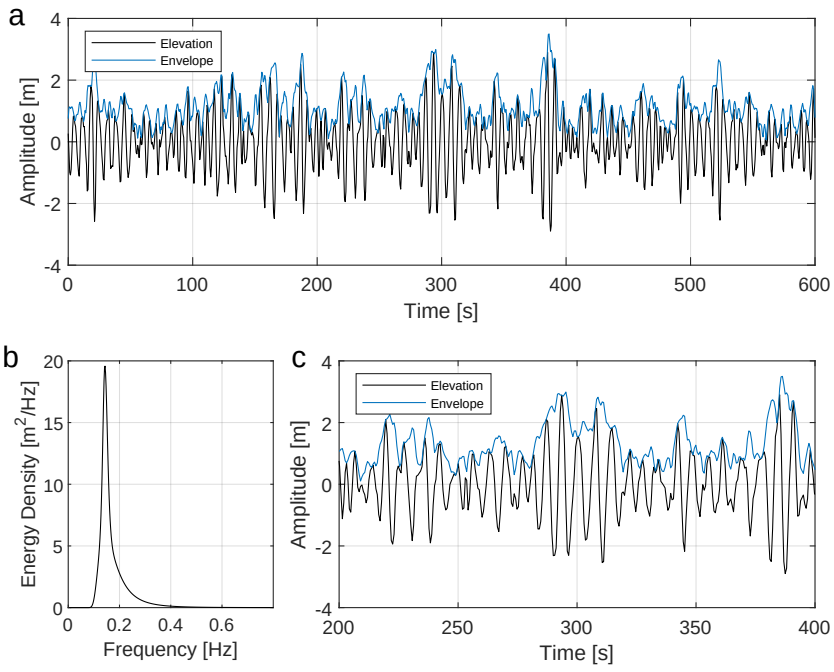


Figure 5.2: **a**. Example of a time series of surface wave elevation (black line) generated by JONSWAP spectrum with random phases. The blue line represents the magnitude of the complex envelope. **b**. The JONSWAP spectrum with $f_0 = 1/7\text{Hz}, \alpha = 0.02, \gamma = 3.3$. **b**. Zoom in the time series of surface wave elevation from 200 s to 400 s.

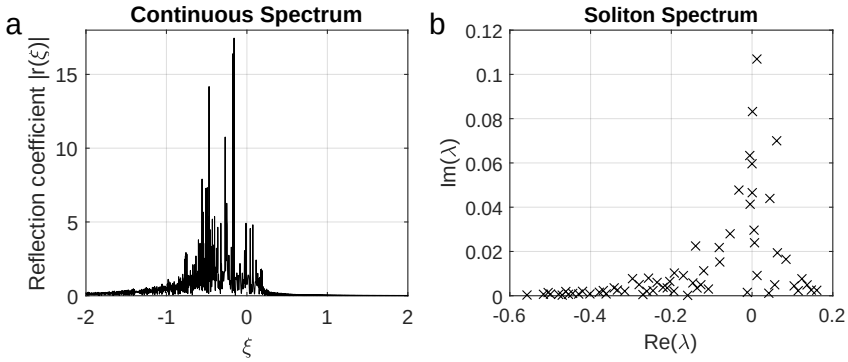


Figure 5.3: The non-linear spectrum is divided into two parts: **a**. The continuous spectrum and **b**. The soliton spectrum.

5.5. SOLITON ENERGY RATIOS OF JONSWAP MODELS

We investigate how dominant the soliton energy in the wave field is for surface elevation time series generated by the JONSWAP model with random phases, as explained in Sec. 5.2. There are 9180 JONSWAP spectra in total. For each peak period, there are 1530 spectra. For each JONSWAP spectrum, we generate 10 time series of surface wave elevation with random phases, so there are in total 98100 elevation samples. The nonlinear Fourier spectra are obtained from normalized complex envelopes of these time series.

The energy of solitons and radiation waves and the soliton energy ratio are calculated. The soliton energy ratio in this study is the mean soliton energy ratio of the 10 surface wave elevation data. In Figure 5.5, we show the mean soliton energy ratio over the JONSWAP parameters α and γ. Different values of the peak period of the JONSWAP spectra are considered separately from short waves to long waves, as shown from Fig. 5.5a to Fig. 5.5f.

Recall that the nonlinear Fourier spectra are classified into four types: radiation wave dominance, radiation wave and soliton combination, soliton dominance, and soliton gas. The classification is based on the soliton energy ratio. In terms of the distribution of the soliton energy ratio, the spectra with radiation wave dominance (blue dots) are distributed in the region with smaller α. The area with smaller γ has more spectra with radiation wave dominance (blue dots). The spectra with radiation wave and soliton combination (cyan and green dots) are distributed on the right of the radiation wave dominance cases with larger α. Most of the spectra with soliton dominance (orange dots) are distributed right of the radiation wave and soliton combination with larger α. These soliton-dominant cases are the majority of the simulated spectra. The spectra of soliton gas-like cases (yellow dots) are distributed in the right-up region with large α and γ. With regard to the peak periods, the spectra with longer peak periods also have more cases with radiation wave dominance and radiation wave and soliton combination conditions. The spectra with shorter peak periods have more cases with soliton gas.

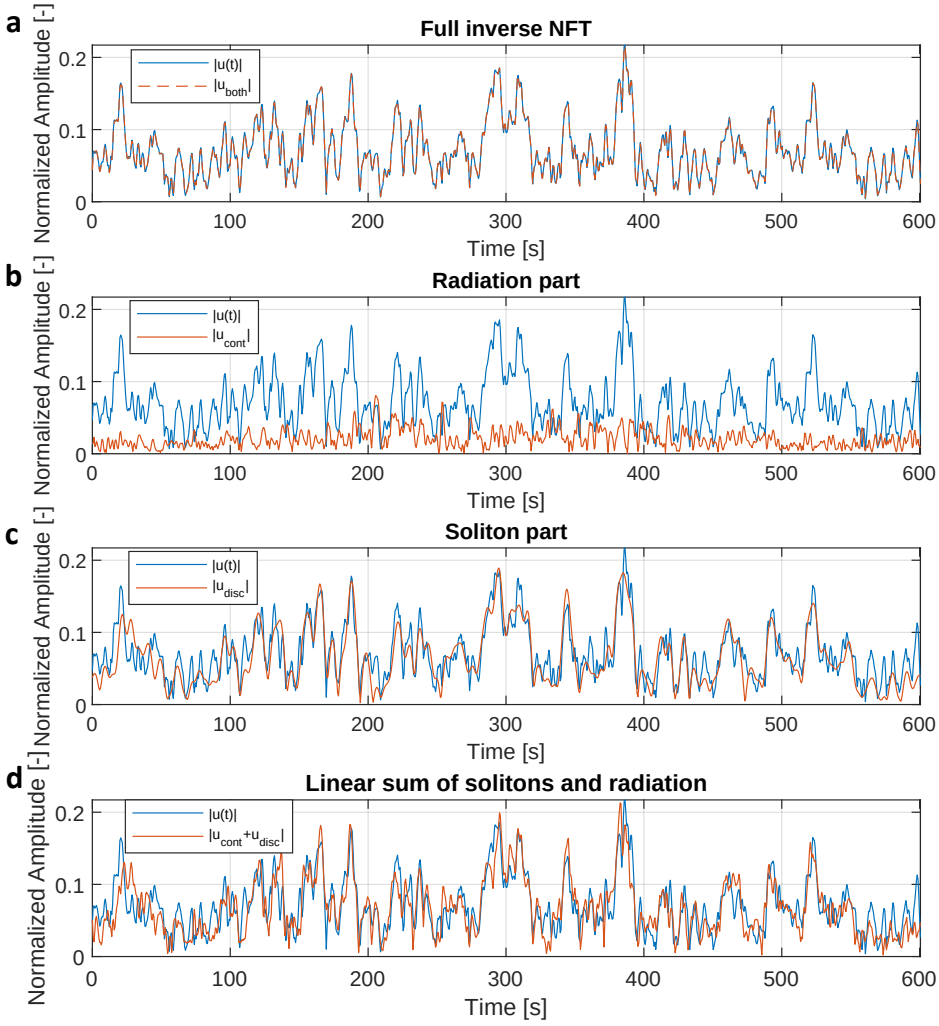


Figure 5.4: Comparison between the initial signal and the complex envelope of nonlinear spectrum recovered from the iNFT. The blue line represents the initial envelope in Figure 5.2. **a**. Time series calculated from the nonlinear sum of radiation spectrum and soliton spectrum based on the inverse nonlinear Fourier transform. **b**. Time series calculated from the radiation spectrum. **c**. Time series calculated from the soliton spectrum. **d**. Time series calculated from the linear sum of time series corresponding to only the radiation spectrum and only soliton spectrum.

Table 5.2 illustrates the occurrence of four classes based on the soliton energy ratio of JONSWAP spectra with different values of peak periods from 5 s to 15 s with an interval of 2 s. The percentage of four classes with radiation wave dominance, equal combination of radiation wave and soliton, soliton dominance and soliton gas-like of all spectra accounts for 7%, 9%, 71%, and 13%, respectively. If we sum up the percentage of spectra with soliton dominance and soliton gas-like, they are up to 84%, which account for a high proportion in our simulation. This high percentage might seem surprising, but similar observations have been made in the area of optical fiber communications, where it was found that "linear" communication signals nevertheless are dominated by solitons [236, 256, 257]. If we consider the spectra from short peak period 5 s to long peak period 15 s, it is found that the percentage of radiation wave dominated spectra is increasing, the percentage of spectra of radiation wave and soliton combination is increasing, and the percentage of spectra of soliton gas is decreasing. This suggests that sea states with soliton dominance and soliton gas-like sea states tend to appear in shorter peak period conditions.

Interestingly, if we compare the soliton energy ratio in Fig. 5.5 to the significant wave height in Fig. 5.1, the spectra with $H_s < 5$m (dark blue dots) in Fig. 5.1 can correspond to any classes according to the soliton energy ratio in Fig. 5.5. This indicates that the total energy does not determine how dominant the soliton energy is in the whole system. However, the spectra with larger significant wave heights (right-up region) are likely related to the conditions with higher ratio of soliton energy. The larger significant wave heights of JONSWAP spectra occur as a result of the shapes of JONSWAP spectra with longer peak period, larger α and larger γ. Our results show that the shapes of JONSWAP spectra actually affect the ratio of soliton energy.

As we mentioned in Section 5.2, our dataset of the simulated JONSWAP sea states differs from realistic sea states. Several studies discuss the selection of JONSWAP parameters based on in situ measurements [258, 259]. If we follow the joint probability of JONSWAP parameters from the sea in the north of Colombia by Rueda-Bayona et al. (2020) [259], the approximate range with higher probability of JONSWAP parameters is located in $\{0 < \alpha < 0.01$ and $0 < \gamma < 3\}$, $\{0 < \alpha < 0.005$ and $3 < \gamma < 6\}$, and $\{0.01 < \alpha < 0.02$ and $0 < \gamma < 2\}$. In Fig. 5.5, these ranges mostly belong to the classes of radiation wave dominance and radiation wave and soliton combination.

5.6. JONSWAP SPECTRAL CHARACTERISTICS OF THE SOLITON GAS-LIKE SEA STATES

We now focus on the soliton gas-like case ($90\% \leq E_{\text{sol_ratio}}$). In our simulation, the soliton gas-like sea states account for 13% of the 9180 spectra in total. The number of soliton gas-like spectra from the peak period of 5 s to 15 s is 677, 337, 142, 30, 6, and 1, respectively. The distribution of the JONSWAP parameters for soliton gas-like sea states is shown in Figure 5.7. As you can see in Fig. 5.7a, the soliton gas-like sea states occur in the range of α from 0.01 to 0.03. It can be seen that increasing

Table 5.2: **Four classes of sea states**

Class	$T_p = 5s$	$T_p = 7s$	$T_p = 9s$	$T_p = 11s$	$T_p = 13s$	$T_p = 15s$	Total
Radiation wave dominance	3%	4%	6%	8%	10%	12%	7%
Radiation wave and soliton combination	4%	6%	8%	10%	12%	13%	9%
Soliton dominance	49%	67%	77%	80%	78%	75%	71%
Soliton gas-like	44%	22%	9%	2%	0%	0%	13%

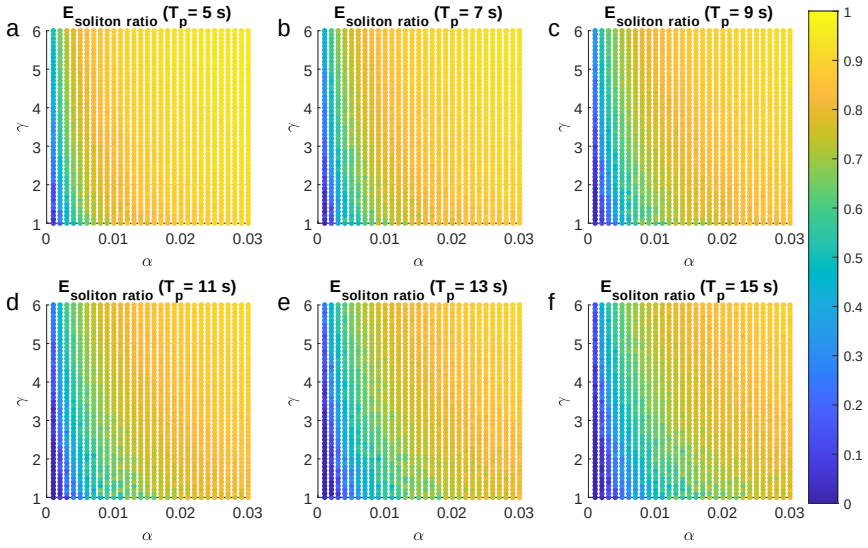


Figure 5.5: Scatter plots of soliton energy ratio over α and γ calculated from simulated JONSWAP time series for different ranges of T_p

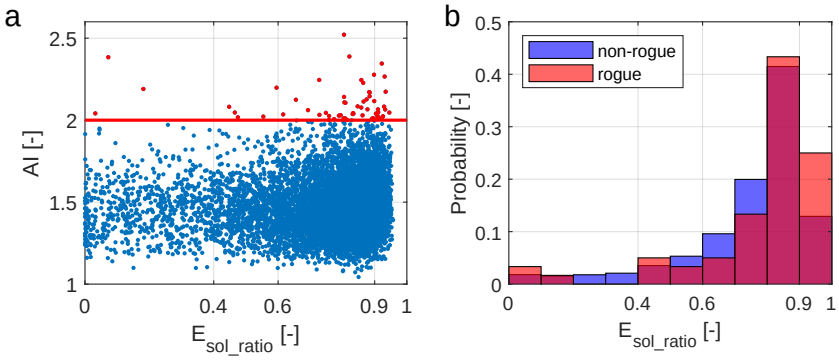


Figure 5.6: Comparison between non-rogue waves and rogue waves. **a**. Scatter plot of soliton energy ratio versus abnormality index (AI). The red line represents the rogue wave threshold, which separates all data into non-rogue waves (blue dots) and rogue waves (red dots). **b**. Histogram of probability density for non-rogue waves (blue bars) and rogue waves (red bars).

α leads to an increase in the number of soliton gas-like spectra. Note that soliton gas-like sea states are never observed when the Phillip's parameter α is less than 0.01. According to the distribution of the peak enhancement parameter γ of soliton gas-like sea states in Fig. 5.7b, the soliton gas-like sea states occur in full range of

γ from 1 to 6. However, the number of soliton gas-like sea states increases with increasing peak enhancement parameter γ. Meanwhile, shorter peak periods have more soliton gas-like sea states, as shown in 5.7c. There are 97% of soliton gas-like sea states with peak period lower than 11 s in our simulation. The above results indicate that a larger α leading to more energy in the system, a larger γ leading to more energy concentration in the peak, and a shorter peak period are related to the soliton gas-like sea states.

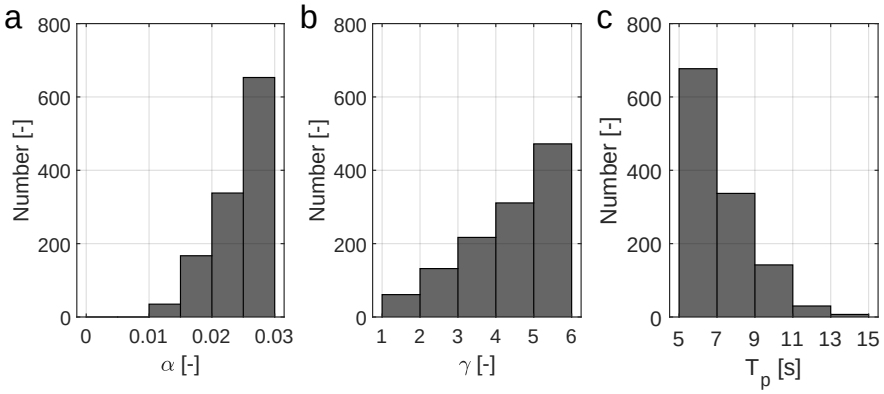


Figure 5.7: Histogram of JONSWAP parameters in soliton gas-like sea states. Distribution of α, γ and T_p is shown in Fig. 5.7**a**, 5.7**b** and 5.7**c**, respectively.

The sea states with appearance of rogue waves

Rogue waves emerging in soliton gases due to collisions of solitons were found in Ref. [254]. Next, we therefore investigate the occurrence of rogue waves with respect to the soliton gas energy ratio. A rogue wave is a wave with a wave height larger than twice the significant wave height $H_{1/3}$. The abnormality index (AI) is defined as the ratio between the maximum wave height $H_{\max}$ and the significant wave height $H_{1/3}$. There are 9810 surface wave time series, which were randomly selected from 10 time series of 9180 JONSWAP spectra. We show the relation between the soliton energy ratio and AI in Fig. 5.6a. The red line is the rogue wave threshold $AI = 2$. The data with $AI > 2$ are considered rogue waves (red dots). The data with $AI \leq 2$ are non-rogue waves (blue dots). There are totally 60 rogue wave data in whole 9180 data set.

We classify these rogue wave data into four types, as shown in Table 5.3. The four classes from radiation wave dominance, radiation wave and soliton combination, soliton dominance to soliton gas-like conditions account for 5%, 8%, 62%, 25% of all rogue-wave spectra, respectively. Clearly, most rogue waves time series (87%) have a high soliton energy ratio (60% or more). If we compare the distribution of the soliton energy ratio for rogue wave data (red bars) with non-rogue wave data (blue

bars), as shown in Fig. 5.6b, we find that the probability of rogue wave is higher than non-rogue wave under soliton gas-like conditions.

Table 5.3: **Classification of the sea states based on the soliton energy ratio**

Class	Non-rogue	Rogue
Radiation wave dominance	7%	5%
Radiation wave and soliton combination	9%	8%
Soliton dominance	71%	62%
Soliton gas-like	13%	25%

5.7. CONCLUSIONS

In this work, we investigated what kind of JONSWAP spectra lead to soliton gases in deep water conditions. We used the nonlinear Fourier transform (NFT) based on the nonlinear Schrödinger (NLS) equation for the analysis of surface waves. We generated 91800 surface wave time series from 9180 JONSWAP spectra for which the Phillip's parameter ranged from 0.001 to 0.03, the peak enhancement parameter γ from 1 to 6, and the peak period T_p with from 5 s to 15 s. Based on the nonlinear Fourier spectra obtained from nonlinear analysis, we found that the majority of data fall into the soliton dominance and soliton gas-like categories. Higher values of α, higher values of γ and shorter peak periods contribute to the occurance of soliton gas-like sea states. We then studied sea states that contained rogue waves. We found that 87% of the rogue waves in our data set exist in sea states with soliton dominance and soliton gas-like conditions. The distribution of the JONSWAP parameters however does not reflect their probability of occurrence for real sea conditions in the field. For future study, it would be interesting to assess how dominant solitons are for realistic JONSWAP parameters.

6

INTERPRETATION OF SOLITON ENERGY RATIOS MEASURED IN DIRECTIONAL WAVE FIELDS

CHAPTER ABSTRACT

Highly nonlinear soliton-dominated sea states in deep water have been explored in previous studies through nonlinear theory and physical experiments. Deep water solitons are known to retain their characteristic properties during evolution within one-dimensional wave fields that are described by the nonlinear Schrödinger (NLS) equation, which is the most important model for their study. However, realistic ocean wave fields are typically multidirectional, a condition that can destabilize solitons and challenge the direct application of NLS-based interpretations. To address this gap, we generate directional JONSWAP wave fields with different directional spreadings that can be directly compared to field measurements to discuss the directional effects on soliton-dominated seas. The soliton energy ratio derived from the nonlinear Fourier spectrum is used as an indicator to assess dominant components of directional sea states. We investigate the relation between the soliton energy ratio obtained from the original time series, where the full directionality is present, to that obtained from the time series with reduced directionality using a directional filtering approach. For small directional spreading without filtering, the soliton energy ratio in the main direction is only slightly lower compared to initial wave fields, as expected. With increasing directional spreading, the soliton energy ratio decreases more significantly in most cases. However, in highly nonlinear soliton-dominated directional sea states, soliton energy is found to be concentrated in the main propagation direction, as the soliton ratio remains large after the directional interference has been removed.

The text in this chapter has previously appeared in "Lee, Yu-Chen and Sander Wahls. "Interpretation of Soliton Energy Ratios Measured in Directional Wave Fields." Applied Ocean Research (Under review). Preprint: [260]. http://dx.doi.org/10.2139/ssrn.5669630

6.1. Introduction

When an ensemble of solitons dominates the dynamics of a nonlinear dispersive system, the resulting statistical state is referred to as a soliton gas, which has gained popularity in theoretical studies [30–33]. Solitons were first mathematically described by the Korteweg–de Vries (KdV) equation [10], which models the evolution of weakly nonlinear and dispersive unidirectional free surface waves in shallow water with a constant depth. For deep water waves, solitons are envelope solitons, which are obtained by the nonlinear Schrödinger (NLS) equation [49, 261]. Envelope solitons are regarded as a fundamental mechanism for unidirectional rogue wave formation in deep water [158]. The NLS equation is a fundamental model for describing the propagation of weakly nonlinear, narrow-banded wave envelopes in deep water with a constant depth in one dimension. The NLS equation can be analytically solved using the Nonlinear Fourier Transform (NFT), also known as the direct scattering transform in the inverse scattering method, which is a powerful technique developed for integrable nonlinear systems [12, 13]. Analogously to the linear Fourier transform, the NFT decomposes complex nonlinear waveforms into simpler components. This decomposition is based on the eigenvalues and eigenfunctions of an associated linear scattering problem, which together define the nonlinear Fourier spectrum.

The nonlinear Fourier spectrum comprises two parts: a continuous spectrum, which corresponds to dispersive radiation waves, and a discrete spectrum, which represents the number and characteristics of solitons. In optical communications, the NFT has shown that supposedly linear signals in nonlinear fiber channels can actually contain solitonic components [256, Fig. 8], [257, 262]. To quantify this solitonic content, we adapt a parameter known as the soliton energy ratio, which measures how closely a given sea state resembles a soliton gas [2, 13]. It can be calculated directly from the nonlinear Fourier spectrum as the ratio of soliton energy to total energy, ranging from zero representing a purely radiation wave dominated state to one indicating a system fully dominated by solitons. Unfortunately, it can be difficult to interpret the soliton energy ratio in practice when dealing with more complex sea states, particularly those with directionality. The one-dimensional NLS equation assumes unidirectional wave propagation, so directional spreading violates the assumptions of the NLS model, causing the nonlinearity to become defocusing in the lateral direction [263]. As a result, solitons become transversely unstable when evolving in multidimensional wave fields. Other factors such as wind forcing and wave breaking can also contribute to unstable solitons [264–268], but these effects are not studied here.

Highly nonlinear sea states dominated by NLS solitons have been successfully generated in controlled wave flume experiments [65, 88]. Under ideal experimental conditions, the collective behavior of soliton ensembles can be characterized statistically. However, the idealized conditions of laboratory experiments cannot be directly compared to the real ocean, primarily due to the presence of directional spreading. The NFT has been used to detect solitons in field measurements of sea states, including those with small directional spreading, such as in Currituck Sound, North Carolina [28], and those with larger directional spreading, such as in the Northeast Pacific Ocean [3] and the Northeast Atlantic Ocean [29]. It remains

uncertain how to properly explain the detected solitons under directional seas, given that the NLS equation assumes unidirectional wave propagation. It is known that solitons usually do not remain stable and reduce their amplitudes during evolution in the presence of strong directional effects. A recent study however has observed that solitons can persist under directional wave fields [215]. It is found that under moderate directional sea states in deep water, solitons can persist continuously for a few tens of wave periods. Under conditions with minimal directional spreading, these solitons can maintain an even longer lifetime.

The gap between idealized theory and real oceanic conditions motivates the present study to further investigate the interpretation of soliton energy ratios calculated from the nonlinear spectrum in directional seas. To better align theoretical assumptions with realistic sea conditions, we focus on waves propagating in the primary direction, thereby constraining directional effects to more closely approximate the validity of the NLS regime. By removing energy outside specific directional ranges, we generate modified wave fields that propagate within a narrower range of directions. These modified wave fields with different spreading scenarios are compared with the original sea states to examine how the soliton energy ratio changes between the initial condition and that in the main direction only. The directional spreading settings in our simulations are designed to be directly comparable to those observed in realistic oceanic sea states.

This chapter is organized as follows. In Sec. 6.2, we review the nonlinear Fourier transform based on the NLS equation. Sec. 6.3 describes how we generate wave fields from directional spectra. The extracted time series are processed with the nonlinear Fourier transform to calculate soliton energy ratios. The statistical relationships between the soliton energy ratio and fundamental wave parameters are presented in Sec. 6.4. The primary findings of this study, examining how truncated directionality influences soliton energy ratio, are detailed in Sec. 6.5. Finally, we present our conclusions in Sec. 6.6.

6.2. METHODS

6.2.1. NONLINEAR SCHRÖDINGER EQUATION FOR DEEP WATER WAVES

The nonlinear dynamics of deep water waves can be described by the nonlinear Schrödinger (NLS) equation [49, 261], where deep water waves are represented by the complex wave envelope $A(x,t) = a(x,t)\exp(i(k_0 x - \omega_0 t))$ related to the carrier frequency ω_0 and the wave number k_0. This expression represents a decomposition of the wave field into a slowly varying envelope and a rapidly oscillating carrier wave. The focusing 1D NLS equation is considered valid for $k_0 h \geq 1.363$, where h is the water depth. When considering one-dimensional spatial deep water wave envelopes propagating in time t, the 1D spatial NLS equation is given by

$$\mathrm{i}\left[A_t + C_g A_x\right] + \mu A_{xx} + \nu |A|^2 A = 0, \tag{6.1}$$

where $C_g = \omega_0/2k_0$ is the group velocity, $\mu = -\omega_0/8k_0^2$ is the coefficient of the second-order dispersion term and $\nu = -\omega_0 k_0^2/2$ is the coefficient of the cubic nonlinear term. The subscripts x and t indicate partial derivatives with respect to

these variables. The coefficients are given here for the case of infinite water depth. These coefficients can be revised when considering finite water depth [62, 177].

Field measurements of surface waves are typically single-point time series measurements, such as those obtained from wave height gauges and buoys. As a result, a temporal NLS equation describing the spatial evolution is required. The transformation from the spatial NLS equation into the temporal NLS equation can be followed in Refs. [63, 269]. By applying the spatial-temporal transformation, the temporal NLS equation in normalized form can be expressed as

$$\mathrm{i}u_X + u_{TT} + 2|u|^2 u = 0. \tag{6.2}$$

where $u(X,T) = \rho A(X,T)$ is the scaled envelope, $\rho = \sqrt{C_g^2 \nu / 2\mu}$ is a nonlinear parameter that converts the physical wave field into the nonlinear domain [6], $X = \mu / C_g^3 x$ is the scaled space and $T = t - x/C_g$ is the scaled time. We note that these transformations lead to the unexpected result that the unit of u is s^{-3}. This is no problem in our case, since their sole purpose is to bring the data into an intermediate computational domain where it can be processed more easily. Nevertheless, in cases where the normalized data is of direct interest, slightly extended transformations that make u dimensionless are available [270]. Formally, the NLS equation describes the evolution of unidirectional deep-water waves over a flat bottom, capturing the effects of both dispersion and nonlinearity. The main assumptions in its derivation beyond unidirectionality are narrow bandwidth and weak nonlinearity.

6.2.2. Nonlinear Fourier Transform for Vanishing Boundary Conditions

The Nonlinear Fourier Transform (NFT) is a useful tool for solving the NLS equation by taking advantage of its integrability [12, 13]. It is based on the Zakharov–Shabat system, a Lax pair formulation linked to the NLS equation [19]. The direct spatial or temporal evolution of complex envelopes governed by the NLS equation can be complicated, but the evolution of nonlinear spectral modes found by the NFT is much simpler [271]. As a result, the NLS equation can be interpreted as governing the evolution of nonlinear spectral modes that propagate effectively in a linear way. Eventually, one can apply the inverse nonlinear Fourier transform (iNFT) to the nonlinear spectrum to obtain the solution after propagation [91, 272].

In this study, we adopt vanishing boundary conditions to simplify NFT computations [12, 91]. The Zakharov-Shabat system underlying this NFT is

$$\Psi_T = Q(\zeta)\Psi, \quad Q = \begin{pmatrix} -\mathrm{i}\zeta & u(X_0,T) \\ -u(X_0,T)^* & \mathrm{i}\zeta \end{pmatrix}, \quad \Psi = \Psi(T;\zeta) \tag{6.3}$$

where ζ is the complex spectral parameter, and * represents complex conjugation. Two pairs of linearly independent Jost functions $\Psi = [\phi \quad \overline{\phi}]$ and $\Psi = [\psi \quad \overline{\psi}]$ are

found by solving Eq. (7.4). The Jost functions are defined by

$$\begin{aligned}\phi(T;\zeta) &= \begin{bmatrix} 0 \\ e^{-i\zeta T} \end{bmatrix} + o(1) \quad \text{as} \quad T \to -\infty, \\ \psi(T;\zeta) &= \begin{bmatrix} e^{i\zeta T} \\ 0 \end{bmatrix} + o(1) \quad \text{as} \quad T \to \infty,\end{aligned} \tag{6.4}$$

The above pairs of functions are related through the scattering coefficients $a(\zeta)$, $b(\zeta)$, $\overline{a}(\zeta)$, $\overline{b}(\zeta)$

$$\begin{aligned}\Phi(T;\zeta) &= a(\zeta)\psi(T;\zeta) + b(\zeta)\overline{\psi}(T;\zeta), \\ \overline{\Phi}(T;\zeta) &= \overline{b}(\zeta)\psi(T;\zeta) + \overline{a}(\zeta)\overline{\psi}(T;\zeta).\end{aligned} \tag{6.5}$$

The scattering coefficients $a(\zeta)$ and $b(\zeta)$ form the basis for constructing the nonlinear spectrum and are sufficient to describe the signal completely. The nonlinear spectrum consists of two parts: the continuous spectrum and the discrete spectrum. The continuous spectrum is formed by the *reflection coefficient*

$$r(\zeta) = b(\zeta)/a(\zeta), \quad \zeta \in \mathbb{R}. \tag{6.6}$$

The discrete spectrum contains the discrete eigenvalues $\{\zeta_k = \xi_k + i\eta_k\}$, $k = 1, ..., N$, where N is the total number of eigenvalues. They are the zeros of the scattering coefficient $a(\zeta)$ with positive imaginary part. The eigenvalues are complemented by the residues [9, 273]

$$r_k = b(\zeta_k)/a'(\zeta_k), \quad \text{where} \quad a'(\zeta) = \partial a(\zeta)/\partial\zeta \tag{6.7}$$

The continuous spectrum represents the radiation components in the time series. These dispersive waves are an integral part of the overall solution, but do not maintain a localized shape. The discrete spectrum consists of a set of isolated eigenvalues, each associated with a soliton. Solitons are stable, localized wave structures that not only retain their shape and speed over time in the absence of interactions, but also recover their initial shape after interactions have taken place. Note that a soliton in the NLS equation is always an envelope soliton [6, 261, 270, 274–276]. For small-amplitude envelopes, the nonlinear Fourier spectrum typically contains only linear components, meaning there are no discrete eigenvalues present in the discrete spectrum [63, 253]. Under unidirectional propagation, typical rogue waves can be represented as a nonlinear superposition of an envelope soliton and background waves [158].

For our study, the NFT is computed by the software library "Fast Nonlinear Fourier Transforms" (FNFT) [191]. Fast NFT can match the accuracy of conventional NFT by using exponential splitting schemes to achieve faster numerical computation [90, 277, 278]. More information about FNFT can be obtained online at https://github.com/FastNFT/FNFT.

6.2.3. CALCULATION OF SOLITON ENERGY RATIO

As mentioned previously, the nonlinear spectrum comprises a discrete spectrum related to the solitons and a continuous spectrum related to dispersive radiation

waves. The total energy of the time series is calculated by integrating the absolute value of the signal squared over time. It equals the sum of the energy in the solitons and the dispersive radiation waves [2, 13]:

$$E_{\text{total}} = \int_{-\infty}^{\infty} |u(t)|^2 \, dt = E_{\text{sol}} + E_{\text{rad}}, \tag{6.8}$$

where the soliton energy is calculated based on the imaginary parts of discrete eigenvalues,

$$E_{\text{sol}} = 4 \sum_{k=1}^{N} \text{Im}\,(\zeta_k), \tag{6.9}$$

and the radiation wave energy is calculated based on the reflection coefficient

$$E_{\text{rad}} = 4 \int_{-\infty}^{\infty} \log(1 + |r(\zeta)|^2). \tag{6.10}$$

The above formulas allow us to define the soliton energy ratio as

$$E_{\text{sol_ratio}} = E_{\text{sol}} / E_{\text{total}} = (E_{\text{total}} - E_{\text{rad}}) / E_{\text{total}}. \tag{6.11}$$

where $E_{\text{sol_ratio}}$ ranges from zero to one. If the soliton energy ratio is high, the solitons are the dominant components in the system. We use the formula that utilizes the radiation energy to compute the energy ratio because it is easier to compute the continuous spectrum numerically.

6.3. Simulation Setup for Directional Wave Fields

The directional wave fields are generated from two-dimensional directional spectra with random phases. The directional spectrum $S(f,\theta)$ is a product of a frequency spectrum $S(f)$ and a directional spreading function $D(\theta)$:

$$S(f,\theta) = S(f) D(\theta), \tag{6.12}$$

where f is the frequency and θ is the wave direction. We adopt a Gaussian distribution, which is commonly used to model directional seas [279–282]. The function is expressed as

$$D(\theta) = \frac{1}{\sqrt{2\pi}\,\sigma_\theta} \exp\left(-\frac{(\theta - \theta_p)^2}{2\sigma_\theta^2} \right) \quad \text{with } \theta \in [0, 2\pi) \tag{6.13}$$

where θ represents the direction, θ_p is the peak direction, and σ_θ is the amount of spreading (standard deviation). The directional spreading function $D(\theta)$ is defined over the range from 0 to 2π, and its integral is nearly 1 because some energy is truncated in the Gaussian tails when the spreading is large. This function describes how the wave energy is distributed around a central peak direction, with a narrow width indicating more directional focus and a broader width representing a wider spread of energy. There are no opposite directional components propagating

backward against the central peak direction. Other forms of directional spreading functions can be found in [283].

The frequency spectrum is based on the JONSWAP (Joint North Sea Wave Project) spectrum [195], which extends the Pierson–Moskowitz spectrum by introducing a peak enhancement parameter γ to account for the enhancement of wave energy around the spectral peak. The JONSWAP spectrum is widely used for representing wind-generated sea states and is defined as

$$S(f) = \alpha g^2 (2\pi)^{-4} f^{-5} \exp\left[-\frac{5}{4}\left(\frac{f_p}{f}\right)^4\right] \gamma^{\exp\left[-\frac{(f-f_p)^2}{2\sigma^2 f_p^2}\right]}, \tag{6.14}$$

where $S(f)$ is the spectral energy density as a function of frequency f, α is the Phillips constant, g is the acceleration due to gravity, f_p is the peak frequency, γ is the peak enhancement factor, and σ is the spectral width parameter. The Phillips constant α governs the overall energy level of the wave spectrum reflecting the influence of wind energy input. The peak enhancement parameter γ adjusts the sharpness of the spectral peak and is used to characterize the developmental stage of sea states. The parameter σ is defined piecewise to reflect the asymmetry of the spectral shape around the peak frequency: $\sigma = \begin{cases} 0.07, & f \le f_p \\ 0.09, & f > f_p \end{cases}$. We initially consider frequency spectra with Phillips constant values $\alpha = 0.0025, 0.005, 0.0075, 0.01, 0.02, 0.03$ and peak enhancement parameters $\gamma = 1, 2, 3, 4, 5, 6$. This setup is later used to construct the wave fields. These initial parameters have been chosen such that some extreme cases are included. Recall that the NLS equation assumes narrow bandwidth ($\Delta f / f_0 \ll 1$) and weak nonlinearity ($k_0 H_s \ll 1$). Table 6.1 presents the relative bandwidths of the considered JONSWAP spectra. From Fig. 8 in [274], we expect that the narrow bandwidth condition is sufficiently well satisfied for $\Delta f / f_0 \lesssim 0.25$. This is the case in all cases except $\gamma = 1$, where we only have $\Delta f / f_0 = 0.5762$. We will therefore later completely exclude the case $\gamma = 1$. Table 6.2 presents the values of the nonlinearity parameter $k_0 H_s$. Experiments and simulations have shown that solitons can exist for $k_0 A_0 \lesssim 0.3$ [274], where A_0 is the soliton amplitude. Most, but not all of the considered JONSWAP spectra fulfill this condition. The cases with $\alpha = 0.02$, $\gamma \ge 4$ and $\alpha = 0.03$, $\gamma \ge 2$ will therefore later be additionally excluded as well.

Table 6.1: Relative bandwidth of various JONSWAP spectra. The influence of α and T_p on the results is minimal. Δ_f denotes the 3dB bandwidth.

γ	1	2	3	4	5	6
Δ_f / f_0	0.5762	0.2674	0.2001	0.1740	0.1595	0.1500

In Appendix 6.7, we furthermore show that the peak frequency in the JONSWAP spectrum can be normalized to one without changing the soliton energy ratio – if time and frequency grids are rescaled. Here, we however always consider the same grids to mimick the situation in real-word buoy measurements, where the length of the recording is fixed and in particular independent of the peak period. We will

Table 6.2: The nonlinearity parameter $k_0 H_s$ for various JONSWAP spectra. The influence of T_p on the values is minimal.

$\alpha \backslash \gamma$	1	2	3	4	5	6
0.0025	0.0895	0.0999	0.1082	0.1155	0.1220	0.1279
0.0050	0.1265	0.1412	0.1530	0.1633	0.1725	0.1809
0.0075	0.1550	0.1729	0.1874	0.2000	0.2113	0.2216
0.0100	0.1789	0.1997	0.2164	0.2309	0.2439	0.2559
0.0200	0.2530	0.2824	0.3061	0.3266	0.3450	0.3619
0.0300	0.3099	0.3459	0.3749	0.4000	0.4225	0.4432

observe later that this lets the estimated soliton energy ratios decrease slightly with the peak period.

To reconstruct a realistic sea surface elevation from a given directional wave spectrum, the surface can be modeled as a linear superposition of oscillations [281, 283–285]. Specifically, it is represented as a superposition of infinitely many simple cosine waves, each with varying amplitude, frequency, phase, and propagation direction. The sea surface elevation $\eta(x, y, t)$ at a spatial location (x, y) and time t is then given by

$$\eta(x,y,t) = \sum_{i=1}^{N_f} \sum_{j=1}^{N_\theta} \sqrt{2S(f_i,\theta_j)\Delta f \Delta\theta}\cos\left(k_i(x\cos\theta_j + y\sin\theta_j) - 2\pi f_i t + \phi_{ij}\right), \tag{6.15}$$

where N_f and N_θ are the total number of discrete frequency and direction bins, respectively. The term Δf is the frequency increment, and $\Delta\theta$ is the directional increment. The wave number k_i corresponding to frequency f_i is calculated using the deep water dispersion relation. ϕ_{ij} represents a random phase uniformly distributed in the interval $[0, 2\pi]$. This allows us to generate multidirectional wave fields by linearly combining unidirectional wave systems propagating along a discrete set of directions. The directional spreading function determines how wave energy is spread across these directions.

In this study, we consider directional spreadings σ_θ of 10, 20, 30, 40, 50, 60, 70, and 80 degrees, which can be shown from Fig. 6.1 (c). When the spreading is narrow, most of the wave energy is concentrated in a single direction, resulting in long-crested waves. In contrast, wide spreading distributes the energy over many directions, leading to short-crested waves that appear more irregular. We summarize our setup of frequency and directional parameters used to construct the directional spectrum in Table 6.3. Previous studies have shown that higher values of α and γ can lead to soliton-dominated sea states for deep water waves [2]. We will classify the data by soliton energy ratio to further discuss sea states with different nonlinearity. This will be illustrated in a later section.

Fig. 6.2 shows typical wave fields generated with different directional spreading angles. The initial setting of the frequency spectrum is considered with $\alpha = 0.01$, $\gamma = 1.0$ and $T_p = 10$ s in this example. A single wave gauge is placed at $x = 0$, $y = 0$ to measure the time series. The time series is recorded for 600 seconds with a sampling

rate of 1.7 Hz. It can be observed that the wave fields change from long-crested seas at 10 degrees (Fig. 6.2(a)) to short-crested seas at 80 degrees (Fig. 6.2(b)) as the directional spreading increases.

Using the basic wave parameters of the directional spectrum summarized in Table 6.3, we generate various wave fields with random phases. Time series are extracted using a virtual wave gauge positioned at the center of each wave field. In total, 2,880 time series are included in our dataset. The significant wave height in this dataset ranges from 1 m to 19 m. The distribution of significant wave height for each peak period is illustrated using boxplots in Fig. 6.3 (a). It can be observed that in general larger peak periods are associated with higher significant wave heights in our simulations. We are also interested in the distribution of wave steepness, where the wave steepness is calculated as Steepness $= 2\pi H_s / g T_p^2$, with H_s representing the significant wave height, calculated as four times the square root of the zeroth moment, and T_p the peak period. The distribution of wave steepness for each peak period is shown in Fig. 6.3 (b). For each peak period, the wave steepness follows the same distribution ranging from 0.016 to 0.049. (We use identical values of α and γ within each group, which results in the same distribution of wave steepness [286].) This figure provides a basic overview of our dataset.

Table 6.3: Parameter setup used to construct the directional wave spectra.

Parameter	**Values**
Peak period T_p	4, 5, 6, 7, 8, 9, 10, 11, 12, 13
Phillips constant α	0.0025, 0.005, 0.0075, 0.01, 0.02*
Peak enhancement factor γ	2*, 3*, 4*, 5*, 6*
Directional spreading σ_θ	10°, 20°, 30°, 40°, 50°, 60°, 70°, 80°

*Data corresponding to $(\alpha, \gamma) = (0.02, \gamma \geq 4)$ were excluded from the simulation.

6.4. CHARACTERISTICS OF THE SOLITON ENERGY RATIO

Before applying the nonlinear Fourier transform based on the NLS equation to all time series, we first provide an examplary analysis of a single time series to reveal its nonlinear spectrum. The time series analyzed here is extracted from the wave field with parameters $\alpha = 0.03$, $\gamma = 6.0$ and $T_p = 6$ s, as shown by the black line in Fig. 7.2 (a). The blue line shows the magnitude of the complex envelope, which is calculated from the surface wave elevation using the Hilbert transform [60]. Note that while only the magnitude is shown here, the NFT requires the full complex envelope, including both magnitude and phase information. The envelope time series is used as input for nonlinear Fourier analysis. By the nonlinear Fourier transform based on the NLS equation, we obtain the nonlinear spectrum including continuous spectrum (Fig. 7.2 (b)) and soliton spectrum Fig. 7.2 (c). The continuous spectrum displays the spectral parameter ζ on the x-axis and the absolute value of the reflection coefficient $r(\zeta)$ on the y-axis, representing components of linear dispersive waves. In the soliton spectrum, the real part of the eigenvalue on the x-axis indicates soliton

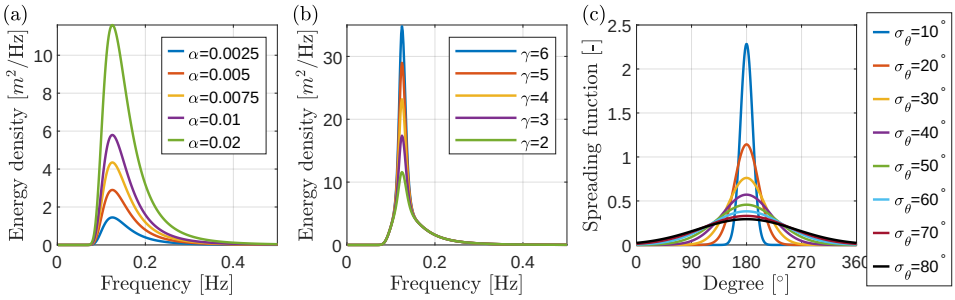


Figure 6.1: Representative input components used to construct the two-dimensional wave spectrum. (a) Frequency spectrum corresponding to the Phillips constant α, (b) frequency spectrum associated with the peak enhancement parameter γ, and (c) directional spreading function based on the directional spreading parameter σ_θ.

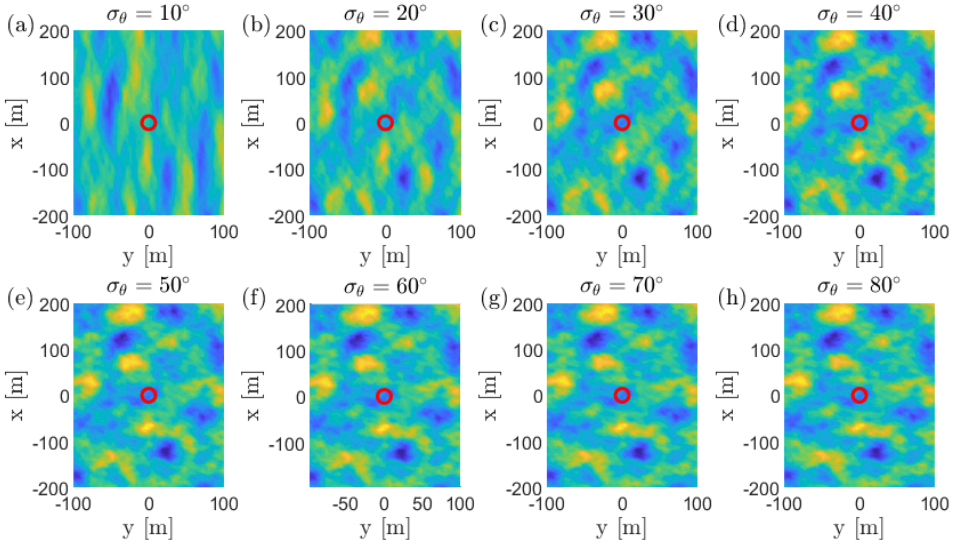


Figure 6.2: Directional wave fields with spreading σ_θ varying from (a) 10° to (h) 80°. The wave gauge location at $(x, y) = (0, 0)$ is indicated by a red circle.

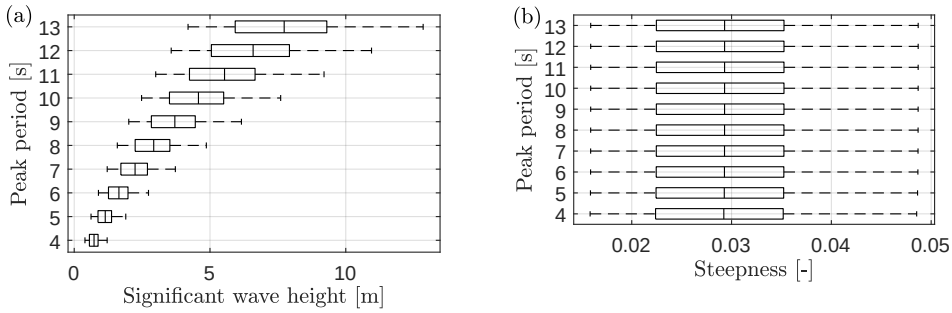


Figure 6.3: Basic wave parameters of the dataset. (a) Boxplot of significant wave height versus peak period. (b) Boxplot of wave steepness versus peak period.

velocity, while the imaginary part on the y-axis represents soliton amplitude. A total of 77 solitons are identified, with most exhibiting small amplitudes. It has been found that a dense ensemble of solitons can give rise to large wave events in the time series through strong nonlinear interactions [254]. Meanwhile, it is important to note that the solitons of the NLS equation here are envelope solitons [6, 261, 270, 274–276]. From the nonlinear spectrum, we calculate the energy of the continuous spectrum and the soliton spectrum using Eq. (7.13) and Eq (6.9), respectively. The soliton energy ratio is then obtained using Eq. (7.15). In this example, the soliton energy ratio is 0.93, indicating a highly soliton-dominated sea state.

We apply nonlinear Fourier analysis to our dataset and calculate the soliton energy ratios. The results showing the soliton energy ratio across all parameters are presented as a set of boxplots in Fig. 6.5. The soliton energy ratio is shown on the horizontal axis, while the vertical axes in subplots (a) to (f) correspond to Phillips constant α, peak enhancement parameter γ, directional spreading σ_θ, significant wave height H_s, peak period T_p, and wave steepness, respectively. In Fig. 6.5 (a) and (b), it can be observed that both α and γ increase with higher soliton energy ratios. This indicates that more energy in the system and a sharper spectral peak may be associated with the presence of more solitons. In Fig. 6.5(c), it can be seen that different directional spreadings do not influence the soliton energy ratio. In reality, directional spreading should destabilize solitons. However, because our measurement relies on a single-point wave gauge within the wave field, it cannot capture the directional characteristics from the recorded time series. We will investigate this further in the next section by truncating the energy in the directional sidebands to assess how spreading affects the soliton energy ratio. In Fig.6.5(d), significant wave height does not exhibit a clear correlation with the soliton energy ratio, suggesting that soliton presence is not directly dependent on wave height alone. Nevertheless, Fig.6.5(e) indicates a slight tendency for higher soliton energy ratio to be associated with shorter peak period. This trend is attributed to the use of a fixed recording window of ten minutes. As T_p increases, the average duration

of the solitons increases as well, and they are more likely cut off at the boundaries of the recording window. This leads the NFT to overestimate the radiation content in the time series. Consequently, the soliton energy ratio decreases with T_p. More notably, Fig. 6.5(f) reveals a strong positive correlation between soliton energy ratio and wave steepness, implying that steeper wave conditions are more favorable for soliton existence.

Overall, these figures provide a fundamental understanding of the conditions when the soliton energy ratio based on a single buoy measurement is high. However, because of the unaccounted for directionality of the underlying wave field, the detected solitons might not have a clear physical interpretation. To address this issue, we now study how the soliton energy ratio changes when only the main propagation direction is considered. In the absence of directional interference, the detected solitons can remain more stable as the filtered time series evolves nearly unidirectionally.

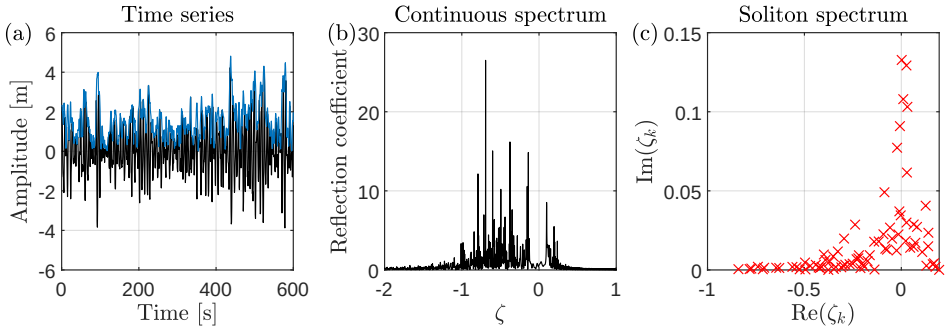


Figure 6.4: Example of the nonlinear Fourier transform to time series. (a) Time series (black line) and the magnitude of its complex envelope (blue line). (b) Continuous spectrum. (c) Soliton spectrum.

6.5. Influence of retention angle after directional truncation

Regarding our objective to investigate when soliton energy ratios calculated in directional seas will remain stable, we address this by removing the energy that is not on principal wave directions to generate modified wave fields with minimal directional interference. Before starting directional truncation on directional wave fields, we emphasize that this study does not account for wave evolution. We consider four retention angles $\Delta\theta$ for directional truncation analysis in the directional domain: 20°, 40°, 60°, and 120°. For each scenario, wave energy outside the specified angular range is removed from the directional spectrum, preserving only the energy within the defined range for subsequent analysis. The retention angles $\Delta\theta$ correspond to varying levels of directional energy removal. Smaller values of $\Delta\theta$ indicate greater truncation of energy in the directional sidebands, while larger

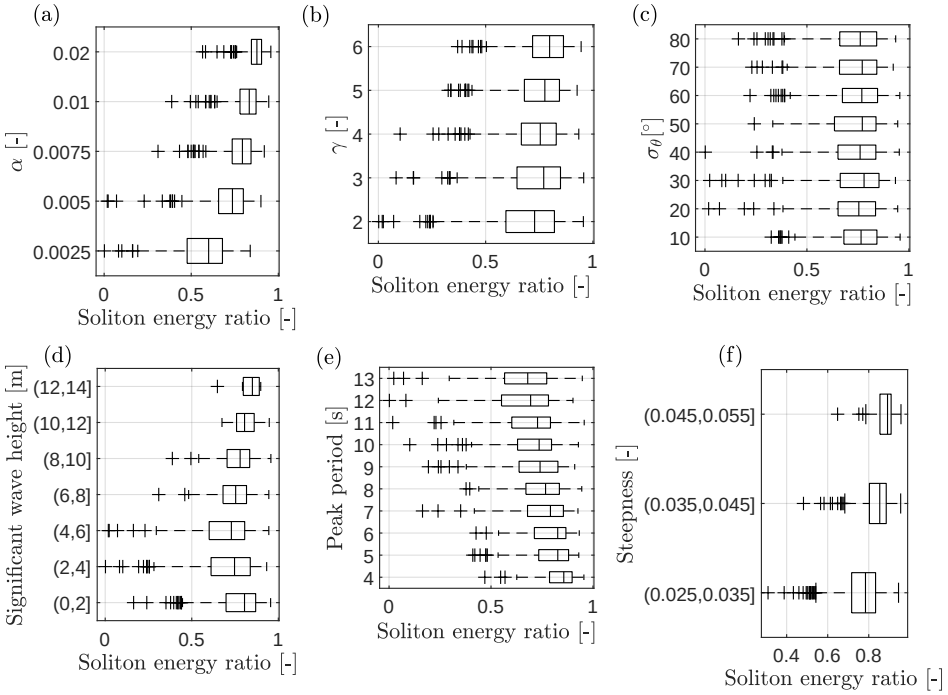


Figure 6.5: Boxplots of soliton energy ratio versus key wave parameters: (a) Phillips constant α, (b) peak enhancement factor γ, (c) directional spreading σ_θ, (d) significant wave height, (e) peak period, (f) steepness.

values retain a broader range of energy in the principal wave directions. The case $\Delta\theta = 360°$ represents the initial wave field, where no directional energy is removed. While ultimately only small retention angles are of interest, we also consider larger cases to see how the soliton energy ratio depends on this parameter. During the reconstruction stage, following the removal of energy in the sidebands, the modified wave fields are linearly synthesized using the original phase information.

In Fig 6.6, we show an example of how to generate modified wave fields with retention angles and the corresponding time series. First, we consider a directional spectrum with spreading set to $\sigma_\theta = 30°$, as shown in Fig 6.6 (a), which is generated by multiplying a directional spreading function with a JONSWAP spectrum using parameters $\alpha = 0.03$, $\gamma = 3$, and $T_p = 8$ s. The wave field is generated with random phases including a virtual wave gauge located at the center of the wave field (red circle), as shown in Fig. 6.6(b). The time series is extracted, as shown in Fig. 6.6(c).

Subsequently, we truncate specific directional ranges to construct wave fields with more concentrated directional characteristics. The retention angles are set as $\Delta\theta = 120°$, $60°$, $40°$, and $20°$, corresponding to Fig. 6.6 (d) to (f), (g) to (i), (j) to (l) and (m) to (o), respectively. In Fig. 6.6 (d), the energy outside the retention angle $\Delta\theta = 120°$ (red lines) is filtered out. Using the original phases, we then generate the wave fields corresponding to the truncated spectra, as shown in Fig. 6.6 (e). The time series data are subsequently re-extracted using virtual wave gauges, with the red line in Fig. 6.6 (f). It can be observed that the time series loses some energy after directional truncation, resulting in slightly smaller wave crests and troughs compared to the initial time series (black line). Meanwhile, with smaller retention angles, more energy is filtered out from the spectrum, causing the wave field to become more long-crested, as seen in Fig. 6.6 (n). The wave height in the time series also decreases as more energy is removed, as seen in Fig. 6.6 (o).

After obtaining the time series via directional spectrum truncation, we applied the NFT based on the NLS equation to derive the nonlinear spectrum and subsequently calculate the soliton energy ratio. The soliton energy ratio of the initial time series is 0.847. For retention angles of $\Delta\theta = 120°$, $60°$, $40°$, and $20°$, the corresponding soliton energy ratios are 0.836, 0.808, 0.796, and 0.726, respectively. Although the soliton energy ratio decreases as wave energy in the directional sidebands is removed, the values remain sufficiently high to be classified as soliton-dominated wave fields. It is worth noting that the directional spreading used in this case, $\sigma_\theta = 30°$, is comparable to the dominant spreading conditions observed in the North Sea [287, 288]. This possibly suggests that if soliton-dominated wave conditions are observed in directional seas, surface waves propagating within a narrow range of the primary direction would be dominated by solitons in the absence of directional interference. The current case is only one example and all simulation results will be presented in the following to support this finding.

To better understand soliton characteristics in the nonlinear spectrum, we classify all wave fields based on the soliton energy ratio into three categories: general cases, soliton-dominated cases, and highly nonlinear soliton-dominated cases. The classification thresholds are defined as follows. Cases with a soliton energy ratio below 60% are categorized as general cases, where the wave field is dominated by

radiation waves or exhibits a near-equal contribution from both radiation waves and solitons. Cases with a soliton energy ratio between 60% and 90% are classified as soliton-dominated. Finally, cases with a soliton energy ratio exceeding 90% are considered highly nonlinear soliton-dominated conditions.

Based on the above classification, we first focus on the general cases ($E_{\text{sol_ratio}} < 60\%$), which correspond to sea states dominated by radiation waves or exhibiting a near-equal contribution from radiation waves and solitons. A total of 285 time series are identified in this category. The soliton energy ratios for the initial time series and those obtained after directional truncation under different directional spreading conditions are shown in Fig. 6.7. There are eight directional spreading conditions, ranging from 10° to 80°, corresponding to subfigures (a) through (h), respectively. Each gray line represents one time series, showing the soliton energy ratio and its variation with the retention angle $\Delta\theta$. We first focus on the case with small directional spreading, $\sigma_\theta = 10°$, shown in Fig. 6.7(a). It can be seen that a large portion of the soliton energy ratios decrease as the retention angle $\Delta\theta$ becomes smaller. However, in some cases, the soliton energy ratio may increase with a smaller $\Delta\theta$, possibly because the truncated energy in the sidebands is more dominated by radiation waves in those cases. Thus, the removal of radiation wave energy leads to an increased soliton energy ratio. The red line represents the mean soliton energy ratio for all cases in this classification. The mean soliton energy ratios of initial wave fields are around 0.472, which indicates the dataset is nearly equally dominated by radiation waves and solitons. As directional spreading σ_θ increases, the mean soliton energy ratio decreases more significantly when the retention angle $\Delta\theta$ becomes small. For the small directional spreading, $\sigma_\theta = 10°$, shown in Fig. 6.7(a), the mean soliton energy ratio does not decrease significantly. It only decreases slightly under a small retention angle of $\Delta\theta = 20°$. For moderate directional spreading $\sigma_\theta = 40°$, as shown in Fig. 6.7(d), the mean soliton energy ratio under $\Delta\theta = 20°$ decreases to 0.127, indicating that only a small portion of solitons still exist, while the remaining energy is mainly dominated by radiation waves. For the largest directional spreading $\sigma_\theta = 80°$, shown in Fig.6.7(h), the mean soliton energy ratio under $\Delta\theta = 20°$ drops to 0.055 at $\Delta\theta = 20°$, indicating that the energy in the main direction with narrow directional bands is identified as high radiation waves dominance.

We subsequently examine the results for analysis of soliton dominated cases ($60\% \leq E_{\text{sol_ratio}} < 90\%$), as shown in Fig. 6.8. There are a total of 1378 time series identified in this class. The mean soliton energy ratios of initial wave fields are around 0.774. A similar trend of decreasing soliton energy ratios as the retention angle $\Delta\theta$ becomes smaller can be observed. The initial mean soliton energy ratio reduces to 0.702 with a retention angle of $\Delta\theta = 20°$ for small directional spreading $\sigma_\theta = 10°$, to 0.416 for moderate directional spreading $\sigma_\theta = 40°$ and to 0.253 for large directional spreading $\sigma_\theta = 80°$. This indicates that in soliton dominated seas with small spreading, the soliton energy ratio in general decreases less, while for moderate and large spreading, it decreases more.

Finally, we focus on the results of the analysis for highly nonlinear soliton-dominated cases ($E_{\text{sol_ratio}} \geq 90\%$), as shown in Fig. 6.9. A total of 97 time series have been identified in this classification. The mean soliton energy ratio of the

initial wave fields is approximately 0.917. For small directional spreading $\sigma_\theta = 10°$, the mean soliton energy ratio remains nearly unchanged under a retention angle of $\Delta\theta = 20°$. For moderate directional spreading $\sigma_\theta = 10°$, the mean soliton energy ratio decreases slightly to 0.686 under $\Delta\theta = 20°$. For large directional spreading $\sigma_\theta = 80°$, although the mean soliton energy ratio decreases under small retention angles, its value equals to 0.525, which corresponds to being nearly equally dominated by solitons and radiation waves. Overall, the analysis of soliton energy ratios under varying directional spreading and retention angles reveals similar trends across different classifications of sea states. The overall results of the mean soliton energy ratios for the three classifications are shown in Table 6.4. This information helps estimate the significance of the solitons detected by the system in relation to the current directional spreading, providing insight for applying this approach to other datasets.

6.6. Discussion and Conclusions

Here, we investigated by how much soliton energy ratios from directional seas reduce when directional interference outside the main direction is filtered out. Here, soliton energy ratio is a parameter used to quantify the nonlinearity of a sea state [2, 13]. We generate directional wave fields under linear superposition of sine waves based on the JONSWAP spectrum with varying directional spreading parameters that are directly comparable to field measurements. The evolution of wave fields is not considered in this study. By removing energy outside specific directional ranges, the modified wave fields retain energy only within a targeted range of directional bands, resulting in reduced directional interference. Time series extracted from virtual wave gauges placed at the center of the wave fields are analyzed using the nonlinear Fourier transform to calculate the soliton energy ratio.

Solitons have been found to persist in small to moderate directional sea states over a number of wave periods [215]. Building on this, our results further examine highly nonlinear soliton-dominated wave fields under various directional spreading scenarios to interpret soliton energy ratios in directional wave fields. It is observed that for small directional spreading (e.g., $\sigma_\theta = 10°$), the soliton energy ratio only slightly decreases compared to the initial value under a narrow propagating direction ($\Delta\theta = 20°$) in the main directions. For a broad propagation direction ($\Delta\theta = 120°$), directional filtering may not remove energy from the directional sidebands, causing the soliton energy ratio to remain constant. In contrast, under large directional spreading (e.g., $\sigma_\theta = 80°$), the soliton energy ratio decreases significantly. This indicates that portions of the initially detected solitons cannot retain their energy due to spreading effects. It should be noted that the variation in soliton energy ratio is highly case-dependent and is mainly influenced by the phase structure of the directional wave fields.

Meanwhile, different initial soliton energy ratios can lead to varying degrees of change. For our wave fields characterized by radiation wave-dominated or mixed sea states ($E_{\text{sol_ratio}} < 60\%$), the mean soliton energy ratio decreases slightly under small directional spreading (e.g., $\sigma_\theta = 10°$), but drops significantly under large spreading

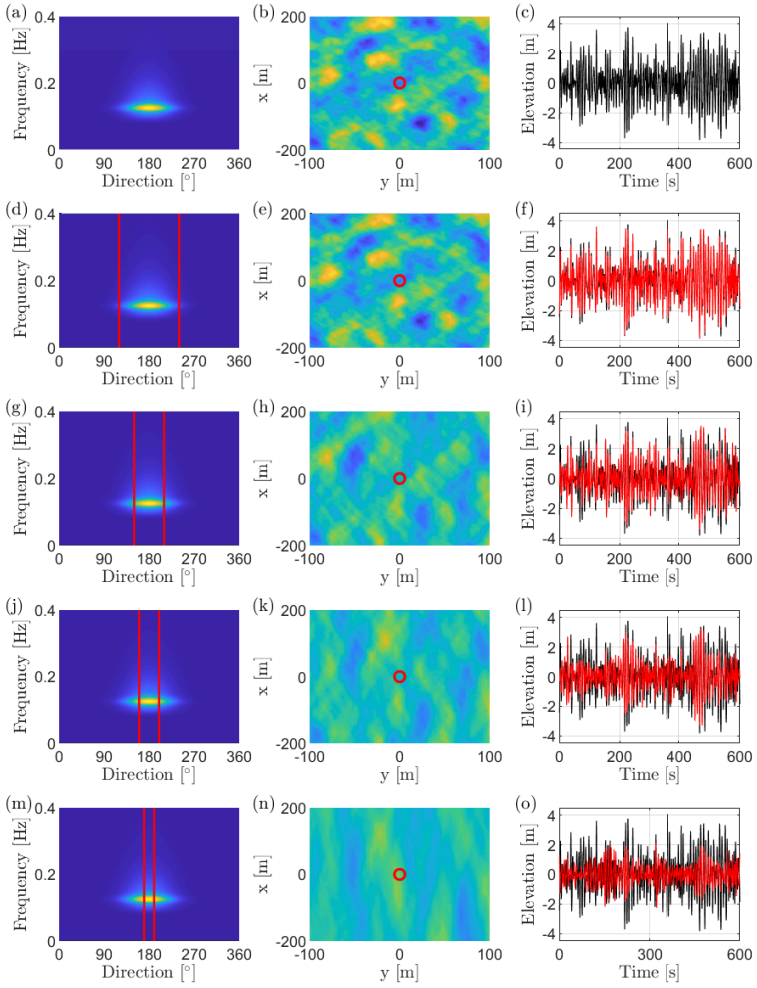


Figure 6.6: Directional spectrum truncation and the resulting wave field and time series. The directional spreading is set to $\sigma_\theta = 30°$, and the JONSWAP spectrum is generated with parameters $\alpha = 0.03$, $\gamma = 3$, and $T_p = 8$ s. Retention angles after directional truncation $\Delta\theta = 120°$ (in (e)-(h)), 60° (in (i)-(l)), 40° (in (m)-(p)), and 20° (in (q)-(t)) are considered. The resulting wave fields are reconstructed from the truncated directional spectra, and time series are extracted using a virtual wave gauge located at the center of the computational domain, as labeled by the red circle.

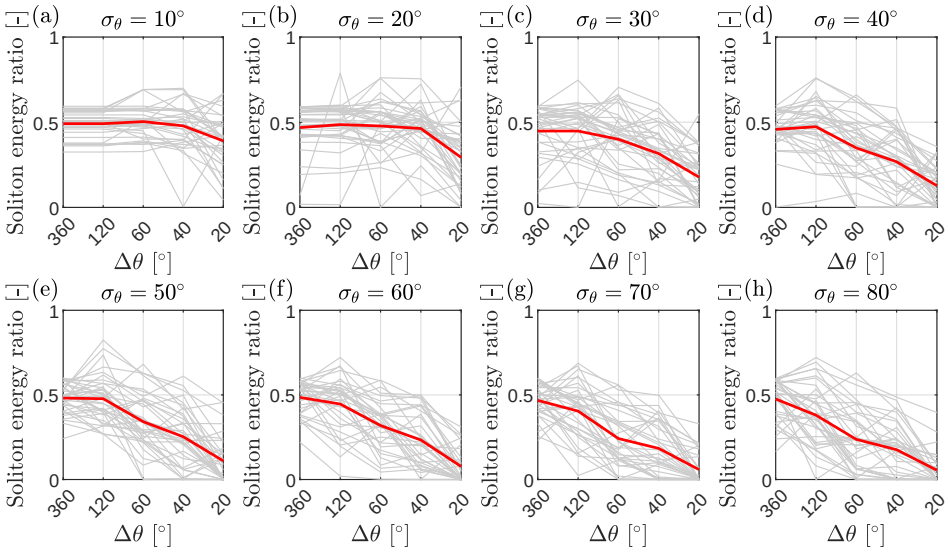


Figure 6.7: Effect of directional truncation on the soliton energy ratio for **general cases** ($E_{\text{sol_ratio}} < 60\%$) with directional spreadings from 10° to 80°. The red line is the mean soliton energy ratio for each retention angle.

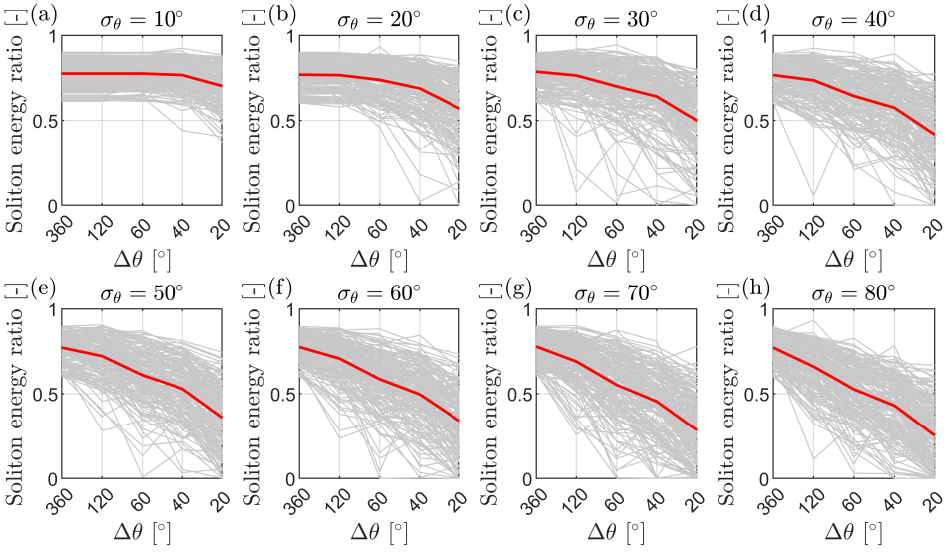


Figure 6.8: Effect of directional truncation on the soliton energy ratio for **soliton-dominated cases** ($60\% \leq E_{\text{sol_ratio}} < 90\%$) with directional spreadings from 10° to 80°. The red line is the mean soliton energy ratio for each retention angle.

Table 6.4: Mean soliton energy ratio for different directional spreadings and retention angles

General sea states ($E_{sol_ratio} < 60\%$)					
σ_θ	Initial	$\Delta\theta = 120°$	$\Delta\theta = 60°$	$\Delta\theta = 40°$	$\Delta\theta = 20°$
10°	0.492	0.492	0.504	0.479	0.391
20°	0.469	0.486	0.478	0.463	0.293
30°	0.448	0.448	0.400	0.316	0.178
40°	0.458	0.474	0.349	0.268	0.127
50°	0.481	0.478	0.342	0.253	0.110
60°	0.485	0.446	0.319	0.234	0.077
70°	0.468	0.404	0.242	0.184	0.059
80°	0.476	0.380	0.237	0.176	0.055
Soliton-dominated sea states ($60\% \leq E_{sol_ratio} < 90\%$)					
σ_θ	Initial	$\Delta\theta = 120°$	$\Delta\theta = 60°$	$\Delta\theta = 40°$	$\Delta\theta = 20°$
10°	0.775	0.775	0.775	0.767	0.702
20°	0.769	0.766	0.738	0.688	0.570
30°	0.786	0.764	0.700	0.641	0.499
40°	0.766	0.736	0.643	0.575	0.416
50°	0.772	0.722	0.609	0.529	0.359
60°	0.775	0.707	0.586	0.497	0.339
70°	0.778	0.690	0.552	0.455	0.285
80°	0.772	0.660	0.526	0.430	0.253
Highly nonlinear soliton-dominated sea states ($E_{sol_ratio} \geq 90\%$)					
σ_θ	Initial	$\Delta\theta = 120°$	$\Delta\theta = 60°$	$\Delta\theta = 40°$	$\Delta\theta = 20°$
10°	0.918	0.916	0.916	0.916	0.880
20°	0.915	0.902	0.902	0.843	0.724
30°	0.918	0.907	0.882	0.789	0.695
40°	0.919	0.890	0.863	0.804	0.686
50°	0.916	0.881	0.830	0.776	0.648
60°	0.921	0.861	0.817	0.647	0.610
70°	0.910	0.867	0.774	0.678	0.543
80°	0.916	0.845	0.776	0.700	0.525

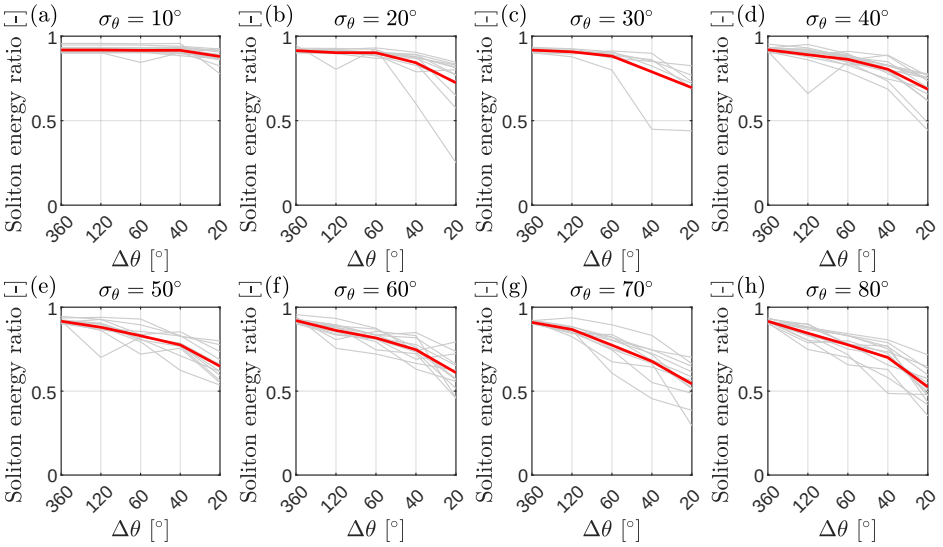


Figure 6.9: Effect of directional truncation on the soliton energy ratio for **highly nonlinear soliton-dominated cases ($E_{\text{sol_ratio}} \geq 90\%$)** with directional spreadings from 10° to 80°. The red line is the mean soliton energy ratio for each retention angle.

conditions (e.g., $\sigma_\theta = 80°$). This indicates that solitons can still account for a small portion of the energy in radiation wave-dominated seas when directional spreading is small; however, under large directional spreading, the initial detected solitons may not be representative, as the soliton energy ratio is quite low by directional truncation, indicating that almost no solitons are retained in the main directions. For soliton-dominated sea states ($60\% \leq E_{\text{sol_ratio}} < 90\%$), a similar decreasing trend in the mean soliton energy ratio is observed. These seas remain soliton-dominant under small directional spreading but change to radiation wave dominance under larger spreading conditions. Nevertheless, on average significant amounts of soliton energy remain on average even for large spreading. In highly nonlinear soliton-dominated cases ($E_{\text{sol_ratio}} \geq 90\%$), the sea state remains strongly soliton-dominated under small directional spreading; however, with increasing directional spreading, the dominance gradually weakens, although solitons still dominate in the overall energy. This result is particularly noteworthy, as it reveals that soliton energy can remain dominant in the main propagation directions even under conditions of large directional spreading.

Our study has demonstrated that, under highly nonlinear soliton-dominated directional sea states, the waves propagating in the main directions remain dominated by soliton energy. Meanwhile, it remains unclear how relevant these highly nonlinear soliton-dominated sea states actually are for the real ocean, as real wave fields may deviate from JONSWAP simulations and some of the considered JONSWAP configurations might occur only rarely in practice. To the best of our

knowledge, the soliton energy ratio has not been previously applied in existing studies. In particular, the directional spreading settings used in our simulations can be directly comparable to field measurement data. Measurements such as those conducted in Currituck Sound, North Carolina [28], in the Bay of Biscay, Northeast Atlantic Ocean [29] and in the Northwest Pacific Ocean [3] would be valuable for further investigation of the soliton energy ratio in future research. Our study offers a novel approach able to interpret such observations and provides new insight into the physical relevance of solitons in directional seas.

6.7. Appendix: The peak period does not influence the soliton energy ratio for JONSWAP spectra (if the time and frequency grids are rescaled)

In this appendix, we show that the peak period T_p does not influence the soliton energy ratio if the time and frequency grids are rescaled correctly. We start by noticing that the JONSWAP spectrum satisfies

$$\begin{aligned}
S(f;\alpha,\gamma,f_p) &= \alpha g^2 (2\pi)^{-4} f^{-5} \exp\left[-\frac{5}{4}\left(\frac{f_p}{f}\right)^4\right] \gamma^{\exp\left[-\frac{(f-f_p)^2}{2\sigma^2 f_p^2}\right]} \\
&= \alpha g^2 (2\pi)^{-4} \left(\frac{f}{f_p}\right)^{-5} \left(\frac{f_p}{1}\right)^{-5} \exp\left[-\frac{5}{4}\left(\frac{f_p}{f}\right)^4\right] \gamma^{\exp\left[-\frac{(f/f_p-1)^2}{2\sigma^2}\right]} \\
&= \frac{\alpha}{f_p^5} g^2 (2\pi)^{-4} \left(\frac{f}{f_p}\right)^{-5} \exp\left[-\frac{5}{4}\left(\frac{1}{f/f_p}\right)^4\right] \gamma^{\exp\left[-\frac{(f/f_p-1)^2}{2\sigma^2}\right]} \\
&= \frac{1}{f_p^5} S\left(\tilde{f};\alpha,\gamma,1\right), \quad \text{where} \quad \tilde{f} = \frac{f}{f_p}.
\end{aligned}$$

A signal generated from the JONSWAP spectrum $S(f;\alpha,\gamma,f_p)$ thus satisfies

$$\begin{aligned}
u(t) &= \sum_{n=1}^{N} \sqrt{2S(f_n;\alpha,\gamma,f_p)\Delta f}\cos(2\pi f_n t - \phi_n) \\
&= \sum_{n=1}^{N} \sqrt{2\frac{1}{f_p^5} S(\tilde{f}_n;\alpha,\gamma,1)\Delta f}\cos(2\pi f_n t - \phi_n) \\
&= \sum_{n=1}^{N} \sqrt{2\frac{1}{f_p^5} S(\tilde{f}_n;\alpha,\gamma,1)\Delta \tilde{f} f_p}\cos(2\pi \tilde{f}_n f_p t - \phi_n) \\
&= \frac{1}{f_p^2} \sum_{n=1}^{N} \sqrt{2S(\tilde{f}_n;\alpha,\gamma,1)\Delta \tilde{f}}\cos(2\pi \tilde{f}_n f_p t - \phi_n).
\end{aligned}$$

If we instead sample a signal from the JONSWAP spectrum $S(\tilde{f};\alpha,\gamma,1)$ and use the same phases ϕ_n as before, we get

$$\tilde{u}(t) = \sum_{n=1}^{N} \sqrt{2S(\tilde{f}_n;\alpha,\gamma,1)\Delta \tilde{f}}\cos(2\pi \tilde{f}_n t - \phi_n).$$

Comparing $u(t)$ and $\tilde{u}(t)$, we see that

$$u(t) = f_p^{-2}\tilde{u}(f_p t).$$

The corresponding signals passed to the NFT are

$$Q(t) = \rho u(t), \quad \tilde{Q}(t) = \tilde{\rho}\tilde{u}(t),$$

where, using the deep-water dispersion relation $\omega_0^2 = g k_0$,

$$\rho = C_g\sqrt{2}k_0^2 = \frac{\omega_0}{2\cancel{k_0}}\sqrt{2}\cancel{k_0^2} = \frac{\omega_0^3}{\sqrt{2}g} = \frac{(2\pi)^3}{\sqrt{2}g}f_p^3, \quad \tilde{\rho} = \cdots = \frac{(2\pi)^3}{\sqrt{2}g}\cancel{\tilde{f}_p^3}^{1}.$$

We see that the signals scaled for the NFT satisfy

$$Q(t) = \frac{(2\pi)^3}{\sqrt{2}g}f_p^3 u(t) = \frac{(2\pi)^3}{\sqrt{2}g}f_p^3 f_p^{-2}\tilde{u}(f_p t) = f_p\tilde{\rho}\tilde{u}(f_p t) = f_p\tilde{Q}(f_p t).$$

This is exactly the relation that appears in the scaling invariance of the NLSE[1]. In this specific case, it can be proven that the change of the nonlinear Fourier transform reduces to scaling operations as well [290, Sec. IV.D-4]. These scaling operations do not change the soliton energy ratio.

In summary, we found that the soliton energy ratios of $u(t)$ and $\tilde{u}(t)$ are the same. Since this result works for any combination of the random phases, we see that the distribution of the solitons energy ratio resulting from the JONSWAP spectra $S(f;\alpha,\gamma,f_p)$ and $S(\tilde{f};\alpha,\gamma,1)$ with random phases must be the same. The peak period $T_p = f_p^{-1}$ therefore cannot influence the distribution of the soliton energy ratios for time series obtained from JONSWAP spectra, if the time and frequency grids are scaled accordingly and α and γ are kept constant.

[1] See, e.g., [289, Eq. 6]. The roles of X and T are reversed here.

7

FIELD OBSERVATION OF SOLITON GASES IN THE DEEP OPEN OCEAN

CHAPTER ABSTRACT

Soliton gases are large ensembles of random solitons with distinct characteristics arising from integrable system dynamics. They have been widely studied in theory and experiments, and were observed in natural lagoons. However, it remains an open question whether they occur naturally in the open ocean. Nonlinear ocean states containing solitons have been observed in the literature, but the dominance of solitons over other wave components required for a soliton gas has not been demonstrated. Our study provides the first field evidence of soliton gas sea states in the deep ocean, measured in Taiwan waters. The soliton energy ratio derived from the nonlinear Fourier transform (NFT) is used as a key parameter to quantify how close sea states are to soliton gases. We identify eleven measurements with extremely high soliton energy ratios. They are characterized by short-period waves with relatively small wave heights, accompanied by extreme steepness and Benjamin–Feir Index (BFI) values. These states are exceptionally rare, representing only 0.054% of our dataset. Since directional interference can artificially increase the soliton energy ratio, we further apply a probabilistic directional filtering method to remove the directional interference. Three wave records from the Eluanbi station are found to retain high soliton energy ratios after the directional interference has been removed, confirming that they are indeed soliton gases.

The text in this chapter has previously appeared in Lee, Y. C., & Wahls, S. (2026). Field observation of soliton gases in the deep open ocean. Results in Physics, 108726.

This article is distributed under the terms of the Creative Commons Attribution 4.0 International License (CC BY 4.0), which permits unrestricted use, distribution, and reproduction in any medium, provided the original author and source are credited.

7.1. Introduction

Solitons are nonlinear localized waves that exhibit unique particle-like properties, retain their shape and velocity after collisions, and their amplitude directly determines their speed [13, 291, 292]. Soliton gases are solutions of integrable systems consisting of a large number of randomly distributed, nonlinearly interacting solitons [33]. The properties of a soliton gas are fundamentally different from the Gaussian linear dispersive radiation typically used to describe ocean waves [36, 293, 294]. There are kinetic equations that describe the evolution of the soliton density function characterizing the soliton gas dynamics. The first kinetic equation for a rarefied soliton gas based on the Korteweg-de Vries (KdV) equation for shallow water conditions was initially derived by Zakharov in 1971 [30]. Later, the kinetic equations for a dense soliton gas for both the KdV and nonlinear Schrödinger (NLS) equations were obtained by El and Kamchatnov in 2005 [31]. While the KdV equation applies to waves in shallow water, the NLS equation describes the complex envelope of deep water waves; the corresponding NLS solitons are thus envelope solitons [158]. The KdV and NLS equations can be solved analytically using nonlinear Fourier transforms (NFTs), which are also known as (direct) scattering transforms in the literature [13]. NFTs simplify the evolution of solutions of integrable nonlinear systems and reveal potentially hidden solitons and breathers within these solutions [6, 28, 145].

Soliton gases are solutions of integrable systems consisting of a large number of randomly distributed, nonlinearly interacting solitons [30–33]. Over the last decade, soliton gases have become a fruitful research area due to their nontrivial mathematical and physical implications [32, 254, 255, 295]. Experimental demonstrations of soliton gases were first carried out in optical fiber systems [296, 297]. For water waves, an experimental realization of a soliton gas in a one-dimensional wave flume has been demonstrated for the KdV type [86], and for the NLS type [65]. In addition, field measurements of sea states exhibiting soliton turbulence have been reported under wind-wave conditions in the Currituck Sound, North Carolina [36], and in the Laguna Cáhuil, Chile [298]. These studies describe sea states dominated by KdV solitons in natural environments (both lagoons). For deep water waves, highly nonlinear NLS-type soliton dominated sea states have been observed in the Currituck Sound as well [28]. These field observations of soliton gases were all made in lagoons, and are thus not representative for the open ocean. To the best of our knowledge, no field observations of soliton gases in the open ocean have been reported so far.

In this study, we aim to identify soliton gas sea states under intermediate and deep water conditions in buoy measurements collected in Taiwanese waters. The buoys are operated by the Coastal Monitoring Center at National Cheng Kung University, Tainan, Taiwan [165, 169]. A key challenge in identifying soliton gases in the open ocean from time series is the presence of directional interference, which is not captured by the NLS equation underlying the NFT considered in this paper. We address this issue using a specialized directional filtering technique applied to simulated wave fields, which are based on directional power spectra provided by the buoys.

This paper is organized as follows. Section 7.2 describes the data acquisition

process. Section 7.3 introduces the theoretical framework, including the nonlinear Schrödinger equation, the nonlinear Fourier transform, and the calculation of soliton parameters. Section 7.5 presents the main results on the identification and statistical analysis of soliton gas sea states, including a discussion on directional interference. Finally, Section 7.6 summarizes the findings and offers concluding remarks.

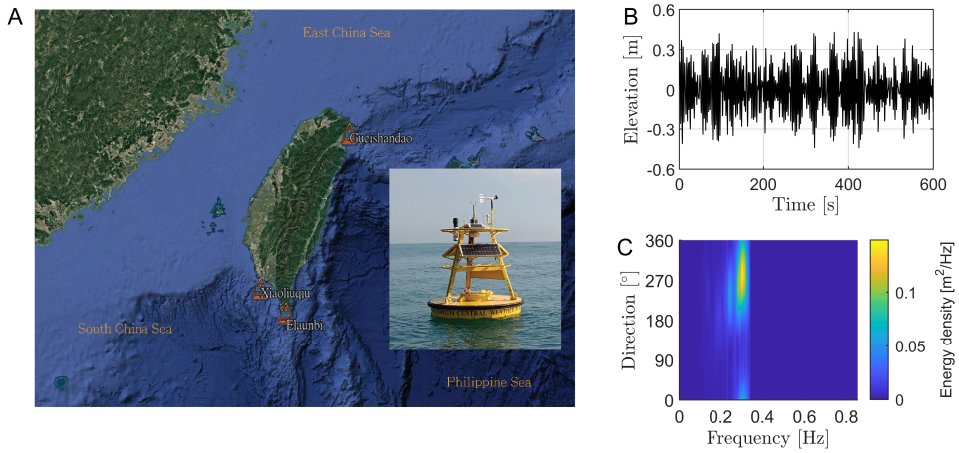


Figure 7.1: Data collection from buoy measurements in Taiwanese waters. (A) Locations of three buoy stations, Eluanbi (south), Gueishandao (northeast) and Xiaoliuqiu (southwest). (B) Example of a soliton gas (surface elevation time series) recorded at the Eluanbi station on 2019/05/16 at 14:00. (C) Corresponding directional wave spectrum.

Table 7.1: Overview of wave measurement buoy stations and basic parameters in Taiwan waters

Station	Latitude	Longitude	Depth	Year
Elaunbi	21°55'06"N	120°48'57"E	40 m	2017,2019
Gueishandao	24°50'55"N	121°55'53"E	38 m	2018-2019
Xiaoliuqiu	22°18'46"N	120°21'42"E	82 m	2017-2019
Number of data	kh	H_s [m]	T_p [s]	σ_θ [°]
5,977	1.363-18.608	0.17-5.32	3.31-10.71	53.86-80.33
5,285	1.363-15.823	0.19-6.72	3.77-10.53	57.89-80.76
9,261	1.363-38.147	0.02-6.35	3.77-15.38	51.14-80.17

7.2. Data acquisition

The surface wave data used in this study were measured by buoys operated by the Coastal Ocean Monitoring Center (COMC) at National Cheng Kung University (NCKU), Taiwan [165, 166, 169]. The discus buoy is equipped with an accelerometer-tiltcompass (ATC) sensor that can measure six degrees of freedom. Measured buoy accelerations in six degrees of freedom are used to calculate directional wave spectra by applying a Fourier transform to the cross-correlation of the motion signals [166, 299]. Three buoy stations named Eluanbi, Gueishandao and Xiaoliuqiu are located in the south, northeast and southeast of Taiwan, respectively. The water depths at the three stations are 40 m, 38 m and 82 m, corresponding to intermediate and deep water conditions. The locations of the buoy stations and the buoy type are shown in Fig. 7.1A. An example of a time series after data quality control is presented in Fig.7.1B, along with its corresponding directional wave spectrum in Fig.7.1C. Table 7.1 presents buoy information and also includes the measured ranges of relative water depth, significant wave height, peak period, and directional spreading for each station. These data span conditions ranging from normal sea states to extreme events driven by local winds and large-scale Pacific systems, including monsoons and typhoons, thereby capturing a wide diversity of wave fields in the Pacific region. The data used in this study were collected between 2017 and 2019. The measured accelerations from six degrees of freedom were analyzed using preprocessing methods involving noise filtering to obtain time series of wave elevation, following Appendix A in Ref. [169]. The data were recorded hourly, with each record having a duration of 10 minutes. An example, measured at the Xiaoliuqiu buoy on 2018/04/22 at 16:00, is shown in Fig.7.1B of the main manuscript. The sampling rate of the time series is 1.7 Hz. The directional wave spectrum from the ATC data was obtained following Appendix B in Ref. [169].

The nonlinear Schrödinger (NLS) equation assumes deep water conditions with narrow-banded and unidirectional wave fields, which do not always correspond to real ocean conditions. Therefore, the data are specifically selected to better satisfy NLS assumptions. First, the applicability of the NLS equation requires $kh > 1.363$ for deep water conditions, where k is the peak wave number and h is the water depth. (This condition marks the focusing regime of the NLS equation. Only in the focusing regime, do conventional "bright" soliton solutions exist.) We select data based on this threshold to ensure appropriate depth conditions. Second, to reduce spectral broadness in both frequency and directional domains, we retain only single-peak spectra and filter out data with double or multi-peak spectra. The coexistence of local wind seas and distant swells often results in double- or multi-peaked wave spectra [300]. This phenomenon is quite dominant in the real ocean but still depends on local climate and environmental conditions. Significant peaks in the one-dimensional wave spectra were identified using the method described in Ref [301]. This approach limits the dataset to single wave systems, thereby minimizing the effects of spectral bandwidth that can violate the narrow-band assumption fundamental to NLS equation validity. Based on the above selection criteria, we obtained 5,977, 5,285 and 9,261 deep water unimodal spectra for Eluanbi, Gueishandao and Xiaoliuqiu stations, respectively. These represent 47.0%, 34.5% and

42.7% of the total datasets for each station.

7.3. METHOD

7.3.1. NONLINEAR SCHRÖDINGER EQUATION

Different nonlinear Fourier transforms (NFTs) exist to deal with different types of integrable dynamics. In the paper, we consider the NFT for the NLS equation [9, 13, 302]. The NLS equation describes the unidirectional propagation of complex wave envelopes in deep water under the assumptions of narrow bandwidth and weak nonlinearity. It is typically expressed in spatial form, but since this study uses field measurement data in time series, the temporal NLS formulation is required. The temporal NLS equation can be expressed as [6, 28, 63]:

$$\mathrm{i}\left[C_g^{-1}A_t + A_x\right] + \mu C_g^{-3}A_{tt} + \nu C_g^{-1}|A|^2 A = 0. \tag{7.1}$$

where $A(x,t)$ is the complex envelope, C_g is the group velocity, μ is the second-order dispersion coefficient, ν is the nonlinear coefficient, x is the spatial coordinate, and t is time. We used the coefficients for finite depth, which are quite complicated and can be found, e.g., in [28, 62]. The complex envelope is obtained from the surface elevation by taking the Hilbert transform and then removing the carrier [6, 63]. Conversely, the surface elevation can be recovered from the complex envelope by adding the carrier back in and taking the real part of the result. The NFT assumes that the data is governed by the following normalized form of the NLS equation:

$$\mathrm{i}u_X + u_{TT} + 2|u|^2 u = 0, \tag{7.2}$$

where $u(X,T)$ is the normalized complex envelope, X is the normalized spatial coordinate, and T is the normalized temporal coordinate. The change of coordinates is

$$\begin{aligned} X &= \frac{\mu}{C_g^3}x, \quad T = t - \frac{x}{C_g}, \\ u(X,T) &= \rho A(x,t), \quad \rho := \sqrt{\frac{C_g^2\nu}{2\mu}}. \end{aligned} \tag{7.3}$$

where ρ is the nonlinear parameter. This change of coordinates is applied before the data are passed to the NFT.

7.3.2. NONLINEAR FOURIER TRANSFORM

Since the direct spatial evolution of the complex envelope governed by the NLS equation can be complicated, the nonlinear Fourier transform (NFT) provides a major advantage because the evolution of the nonlinear Fourier components follows simple analytic formulas. By applying the inverse nonlinear Fourier transform (iNFT) to the propagated spectrum, one can efficiently obtain the solution at different spatial points [13, 90]. In this study, we used the NFT for vanishing signals

since solitons are vanishing waveforms. They have a natural representation in the nonlinear spectrum of the vanishing NFT. The NFT for periodic signals, in contrast, can only approximate solitons through cnoidal waves with very high modulus [99]. It has been shown that both approaches in general return the same soliton content [7, 99], but the determination of the soliton amplitudes with the periodic NFT requires the computation of a heuristic "reference level", which can be difficult to use in practice [4, 303]. We also remark that time series measured in the real ocean are generally not strictly periodic. We utilized the open-source software library 'Fast Nonlinear Fourier Transforms' (FNFT) for the numerical computations [63, 191]. This library provides efficient numerical algorithms for the computation of various types of NFTs. We now outline the computation of the NFT for the NLS equation [9, 302].

The scattering problem for the NLS equation is

$$\Psi_T = Q(\zeta)\Psi, \quad Q = \begin{pmatrix} -\mathrm{i}\zeta & u(X_0,T) \\ -u(X_0,T)^* & \mathrm{i}\zeta \end{pmatrix}, \tag{7.4}$$

where ζ is the complex spectral parameter, * represents complex conjugation, and X_0 is an arbitrary spatial reference point for the time series. Two pairs of linearly independent solutions called Jost functions, $[\phi(T,\zeta) \quad \bar{\phi}(T,\zeta)]$ and $[\psi(T,\zeta) \quad \bar{\psi}(T,\zeta)]$, are found by solving (7.4) with

$$\begin{aligned} \phi(T,\zeta) &\to \begin{bmatrix} e^{-\mathrm{i}\zeta T} \\ 0 \end{bmatrix}, \ \bar{\phi}(T,\zeta) \to \begin{bmatrix} 0 \\ -e^{\mathrm{i}\zeta T} \end{bmatrix} \quad \text{as} \quad T \to -\infty, \\ \psi(T,\zeta) &\to \begin{bmatrix} 0 \\ e^{\mathrm{i}\zeta T} \end{bmatrix}, \ \bar{\psi}(T,\zeta) \to \begin{bmatrix} e^{-\mathrm{i}\zeta T} \\ 0 \end{bmatrix} \quad \text{as} \quad T \to \infty. \end{aligned} \tag{7.5}$$

The pairs of Jost functions are related through the scattering coefficients $a(\zeta)$, $b(\zeta)$, $\overline{a}(\zeta)$, $\overline{b}(\zeta)$:

$$\begin{aligned} \phi(T,\zeta) &= a(\zeta)\bar{\psi}(T,\zeta) + b(\zeta)\psi(T,\zeta), \\ \bar{\phi}(T,\zeta) &= \bar{b}(\zeta)\bar{\psi}(T,\zeta) + \bar{a}(\zeta)\psi(T,\zeta). \end{aligned} \tag{7.6}$$

The scattering coefficients $a(\zeta)$ and $b(\zeta)$ are the basis for forming the nonlinear spectrum, which has a continuous part and a discrete part. The continuous spectrum is described by the *reflection coefficient*

$$r(\zeta) = b(\zeta)/a(\zeta), \quad \zeta \in \mathbb{R}. \tag{7.7}$$

It represents the radiation components in the time series. The discrete spectrum contains the discrete eigenvalues $\{\zeta_n = \xi_n + \mathrm{i}\eta_n\}$, $n = 1,\ldots,N$, where N is the total number of solitons in the signal. They are the zeros of the scattering coefficient $a(\zeta)$ with positive imaginary part. The eigenvalues are complemented by the residues

$$r_n = b(\zeta_n)/a'(\zeta_n), \quad \text{where} \quad a' = da/d\zeta. \tag{7.8}$$

Each eigenvalue in the discrete spectrum corresponds to one solitonic component in the time series.

The inverse NFT is, in contrast to the linear Fourier transform, quite different from the forward NFT. There are several ways to perform the inversion. In our case, where only the discrete spectrum containing the solitons is being inverted, FNFT employs the so-called Darboux transform to recover the time domain signal [304].

7.3.3. Soliton Amplitudes and Velocities

We now describe how the physical soliton amplitudes and velocities can be obtained from the discrete part of the NFT, which has been computed from normalized data. The magnitude of an envelope soliton arising from a single complex eigenvalue $\zeta_n = \xi_n + \mathrm{i}\eta_n$ is [13]

$$|u(X,T)| = 2\eta_n \operatorname{sech}\left[2\eta_n(T + 4\xi_n X)\right]. \tag{7.9}$$

Reverting the data normalization discussed earlier, we bring this soliton into physical dimensions:

$$\begin{aligned} |A(x,t)| &= \left|\frac{u(X,T)}{\rho}\right| = \left|\frac{1}{\rho}u\left(\frac{\mu}{C_g^3}x,\ t - \frac{x}{C_g}\right)\right| \\ &= \frac{2\eta_n}{\rho}\operatorname{sech}\left[2\eta_n\left(t - \left(\frac{1}{C_g} - 4\xi_n\frac{\mu}{C_g^3}\right)x\right)\right] \\ &= \frac{2\eta_n}{\rho}\operatorname{sech}\left[2\eta_n\frac{-1}{C_{\mathrm{sol}}}\left(x - C_{\mathrm{sol}}\,t\right)\right]. \end{aligned} \tag{7.10}$$

where

$$C_{\mathrm{sol}} = \frac{C_g}{1 - 4\xi_n\mu/C_g^2} \approx C_g + \frac{4\xi_n\mu}{C_g}. \tag{7.11}$$

is the soliton velocity and $2\eta_n/\rho$ is the soliton amplitude, both in physical dimensions. The approximation holds under the condition $4\xi_n\mu/C_g^2 \ll 1$.

7.3.4. Soliton Energy Ratio Calculation

To detect envelope solitons in the measured time series, the complex envelope is first computed and normalized. In general, NFTs are a class of transforms that decompose time (or space) series into physically meaningful components w.r.t. integrable dynamics [9]. They play a key role in the inverse scattering method to solve integrable partial differential equations and are also known as forward scattering transforms. In light of their unique capability to uncover hidden solitons, NFTs have been applied successfully to many real-world systems, even if the underlying physical models are not fully integrable [3, 6, 21–23, 305]. In particular, they are widely used to study soliton gases. With the NFT for the NLS employed here, solitons correspond to discrete spectral components, while dispersive radiation waves are associated with a continuous spectrum. The soliton energy ratio is found from the NFT and lets us quantify the soliton content in time series. It is based on the nonlinear Parseval formula [13]

$$E_{\mathrm{total}} = \int_{-\infty}^{\infty} |u(X_0,T)|^2\,dT = E_{\mathrm{sol}} + E_{\mathrm{rad}}, \tag{7.12}$$

where we set $u(X_0,T) = 0$ for times outside the measurement interval. E_{sol} is the energy of the solitons, and E_{rad} is the energy of the radiation waves. The energy of the radiation waves can be calculated using the reflection coefficient:

$$E_{\mathrm{rad}} = \frac{1}{\pi}\int_{-\infty}^{\infty} \log(1 + |r(\zeta)|^2)\,d\zeta \tag{7.13}$$

is computed from the continuous part of the NFT and represents the energy in the radiation components, and

$$E_{\text{sol}} = 4 \sum_{n=1}^{N} \eta_n^2 \tag{7.14}$$

is computed from the discrete part of the NFT and represents the energy in the solitonic components. The soliton energy ratio can be computed :

$$E_{\text{sol.ratio}} = \frac{E_{\text{sol}}}{E_{\text{total}}} = \frac{E_{\text{total}} - E_{\text{rad}}}{E_{\text{total}}} \in [0,1]. \tag{7.15}$$

This serves as a quantitative measure of the degree of nonlinearity in the sea state. It is zero in the complete absence of solitons, and one for a pure soliton gas. Soliton gases are thus indicated by high soliton energy ratios.

7.4. Statistical Wave Parameters for Sea State Characterization

We discuss the wave parameters used to statistically quantify sea state properties. To analyze surface wave elevations, we use the downward zero-crossing method [159]. This involves identifying individual waves by finding points where the surface falls below its average level. From the waves in the record, we calculate the maximum wave height $H_{\max}$, which is the largest individual height The significant wave height $H_{1/3}$ represents the average height of the highest one-third of all waves within the record found with the downward zero-crossing method. It is a statistical parameter used to characterize the wave conditions of a sea state. The abnormality index (AI) quantifies the maximum wave height compared to the significant wave height [160, 178]:

$$\text{AI} = \frac{H_{\max}}{H_{1/3}}. \tag{7.16}$$

Waves with an abnormality index $\text{AI} \geq 2$ are classified as rogue waves.

The directional spreading quantifies the angular distribution of wave energy around the peak direction and is calculated using directional moments [161, 162]:

$$\sigma_\theta = \left[2 \left\{ 1 - \left(\frac{p^2 + q^2}{m_0^2} \right)^{\frac{1}{2}} \right\} \right]^{\frac{1}{2}}, \tag{7.17}$$

where $p = \int_0^{2\pi} \int_0^{\infty} \cos(\theta) S(\omega,\theta)\, d\omega\, d\theta$, $q = \int_0^{2\pi} \int_0^{\infty} \sin(\theta) S(\omega,\theta)\, d\omega\, d\theta$, $m_0 = \int_0^{2\pi} \int_0^{\infty} S(\omega,\theta)\, d\omega\, d\theta$ is the zeroth spectral moment, and $S(\omega,\theta)$ is the directional spectrum, representing the distribution of surface wave energy across both angular frequency ω and direction θ.

Kurtosis quantifies the fourth standardized moment of the surface elevation time series [16]. Higher kurtosis values indicate an increased probability of encountering extreme wave events. Skewness, the third standardized moment of the surface

elevation time series, measures the asymmetry of the surface elevation distribution, indicating the vertical asymmetry between wave crests and troughs [16]:

$$\text{Kurtosis} = \frac{\overline{\eta^4}}{\sigma^4}, \tag{7.18}$$

$$\text{Skewness} = \frac{\overline{\eta^3}}{\sigma^3}, \tag{7.19}$$

where η is the surface elevation, and σ is the standard deviation. Wave steepness characterizes the ratio of significant wave height to wavelength and is commonly expressed as [306]

$$\text{Steepness} = \frac{2\pi H_s}{g T_p^2}, \tag{7.20}$$

where g is gravitational acceleration. Here, H_s denotes four times the standard deviation of the surface elevation. It is another commonly used parameter for the significant wave height. Under certain statistical assumptions, it coincides exactly with $H_{1/3}$. The peak period T_p is defined as the wave period corresponding to the maximum spectral energy density. The Benjamin-Feir Index (BFI) measures the potential for modulational instability and nonlinear wave interactions [3, 16, 115]:

$$\text{BFI} = \frac{\sqrt{2}\varepsilon}{\delta_\omega}, \tag{7.21}$$

where ε is the wave steepness, δ_ω is the spectral bandwidth calculated from Goda's peakedness parameter [163]. The BFI can be interpreted as a ratio between nonlinear focusing and linear dispersive spreading. A large BFI means that nonlinear effects are strong compared to spectral spreading, so the sea state is more susceptible to modulational instability and soliton-like dynamics.

7.5. Results

7.5.1. Identifying Soliton Gas Sea States

Using field measurement data from three buoy stations, we applied the NFT and calculated the soliton energy ratio for records that satisfied both unimodal spectrum and deep water criteria. Selecting a unimodal spectrum restricts the wave field to the influence of a single wind system, thereby avoiding crossing seas and broadened spectral bandwidth. We initially looked for seas that exhibit a very high soliton energy ratio of at least 0.9. Based on this criterion, we identified 3, 2 and 6 events among the 5,977, 5,285 and 9,261 qualified records from Eluanbi, Gueishandao and Xiaoliuqiu stations, respectively. These correspond to occurrence rates of 0.050%, 0.038% and 0.065% under unimodal spectrum and intermediate and deep water conditions. Although some records were in intermediate depth, the soliton gases identified in this study fully satisfy the deep water conditions. In total, 11 time series with very high soliton energy ratios were identified from 20,523 records from three buoy stations, which yields an overall occurrence rate of 0.054%. This indicates

that seas with very high soliton energy ratios are extremely rare events, at least for the high soliton energy ratio cut-off considered here. To our knowledge, such sea states have not been previously observed in the literature. We note that buoy measurements tend to underestimate extreme wave heights and suppress higher wave crests compared to radar observations [147, 307]. This study, which is based on buoy data, therefore likely underestimates the occurrence of soliton gases. The application of the same method to radar measurements should reveal a greater prevalence.

Fig. 7.1B shows one of the identified time series with very high soliton energy ratio, measured on 2019/05/16 at 14:00 at the Eluanbi station; the corresponding directional spectrum is shown in Fig. 7.1C. The complex envelope of the surface wave elevation time series was obtained using the Hilbert transform [60], which then served as input for the NLS-NFT after the carrier frequency had been removed. The resulting soliton spectrum is shown in Fig. 7.2A. Each red dot corresponds to a point in the discrete part of the NFT and indicates a soliton. A total of 64 solitons were detected. These axes were transformed back to the physical domain. The largest soliton amplitude is 0.51 m. The soliton energy ratio is 0.96. This soliton spectrum is typical for seas with high soliton energy ratio. To illustrate the dominance of solitons in the time domain, we applied the inverse NFT to the discrete spectrum only. By not considering the continuous spectrum in the inverse NFT step, we filter the signal nonlinearly and obtain the complex envelope of the underlying solitonic part. Using the same carrier frequency as the initial time series, the surface elevation of the soliton components was reconstructed (red line in Fig. 7.2B). The reconstructed soliton time series (red line) closely matches the original measurement (black line), confirming the very high soliton energy ratio. The residual radiation wave components may either amplify or attenuate the soliton part.

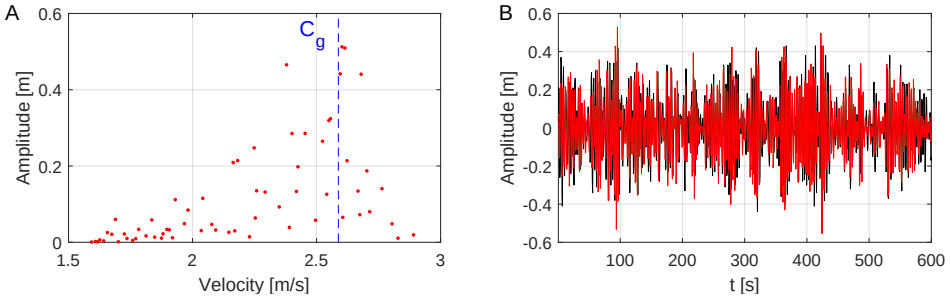


Figure 7.2: NFT analysis of a sea state with high soliton energy ratio. (A) Soliton spectrum. (B) Corresponding initial surface wave elevation (black) compared with soliton time series (red) reconstructed from the soliton spectrum.

7.5.2. Statistical Properties of Soliton Gas Sea States

To further explore the characteristics of the 11 sea states with high soliton energy ratios (above 0.9), we analyze the statistical properties of various wave parameters including significant wave height, peak period, directional spreading, abnormality index (AI), kurtosis, skewness, steepness, and the Benjamin-Feir Index (BFI). The statistical distributions of these parameters for the eleven sea states are compared with the overall dataset, as shown in Fig. 7.3, where (A)–(D), (E)–(H), and (I)–(L) correspond to data from the Eluanbi, Gueishandao and Xiaoliuqiu stations, respectively. In the figure, red dots represent very high soliton energy ratios, while black dots denote the entire dataset. We first focus on the scatter plots of significant wave height versus peak period (Fig. 7.3A, E, I), which reveal that these seas have relatively smaller wave heights and shorter peak periods. This observation deviates from the concept that individual solitons or breathers can exhibit their characteristic shapes in time series, forming large-amplitude rogue waves [3, 29]. However, our data share similar characteristics of small wave heights and short peak periods with highly nonlinear breather turbulence wind waves measured in Currituck Sound, North Carolina [28]. We then examine the scatter plots of AI versus directional spreading (Fig. 7.3B, F, J). It can be observed that the seas with high soliton energy ratios do not exhibit large AI values, indicating that rogue waves are absent under these conditions. Moreover, these seas are not correlated with directional spreading. Subsequently, we analyze kurtosis versus skewness (Fig.7.3C, G, K). The results show that seas with high soliton energy ratios do not display large kurtosis. However, they exhibit skewness values close to zero, indicating that the time series are nearly symmetric. The most interesting results are the scatter plots of steepness versus BFI (Fig. 7.3D, H, L), which reveal that sea states with high soliton energy ratios exhibit exceptionally high wave steepness and BFI values. Specifically, all of these events have steepness exceeding 0.029 and BFI values above 0.31. As expected, the results confirm that seas with high soliton to energy ratios are characterized by high wave steepness and BFI, a finding consistent with their strong nonlinearity. We additionally note that the wave ages of highly nonlinear soliton dominated seas range from 0.30–0.45 at Eluanbi, 0.63–0.65 at Gueishandao, and 0.60–0.90 at Xiaoliuqiu. These values all correspond to young wind seas, indicating that they represent wind-generated waves consistent with the findings of Osborne et al. (2019) [28].

7.5.3. Discussion on Directional Interference in Soliton Gas Seas

Integrable models like the KdV or NLS equation describe real-world ocean waves only approximately. Directional interference in particular can suppress the dynamics of NLS soliton gases by disrupting nonlinear focusing mechanisms and redistributing energy across different propagation directions. Such suppressed soliton gases represent states in which initially detected solitons are subsequently weakened by directional spreading. In simulations of directional JONSWAP wave fields, the soliton energy ratio computed directly from time series was found to typically overestimate

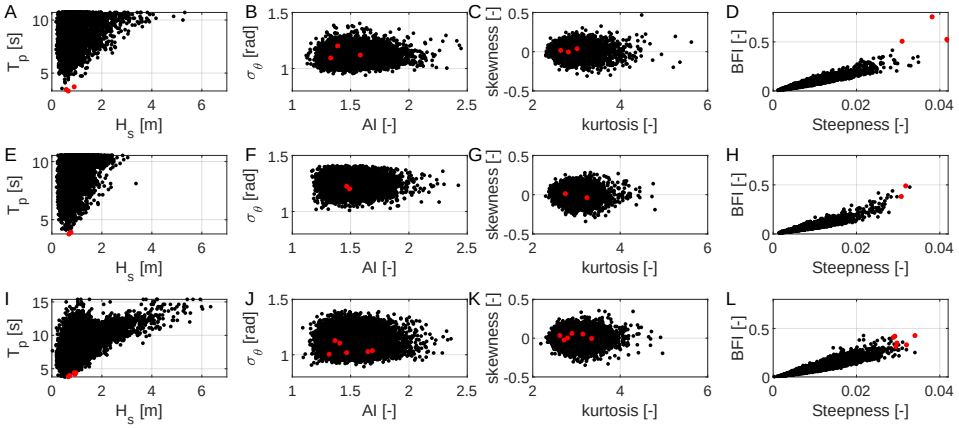


Figure 7.3: Statistical properties of seas states with high soliton energy ratios of at least 0.9 (red) compared with all data (black) at Eluanbi (A–D), Gueishandao (E–H), and Xiaoliuqiu (I–L). (A), (E), (I): scatter plots of significant wave height H_s versus peak period T_p; (B), (F), (J): abnormality index (AI) versus directional spreading σ_θ; (C), (G), (K): kurtosis versus skewness; (D), (H), (L): wave steepness versus Benjamin–Feir Index (BFI).

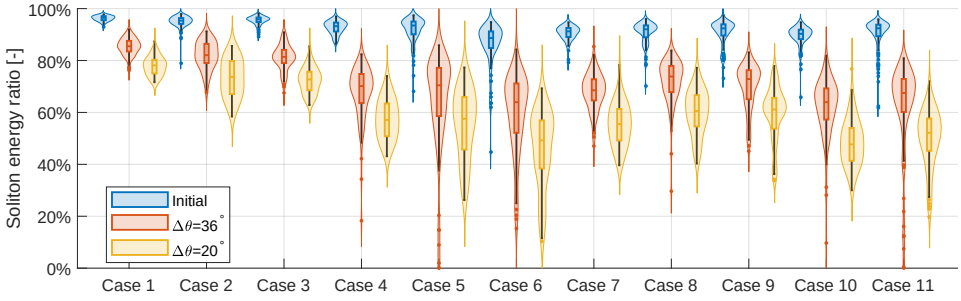


Figure 7.4: Investigation of reduced directional effects on field-measured soliton gases: distribution of soliton energy ratios for the 11 soliton gas cases after directional filtering with 100 sets of random phases per case. Violin plots show the analyzed soliton energy ratio for: the initial wave field (blue), retention angle $\Delta\theta = 36°$ (orange), and retention angle $\Delta\theta = 20°$ (yellow).

the soliton content in the main propagation direction due to directional interference, although the effect was less pronounced for strongly nonlinear sea states [308]. To ensure that the soliton energy ratios computed from the time series in our data set are not overestimated, we reconstruct the part of the wave fields propagating in the main direction under the linear assumption. Since only the magnitudes of the directional spectrum are available in our data, we choose the phases uniformly at random. To ensure representativeness, many different sets of random phases are considered. The directional magnitude spectrum of each simulated time series coincides with that of the original time series in the main propagation direction, but the directional interference has been removed. By computing the soliton energy ratios for different realizations of the random phases, we obtain a probability distribution of the possible soliton energy ratios for the true time series without directional interference.

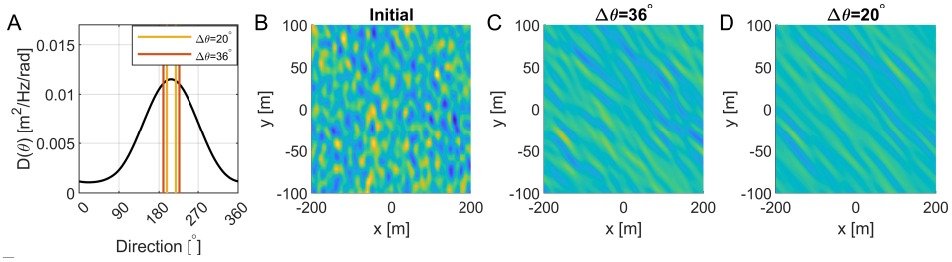


Figure 7.5: Investigation of reduced directional effects on field-measured soliton gases (A) Directional spectrum with retention angles $\Delta\theta = 36°$ (orange lines) and $\Delta\theta = 20°$ (yellow lines) with energy outside the angles truncated. (B) Simulated wave field from random phases with the full spectrum. (C–D) Reconstructed wave fields with the same phases but truncated spectra at $\Delta\theta = 36°$ and $\Delta\theta = 20°$, respectively.

In our data acquisition, we focus on cases with a unimodal spectrum to minimize spectral width and directional effects. However, for field measurement data, the directional spreading can still be substantial. Directional interference may lead to an overestimation of the soliton energy ratio, as wave components from multiple directions contribute spurious energy to the single-point measurement, which does not reflect the true soliton content in the primary propagation direction. To address this, we further examine how the soliton energy ratio changes when only waves propagating in the main direction are considered. Here, we apply directional truncation with two retention angles, $\Delta\theta = 36°$ and $\Delta\theta = 20°$, whereby energy outside the retention angle of the main spectral peak is excluded.

To reconstruct surface wave fields from a given directional wave spectrum, the surface is modeled as a linear superposition of small-amplitude oscillations with random phases [281, 283–285]. Specifically, it is represented as a superposition of many simple cosine waves, each with varying amplitude, frequency, phase, and propagation direction. The sea surface elevation $\eta(x, y, t)$ at a spatial location (x, y)

and time t is then given by

$$\eta(x,y,t) = \sum_{i=1}^{N_\omega}\sum_{j=1}^{N_\theta}\sqrt{2S(\omega_i,\theta_j)\Delta\omega\Delta\theta}\cos\left(k_i(x\cos\theta_j + y\sin\theta_j) - \omega_i t + \phi_{ij}\right), \quad (7.22)$$

where N_f and N_θ are the total number of discrete frequency and direction bins, respectively. The term $\Delta\omega$ is the angular frequency increment, and $\Delta\theta$ is the directional increment. The directional wave density spectrum $S(\omega_i,\theta_j)$ is derived from buoy measurements for each time series. The wave number k_i corresponding to frequency ω_i is calculated using the deep water dispersion relation. Since the phases ϕ_{ij} have not been measured, they are chosen randomly from a uniform distribution in the interval $[0,2\pi]$. To capture the influence of the random phases, 100 sets of random phases are considered for each time series.

For the spatial domain, we set $x \in [-200,200]$ m and $y \in [-100,100]$ m, with a grid resolution of $N_x = 101$ and $N_y = 51$. The time is initialized at $t = 0$, with a 0.59 s interval, for a total duration of 600 s. Subsequently, we generate wave fields constrained to specific retention angles, where the energy of the directional spectrum outside the peak retention range is removed. To ensure that only the components in the main direction are extracted, the same random phases as those of the initial wave field are retained. Under the assumption of linear superposition, this approach enables the successful reconstruction of wave fields propagating exclusively in the main direction. The other directions thus contribute additive perturbations to the main direction in our framework, which is a standard model in the study of transversal perturbations of line solitons [309, 310]. However, note that the reconstructed main direction may still contain features that arose from nonlinear interactions with the rest of the wave field. Moreover, the use of wave numbers obtained from the deep water dispersion relation means that nonlinear dispersion effects and bound-wave contributions are not explicitly represented.

As an illustration, we present an example based on one of our seas with high soliton energy ratios in Fig. 7.5. In this case, the directional spreading is $\sigma_\theta = 57.58°$, and the corresponding directional spectrum is shown in Fig.7.5A. The retention angles of $\Delta\theta = 36°$ and $20°$ are indicated by the orange and yellow lines, respectively. Under the linear superposition of waves with random phases, the simulated wave field corresponding to the initial spectrum is shown in Fig.7.5B. By removing the energy outside the retention angles in the directional sidebands while preserving the original phases, we reconstructed the wave fields, as shown in Fig.7.5C for $\Delta\theta = 36°$ and Fig.7.5D for $\Delta\theta = 20°$. It can be seen that after the removal of energy in the directional sideband, the initial short-crested wave field changes into long-crested wave fields. A virtual wave gauge was placed at the center of the domain ($x = 0$, $y = 0$) to extract simulated time series for nonlinear Fourier analysis.

We applied the above method to the 11 states with high soliton energy ratios identified before to examine how the removal of directional interference in the sidebands affects the soliton energy ratio. Slunyaev (2024) recently observed that solitons can persist in broadbanded and moderately directional sea states ($\Delta\theta \leq 30°$) in deep water, where they remained stable for several tens of wave periods [215]. With less directional spreading, their lifetime can be even longer. In light of

these results, wave energy outside the principal wave directions was removed with retention angles of $\Delta\theta = 36°$ and $\Delta\theta = 20°$; only energy within these ranges was preserved. Since the directional phases were unknown, we generated 100 random phase realizations for each measured directional (power) spectrum to construct simulated wave fields. The resulting soliton energy ratios for all cases under different retention angles $\Delta\theta$ are shown in Fig. 7.4. They are depicted as violin plots that indicate the distribution the soliton energy ratios resulting from considering 100 sets of random phases. The "initial" cases corresponds to the initial, unfiltered directional spectrum equipped with random phases. The cases 1–3 were measured at the Eluanbi station, the cases 4–5 at the Gueishandao station, and the cases 6–11 at the Xiaoliuqiu station. For simulations using the full directional spectrum (blue boxes), most reconstructed time series have mean soliton energy ratios exceeding 0.9. As expected, the mean soliton energy ratio decreases after directional truncation. This is because removing energy from the system leads to a reduction in its nonlinearity. A larger retention angle ($\Delta\theta = 36°$) leads to a moderate reduction in the mean soliton energy ratio (orange boxes), while a smaller retention angle ($\Delta\theta = 20°$) results in a stronger reduction in the mean soliton energy ratio (yellow boxes). Averaged over all simulations, the mean soliton energy ratio is 0.92 for the full spectrum (blue boxes), decreases to 0.70 at $\Delta\theta = 36°$ (orange boxes), and further decreases to 0.60 at $\Delta\theta = 20°$ (yellow boxes). For the cases 1 to 3 (Eluanbi station), the distributions stay completely above the threshold of 0.5, above which solitons are dominating. Furthermore, as shown in Table 7.2, these three cases also satisfy the other assumptions of the NSE equation sufficiently well. *We can thus consider them soliton gases even with directional interference taken into account.* For the cases 4 to 11 (Gueishandao and Xiaoliuqiu), the distributions in Fig. 7.4 reach below 0.5. Thus, with directional interference taken into account, we can only consider them soliton gases with a certain probability. This probability is lower for the cases 4 to 6 and 10 to 11, where the phase information has a larger impact on the soliton energy ratios, leading to wide distributions. For the cases 7 to 8, the phases appear to be less important as the distributions are narrower.

Table 7.2: Parameters related to the narrow bandwidth, weak nonlinearity and deep water assumptions of the NLS equation for the three soliton gases at Eluanbi station. Δf denotes the 3dB bandwidth, $f_{\max}$ the peak frequency and H_s the significant wave height. k was determined from $f_{\max}$ using the deep water dispersion relation. Solitons have been observed for $\Delta f / f_{\max} \lesssim 0.25$ and $kH_s \lesssim 0.3$ in the literature [274]. The value of kh should be at least 1.31.

Case	$\Delta f / f_{\max}$	kH_s	kh
1	0.17	0.24	14.65
2	0.23	0.19	13.54
3	0.25	0.26	11.74

7.6. CONCLUSION AND OUTLOOK

Summarizing, we have analyzed field measurements from buoys in Taiwan waters and identified 11 sea states with extremely high soliton energy ratios. These sea states are associated with relatively small wave heights and short peak periods. Their highly nonlinear character is evidenced by large wave steepness and elevated Benjamin–Feir Index (BFI) values, while skewness and kurtosis do not differ significantly from other conditions. These properties are consistent with highly nonlinear NLS soliton seas previously observed in Currituck Sound, North Carolina [28]. To investigate the influence of directional interference on the soliton energy ratios, we applied a directional filtering technique, which reconstructs wave fields from measured directional power spectra using random phases and wave numbers obtained from the deep water dispersion relation. For each measurement, we simulated wave fields with 100 random phase realizations to assess the distribution of the soliton energy ratio under directional truncation. *The soliton energy ratios consistently remain high for all three cases measured at Eluanbi station even after directional interference has been removed, which qualifies them as soliton gases in our framework.* We believe that this is the first time that soliton gases have been identified in the open ocean. The cases measured at the Gueishandao and Xiaoliuqiu stations may or may not qualify as soliton gases with directionality taken into account. Due to the probabilistic nature of our directional filtering technique and the wideness of the distributions obtained for the cases, no definite answer can be given for these cases.

The reconstruction of the wave fields utilized directional power spectra derived from single-point buoy measurements. It was not exact due to the use of random phases and the deep water dispersion relation. Future work should therefore extend the present analysis to other measurement systems, such as radar or stereo-video systems, to obtain spatial data that can better resolve directional structure and phase information. Such data could also be used to verify the kinetic equations for soliton gases. Another important direction is to examine the influence of wind input and wave dissipation, as well as other factors that break the integrability assumption behind the NFT.

8

CONCLUSIONS AND RECOMMENDATIONS

CHAPTER ABSTRACT

In this final chapter, we assess the progress in this dissertation concerning the application of nonlinear Fourier transforms in hydrodynamics. We explore the significance of these developments and their interpretation. Additionally, we offer suggestions for future research that could enhance our understanding and application of NFT-based tools, leading to further advancements in the thesis of nonlinear water waves.

8.1. Conclusions

The nonlinear Fourier transform (NFT) has been extensively applied in the fields of fiber optics [22, 23, 91], and hydrodynamics [6, 28, 29, 154]. Several studies have successfully applied that the NFT to experimental data under relatively ideal conditions [65, 86], but it is also used as a signal processing tool for analyzing non-integrable systems [22]. Real-world ocean waves often deviate from the integrable framework due to directional spreading, wind effects, and other non-integrable effects. The impact of these effects on the nonlinear spectrum is not yet fully understood, limiting the practical application of the NFT to realistic ocean conditions. This thesis demonstrated NFT analysis on non-integrable field measurements and simulations and investigated how directional effects influence the nonlinear spectrum. Several datasets of ocean waves were considered: (1) field measurement data collected by buoys from the North Sea and the waters near Taiwan; (2) simulated time series generated from the JONSWAP spectrum with random phases; (3) simulated nonlinear wave fields derived from the High Order Spectral method; and (4) simulated linear wave fields with directional spreadings. Each dataset contains unique features that result in different nonlinear spectral characteristics when the NFT is applied. We briefly summarize the results of each chapter of this dissertation in the following.

We first discussed one of the most popular topics: rogue waves. Rogue waves are waves that appear from nowhere and disappear without a trace [71]. They are characterized by extremely large wave heights, which exceed twice the significant wave height. The impact of rogue waves on both coastal and offshore structures as well as ship management is of vital importance. Currently, the generation mechanisms of rogue waves are still under debate. Some scientists propose that rogue waves can be generated by the Benjamin-Feir instability, while others suggest that they result from linear focusing of regular waves. Additionally, various environmental factors can contribute to the formation of rogue waves, including crossing waves [108], ocean currents [109], winds [311], and bathymetry [111, 112, 114]. In Chapter 2, we collected rogue wave data from measurements taken at a buoy station with a water depth of 5,000 meters in the Philippine Sea. In total, 663 rogue waves were measured over more than 10 years of data, with the largest recorded wave height reaching 28.83 m. We also selected 600 non-rogue wave data for comparison. It was the first time in the literature that the NFT was applied to a large dataset of field-measured rogue waves. By applying the periodic NFT based on the nonlinear Schrödinger equation to these data, we classified the obtained nonlinear spectrum into four types: stable modes (sine or Stokes waves), small breathers, large breathers, and solitons. For the rogue wave data, we found that the majority class corresponded to stable mode spectra, which accounted for 75.1%. This finding that rogue waves are primarily generated through linear superposition aligns with [118, 175]. Furthermore, it complements the different observations in [28, 29], where the existence of unstable modes in the nonlinear spectrum was attributed to rogue waves. Another interesting finding is that a large portion (90.9%) of the rogue wave samples with maximum wave heights larger than 15 m are of the breather or soliton type. When analyzing the non-rogue samples a

similar picture was found. Meanwhile, we would like to emphasize some important considerations when applying the NFT to field measurement data. It is evident that the nonlinear equations governing deep water waves in the real ocean may differ from the nonlinear Schrödinger (NLS) equation, particularly under the assumptions of unidirectionality and narrow bandedness. Consequently, the nonlinear spectrum will change during the evolution, i.e. [35]. We thus highlight that we use the NFT as a signal processing tool, similar to the concepts applied in linear FFT. Nevertheless, while the evolution of the nonlinear spectrum may vary, it at least reveals the nonlinear spectral components of the current sea states, which represents a significant advancement over the linear FFT [7].

The NFT-based method effectively captures the nonlinear evolution of time and spatial series. It can predict behavior of the waves after they propagate over a certain distance, provided that the dynamics are fully governed by their corresponding partial differential equations. Even in non-ideal conditions (i.e. under multidirectional conditions [215]), the nonlinear spectrum remains representative if the distance is not too long and the non-integrable effects are not too large, suggesting that short-distance predictions are feasible. Therefore, in chapter 3, we first discussed the prediction of rogue waves in deep water under the ideal evolution by the NLS equation. Two predictors based on the splitting distance [24, 25, 189] and unstable modes [6, 28] were evaluated for predicting maximum wave height after evolution. Our results revealed that with suitably optimized coefficients, a NFT-based parameter based on the largest unstable mode has a good correlation with the overall maximum wave amplitude. We also proposed a new spectral criterion that has better correlation than other predictors for predicting maximum wave height.

Under ideal integrable conditions, if the wave dynamics are fully governed by its corresponding PDE, the obtained nonlinear spectrum remains invariant during evolution. Following the study by Slunyaev (2024), which stated that the NFT-based method can predict deep water waves for certain distances depending on directional spreading [215], we investigate whether the KdV equation for shallow water waves can represent wave dynamics for certain distances under directional spreading. Therefore, in Chapter 4, we first investigate the effectiveness of KdV-NFT in representing shallow water wave dynamics under different directional spreads. To generate various conditions, we use the High-Order Spectral Ocean (HOS-ocean) model [216] to generate wave fields with different directional spreads. By applying the NFT-KdV to extracted time series from simulated wave fields, we find that the KdV-soliton spectra remain quite stable for small directional spreading. For large directional spreading, the applicability is limited to short propagation time and distance. Moreover, we observed that except for strong spreading conditions, the largest soliton is more stable than the largest linear Fourier mode. This shows that even though the NFT might not fully capture the behavior of directional seas, it is still better than the traditional linear FFT. Such results are important to further interpret the results of real-world studies based on the KdV-NFT such as [34, 36, 55, 98, 214].

The study by Gelash et al. (2018) demonstrates that rogue waves emerging in a soliton gas are generated by multi-soliton collisions, many of which exhibit

spatial profiles closely resembling Peregrine-type solutions [254]. Therefore, we are particularly interested in identifying soliton gas sea states. The NLS soliton gases have been generated in physical experiments [65], but it was not clear what kind of sea states in the ocean might lead to soliton gases. In order to determine the wave parameters for sea states that lead to soliton gases, we began an investigation through numerical simulations, as shown in Chapter 5. Large numbers of surface wave elevations were generated using the JONSWAP spectrum, covering different developed stages of deep water waves. We found that a large Phillip's parameter α, a large peak enhancement parameter γ and a short peak period T_p are important factors for the occurrence of soliton gas-like conditions.

After identifying soliton gases from JONSWAP simulations, we further investigated the effects of directional spreading that break integrability through numerical simulations. The gap from idealized theory to realistic ocean conditions motivates this thesis as shown in Chapter 6. The soliton energy ratio derived from the nonlinear spectrum is used to identify soliton gas seas. By applying directional filtering to directional sidebands, we compare soliton energy ratios from original directional time series to those from filtered data. Results show that for small directional spreading, soliton energy ratios remain stable, but they decrease significantly with increasing directionality. Notably, in highly nonlinear soliton-dominated states, soliton energy concentrates in the main propagation direction, suggesting that robust soliton structures persist despite directional interference.

Soliton gases are widely studied in theory and experiments, and have been observed in natural lagoons. However, whether they naturally occur in the open ocean remained a question. We therefore subsequently investigated the existence of soliton gases in the real ocean, as discussed in Chapter 7. We considered field-measured data collected by buoys in Taiwan waters. All the data were selected based on intermediate deep water conditions ($k_0 h > 1.363$) and unimodal spectrum criteria, including 20,523 time series. We identify eleven measurements with extremely high soliton energy ratios. They are characterized by short-period waves with relatively small wave heights, accompanied by extreme steepness and Benjamin–Feir Index (BFI) values. Our results revealed that NLS soliton gas sea states do exist but are quite rare in the real ocean, accounting to around 0.054% in our dataset. Among them, three wave records from the Eluanbi station retain high soliton energy ratios after the directional filtering, confirming their identification as soliton gases.

8.2. Recommendations for Future Work

In this section we discuss some of the possible directions for further research on the topic of nonlinear Fourier transforms in hydrodynamics.

1). Evaluation of the application of the one-dimensional NFTs to directional seas using ocean surface measurements

This thesis evaluated the application of the NFT to directional seas using simulated wave fields. However, the real ocean presents more complexities, such as wave

breaking, broad directional spreading from multiple wind systems, and wave-current interactions. Typically, time series of surface waves are measured by buoys at a single location, resulting in a lack of spatial data for the entire wave field. Consequently, data on the evolution of wave fields is quite rare. With advancements in ocean observation technologies, such as radar, drones, and cameras, there is potential to collect such data for research. Further investigation on this topic could enhance the interpretation of NFT-based methods.

2). Development of NFTs based on the Boussinesq equation for wave refraction

The Boussinesq equation captures the essential nonlinear and dispersive effects of wave propagation in shallow to intermediate water depths similar to the KdV equation, but allows bi-directional propagation for more complex nearshore process. Popular nearshore models such as FUNWAVE, Xbeach, Delft3D and SMS that consider more real-world ocean waves effects such as wave breaking, wave refraction, and wave shoaling are based on the Boussinesq-type equations. The integrable Boussinesq equation is a specific case, which is strictly conservative and has exact integrability allowing a Lax pair formulation. The NFT for the Boussinesq equation has been limited in application because implementations break mathematical integrability. Future work investigating NFT-based spectral analysis on integrable Boussinesq equations and related non-integrable formulations could expand the applicability of NFT methods to diverse sea conditions.

3). Development of two-dimensional NFTs

While one-dimensional NFT applications have been successfully applied in this thesis, the extension to two dimensions remains an interesting topic. Theoretical two-dimensional nonlinear Fourier transforms (2D NFTs) are established for specific integrable systems, such as the Kadomtsev–Petviashvili equation [312], the Novikov-Veselov equation [313, 314], and the Davey–Stewartson equation [315]. However, practical applications to ocean waves are scarce due to the difficulty in matching realistic ocean conditions to the strict integrability constraints of these 2D mathematical models. Future work investigating the robustness of these 2D NFTs under realistic oceanic conditions is therefore essential.

BIBLIOGRAPHY

[1] Y.-C. Lee, S. Wahls, and M. Brühl. “Evaluation of Nonlinear Fourier-Based Maximum Wave Height Predictors Under the Nonlinear Schrödinger Equation”. In: *International Conference on Offshore Mechanics and Arctic Engineering*. Vol. 85901. American Society of Mechanical Engineers. 2022, V05BT06A060.

[2] Y.-C. Lee, M. Brühl, and S. Wahls. “When Do JONSWAP Spectra Lead to Soliton Gases in Deep Water Conditions?” In: *International Conference on Offshore Mechanics and Arctic Engineering*. Vol. 86878. American Society of Mechanical Engineers. 2023, V005T06A101.

[3] Y.-C. Lee, M. Brühl, D.-J. Doong, and S. Wahls. “Nonlinear Fourier classification of 663 rogue waves measured in the Philippine Sea”. In: *PloS one* 19.5 (2024), e0301709.

[4] Y.-C. Lee and S. Wahls. “Impact of directional spreading on nonlinear KdV-soliton spectra in intermediate water”. In: *Wave Motion* 137 (2025), p. 103542.

[5] M. S. Longuet-Higgins. “On the Statistical Distribution of the Heights of Sea Waves”. In: *Journal of Marine Research* 11.3 (1953), pp. 245–266.

[6] A. R. Osborne. *Nonlinear Ocean Waves and the Inverse Scattering Transform*. Vol. 97. International Geophysics. San Diego, CA: Academic Press, 2010. ISBN: 9780125286299.

[7] M. Bruehl, P. J. Prins, S. Ujvary, I. Barranco, S. Wahls, and P. L.-F. Liu. “Comparative analysis of bore propagation over long distances using conventional linear and KdV-based nonlinear Fourier transform”. In: *Wave Motion* 111 (2022), p. 102905.

[8] Y. Goda. *Random seas and design of maritime structures*. Vol. 33. World Scientific Publishing Company, 2010.

[9] M. J. Ablowitz, D. J. Kaup, A. C. Newell, and H. Segur. “The inverse scattering transform-Fourier analysis for nonlinear problems”. In: *Studies in Applied Mathematics* 53.4 (1974), pp. 249–315.

[10] N. J. Zabusky and M. D. Kruskal. “Interaction of" solitons" in a collisionless plasma and the recurrence of initial states”. In: *Physical Review Letters* 15.6 (1965), p. 240.

[11] C. S. Gardner, J. M. Greene, M. D. Kruskal, and R. M. Miura. “Method for solving the Korteweg-deVries equation”. In: *Physical Review Letters* 19.19 (1967), p. 1095.

[12] A. Shabat and V. Zakharov. “Exact theory of two-dimensional self-focusing and one-dimensional self-modulation of waves in nonlinear media”. In: *Sov. Phys. JETP* 34.1 (1972), p. 62.

[13] M. J. Ablowitz and H. Segur. *Solitons and the inverse scattering transform*. SIAM, 1981.

[14] G. G. Stokes. “On the theory of oscillatory waves”. In: *Trans. Cam. Philos. Soc.* 8 (1847), pp. 441–455.

[15] M. S. Longuet-Higgins. “The effect of non-linearities on statistical distributions in the theory of sea waves”. In: *Journal of fluid mechanics* 17.3 (1963), pp. 459–480.

[16] P. A. Janssen. “Nonlinear four-wave interactions and freak waves”. In: *Journal of Physical Oceanography* 33.4 (2003), pp. 863–884.

[17] M. Bruehl and H. Oumeraci. “Analysis of long-period cosine-wave dispersion in very shallow water using nonlinear Fourier transform based on KdV equation”. In: *Applied Ocean Research* 61 (2016), pp. 81–91.

[18] A. V. Slunyaev and V. I. Shrira. “On the highest non-breaking wave in a group: fully nonlinear water wave breathers versus weakly nonlinear theory”. In: *Journal of Fluid Mechanics* 735 (2013), pp. 203–248.

[19] P. D. Lax. “Integrals of nonlinear equations of evolution and solitary waves”. In: *Communications on Pure and Applied Mathematics* 21.5 (1968), pp. 467–490.

[20] P. Ryczkowski, M. Närhi, C. Billet, J.-M. Merolla, G. Genty, and J. M. Dudley. “Real-time full-field characterization of transient dissipative soliton dynamics in a mode-locked laser”. In: *Nature Photonics* 12.4 (2018), pp. 221–227.

[21] I. Chekhovskoy, O. V. Shtyrina, M. P. Fedoruk, S. B. Medvedev, and S. K. Turitsyn. “Nonlinear Fourier transform for analysis of coherent structures in dissipative systems”. In: *Physical Review Letters* 122.15 (2019), p. 153901.

[22] S. Sugavanam, M. K. Kopae, J. Peng, J. E. Prilepsky, and S. K. Turitsyn. “Analysis of laser radiation using the Nonlinear Fourier transform”. In: *Nature Communications* 10.1 (2019), p. 5663.

[23] S. Turitsyn, I. Chekhovskoy, and M. Fedoruk. “Nonlinear Fourier transform for analysis of optical spectral combs”. In: *Physical Review E* 103.2 (2021), p. L020202.

[24] A. Islas and C. Schober. “Predicting rogue waves in random oceanic sea states”. In: *Physics of Fluids* 17.3 (2005), p. 031701.

[25] A. Calini and C. M. Schober. “Characterizing JONSWAP rogue waves and their statistics via inverse spectral data”. In: *Wave Motion* 71 (2017), pp. 5–17.

[26] A. Osborne and M. Petti. “Laboratory-generated, shallow-water surface waves: Analysis using the periodic, inverse scattering transform”. In: *Physics of Fluids* 6.5 (1994), pp. 1727–1744.

[27] S. Randoux, P. Suret, A. Chabchoub, B. Kibler, and G. El. “Nonlinear spectral analysis of Peregrine solitons observed in optics and in hydrodynamic experiments”. In: *Physical Review E* 98.2 (2018), p. 022219.

[28] A. R. Osborne, D. T. Resio, A. Costa, S. Ponce de León, and E. Chirivı̀. “Highly nonlinear wind waves in Currituck Sound: dense breather turbulence in random ocean waves”. In: *Ocean Dynamics* 69.2 (2019), pp. 187–219.

[29] M. Onorato, L. Cavaleri, S. Randoux, P. Suret, M. I. Ruiz, M. de Alfonso, and A. Benetazzo. “Observation of a giant nonlinear wave-packet on the surface of the ocean”. In: *Scientific Reports* 11.1 (2021), p. 23606.

[30] V. Zakharov. “Kinetic equation for solitons”. In: *Sov. Phys. JETP* 33.3 (1971), pp. 538–540.

[31] G. El and A. Kamchatnov. “Kinetic equation for a dense soliton gas”. In: *Physical Review Letters* 95.20 (2005), p. 204101.

[32] G. A. El, A. M. Kamchatnov, M. V. Pavlov, and S. Zykov. “Kinetic equation for a soliton gas and its hydrodynamic reductions”. In: *Journal of Nonlinear Science* 21 (2011), pp. 151–191.

[33] P. Suret, S. Randoux, A. Gelash, D. Agafontsev, B. Doyon, and G. El. “Soliton gas: Theory, numerics, and experiments”. In: *Physical Review E* 109.6 (2024), p. 061001.

[34] I. Teutsch, M. Brühl, R. Weisse, and S. Wahls. “Contribution of solitons to enhanced rogue wave occurrence in shallow depths: a case study in the southern North Sea”. In: *Natural Hazards and Earth System Sciences* 23.6 (2023), pp. 2053–2073.

[35] A. Tikan, F. Bonnefoy, G. Roberti, G. El, A. Tovbis, G. Ducrozet, A. Cazaubiel, G. Prabhudesai, G. Michel, F. Copie, *et al.* “Prediction and manipulation of hydrodynamic rogue waves via nonlinear spectral engineering”. In: *Physical Review Fluids* 7.5 (2022), p. 054401.

[36] A. Costa, A. R. Osborne, D. T. Resio, S. Alessio, E. Chrivi, E. Saggese, K. Bellomo, and C. E. Long. “Soliton turbulence in shallow water ocean surface waves”. In: *Physical Review Letters* 113.10 (2014), p. 108501.

[37] G. B. Whitham. *Linear and Nonlinear Waves*. John Wiley & Sons, 1974.

[38] L. Euler. “Principles of the Motion of Fluids”. In: *Memoirs of the Academy of Sciences of Berlin* (1757).

[39] J. C. Maxwell. “A Dynamical Theory of the Electromagnetic Field”. In: *Philosophical Transactions of the Royal Society* 155 (1865), pp. 459–512.

[40] E. Schrödinger. “An Undulatory Theory of the Mechanics of Atoms and Molecules”. In: *Physical Review* 28.6 (1926), pp. 1049–1070.

[41] H. Brezis and F. Browder. “Partial differential equations in the 20th century”. In: *Advances in Mathematics* 135.1 (1998), pp. 76–144.

[42] A. R. Oliveira. “D’Alembert and the wave equation”. In: *The International Conference of IFToMM ITALY*. Springer. 2020, pp. 29–36.

[43] U. Dierkes, S. Hildebrandt, A. Küster, and O. Wohlrab. “Minimal surfaces”. In: *Minimal Surfaces I: Boundary Value Problems*. Springer, 2010, pp. 53–88.

[44] P.-S. Laplace. *Traité de Mécanique Céleste*. Bachelier, 1825.

[45] J. B. J. Fourier. *Théorie analytique de la chaleur*. Firmin Didot, 1822.

[46] C. Navier. “Mémoire sur les lois du mouvement des fluides”. In: *Mémoires de l’Académie Royale des Sciences de l’Institut de France* 6.1823 (1823), pp. 389–440.

[47] G. G. Stokes. “On the theories of the internal friction of fluids in motion”. In: *Transactions of the Cambridge Philosophical Society* (1845).

[48] D. J. Korteweg and G. De Vries. “XLI. On the change of form of long waves advancing in a rectangular canal, and on a new type of long stationary waves”. In: *The London, Edinburgh, and Dublin Philosophical Magazine and Journal of Science* 39.240 (1895), pp. 422–443.

[49] V. E. Zakharov. “Stability of periodic waves of finite amplitude on the surface of a deep fluid”. In: *Journal of Applied Mechanics and Technical Physics* 9.2 (1968), pp. 190–194.

[50] Anon. “Soliton wave receives crowd of admirers”. In: *Nature* 376 (1995). News article, p. 373.

[51] J. Boussinesq. *Essai sur la théorie des eaux courantes*. Impr. nationale, 1877.

[52] J. Boussinesq. “Théorie de l’intumescence liquide appelée onde solitaire ou de translation se propageant dans un canal rectangulaire”. In: *CR Acad. Sci. Paris* 72.755-759 (1871), p. 1871.

[53] J. Boussinesq. “Théorie des ondes et des remous qui se propagent le long d’un canal rectangulaire horizontal, en communiquant au liquide contenu dans ce canal des vitesses sensiblement pareilles de la surface au fond”. In: *Journal de mathématiques pures et appliquées* 17 (1872), pp. 55–108.

[54] A. Osborne. “The inverse scattering transform: tools for the nonlinear Fourier analysis and filtering of ocean surface waves”. In: *Chaos, Solitons & Fractals* 5.12 (1995), pp. 2623–2637.

[55] A. Osborne, M. Serio, L. Bergamasco, and L. Cavaleri. “Solitons, cnoidal waves and nonlinear interactions in shallow-water ocean surface waves”. In: *Physica D: Nonlinear Phenomena* 123.1 (1998). Annual International Conference of the Center for Nonlinear Studies, pp. 64–81. ISSN: 0167-2789.

[56] T. B. Benjamin. “Instability of periodic wavetrains in nonlinear dispersive systems”. In: *Proceedings of the Royal Society of London. Series A. Mathematical and Physical Sciences* 299.1456 (1967), pp. 59–76.

[57] R. Johnson. “On the modulation of water waves in the neighbourhood of kh ≈ 1.363”. In: *Proceedings of the Royal Society of London. A. Mathematical and Physical Sciences* 357.1689 (1977), pp. 131–141.

[58] R. Cienfuegos, P. A. Catalán, R. P. Flores, M. Guerra, F. Lucero, J. Galaz, S. Wahls, P. Díaz, R. Gómez, and C. Esparza. “Soliton gas dynamics and rogue wave enhancement in a natural coastal environment”. In: *Physical Review Research* 7.4 (2025), p. 043129.

[59] R. T. Hudspeth and J. R. Medina. “Wave group analysis by the Hilbert transform”. In: *Coastal Engineering 1988*. Coastal Engineering 1988, 1989, pp. 884–898.

[60] J. R. Medina and R. Hudspeth. “A review of the analyses of ocean wave groups”. In: *Coastal Engineering* 14.6 (1990), pp. 515–542.

[61] L. Marple. “Computing the discrete-time" analytic" signal via FFT”. In: *IEEE Transactions on signal processing* 47.9 (1999), pp. 2600–2603.

[62] H. Hasimoto and H. Ono. “Nonlinear modulation of gravity waves”. In: *Journal of the Physical Society of Japan* 33.3 (1972), pp. 805–811.

[63] S. Wahls, M. Bruehl, Y.-M. Fan, and C.-J. Huang. “Nonlinear Fourier Analysis of Free-Surface Buoy Data Using the Software Library FNFT”. In: *International Conference on Offshore Mechanics and Arctic Engineering*. Vol. 84386. American Society of Mechanical Engineers. 2020, V06BT06A070.

[64] A. Slunyaev. “A high-order nonlinear envelope equation for gravity waves in finite-depth water”. In: *Journal of Experimental and Theoretical Physics* 101 (2005), pp. 926–941.

[65] P. Suret, A. Tikan, F. Bonnefoy, F. Copie, G. Ducrozet, A. Gelash, G. Prabhudesai, G. Michel, A. Cazaubiel, E. Falcon, *et al.* “Nonlinear spectral synthesis of soliton gas in deep-water surface gravity waves”. In: *Physical Review Letters* 125.26 (2020), p. 264101.

[66] J. M. Dudley, F. Dias, M. Erkintalo, and G. Genty. “Instabilities, breathers and rogue waves in optics”. In: *Nature Photonics* 8.10 (2014), pp. 755–764.

[67] K. B. Dysthe and K. Trulsen. “Note on breather type solutions of the NLS as models for freak-waves”. In: *Physica Scripta* 1999.T82 (1999), p. 48.

[68] V. I. Shrira and V. V. Geogjaev. “What makes the Peregrine soliton so special as a prototype of freak waves?” In: *Journal of Engineering Mathematics* 67.1 (2010), pp. 11–22.

[69] M. Onorato, D. Proment, G. Clauss, and M. Klein. “Rogue waves: from nonlinear Schrödinger breather solutions to sea-keeping test”. In: *PloS one* 8.2 (2013), e54629.

[70] D. H. Peregrine. “Water waves, nonlinear Schrödinger equations and their solutions”. In: *The ANZIAM Journal* 25.1 (1983), pp. 16–43.

[71] N. Akhmediev, A. Ankiewicz, and M. Taki. “Waves that appear from nowhere and disappear without a trace”. In: *Physics Letters A* 373.6 (2009), pp. 675–678.

[72] E. A. Kuznetsov. “Solitons in a parametrically unstable plasma”. In: *Akademiia Nauk SSSR Doklady*. Vol. 236. 1977, pp. 575–577.

[73] Y.-C. Ma. “The perturbed plane-wave solutions of the cubic Schrödinger equation”. In: *Studies in Applied Mathematics* 60.1 (1979), pp. 43–58.

[74] N. Akhmediev, V. Eleonskii, and N. Kulagin. “Generation of periodic trains of picosecond pulses in an optical fiber: exact solutions”. In: *Sov. Phys. JETP* 62.5 (1985), pp. 894–899.

[75] B. Kibler, J. Fatome, C. Finot, G. Millot, G. Genty, B. Wetzel, N. Akhmediev, F. Dias, and J. M. Dudley. “Observation of Kuznetsov-Ma soliton dynamics in optical fibre”. In: *Scientific Reports* 2.1 (2012), p. 463.

[76] T. B. Benjamin and J. E. Feir. “The disintegration of wave trains on deep water Part 1. Theory”. In: *Journal of Fluid Mechanics* 27.3 (1967), pp. 417–430.

[77] N. Akhmediev and V. Korneev. “Modulation instability and periodic solutions of the nonlinear Schrödinger equation”. In: *Theoretical and Mathematical Physics* 69.2 (1986), pp. 1089–1093.

[78] N. N. Akhmediev, V. M. Eleonskii, and N. Kulagin. “Exact first-order solutions of the nonlinear Schrödinger equation”. In: *Theoretical and Mathematical Physics* 72.2 (1987), pp. 809–818.

[79] V. E. Zakharov and L. A. Ostrovsky. “Modulation instability: The beginning”. In: *Physica D: Nonlinear Phenomena* 238.5 (2009), pp. 540–548.

[80] A. Chabchoub, N. Hoffmann, and N. Akhmediev. “Rogue wave observation in a water wave tank”. In: *Physical Review Letters* 106.20 (2011), p. 204502.

[81] A. Chabchoub, N. Hoffmann, M. Onorato, and N. Akhmediev. “Super rogue waves: observation of a higher-order breather in water waves”. In: *Physical Review X* 2.1 (2012), p. 011015.

[82] A. Chabchoub and M. Fink. “Time-reversal generation of rogue waves”. In: *Physical Review Letters* 112.12 (2014), p. 124101.

[83] G. Michel, F. Bonnefoy, G. Ducrozet, G. Prabhudesai, A. Cazaubiel, F. Copie, A. Tikan, P. Suret, S. Randoux, and E. Falcon. “Emergence of Peregrine solitons in integrable turbulence of deep water gravity waves”. In: *Physical Review Fluids* 5.8 (2020), p. 082801.

[84] G. El. “The thermodynamic limit of the Whitham equations”. In: *Physics Letters A* 311.4-5 (2003), pp. 374–383.

[85] G. El and A. Tovbis. “Spectral theory of soliton and breather gases for the focusing nonlinear Schrödinger equation”. In: *Physical Review E* 101.5 (2020), p. 052207.

[86] I. Redor, E. Barthélemy, H. Michallet, M. Onorato, and N. Mordant. “Experimental evidence of a hydrodynamic soliton gas”. In: *Physical Review Letters* 122.21 (2019), p. 214502.

[87] I. Redor, E. Barthélemy, N. Mordant, and H. Michallet. “Analysis of soliton gas with large-scale video-based wave measurements”. In: *Experiments in Fluids* 61 (2020), pp. 1–14.

[88] L. Fache, F. Bonnefoy, G. Ducrozet, F. Copie, F. Novkoski, G. Ricard, G. Roberti, E. Falcon, P. Suret, G. El, *et al.* “Interaction of soliton gases in deep-water surface gravity waves”. In: *Physical Review E* 109.3 (2024), p. 034207.

[89] M. J. Ablowitz, M. Ablowitz, B. Prinari, and A. Trubatch. *Discrete and continuous nonlinear Schrödinger systems*. Vol. 302. Cambridge University Press, 2004.

[90] S. Wahls and H. V. Poor. “Fast numerical nonlinear Fourier transforms”. In: *IEEE Transactions on Information Theory* 61.12 (2015), pp. 6957–6974.

[91] S. K. Turitsyn, J. E. Prilepsky, S. T. Le, S. Wahls, L. L. Frumin, M. Kamalian, and S. A. Derevyanko. “Nonlinear Fourier transform for optical data processing and transmission: advances and perspectives”. In: *Optica* 4.3 (2017), pp. 307–322.

[92] S. Randoux, P. Suret, and G. El. “Inverse scattering transform analysis of rogue waves using local periodization procedure”. In: *Scientific Reports* 6.1 (2016), pp. 1–11.

[93] V. Kotlyarov. “Periodic problem for the Schrödinger nonlinear equation”. In: *Voprosy Matematicheskoi Fiziki i Funkcionalnogo Analiza* 1 (1976), pp. 121–31.

[94] A. I. Bobenko. *Computational approach to Riemann surfaces*. Vol. 2013. Springer Science & Business Media, 2011.

[95] M. G. Forest and J.-E. Lee. “Geometry and modulation theory for the periodic nonlinear Schrodinger equation”. In: *Oscillation Theory, Computation, and Methods of Compensated Compactness*. Springer, 1986, pp. 35–69.

[96] E. D. Belokolos, A. I. Bobenko, V. Z. Enolskii, A. R. Its, and V. B. Matveev. *Algebro-geometric approach to nonlinear integrable equations*. Vol. 1994. Springer, 1994.

[97] A. Osborne and E. Segre. “The numerical inverse scattering transform for the periodic Korteweg-de Vries equation”. In: *Physics Letters A* 173.2 (1993), pp. 131–142.

[98] A. R. Osborne, E. Segre, G. Boffetta, and L. Cavaleri. “Soliton basis states in shallow-water ocean surface waves”. In: *Phys. Rev. Lett.* 67 (5 July 1991), pp. 592–595.

[99] A. Osborne and L. Bergamasco. “The solitons of Zabusky and Kruskal revisited: Perspective in terms of the periodic spectral transform”. In: *Physica D: Nonlinear Phenomena* 18.1-3 (1986), pp. 26–46.

[100] M. Brühl. “Direct and inverse nonlinear Fourier transform based on the KortewegdeVries equation (KdV-NLFT)-A spectral analysis of nonlinear surface waves in shallow water”. PhD thesis. Dissertation, Braunschweig, Technische Universität Braunschweig, 2014.

[101] I. J. Losada, J. L. Lara, R. Guanche, and J. M. Gonzalez-Ondina. “Numerical analysis of wave overtopping of rubble mound breakwaters”. In: *Coastal engineering* 55.1 (2008), pp. 47–62.

[102] A. Osborne and L. Bergamasco. “The small-amplitude limit of the spectral transform for the periodic Korteweg-de Vries equation”. In: *Il Nuovo Cimento B (1971-1996)* 85.2 (1985), pp. 229–243.

[103] Y.-C. Lee and S. Wahls. “Field observation of soliton gases in the deep open ocean”. In: *Results in Physics* (2026), p. 108726.

[104] W. Rosenthal and S. Lehner. “Rogue Waves: Results of the MaxWave Project”. In: *Journal of Offshore Mechanics and Arctic Engineering* 130.2 (2008).

[105] J. Gemmrich and L. Cicon. “Generation mechanism and prediction of an observed extreme rogue wave”. In: *Scientific Reports* 12.1 (2022), pp. 1–10.

[106] M. Onorato, A. R. Osborne, M. Serio, and L. Cavaleri. “Modulational instability and non-Gaussian statistics in experimental random water-wave trains”. In: *Physics of Fluids* 17.7 (2005), p. 078101.

[107] M. Onorato, A. R. Osborne, and M. Serio. “Modulational Instability in Crossing Sea States: A Possible Mechanism for the Formation of Freak Waves”. In: *Physical Review Letters* 96.1 (2006), p. 014503.

[108] O. Gramstad, E. Bitner-Gregersen, K. Trulsen, and J. C. Nieto Borge. “Modulational instability and rogue waves in crossing sea states”. In: *Journal of Physical Oceanography* 48.6 (2018), pp. 1317–1331.

[109] I. Lavrenov. “The wave energy concentration at the Agulhas current off South Africa”. In: *Natural hazards* 17.2 (1998), pp. 117–127.

[110] L. Cavaleri, L. Bertotti, L. Torrisi, E. Bitner-Gregersen, M. Serio, and M. Onorato. “Rogue waves in crossing seas: The Louis Majesty accident”. In: *Journal of Geophysical Research: Oceans* 117.C11 (2012).

[111] K. Trulsen, H. Zeng, and O. Gramstad. “Laboratory evidence of freak waves provoked by non-uniform bathymetry”. In: *Physics of Fluids* 24.9 (2012), p. 097101.

[112] C. T. Bolles, K. Speer, and M. Moore. “Anomalous wave statistics induced by abrupt depth change”. In: *Physical Review Fluids* 4.1 (2019), p. 011801.

[113] L. Zou, A. Wang, Z. Wang, Y. Pei, and X. Liu. “Experimental study of freak waves due to three-dimensional island terrain in random wave”. In: *Acta Oceanologica Sinica* 38.6 (2019), pp. 92–99.

[114] A. Wang, A. Ludu, Z. Zong, L. Zou, and Y. Pei. “Experimental study of breathers and rogue waves generated by random waves over non-uniform bathymetry”. In: *Physics of Fluids* 32.8 (2020), p. 087109.

[115] M. Onorato, S. Residori, U. Bortolozzo, A. Montina, and F. Arecchi. “Rogue waves and their generating mechanisms in different physical contexts”. In: *Physics Reports* 528.2 (2013), pp. 47–89.

[116] T. A. Adcock and P. H. Taylor. “The physics of anomalous (’rogue’) ocean waves”. In: *Reports on Progress in Physics* 77.10 (2014), p. 105901.

[117] J. M. Dudley, G. Genty, A. Mussot, A. Chabchoub, and F. Dias. “Rogue waves and analogies in optics and oceanography”. In: *Nature Reviews Physics* 1.11 (2019), pp. 675–689.

[118] D. Häfner, J. Gemmrich, and M. Jochum. “Real-world rogue wave probabilities”. In: *Scientific Reports* 11.1 (2021), p. 10084.

[119] G. Lindgren and I. Rychlik. “Wave characteristic distributions for Gaussian waves wave length, amplitude and steepness”. In: *Ocean Engineering* 9.5 (1982), pp. 411–432.

[120] A. Naess. “On the distribution of crest to trough wave heights”. In: *Ocean Engineering* 12.3 (1985), pp. 221–234.

[121] M. A. Tayfun. “Narrow-band nonlinear sea waves”. In: *Journal of Geophysical Research: Oceans* 85.C3 (1980), pp. 1548–1552.

[122] M. Prevosto. “Effect of directional spreading and spectral bandwidth on the nonlinearity of the irregular waves”. In: *ISOPE International Ocean and Polar Engineering Conference*. ISOPE. 1998, ISOPE–I.

[123] G. Z. Forristall. “Wave crest distributions: Observations and second-order theory”. In: *Journal of Physical Oceanography* 30.8 (2000), pp. 1931–1943.

[124] G. Z. Forristall. “On the statistical distribution of wave heights in a storm”. In: *Journal of Geophysical Research: Oceans* 83.C5 (1978), pp. 2353–2358.

[125] M. Prevosto, H. E. Krogstad, and A. Robin. “Probability distributions for maximum wave and crest heights”. In: *Coastal Engineering* 40.4 (2000), pp. 329–360.

[126] N. Mori and P. A. Janssen. “On kurtosis and occurrence probability of freak waves”. In: *Journal of Physical Oceanography* 36.7 (2006), pp. 1471–1483.

[127] M. A. Tayfun and F. Fedele. “Wave-height distributions and nonlinear effects”. In: *Ocean Engineering* 34.11-12 (2007), pp. 1631–1649.

[128] M. A. Tayfun. “Distributions of envelope and phase in wind waves”. In: *Journal of Physical Oceanography* 38.12 (2008), pp. 2784–2800.

[129] S. Mendes, A. Scotti, and P. Stansell. “On the physical constraints for the exceeding probability of deep water rogue waves”. In: *Applied Ocean Research* 108 (2021), p. 102402.

[130] N. Fonseca. “Prediction of ship dynamic loads in ship in heavy weather”. In: *Proceedings of the conference on design and operation for abnormal conditions II. RINA, London, 2001*. 2001.

[131] C. Guedes Soares, N. Fonseca, R. Pascoal, G. F. Clauss, C. E. Schmittner, and J. Hennig. “Analysis of design wave loads on an FPSO accounting for abnormal waves”. In: *J. Offshore Mech. Arct. Eng.* (2006).

[132] A. Cattrell, M. Srokosz, B. Moat, and R. Marsh. “Can rogue waves be predicted using characteristic wave parameters?” In: *Journal of Geophysical Research: Oceans* 123.8 (2018), pp. 5624–5636.

[133] M. Onorato, A. R. Osborne, M. Serio, and S. Bertone. “Freak waves in random oceanic sea states”. In: *Physical Review Letters* 86.25 (2001), p. 5831.

[134] O. Gramstad and K. Trulsen. “Influence of crest and group length on the occurrence of freak waves”. In: *Journal of Fluid Mechanics* 582 (2007), pp. 463–472.

[135] P. Janssen and J.-R. Bidlot. *On the extension of the freak wave warning system and its verification*. European Centre for Medium-Range Weather Forecasts Reading, UK, 2009.

[136] N. Akhmediev, A. Ankiewicz, J. Soto-Crespo, and J. M. Dudley. “Rogue wave early warning through spectral measurements?” In: *Physics Letters A* 375.3 (2011), pp. 541–544.

[137] N. Akhmediev, J. M. Soto-Crespo, A. Ankiewicz, and N. Devine. “Early detection of rogue waves in a chaotic wave field”. In: *Physics Letters A* 375.33 (2011), pp. 2999–3001.

[138] J. Liu, X. Feng, and J. Cui. “Experimental study of extreme waves based on nonlinear Schrödinger equation under background of a random sea”. In: *Physics of Fluids* 35.4 (2023).

[139] A. Chabchoub, N. Hoffmann, H. Branger, C. Kharif, and N. Akhmediev. “Experiments on wind-perturbed rogue wave hydrodynamics using the Peregrine breather model”. In: *Physics of Fluids* 25.10 (2013).

[140] C. Bayındır. “Early detection of rogue waves by the wavelet transforms”. In: *Physics Letters A* 380.1-2 (2016), pp. 156–161.

[141] R. Fu, Y. Ma, G. Dong, and M. Perlin. “A wavelet-based wave group detector and predictor of extreme events over unidirectional sloping bathymetry”. In: *Ocean Engineering* 229 (2021), p. 108936.

[142] W. Cousins, M. Onorato, A. Chabchoub, and T. P. Sapsis. “Predicting ocean rogue waves from point measurements: An experimental study for unidirectional waves”. In: *Physical Review E* 99.3 (2019), p. 032201.

[143] T. Breunung and B. Balachandran. “Data-driven, high resolution ocean wave forecasting and extreme wave predictions”. In: *Ocean Engineering* 268 (2023), p. 113271.

[144] S. Trillo, G. Deng, G. Biondini, M. Klein, G. Clauss, A. Chabchoub, and M. Onorato. “Experimental observation and theoretical description of multisoliton fission in shallow water”. In: *Physical Review Letters* 117.14 (2016), p. 144102.

[145] A. R. Osborne. “Breather turbulence: exact spectral and stochastic solutions of the nonlinear schrödinger equation”. In: *Fluids* 4.2 (2019), p. 72.

[146] E. Tracy and H. Chen. “Nonlinear self-modulation: An exactly solvable model”. In: *Physical Review A* 37.3 (1988), p. 815.

[147] I. Teutsch, R. Weisse, J. Moeller, and O. Krueger. “A statistical analysis of rogue waves in the southern North Sea”. In: *Natural Hazards and Earth System Sciences* 20.10 (2020), pp. 2665–2680.

[148] N. N. Akhmediev, A. Ankiewicz, *et al. Nonlinear pulses and beams*. Springer, 1997.

[149] J. M. Soto-Crespo, N. Devine, and N. Akhmediev. “Integrable turbulence and rogue waves: breathers or solitons?” In: *Physical Review Letters* 116.10 (2016), p. 103901.

[150] N. Akhmediev, J. Soto-Crespo, and A. Ankiewicz. “How to excite a rogue wave”. In: *Physical Review A* 80.4 (2009), p. 043818.

[151] N. Akhmediev, J. M. Soto-Crespo, and A. Ankiewicz. “Extreme waves that appear from nowhere: on the nature of rogue waves”. In: *Physics Letters A* 373.25 (2009), pp. 2137–2145.

[152] S. Toenger, T. Godin, C. Billet, F. Dias, M. Erkintalo, G. Genty, and J. M. Dudley. “Emergent rogue wave structures and statistics in spontaneous modulation instability”. In: *Scientific Reports* 5.1 (2015), pp. 1–8.

[153] A. Its and V. Kotljarov. “Explicit formulas for solutions of Schrodinger nonlinear equation”. In: *Dopovidi Akademii Nauk Ukrainskoi Rsr Seriya A-Fiziko-Matematichni Ta Technichni Nauki* 11 (1976), pp. 965–968.

[154] A. Slunyaev. “Persistence of hydrodynamic envelope solitons: Detection and rogue wave occurrence”. In: *Physics of Fluids* 33.3 (2021), p. 036606.

[155] A. Chabchoub, K. Mozumi, N. Hoffmann, A. V. Babanin, A. Toffoli, J. N. Steer, T. S. van den Bremer, N. Akhmediev, M. Onorato, and T. Waseda. "Directional soliton and breather beams". In: *Proceedings of the National Academy of Sciences* 116.20 (2019), pp. 9759–9763.

[156] T. Waseda, S. Watanabe, W. Fujimoto, T. Nose, T. Kodaira, and A. Chabchoub. "Directional coherent wave group from an assimilated non-linear wavefield". In: *Frontiers in Physics* 9 (2021), p. 622303.

[157] Y. He, A. Slunyaev, N. Mori, and A. Chabchoub. "Experimental evidence of nonlinear focusing in standing water waves". In: *Physical Review Letters* 129.14 (2022), p. 144502.

[158] A. Slunyaev. "Nonlinear analysis and simulations of measured freak wave time series". In: *European Journal of Mechanics-B/Fluids* 25.5 (2006), pp. 621–635.

[159] C. G. Soares, Z. Cherneva, and E. Antão. "Characteristics of abnormal waves in North Sea storm sea states". In: *Applied Ocean Research* 25.6 (2003), pp. 337–344.

[160] C. Kharif, E. Pelinovsky, and A. Slunyaev. *Rogue waves in the ocean*. Springer Science & Business Media, 2008.

[161] G. Z. Forristall and K. C. Ewans. "Worldwide measurements of directional wave spreading". In: *Journal of Atmospheric and Oceanic Technology* 15.2 (1998), pp. 440–469.

[162] T. Waseda, H. Tamura, and T. Kinoshita. "Freakish sea index and sea states during ship accidents". In: *Journal of Marine Science and Technology* 17 (2012), pp. 305–314.

[163] Y. Goda. "Numerical experiments on wave statistics with spectral simulation". In: *Report Port Harbour Research Institute* 9 (1970), pp. 3–57.

[164] N. Mori, M. Onorato, and P. A. Janssen. "On the estimation of the kurtosis in directional sea states for freak wave forecasting". In: *Journal of Physical Oceanography* 41.8 (2011), pp. 1484–1497.

[165] D. J. Doong, S. H. Chen, C. C. Kao, B. C. Lee, and S. P. Yeh. "Data quality check procedures of an operational coastal ocean monitoring network". In: *Ocean Engineering* 34.2 (2007), pp. 234–246.

[166] D.-J. Doong, B.-C. Lee, and C. C. Kao. "Wave measurements using GPS velocity signals". In: *Sensors* 11.1 (2011), pp. 1043–1058.

[167] M. Earle and K. Bush. "Strapped-down accelerometer effects on NDBO wave measurements". In: *OCEANS 82*. IEEE. 1982, pp. 838–848.

[168] N. Lang. "The empirical determination of a noise function for NDBC buoys with strapped-down accelerometers". In: *OCEANS'87*. IEEE. 1987, pp. 225–228.

[169] Y.-P. Lin, C.-J. Huang, S.-H. Chen, D.-J. Doong, and C. C. Kao. "Development of a GNSS buoy for monitoring water surface elevations in estuaries and coastal areas". In: *Sensors* 17.1 (2017), p. 172.

[170] C.-C. Kao, H. Chien, M.-D. Chiou, and L. Chuang. “Error analysis of the wave directional spectrum measurement by Disc Buoys.” In: *Ocean Engineering/Haiyang Gongcheng* 21.1 (2003), pp. 24–33.

[171] M. Conforti, A. Mussot, A. Kudlinski, S. Trillo, and N. Akhmediev. “Doubly periodic solutions of the focusing nonlinear Schrödinger equation: Recurrence, period doubling, and amplification outside the conventional modulation-instability band”. In: *Physical Review A* 101.2 (2020), p. 023843.

[172] N. Akhmediev and J. Soto-Crespo. “The IST spectral portraits of the first order doubly periodic solutions of the nonlinear Schrödinger equation”. In: *Physica Scripta* 95.11 (2020), p. 115202.

[173] P. G. Grinevich and P. M. Santini. “The finite-gap method and the periodic NLS Cauchy problem of anomalous waves for a finite number of unstable modes”. In: *Russian Mathematical Surveys* 74.2 (2019), p. 211.

[174] N. Ercolani, M. Forest, and D. W. McLaughlin. “Geometry of the modulational instability: III. Homoclinic orbits for the periodic sine-Gordon equation”. In: *Physica D: Nonlinear Phenomena* 43.2-3 (1990), pp. 349–384.

[175] F. Fedele, J. Brennan, S. Ponce de León, J. Dudley, and F. Dias. “Real world ocean rogue waves explained without the modulational instability”. In: *Scientific Reports* 6.1 (2016), pp. 1–11.

[176] J. H. Michell. “XLIV. The highest waves in water”. In: *The London, Edinburgh, and Dublin Philosophical Magazine and Journal of Science* 36.222 (1893), pp. 430–437.

[177] I. Alber. “The effects of randomness on the stability of two-dimensional surface wavetrains”. In: *Proceedings of the Royal Society of London. A. Mathematical and Physical Sciences* 363.1715 (1978), pp. 525–546.

[178] K. Dysthe, H. E. Krogstad, and P. Müller. “Oceanic rogue waves”. In: *Annu. Rev. Fluid Mech.* 40 (2008), pp. 287–310.

[179] S. Hayer and O. J. Andersen. “Freak waves: rare realizations of a typical population or typical realizations of a rare population?” In: *The Tenth International Offshore and Polar Engineering Conference*. OnePetro. 2000.

[180] A. Karin Magnusson and M. A. Donelan. “The Andrea wave characteristics of a measured North Sea rogue wave”. In: *Journal of Offshore Mechanics and Arctic Engineering* 135.3 (2013).

[181] J. Skourup, N.-E. Hansen, and K. Andreasen. “Non-Gaussian extreme waves in the central North Sea”. In: *Oceanographic Literature Review* 3.45 (1998), p. 452.

[182] J. M. Dudley, G. Genty, F. Dias, B. Kibler, and N. Akhmediev. “Modulation instability, Akhmediev Breathers and continuous wave supercontinuum generation”. In: *Optics express* 17.24 (2009), pp. 21497–21508.

[183] N. N. Akhmediev and A. Ankiewicz. *Solitons: nonlinear pulses and beams*. Chapman & Hall, 1997.

[184] J. Soto-Crespo, N. Devine, and N. Akhmediev. “Adiabatic transformation of continuous waves into trains of pulses”. In: *Physical Review A* 96.2 (2017), p. 023825.

[185] M. Christou and K. Ewans. “Field measurements of rogue water waves”. In: *Journal of Physical Oceanography* 44.9 (2014), pp. 2317–2335.

[186] R. Mullyadzhanov and A. Gelash. “Direct scattering transform of large wave packets”. In: *Optics Letters* 44.21 (2019), pp. 5298–5301.

[187] H.-M. Yin, B. Tian, C.-R. Zhang, X.-X. Du, and X.-C. Zhao. “Optical breathers and rogue waves via the modulation instability for a higher-order generalized nonlinear Schrödinger equation in an optical fiber transmission system”. In: *Nonlinear Dynamics* 97.1 (2019), pp. 843–852.

[188] A. R. Osborne. “Nonlinear fourier analysis: Rogue waves in numerical modeling and data analysis”. In: *Journal of Marine Science and Engineering* 8.12 (2020), p. 1005.

[189] A. Calini and C. M. Schober. “Dynamical criteria for rogue waves in nonlinear Schrödinger models”. In: *Nonlinearity* 25.12 (2012), R99.

[190] H. Luo, X. Fang, and B. Ertas. “Hilbert transform and its engineering applications”. In: *AIAA journal* 47.4 (2009), pp. 923–932.

[191] S. Wahls, S. Chimmalgi, and P. J. Prins. “FNFT: A software library for computing nonlinear Fourier transforms”. In: *Journal of Open Source Software* 3.23 (2018), p. 597.

[192] A. Calini. “A note on a Bäcklund transformation for the continuous Heisenberg model”. In: *Physics Letters A* 203.5-6 (1995), pp. 333–344.

[193] P. Grinevich and M. U. Schmidt. “Closed curves in R^3: a characterization in terms of curvature and torsion, the Hasimoto map and periodic solutions of the Filament Equation”. In: *arXiv preprint dg-ga/9703020* (1997).

[194] A. M. Calini and T. A. Ivey. “Connecting geometry, topology and spectra for finite-gap NLS potentials”. In: *Physica D: Nonlinear Phenomena* 152 (2001), pp. 9–19.

[195] K. F. Hasselmann, T. P. Barnett, E. Bouws, H. Carlson, D. E. Cartwright, K. Eake, J. Euring, A. Gicnapp, D. Hasselmann, P. Kruseman, *et al.* “Measurements of wind-wave growth and swell decay during the Joint North Sea Wave Project (JONSWAP).” In: *Ergaenzungsheft zur Deutschen Hydrographischen Zeitschrift, Reihe A* (1973).

[196] J. Gunson and A. K. Magnusson. “Investigating conditions for rogue wave events from spectral wave observations and models”. In: *Proc. 7th International workshop on Wave Hindcasting and Forecasting*. 2002.

[197] H. G. Payer, H. Rathje, and T. E. SCHELLIN. “Shipboard routing assistance: Decision making support for operation of container ships in heavy seas. Discussion”. In: *Transactions-Society of Naval Architects and Marine Engineers* 112 (2004), pp. 1–13.

[198] G. F. Clauss, D. Testa, S. Kosleck, and R. Stück. “Forecast of critical wave groups from surface elevation snapshots”. In: *International Conference on Offshore Mechanics and Arctic Engineering*. Vol. 42681. 2007, pp. 79–88.

[199] T. Hilmer and E. Thornhill. “Observations of predictive skill for real-time deterministic sea waves from the WaMoS II”. In: *OCEANS 2015-MTS/IEEE Washington*. IEEE. 2015, pp. 1–7.

[200] W. M. Milewski, B. S. Connell, V. J. Vinciullo, and I. N. Kirschner. “Reduced order model for motion forecasts of one or more vessels”. In: *International Conference on Offshore Mechanics and Arctic Engineering*. Vol. 56598. American Society of Mechanical Engineers. 2015, V011T12A057.

[201] L. Shemer, E. Kit, H. Jiao, and O. Eitan. “Experiments on nonlinear wave groups in intermediate water depth”. In: *Journal of Waterway, Port, Coastal, and Ocean Engineering* 124.6 (1998), pp. 320–327.

[202] L. Shemer, E. Kit, and H. Jiao. “An experimental and numerical study of the spatial evolution of unidirectional nonlinear water-wave groups”. In: *Physics of Fluids* 14.10 (2002), pp. 3380–3390.

[203] K. Trulsen and C. T. Stansberg. “Spatial evolution of water surface waves: Numerical simulation and experiment of bichromatic waves”. In: *The Eleventh International Offshore and Polar Engineering Conference*. OnePetro. 2001.

[204] K. B. Dysthe, K. Trulsen, H. E. Krogstad, and H. Socquet-Juglard. “Evolution of a narrow-band spectrum of random surface gravity waves”. In: *Journal of Fluid Mechanics* 478 (2003), pp. 1–10.

[205] V. Ruban. “Gaussian variational ansatz in the problem of anomalous sea waves: Comparison with direct numerical simulation”. In: *Journal of Experimental and Theoretical Physics* 120.5 (2015), pp. 925–932.

[206] M. Farazmand and T. P. Sapsis. “Reduced-order prediction of rogue waves in two-dimensional deep-water waves”. In: *Journal of Computational Physics* 340 (2017), pp. 418–434.

[207] B. J. West, K. A. Brueckner, R. S. Janda, D. M. Milder, and R. L. Milton. “A new numerical method for surface hydrodynamics”. In: *Journal of Geophysical Research: Oceans* 92.C11 (1987), pp. 11803–11824.

[208] D. G. Dommermuth and D. K. Yue. “A high-order spectral method for the study of nonlinear gravity waves”. In: *Journal of Fluid Mechanics* 184 (1987), pp. 267–288.

[209] M. Tanaka. “Verification of Hasselmann’s energy transfer among surface gravity waves by direct numerical simulations of primitive equations”. In: *Journal of Fluid Mechanics* 444 (2001), pp. 199–221.

[210] M. Klein, M. Dudek, G. F. Clauss, S. Ehlers, J. Behrendt, N. Hoffmann, and M. Onorato. “On the deterministic prediction of water waves”. In: *Fluids* 5.1 (2020), p. 9.

[211] F. Pedregosa, G. Varoquaux, A. Gramfort, V. Michel, B. Thirion, O. Grisel, M. Blondel, P. Prettenhofer, R. Weiss, V. Dubourg, J. Vanderplas, A. Passos, D. Cournapeau, M. Brucher, M. Perrot, and E. Duchesnay. “Scikit-learn: Machine Learning in Python”. In: *Journal of Machine Learning Research* 12 (2011), pp. 2825–2830.

[212] J. S. Russell. “Report on waves”. In: *Report of the fourteenth meeting of the British Association for the Advancement of Science*. Vol. 25. 1844.

[213] P. de Koster, M. Brühl, and S. Wahls. “Water-depth identification from free-surface data using the KdV-based nonlinear Fourier transform”. In: *International Conference on Offshore Mechanics and Arctic Engineering*. Vol. 85901. American Society of Mechanical Engineers. 2022, V05BT06A056.

[214] I. Teutsch, R. Weisse, and S. Wahls. “Brief communication: Implications of outstanding solitons for the occurrence of rogue waves at two additional sites in the North Sea”. In: *Natural Hazards and Earth System Sciences* 24.6 (2024), pp. 2065–2069.

[215] A. Slunyaev. “Soliton groups and extreme wave occurrence in simulated directional sea waves”. In: *Physics of Fluids* 36.7 (2024).

[216] G. Ducrozet, F. Bonnefoy, D. Le Touzé, and P. Ferrant. “HOS-ocean: Open-source solver for nonlinear waves in open ocean based on High-Order Spectral method”. In: *Computer Physics Communications* 203 (2016), pp. 245–254.

[217] G. Ducrozet, F. Bonnefoy, D. Le Touzé, and P. Ferrant. “3-D HOS simulations of extreme waves in open seas”. In: *Natural Hazards and Earth System Sciences* 7.1 (2007), pp. 109–122.

[218] W. Xiao, Y. Liu, G. Wu, and D. K. Yue. “Rogue wave occurrence and dynamics by direct simulations of nonlinear wave-field evolution”. In: *Journal of Fluid Mechanics* 720 (2013), pp. 357–392.

[219] A. Kokorina and A. Slunyaev. “Lifetimes of rogue wave events in direct numerical simulations of deep-water irregular sea waves”. In: *Fluids* 4.2 (2019), p. 70.

[220] E. M. Bitner-Gregersen, O. Gramstad, A. K. Magnusson, and M. P. Malila. “Extreme wave events and sampling variability”. In: *Ocean Dynamics* 71.1 (2021), pp. 81–95.

[221] C. Kirezci, A. V. Babanin, and D. Chalikov. “Probabilistic assessment of rogue wave occurrence in directional wave fields”. In: *Ocean Dynamics* 71.11-12 (2021), pp. 1141–1166.

[222] S. Davison, A. Benetazzo, F. Barbariol, G. Ducrozet, J. Yoo, and M. Marani. “Space-time statistics of extreme ocean waves in crossing sea states”. In: *Frontiers in Marine Science* 9 (2022), p. 1002806.

[223] A. Slunyaev and A. Kokorina. “Account of occasional wave breaking in numerical simulations of irregular water waves in the focus of the rogue wave problem”. In: *Water Waves* 2.2 (2020), pp. 243–262.

[224] G. Ducrozet, F. Bonnefoy, and Y. Perignon. “Applicability and limitations of highly non-linear potential flow solvers in the context of water waves”. In: *Ocean Engineering* 142 (2017), pp. 233–244.

[225] B. R. Seiffert and G. Ducrozet. “Simulation of breaking waves using the high-order spectral method with laboratory experiments: wave-breaking energy dissipation”. In: *Ocean Dynamics* 68.1 (2018), pp. 65–89.

[226] F. Bonnefoy, G. Ducrozet, D. Le Touzé, and P. Ferrant. “Time domain simulation of nonlinear water waves using spectral methods”. In: *Advances in numerical simulation of nonlinear water waves*. World Scientific, 2010, pp. 129–164.

[227] G. Ducrozet, H. B. Bingham, A. P. Engsig-Karup, F. Bonnefoy, and P. Ferrant. “A comparative study of two fast nonlinear free-surface water wave models”. In: *International Journal for Numerical Methods in Fluids* 69.11 (2012), pp. 1818–1834.

[228] G. Ducrozet, F. Bonnefoy, and P. Ferrant. “Rogue waves in large-scale fully-nonlinear High-Order-Spectral simulations”. In: *Proc. 22nd International Workshop on Water Waves and Floating Bodies (IWWWFB), Croatia*. 2007.

[229] G. Ducrozet, M. Abdolahpour, F. Nelli, and A. Toffoli. “Predicting the occurrence of rogue waves in the presence of opposing currents with a high-order spectral method”. In: *Physical Review Fluids* 6.6 (2021), p. 064803.

[230] Z. Li, G. Deng, P. Queutey, B. Bouscasse, G. Ducrozet, L. Gentaz, D. Le Touzé, and P. Ferrant. “Comparison of wave modeling methods in CFD solvers for ocean engineering applications”. In: *Ocean Engineering* 188 (2019), p. 106237.

[231] Q. Xiao, R. Zhu, and S. Huang. “Hybrid time-domain model for ship motions in nonlinear extreme waves using HOS method”. In: *Ocean Engineering* 192 (2019), p. 106554.

[232] J. R. Cash and A. H. Karp. “A variable order Runge-Kutta method for initial value problems with rapidly varying right-hand sides”. In: *ACM Transactions on Mathematical Software (TOMS)* 16.3 (1990), pp. 201–222.

[233] A. Osborne. “Soliton physics and the periodic inverse scattering transform”. In: *Physica D: Nonlinear Phenomena* 86.1-2 (1995), pp. 81–89.

[234] S. Wahls and H. V. Poor. “Fast inverse nonlinear Fourier transform for generating multi-solitons in optical fiber”. In: *2015 IEEE International Symposium on Information Theory (ISIT)*. IEEE. 2015, pp. 1676–1680.

[235] S. Wahls. “Fiber-optic communication using fast Nonlinear Fourier transforms”. In: *2016 Optical Fiber Communications Conference and Exhibition (OFC)*. IEEE. 2016, pp. 1–3.

[236] P. De Koster and S. Wahls. “Dispersion and nonlinearity identification for single-mode fibers using the nonlinear Fourier transform”. In: *Journal of Lightwave Technology* 38.12 (2020), pp. 3252–3260.

[237] M. S. Longuet-Higgins. “Observation of the directional spectrum of sea waves using the motions of a floating buoy”. In: *Oc. Wave Spectra* (1963).

[238] V. S. Kumar, M. Deo, N. Anand, and P. Chandramohan. “Estimation of wave directional spreading in shallow water”. In: *Ocean Engineering* 26.1 (1998), pp. 83–98.

[239] M. Miche. “Mouvements ondulatoires de la mer en profondeur constante ou décroissante”. In: *Annales de Ponts et Chaussées, 1944, pp (1) 26-78,(2) 270-292,(3) 369-406* (1944).

[240] B. Ruessink, D. Walstra, and H. Southgate. “Calibration and verification of a parametric wave model on barred beaches”. In: *Coastal Engineering* 48.3 (2003), pp. 139–149.

[241] W. Rattanapitikon. “Calibration and modification of energy dissipation models for irregular wave breaking”. In: *Ocean Engineering* 34.11-12 (2007), pp. 1592–1601.

[242] W. Rattanapitikon. “Verification of significant wave representation method”. In: *Ocean Engineering* 35.11-12 (2008), pp. 1259–1270.

[243] R. G. Dean and R. A. Dalrymple. *Water wave mechanics for engineers and scientists*. Vol. 2. world scientific publishing company, 1991.

[244] Z.-J. You. “A close approximation of wave dispersion relation for direct calculation of wavelength in any coastal water depth”. In: *Applied Ocean Research* 30.2 (2008), pp. 113–119.

[245] D. Dommermuth. “The initialization of nonlinear waves using an adjustment scheme”. In: *Wave motion* 32.4 (2000), pp. 307–317.

[246] A. Slunyaev and A. Kokorina. “Numerical simulation of the sea surface rogue waves within the framework of the potential Euler equations”. In: *Izvestiya, Atmospheric and Oceanic Physics* 56 (2020), pp. 179–190.

[247] I.-C. Kim, G. Ducrozet, V. Leroy, F. Bonnefoy, Y. Perignon, and S. Delacroix. “Numerical and experimental investigation on deterministic prediction of ocean surface wave and wave excitation force”. In: *Applied Ocean Research* 142 (2024), p. 103834.

[248] A. Toffoli, M. Onorato, A. Osborne, and J. Monbaliu. “Non-Gaussian properties of shallow water waves in crossing seas”. In: *Extreme Ocean Waves* (2008), pp. 53–69.

[249] E. Pelinovsky and A. Sergeeva. “Numerical modeling of the KdV random wave field”. In: *European Journal of Mechanics-B/Fluids* 25.4 (2006), pp. 425–434.

[250] T. A. Driscoll, N. Hale, and L. N. Trefethen. *Chebfun guide*. 2014.

[251] J. W. Miles. “Solitary waves”. In: *Annual Review of Fluid Mechanics* 12.1 (1980), pp. 11–43.

[252] S. Novikov, S. V. Manakov, L. P. Pitaevskii, and V. E. Zakharov. *Theory of solitons: the inverse scattering method*. Springer Science & Business Media, 1984.

[253] G. Boffetta and A. R. Osborne. “Computation of the direct scattering transform for the nonlinear Schrödinger equation”. In: *Journal of computational physics* 102.2 (1992), pp. 252–264.

[254] A. Gelash and D. Agafontsev. “Strongly interacting soliton gas and formation of rogue waves”. In: *Physical Review E* 98.4 (2018), p. 042210.

[255] G. A. El. “Critical density of a soliton gas”. In: *Chaos: An Interdisciplinary Journal of Nonlinear Science* 26.2 (2016), p. 023105.

[256] S. Wahls, S. T. Le, J. E. Prilepsk, H. V. Poor, and S. K. Turitsyn. “Digital backpropagation in the nonlinear Fourier domain”. In: *2015 IEEE 16th International Workshop on Signal Processing Advances in Wireless Communications (SPAWC)*. IEEE. 2015, pp. 445–449.

[257] E. V. Sedov, A. A. Redyuk, M. P. Fedoruk, A. A. Gelash, L. L. Frumin, and S. K. Turitsyn. “Soliton content in the standard optical OFDM signal”. In: *Optics Letters* 43.24 (2018), pp. 5985–5988.

[258] A. Boukhanovsky and C. G. Soares. “Modelling of multipeaked directional wave spectra”. In: *Applied Ocean Research* 31.2 (2009), pp. 132–141.

[259] J. G. Rueda-Bayona, A. Guzmán, and J. J. Cabello Eras. “Selection of JONSWAP spectra parameters During Water-depth and Sea-state Transitions”. In: *Journal of Waterway, Port, Coastal, and Ocean Engineering* 146.6 (2020), p. 04020038.

[260] Y.-C. Lee and S. Wahls. “Interpretation of Soliton Energy Ratios Measured in Directional Wave Fields”. In: *Available at SSRN 5669630* (2026).

[261] H. C. Yuen and B. M. Lake. “Nonlinear dynamics of deep-water gravity waves”. In: *Advances in Applied Mechanics* 22 (1982), pp. 67–229.

[262] S. Turitsyn, E. Sedov, A. Redyuk, and M. Fedoruk. “Nonlinear spectrum of conventional OFDM and WDM return-to-zero signals in nonlinear channel”. In: *Journal of Lightwave Technology* 38.2 (2019), pp. 352–358.

[263] M. Onorato, T. Waseda, A. Toffoli, L. Cavaleri, O. Gramstad, P. Janssen, T. Kinoshita, J. Monbaliu, N. Mori, A. R. Osborne, *et al.* “Statistical Properties of Directional Ocean Waves: The Role of the Modulational Instability in the Formation of Extreme Events”. In: *Physical Review Letters* 102.11 (2009), p. 114502.

[264] Z. Rapti, P. Kevrekidis, D. Frantzeskakis, and B. Malomed. “On the modulational instability of the nonlinear Schrödinger equation with dissipation”. In: *Physica Scripta* 2004.T113 (2004), p. 74.

[265] J. D. Carter and C. C. Contreras. “Stability of plane-wave solutions of a dissipative generalization of the nonlinear Schrödinger equation”. In: *Physica D: Nonlinear Phenomena* 237.24 (2008), pp. 3292–3296.

[266] M. Onorato and D. Proment. “Approximate rogue wave solutions of the forced and damped nonlinear Schrödinger equation for water waves”. In: *Physics Letters A* 376.45 (2012), pp. 3057–3059.

[267] M. Brunetti, N. Marchiando, N. Berti, and J. Kasparian. “Nonlinear fast growth of water waves under wind forcing”. In: *Physics Letters A* 378.14-15 (2014), pp. 1025–1030.

[268] A. Alberello and E. I. Părău. “A dissipative nonlinear Schrödinger model for wave propagation in the marginal ice zone”. In: *Physics of Fluids* 34.6 (2022).

[269] V. I. Karpman. *Non-linear waves in dispersive media: International series of monographs in natural philosophy*. Vol. 71. Elsevier, 2016.

[270] A. Chabchoub, M. Onorato, and N. Akhmediev. “Hydrodynamic envelope solitons and breathers”. In: *Rogue and Shock Waves in Nonlinear Dispersive Media* (2016), pp. 55–87.

[271] T. Aktosun. “Inverse scattering transform and the theory of solitons”. In: *Solitons*. Springer, 2022, pp. 47–61.

8

[272] V. Vaibhav. “Fast inverse nonlinear Fourier transform”. In: *Physical Review E* 98.1 (2018), p. 013304.

[273] S. Chimmalgi, P. J. Prins, and S. Wahls. “Fast nonlinear Fourier transform algorithms using higher order exponential integrators”. In: *IEEE Access* 7 (2019), pp. 145161–145176.

[274] A. Slunyaev, G. F. Clauss, M. Klein, and M. Onorato. “Simulations and experiments of short intense envelope solitons of surface water waves”. In: *Physics of Fluids* 25.6 (2013), p. 067105.

[275] A. Slunyaev. “Analysis of the nonlinear spectrum of intense sea wave with the purpose of extreme wave prediction”. In: *Radiophysics and Quantum Electronics* 61 (2018), pp. 1–21.

[276] W. Xia, Y. Ma, G. Dong, J. Zhang, and X. Ma. “Emergence of solitons from irregular waves in deep water”. In: *Journal of Marine Science and Engineering* 9.12 (2021), p. 1369.

[277] S. Wahls and H. V. Poor. “Introducing the fast nonlinear Fourier transform”. In: *2013 IEEE International Conference on Acoustics, Speech and Signal Processing*. IEEE. 2013, pp. 5780–5784.

[278] P. J. Prins and S. Wahls. “Higher order exponential splittings for the fast nonlinear Fourier transform of the Korteweg-de Vries equation”. In: *2018 IEEE International conference on acoustics, speech and signal processing (ICASSP)*. IEEE. 2018, pp. 4524–4528.

[279] L. E. Borgman. “Directional spectra models for design use”. In: *Offshore Technology Conference*. OTC. 1969, OTC–1069.

[280] L. E. Borgman. “Directional wave spectra from wave sensors”. In: *Ocean Wave Climate*. Springer, 1979, pp. 269–300.

[281] M. Benoit. “Extensive comparison of directional wave analysis methods from gauge array data”. In: *Proc. 2nd Int. Symp. on Ocean Wave Measurement and Analysis (ASCE)*. 1993, pp. 740–754.

[282] N. Hashimoto. “Analysis of the directional wave spectrum from field data”. In: *Advances in Coastal and Ocean Engineering* 3 (1997), pp. 103–144.

[283] S. Massel and R. Brinkman. “On the determination of directional wave spectra for practical applications”. In: *Journal of computational physics* 20.6 (1998), pp. 357–374.

[284] M. Tucker, P. G. Challenor, and D. Carter. “Numerical simulation of a random sea: a common error and its effect upon wave group statistics”. In: *Journal of computational physics* 6.2 (1984), pp. 118–122.

[285] S. R. Massel. *Ocean surface waves: their physics and prediction*. Vol. 45. World scientific, 2017.

[286] S. Annenkov and V. Shrira. “Evaluation of skewness and kurtosis of wind waves parameterized by JONSWAP spectra”. In: *Journal of Physical Oceanography* 44.6 (2014), pp. 1582–1594.

[287] T. Waseda, M. Hallerstig, K. Ozaki, and H. Tomita. “Enhanced freak wave occurrence with narrow directional spectrum in the North Sea”. In: *Geophysical Research Letters* 38.13 (2011).

[288] T. Teich, N. Groll, and R. Weisse. “Long-term statistics of potentially hazardous sea states in the North Sea 1958–2014”. In: *Ocean dynamics* 68 (2018), pp. 1559–1570.

[289] K. L. Henderson, D. H. Peregrine, and J. W. Dold. “Unsteady water wave modulations: fully nonlinear solutions and comparison with the nonlinear Schrödinger equation”. In: *Wave motion* 29.4 (1999), pp. 341–361.

[290] M. I. Yousefi and F. R. Kschischang. “Information transmission using the nonlinear Fourier transform, Part I: Mathematical tools”. In: *IEEE Transactions on Information Theory* 60.7 (2014), pp. 4312–4328.

[291] P. G. Drazin and R. S. Johnson. *Solitons: an introduction*. Vol. 2. Cambridge university press, 1989.

[292] L. D. Faddeev and L. A. Takhtajan. *Hamiltonian methods in the theory of solitons*. Vol. 23. Springer, 1987.

[293] M. Onorato, A. R. Osborne, M. Serio, L. Cavaleri, C. Brandini, and C. T. Stansberg. “Observation of strongly non-Gaussian statistics for random sea surface gravity waves in wave flume experiments”. In: *Phys. Rev. E* 70 (6 Dec. 2004), p. 067302.

[294] D. S. Agafontsev and V. E. Zakharov. “Integrable turbulence and formation of rogue waves”. In: *Nonlinearity* 28.8 (2015), p. 2791.

[295] F. Carbone, D. Dutykh, and G. El. “Macroscopic dynamics of incoherent soliton ensembles: Soliton gas kinetics and direct numerical modelling”. In: *Europhysics Letters* 113.3 (2016), p. 30003.

[296] F. Mitschke, G. Steinmeyer, and A. Schwache. “Generation of one-dimensional optical turbulence”. In: *Physica D: Nonlinear Phenomena* 96.1-4 (1996), pp. 251–258.

[297] A. Schwache and F. Mitschke. “Properties of an optical soliton gas”. In: *Physical Review E* 55.6 (1997), p. 7720.

[298] R. Cienfuegos, P. A. Catalán, R. P. Flores, M. Guerra, F. Lucero, J. Galaz, S. Wahls, P. Díaz, R. Gómez, and C. Esparza. “Soliton gas dynamics and rogue wave enhancement in a natural coastal environment”. In: *Phys. Rev. Res.* (Sept. 2025).

[299] O. Nwogu. “Maximum entropy estimation of directional wave spectra from an array of wave probes”. In: *Applied Ocean Research* 11.4 (1989), pp. 176–182.

[300] O. M. Mazzaretto and M. Menendez. “A worldwide coastal analysis of the climate wave systems”. In: *Frontiers in Marine Science* 11 (2024), p. 1385285.

[301] J. Portilla, F. J. Ocampo-Torres, and J. Monbaliu. “Spectral partitioning and identification of wind sea and swell”. In: *Journal of Atmospheric and Oceanic Technology* 26.1 (2009), pp. 107–122.

[302] V. Zakharov and A. Shabat. “Exact theory of two-dimensional self-focusing and one-dimensional self-modulation of waves in nonlinear media”. In: *Sov. Phys. JETP* 34.1 (1972), p. 62.

[303] G. Deng, G. Biondini, and S. Trillo. “Small dispersion limit of the Korteweg–de Vries equation with periodic initial conditions and analytical description of the Zabusky–Kruskal experiment”. In: *Physica D: Nonlinear Phenomena* 333 (2016), pp. 137–147.

[304] J. Lin. “Evolution of the scattering data under the classical Darboux transform for su (2) soliton systems”. In: *Acta Mathematicae Applicatae Sinica, English Series* 6.4 (1990), pp. 308–316.

[305] I. M. DesJardin and C. M. Hartzell. “Nonlinear spectral analysis of ion acoustic solitons arising from a streaming charged object using the numerical inverse scattering transform”. In: *Physics of Plasmas* 29.11 (2022).

[306] L. H. Holthuijsen. *Waves in oceanic and coastal waters*. Cambridge university press, 2010.

[307] K. Ewans, G. Feld, and P. Jonathan. “On wave radar measurement”. In: *Ocean Dynamics* 64.9 (2014), pp. 1281–1303.

[308] Y.-C. Lee and S. Wahls. “Interpretation of Soliton Energy Ratios Measured in Directional Wave Fields”. In: *submitted* (Aug. 2025).

[309] B. Deconinck, D. E. Pelinovsky, and J. D. Carter. “Transverse instabilities of deep-water solitary waves”. In: *Proceedings of the Royal Society A: Mathematical, Physical and Engineering Sciences* 462.2071 (2006), pp. 2039–2061.

[310] D. E. Pelinovsky, E. Rouvinskaya, O. E. Kurkina, and B. Deconinck. “Short-wave transverse instabilities of line solitons of the two-dimensional hyperbolic nonlinear Schrödinger equation”. In: *Theoretical and Mathematical Physics* 179.1 (2014), pp. 452–461.

[311] L. Dostal. “The effect of random wind forcing in the nonlinear Schrödinger equation”. In: *Fluids* 4.3 (2019), p. 121.

[312] S. Manakov. “Inverse scattering transform for the time-dependent Schroedinger equation and Kadomtsev-Petviashvili equation”. In: *Physica D (Amsterdam);(Netherlands)* 3.1/2 (1981).

[313] M. Music, P. Perry, and S. Siltanen. “The nonlinear Fourier transform for two-dimensional subcritical potentials”. In: *Inverse Problems and Imaging* 8.4 (2014), pp. 1151–1167.

[314] P. Perry. “Miura maps and inverse scattering for the Novikov–Veselov equation”. In: *Analysis & PDE* 7.2 (2014), pp. 311–343.

[315] P. A. Perry. “Global well-posedness and long-time asymptotics for the defocussing Davey–Stewartson II equation in $H^{1,1}(\mathbb{C})$”. In: *Journal of Spectral Theory* 6.3 (2016), pp. 429–481.

[316] Y.-C. Lee and S. Wahls. “Impact of Errors in Buoy Measurements on Nonlinear Fourier Spectra”. In: *EGU General Assembly Conference Abstracts*. 2024, p. 20078.

[317] Y.-C. Lee and S. Wahls. “Are outstanding spectral solitons indicators for rogue waves in JONSWAP seas?” In: *EGU General Assembly Conference Abstracts*. 2023, EGU–3253.

ACKNOWLEDGEMENTS

This thesis was performed during my PhD studies at the Delft Center for Systems and Control (DCSC), Faculty of Mechanical Engineering (ME), Delft University of Technology. The funding was provided by the "2019 Key Field Scholarship Program" by the Ministry of Education, Taiwan, and the European Research Council (ERC) under the European Union's Horizon 2020 Research and Innovation Programme (grant agreement No 716669). Thanks to the financial support from the above-mentioned funding, which I gratefully acknowledge.

I would like to express my deepest gratitude to Professor Dr.-Ing. Sander Wahls. His passion for researching and uncovering the mysteries of various nonlinear systems inspired my interest in this field. With a background in hydraulic and ocean engineering, the topics on the nonlinear Fourier transform were quite challenging for me due to the required mathematical skills. During my time at TU Delft with Sander, I benefited greatly from his brilliant expertise, his ability to conduct thorough and perfect research, and his clear concepts on how to complete comprehensive research. Sander was very patient in guiding me into the nonlinear world, even though I was new and did not understand much mathematics in the beginning. He has provided me invaluable guidance in conducting research, along with extensive support in enhancing my presentation and writing skills. After Sander's guidance, I am proud to finally present this completed thesis.

I would like to thank my promoter, Prof. Dr. ing. Raf Van de Plas for helping me deal with all the required administrative processes in the final steps leading to my defense. I am also grateful for his valuable comments on my thesis, which greatly improved the quality of the final version.

I also hold deep gratitude for Dr.-Ing. Markus Brühl, who brought me into the field of nonlinear Fourier transform. In 2018, I got an opportunity under the DAAD Short-Term Research Grants, German Academic Exchange Service (DAAD), Germany, to work with Markus Brühl at the Leichtweiß-Institut für Wasserbau, Technische Universität Braunschweig, Germany. He opened the door to the wonderful world of nonlinear waves. We had many discussions in both Braunschweig and Delft that significantly enhanced my knowledge of nonlinear waves. With his support, I was able to publish several papers on nonlinear wave analysis. His insightful feedback and thoughtful comments have been invaluable on my PhD journey.

I would like to express my sincere gratitude to my doctoral committee members, Prof. Dr. Henrik Kalisch (University of Bergen), Prof. dr. Henk M. Schuttelaars (Delft University of Technology), Prof. Dr. Norbert Hoffmann (Hamburg University of Technology), and Prof. dr. ir. Ton van den Bremer (Delft University of Technology), for their time and insightful comments during my defense. Their valuable feedback has greatly improved the quality of this thesis.

I would also like to thank my funding agency, the Ministry of Education, Taiwan, for

supporting me in completing my Ph.D. I am grateful to Ms. Beilei Chen of the Education Division at the Taipei Representative Office in the EU and Belgium for her assistance with my scholarship affairs and for providing me the opportunity to build connections with other scientists and PhD students in the Netherlands and Belgium.

Furthermore, I would like to express my sincere gratitude to Prof. Dong-Jing Doong of National Cheng Kung University, Taiwan, for generously providing the invaluable field data used in this dissertation. I am deeply thankful for his continuous support during my participation in the Ocean Engineering Conference in Taiwan. He also offered me a research position in Taiwan during the 5th and 6th year of my PhD, which allowed me to finalize my studies successfully. With his help, I was able to complete my PhD research and journal papers smoothly. His insightful guidance and encouraging attitude have been a constant source of inspiration, motivating me to persevere in my academic journey. From the very beginning of my studies until now, his mentorship has shaped me into an independent researcher. At the same time, I would like to express my sincere gratitude to Prof. Chia-Chuen Kao for the guidance and direction he has provided throughout my academic journey. Professor Kao also visited me in the Netherlands during my studies there, and the time we spent having dinner together was among my happiest moments.

I would also like to express my gratitude to Dr. Ina Tuetsch, who previously worked at Helmholtz-Zentrum Hereon and is now with the Federal Waterways Engineering and Research Institute (BAW). She started her PhD around the same time as I did, and we had the opportunity to meet at several conferences, where we always enjoyed engaging discussions. We also work on similar research topics and have had many discussions during our meetings. Additionally, I would like to thank Dr. Ralf Weisse at Helmholtz-Zentrum Hereon for his support. I deeply appreciate their generosity in sharing their data for this study, which was indispensable to the completion of my dissertation.

I would also like to express my sincere thanks to Prof. Guillaume Ducrozet of LUNAM Université, École Centrale de Nantes, LHEEA Lab, for his valuable suggestions regarding the setup of the HOS-ocean model simulations. I greatly appreciated the many insightful discussions we had during the conference and workshop, where his recommendations were always thoughtful and meaningful.

Indeed, my academic journey from my master to the present has been a long and transformative one. This journey has been both dramatic and significant, made possible by the unwavering support of my family and friends. My father, Shui-Jin Lee, has always been my guardian angel, watching over me and offering faith during the toughest times. My mother, Li-Hua Huang, is a person of remarkable perseverance, never giving up even in the face of any challenges. Her strength has shaped my own resilience, teaching me to remain optimistic and determined, no matter the difficulties. I am also deeply grateful to my brothers, Po-Wei Lee and Yi-Jie Lee, for their constant companionship and support. My family has always stood by my decisions and encouraged me to pursue the path that led to the completion of my Ph.D. Once again, I express my heart thanks to them all for their love, encouragement, and belief in me.

Last but not least, I would like to express my sincere thanks to my colleagues Pascal, Jacques, Edoardo, Hamed, Shahzeb, Shrinivas, Vinod, Peter, Léonore, Roger, Maria, Sreeshma, and David in DCSC for sharing daily life with me in the office, from lunch,

coffee breaks to travel, and fun activities. I am especially grateful to Pascal for academic discussions, exploring various topics together, playing board games, and cycling in the Netherlands. These moments have greatly enriched my experience and made my time in the Netherlands truly memorable.

I would also like to extend my thanks to my Taiwanese friends Liang-Shin, Chu-Hsuan, Yu-Wen, Chi, Chia-Yo, and Min, who accompanied me through difficult times during COVID. Traveling with all of you in Europe was the most enjoyable experience. To my badminton friends Tianliang, Chia-Yo, Kuan-Wei, Bofan, Junhan, Hu, Ni, Zhenyang, Jiahong, Li, Naqi, and Alice, with whom I played every Tuesday and weekend at TU Delft. And to my teammates from DKC, Jop, Tess, Artur, Marieke, Simen, and Chenji, who made training and competitions so enjoyable. Thanks to the Taiwanese PhD group in Delft, Fan-Hsuan, Yu-Chou, Yu-Wen, Cinco, Quieene, Emilie, Pei-Yu, Yun-Ching, Yu-Fan, Chun-Ting, and Chih-Hsien, for being on separate boats but sailing together toward our shared PhD destination. I would like to thank my colleagues at NCKU, Taiwan, Ying-Chih, Hsu-Min, Min-Feng, Wei-Cheng, Zheng-Hao, Wei-Zhan and other junior lab members for their companionship, support, and inspiring discussions. I would also like to thank those I haven't mentioned here, but who have been with me during my journey. You all have made my life in Delft incredibly happy and unforgettable. Thanks to the friendships and support I've found. You have made this place feel like home, and I'll always cherish the memories. Thank you all for being part of this journey.

Finally, I would like to express my gratitude to myself for having the strength and determination to persist until the end of this PhD journey. The road has been challenging yet remarkable, filled with both difficulties and unforgettable moments. Along the way, I have met many inspiring people who encouraged and supported me. The path of academic research, much like humanity's exploration of the ocean, remains vast and largely uncharted. I hope to continue growing in my academic pursuit and to become the kind of researcher and person I aspire to be.

Yu-Chen, Lee
Delft, September 2026



Turtle Island, Yilan, Taiwan
Paintings by Ms. Li-Hua Huang
October, 2025

CURRICULUM VITÆ

Yu-Chen LEE

09-06-1993 Born in Yilan, Taiwan.

EDUCATION

2011–2015 Bachelor
Department of Hydraulics and Ocean Engineering
National Cheng Kung University, Tainan, Taiwan

2015–2017 Master
Department of Hydraulics and Ocean Engineering
National Cheng Kung University, Tainan, Taiwan

2020-2025 PhD. Systems & Control,
Faculty of Mechanical Engineering,
Delft University of Technology, Delft, The Netherlands

Thesis:	**Applying the Nonlinear Fourier Transform to Non-Integrable Real-World Ocean Waves** - Analysis of Rogue Waves and Soliton Gases
Promoter:	Prof. Dr.- Ing. S. Wahls & Prof. Dr. ing. R. Van de Plas
Former supervisor:	Dr.- Ing. M. Brühl

List of Publications

Journal Articles

4. Y.-C. Lee and S. Wahls. “Field observation of soliton gases in the deep open ocean”. In: *Results in Physics* (2026), p. 108726

3. Y.-C. Lee, and S. Wahls. "Interpretation of Soliton Energy Ratios Measured in Directional Wave Fields." In *Applied Ocean Research* (2025), under review.

2. Y.-C. Lee and S. Wahls. “Impact of directional spreading on nonlinear KdV-soliton spectra in intermediate water”. In: *Wave Motion* 137 (2025), p. 103542

1. Y.-C. Lee, M. Brühl, D.-J. Doong, and S. Wahls. “Nonlinear Fourier classification of 663 rogue waves measured in the Philippine Sea”. In: *PloS one* 19.5 (2024), e0301709

Conference Proceedings

4. Y.-C. Lee and S. Wahls. “Impact of Errors in Buoy Measurements on Nonlinear Fourier Spectra”. In: *EGU General Assembly Conference Abstracts*. 2024, p. 20078

3. Y.-C. Lee, M. Brühl, and S. Wahls. “When Do JONSWAP Spectra Lead to Soliton Gases in Deep Water Conditions?” In: *International Conference on Offshore Mechanics and Arctic Engineering*. Vol. 86878. American Society of Mechanical Engineers. 2023, V005T06A101

2. Y.-C. Lee and S. Wahls. “Are outstanding spectral solitons indicators for rogue waves in JONSWAP seas?” In: *EGU General Assembly Conference Abstracts*. 2023, EGU–3253

1. Y.-C. Lee, S. Wahls, and M. Brühl. “Evaluation of Nonlinear Fourier-Based Maximum Wave Height Predictors Under the Nonlinear Schrödinger Equation”. In: *International Conference on Offshore Mechanics and Arctic Engineering*. Vol. 85901. American Society of Mechanical Engineers. 2022, V05BT06A060


TU Delft